Synthesis and functionalization of hybrid plasmon-semiconductor nanoparticles for cancer phototherapy

Yuzhou Pu

PSL UNIVERSITÉ PARIS

THÈSE DE DOCTORAT
DE L'UNIVERSITÉ PSL

Préparée à Ecole supérieure de physique et de chimie industrielles de la ville de Paris (LPEM)

Synthesis and functionalization of hybrid plasmon-semiconductor nanoparticles for cancer phototherapy

Synthèse et fonctionnalisation de nanoparticules hybrides plasmon-semiconductrices pour la photothérapie du cancer

Soutenue par
Yuzhou PU
Le 22 septembre 2023

Ecole doctorale n° 397
Physique et chimie des matériaux

Spécialité
Chimie des matériaux

Composition du jury :

Souhir Boujday Professeure, Sorbonne Université	*Présidente*
Damien Mertz Chargé de recherche, Université de Strasbourg	*Rapporteur*
Stéphane Roux Professeur, Université de Franche - Comté	*Rapporteur*
Bich-Thuy Doan Chargée de recherche, Chimie ParisTech - PSL	*Examinatrice*
Guilhem Bousquet Professeur, Université Sorbonne Paris Nord	*Examinateur*
Thomas Pons Chargé de recherche, ESPCI - PSL	*Directeur de thèse*

ESPCI PARIS | PSL

Remerciement

Je tiens tout d'abord à remercier les membres de jury de cette thèse, Damien Mertz, Stéphane Roux, Bich-Thuy Doan, Souhir Boujday et Guilhem Bousquet pour l'attention qu'ils ont consacrée à lecture de ma thèse, à l'écoute de ma présentation de soutenance et la discussion scientifique et enrichissante pendant ma soutenance. Je remercie également mes rapporteurs et leurs retours de rapport sur mon manuscrit. Ces remarques, sans lesquels mon manuscrit de thèse ne serait pas complet, sont essentielles et constructives.

Je donne ma reconnaissance la plus profonde et chaleureuse à mon directeur de thèse, Thomas Pons, qui tout d'abord m'a accueilli dans cette famille incroyable, le groupe SI2. Tu m'as accompagné tout au long de ma thèse : tout au début ton aide pour me faire familiariser le domaine de recherche, la liberté que tu m'as conférée à y exploiter, et puis ton guide sur l'orientation de mes recherches, ton assistance à la réalisation d'expérience, et enfin ton support et ton encouragement qui m'ont fait avancer jusqu'au bout. Nous avons travaillé en étroite collaboration au cours des trois dernières années et demie et nous avons vu ce projet s'épanouir de presque zéro à tous les résultats que nous avons obtenus à ce jour. Tu es toujours là pour m'écouter et m'encourager. Je me permets d'utiliser un proverbe chinois pour te décrire : « Les fleurs de pêcher et de prunier n'ont pas besoin de se vanter. Les touristes viennent spontanément en masse ». (Les vrais talents brillent toujours.) Ta brillante intelligence, ton bon sens de l'humour, ta passion pour la vie, ta serviabilité, ta compréhension et considération pour les autres m'ont laissé une impression inoubliable et m'ont profondément influencé. En tant que directeur de ma thèse, tu m'as appris bien plus que la simple manière de faire de la recherche. Je tiens aux trois ans et demi passés à travailler avec toi et j'espère que je pourrai toujours transmettre tout ce que j'ai appris de toi et, un jour, faire briller les autres.

Puis, je tiens à remercier à tous les membres de groupe SI2. Je me souviens encore la journée où je suis passé au labo pour l'entretien de mon stage de M2 : j'entendais les voix plaisantes sortir de la salle de pause et instantanément, cet environnement convivial m'a attiré et j'avais envie d'y rester. Je suis resté car tout au long de ces trois années l'équipe et les personnes qui y ont travaillé et qui y travaillent aujourd'hui ont pu créer un environnement qui a toujours évolué et j'ai toujours trouvé de la satisfaction à en faire partie et à vous côtoyer. Je vous remercie pour avoir m'accompagné et supporté au cours de ces trois ans.

Je remercie d'abord Nicolas, Sandrine, Alexandra et Céline, les permanents qui sont de véritables experts dans leurs domaines de recherche respectifs, sérieux dans leur travail tout en étant toujours passionnés par la vie, du sport à la cuisine. Je suis particulièrement reconnaissant à Xiangzhen, qui m'a apporté son soutien et son aide tout au long de ces trois années, tant au travail que dans la vie. Je remercie également les docteurs qui sont déjà diplômés. Antoine, Subha, Sheila, Mogha, Sophia et Fanny. C'est une grâce de vous avoir rencontré depuis le début de ma thèse. Votre amitié et soutien tout au long de ma thèse m'encourageaient, et vos réussites m'ont fait rêver. Puis, je dois dire que j'ai eu tellement de chance que j'ai commencé ma thèse avec Po, Coco et Mathias. Pendant ces trois ans, nous partageons non seulement nos expériences et sentiments de travail, mais aussi nos loisirs et passions communs comme les jeux, les langues, les voyages ainsi que les moments agréables passés au bars. Et bien sûr je ne peux pas oublier les personnes qui ont rejoint le labo plus tard : Léo, Nini, Lina, Charlie, Nour, Henri et Alice. Vous apportez autant d'énergie à l'équipe que les anciens. Je vous souhaite bon courage pour la suite et profitez bien du temps qui vous reste au labo ! Finalement, un grand merci aux stagiaires avec qui j'ai eu l'occasion de travailler durant ma thèse : Nicolas Kuszla, Juichi Bainvel-Sato et Béatrice Jeffries. Votre motivation, vos réflexions et votre dévouement ont grandement contribué à faire progresser nos projets communs. Sans votre implication, ces projets n'auraient pas atteint un tel niveau d'avancement.

Je tiens à remercier tous mes collaborateurs sans qui ce travail n'aurait pas pu être accompli. Je remercie Guilhem Bousquet, Christophe Leboeuf et Guillaume Gapihan de l'université Paris 13 pour leurs accompagnements et assistances de la partie expérimentale biologique. Je remercie Benoît Caron et Julie Noël de l'université Sorbonne pour leurs aides sur la partie de caractérisation de l'ICP/MS.

Je remercie également les personnes qui m'ont donné un coup de main en matériels ou qui m'ont formé. Je tiens à exprimer ma gratitude à Nicolas Sanson et Mohamed Hanafi du laboratoire SIMM pour leur aide des analyses DLS et GPC. Je remercie Gaël Blivet et Antoine Millereau du Laboratoire LBC pour les formations de la salle SCC et de l'utilisation du cytomètre. Je remercie Diana Zala et Vincenzo Verdi de l'Institut de Psychiatrie et de Neurosciences de Paris pour avoir fourni les cellules HeLa. Enfin, je suis reconnaissant à Frédéric Joubert de l'Université Sorbonne pour les fluorophores Rhodamine.

Je remercie Sophie Carenco et Cécile Sicard, les membres de mon comité de suivi de la thèse, pour leurs accompagnements et leurs conseils précieux.

Je tiens à exprimer ma gratitude envers Dimitri Roditchev, Francis Cassagne, Marie Claude Thème et Sophie Demonchaux pour leurs soutiens dans le bon fonctionnement du laboratoire et leurs assistances en procédures administratives.

Enfin, je remercie tous mes amis et ma famille qui m'ont soutenu tout au long de ma thèse et en particulier, mon bonheur, Huidi.

Table of Contents

Abbreviation List

AIBN	2,2′-Azobis(2-methylpropionitrile)
APMA	N-(3-aminopropyl)methacrylamide hydrochloride
AuNP	Spherical gold nanoparticles
AuNR	Gold nanorod
AuNRmin	Miniaturized gold nanorod
BS3	Bis(sulfosuccinimidyl)suberate
BSA	Bovine serum albumin
CTA	Chain transfer agents
CTAB	Cetyltrimethylammonium Bromide
CTAC	Cetyltrimethylammonium chloride
DLS	Dynamic light scattering
FDTD	Finite-difference time-domain method
FRET	Förster resonance energy transfer
GPC	Gel Permeation Chromatography
ICG	Indocyanine green
ICP-MS	Inductively Coupled Plasma Mass Spectrometry
IONP	Iron oxide nanoparticle
LSPR	Localized surface plasmon resonance
LUMO	Lowest Unoccupied Molecular Orbital
MB	Methylene blue
MPTMS	(3-mercaptopropyl)trimethylsilane
NIR	Near Infrared
PA	Phosphonic acid
PBS	Phosphonate-buffered solution
PC	Phosphorylcholine
PDT	Photodynamic therapy
PEG	Polyethylene glycol
PRET	Plasmon-induced resonance energy transfer

ABBREVIATION LIST

PTT	Photothermal therapy
QD	Quantum dots
RAFT	Reversible Addition-Fragmentation Chain Transfer
ROS	Reactive oxygen species
SERS	Surface-enhanced Raman scattering
SOSG	Singlet oxygen sensor green
SPE	[2-(methacryloyloxy)ethyl]dimethyl-(3-sulfopropyl)ammonium hydroxide
SPP	3-[3-methacrylamidopropyl-(dimethyl)-ammonio]propane-1-sulfonate
TA	Thioctic acid
TEM	Transmission electronic microscope
TEOS	Tetraethyl orthosilicate
V50	2,2′-Azobis(2-methylpropionamidine) dihydrochloride
VIM	Vinylimidazole

General introduction

In the past decades, gold nanoparticles have intrigued scientists and attracted intense research efforts owning to their unique localized surface plasmon resonance effect (LSPR). This plasmon phenomenon arises from the interaction between the electrons at the surface of gold nanoparticles and the incident electromagnetic field, making gold nanoparticles an outstanding nanoobject for harvesting and manipulating the light. As gold nanoparticles exhibit a remarkably high absorption of light at their surface plasmon frequency, they become promising photosensitizers for various biomedical applications such as biosensing, diagnostics, and therapies. Among them, gold nanorods (AuNRs) can effectively absorb light in the near-infrared range, which is the optimal window for light penetration into the human body. As a result, AuNRs hold significant potential as photosensitizers for phototherapy.

When AuNRs absorb light, they generate high-energy electrons within their structure, commonly known as "hot electrons." These hot electrons can directly convert the absorbed energy into heat, leading to a temperature increase in the surrounding environment. This localized heating effect can effectively kill cancer cells. Alternatively, hot electrons can react with water or dioxygen molecules in the surrounding environment, generating cytotoxic reactive oxygen species. These reactive oxygen species can induce programmed cell death. However, current challenges in phototherapies involving AuNRs revolve around the low efficiency of plasmonic energy conversion and utilization, limiting their further clinical trials.

Therefore, the first objective of this thesis is to improve the phototherapy efficiency of AuNRs. We seek to combine AuNRs with specific semiconductors. This combination allows for the transfer of light energy absorbed by AuNRs to the semiconductor material, either through hot electron injection or energy transfer mechanisms. Eventually, absorbed light energy generates electrons at the conduction band of semiconductors. These electrons have sufficient energy to react with oxygen or water molecules in the environment and finally produce reactive oxygen species (ROS) to kill cancer cells.

The second objective of this thesis is to develop suitable surface chemistry for inorganic nanoparticles. The ligands at the surface of nanoparticles have a significant influence on the stability, optical property, and reactivity of nanoparticles. Moreover, these ligands also regulate the interactions between nanoparticles and biomolecules or cells when nanoparticles are placed in a physiological environment. In this thesis, various ligands based on polyethylene glycol or polyzwitterions are designed and prepared to improve the colloidal stability of nanoparticles without hindering their expected optical property. Besides, interactions between these polymer ligands and macrophages are studied, for the purpose of extending the blood circulation time of nanoparticles.

The manuscript is divided in four chapters:

Chapter I is dedicated to a bibliographical introduction of the context of the thesis. Different types of inorganic nanocrystals including semiconductor quantum dots, iron oxide nanoparticles, and plasmonic gold nanoparticles along with their biomedical applications are presented. Next the AuNRs, as the main object studied in this thesis, are introduced. Their physical and chemical properties are presented, as well as synthesis and surface functionalization methods. Then we focus on the phototherapy mediated by AuNRs. The generation and relaxation of hot electrons within AuNRs are explained. The research advances in hybrid gold/semiconductor structures to improve the utilization efficiency of these hot electrons are presented.

In **Chapter II**, we synthesized hybrid dumbbell-shaped nanoparticles consisting of AuNRs and titanium dioxide (TiO_2) named as AuNR/TiO_2. In this heterostructure, the hot electrons generated within the AuNRs were found to be directly injected into the conduction band of TiO_2. This transfer allowed the hot electrons to have an extended lifetime, enabling them to effectively react with dioxygen molecules in the surrounding environment and generate hydroxyl radicals. To ensure the stability of these nanoparticles in a physiological environment, we functionalized the hybrid AuNR/TiO_2 nanoparticles with polyethylene glycol-phosphonate polymer ligands. The density of these polymer ligands on the nanoparticle surface plays a crucial role in achieving optimal photoactivity. We evaluated the photodynamic effect of these hybrid AuNR/TiO_2 nanoparticles *in vitro* using cancer cells and irradiating them with a near-infrared (NIR) laser. The results demonstrated the photoactivity of the nanoparticles, as well as their potential for photodynamic therapy.

In **Chapter III**, we explored the combination of AuNRs with semiconductor materials such as silver sulfide and copper sulfide, resulting in the formation of core-shell hybrid nanostructures. In these hybrid systems, the plasmon energy present in the AuNRs is efficiently transferred to the semiconductor materials through dipole-dipole interactions. This energy transfer process leads to the creation of exciton pairs within the semiconductors, which can further generate reactive oxygen species. To enhance the efficiency of this energy transfer and prevent undesired recombination between excited electrons and holes, we introduced an insulating silica layer at the interface between the gold and semiconductor components. This modification helps to maintain the stability of the exciton pairs and improve efficiency of photochemical reactions. We also assessed the photoactivity of these hybrid nanoparticles under the illumination of a continuous-wave NIR laser.

In **Chapter IV**, for *in vivo* applications, the therapeutic efficacy of nanoparticles is often compromised by poor biodistribution, as the majority of injected nanoparticles are detected and captured by macrophages, a type of immune cell. To address this challenge, based on the previous research conducted at the LPEM laboratory we developed zwitterionic polymers as a novel class of polymer ligands for the functionalization of inorganic nanoparticles. Various types of nanoparticles, including semiconductor quantum dots, iron oxide nanoparticles, and gold nanoparticles decorated with polyzwitterions, were synthesized. Their interactions with proteins and macrophages were investigated *in vitro* to assess their potential for improved biocompatibility and reduced macrophage uptake. Furthermore, we conducted pharmacokinetic studies on AuNRs functionalized with different types of polyzwitterions. These studies aimed to evaluate the behavior of these functionalized nanoparticles within the body and gain insights into their distribution and clearance pathways.

Chapter I. Plasmonic nanoparticles for biomedical applications and phototherapy

Résumé

Ce chapitre donne un résumé bibliographique du contexte et des états de l'art de la recherche sur les nanoparticules d'or plasmoniques et leurs applications thérapeutiques, en particulier dans le domaine de l'oncologie. Dans la première partie, nous mettons en évidence l'importance et les avantages des nanocristaux inorganiques pour diverses applications comme les biocapteurs, l'imagerie, le diagnostic et la thérapie. Nous examinons des exemples représentatifs de nanocristaux inorganiques tels que les nanocristaux de semi-conducteurs (quantum dots), les nanoparticules magnétiques et les nanoparticules plasmoniques, en soulignant leurs propriétés physiques et chimiques ainsi que leur pertinence pour les applications biomédicales. En particulier, cette thèse porte sur les nanoparticules d'or plasmoniques. Les propriétés optiques et l'effet unique de résonance plasmonique à la surface des nanoparticules d'or sont présentées. Dans la deuxième partie, les nanobâtonnets d'or (AuNRs) sont présentés comme l'objet principal étudié dans cette thèse car ces nanoparticules d'or en forme de bâtonnet présentent une bande de plasmon forte et modulable dans la région du proche infrarouge (NIR), ce qui est avantageux en raison de l'absorption minimale de la lumière et de sa meilleure pénétration dans les tissus humains. De plus, différentes méthodes de synthèse et stratégies de fonctionnalisation de surface pour les AuNRs sont explorées. La troisième partie du chapitre aborde les processus impliqués dans la génération, le transfert et la dissipation des électrons chauds à la surface des AuNRs sous irradiation. La thermalisation et la dissipation des électrons chauds entraînent une augmentation de la température dans l'environnement des AuNRs. Cet effet de surchauffe peut être exploité pour tuer les cellules cancéreuses, ce qui rend les AuNR adaptés à la thérapie photothermique. De plus, le couplage des AuNRs avec des matériaux semi-conducteurs permet le transfert d'électrons chauds des AuNRs vers la bande de conduction des semi-conducteurs. Ces électrons chauds transférés peuvent ensuite réduire les molécules de dioxygène, générant des espèces réactives de l'oxygène qui induisent l'apoptose cellulaire, une voie de mort cellulaire programmée. Nous fournissons des exemples pour illustrer le potentiel des nanostructures hybrides AuNR/semi-conducteurs dans l'amélioration de l'efficacité globale de la photothérapie pour le traitement du cancer.

Abstract

This chapter provides an overview of the context and current research advancements in plasmonic gold nanoparticles and their therapeutic applications, particularly in the field of oncology. The first part introduces the significance and advantages of inorganic nanocrystals as essential biomaterials. Inorganic nanoparticles have diverse biomedical applications, including biosensing, imaging, diagnostics, and therapies. Representative examples of inorganic nanocrystals such as semiconductor quantum dots, magnetic nanoparticles, and plasmonic nanoparticles are discussed, highlighting their physical and chemical properties and their relevance to biomedical applications. In particular, this thesis is focused on plasmonic gold nanoparticles. The optical properties and the unique surface plasmonic resonance effect of gold nanoparticles are presented in detail. In the second part, the AuNRs are introduced as the main object studied in this thesis because these rod-shaped gold nanoparticles exhibit a strong and tunable plasmon band in the near-infrared (NIR) region, which is advantageous due to minimal light absorption by human tissues and enhanced deep light penetration. The optical properties and surface plasmonic resonance effect of gold nanoparticles are discussed in detail. Additionally, various synthesis methods and surface functionalization strategies for AuNRs are explored. The third part of the chapter examines the processes involved in the generation, transfer, and dissipation of hot electrons at the surface of AuNRs under irradiation. The thermalization and dissipation of hot electrons result in increased temperature in the surrounding environment of AuNRs. This overheating effect can be leveraged to eliminate cancer cells, making AuNRs suitable for photothermal therapy. Furthermore, the coupling of AuNRs with semiconductor materials enables the transfer of hot electrons from AuNRs to the conduction band of semiconductors. These transferred hot electrons can then reduce dioxygen molecules, generating reactive oxygen species that induce cell apoptosis, a programmed cell death pathway. Examples are provided to demonstrate the potential of hybrid AuNR/semiconductor nanostructures in improving the overall efficacy of phototherapy for cancer treatment.

I.1. Inorganic nanoparticles for biomedical applications

Nanoscience and nanotechnology have experienced rapid development in the past decades and continue to blossom, showing increasing significance in diverse domains including energy[1], electronics[2], agriculture[3], as well as biomedicine[4–6]. Notably, in the wake of the unprecedented Covid-19 pandemic caused by the SARS-CoV-2 virus since 2019, nanotechnology has played a pivotal role in combating the virus in various aspects such as prevention[7,8], detection[9], therapy[10], and immunomodulation[11]. Nowadays, it is undoubted that the integration of nanoscience and technology in biomedicine has become indispensable in driving research and development activities, and in contributing to the discovery of novel theories, strategies, and devices. Its widespread and profound involvement in the biomedical field underscores its significance and transformative potential.

I.1.1. Inorganic nanocrystals

Nanoparticles, the primary focus of nanoscience research, are characterized as small particles with dimensions ranging from a few nanometers to a few hundred nanometers. Understanding the size of nanoparticles in relation to other biological components within the human body is crucial for their biomedical applications. As illustrated in **Figure.I.1**, nanoparticles are typically at least 100 times smaller than cells, while they are roughly 10 to 100 times larger than protein molecules. Besides, nanoparticles share a similar size range as DNA or viruses.

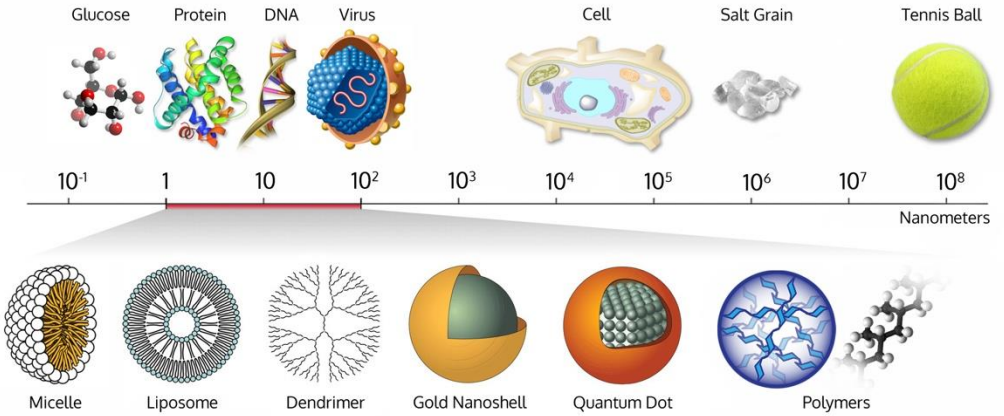

Figure.I.1 Scale comparison of nanoparticles with biological objects[12].

In general, based on the nature and composition, nanoparticles can be categorized into two types: (1). Organic nanoparticles, such as polymeric and lipid nanoparticles; (2). Inorganic nanoparticles, including silica- or carbon-based amorphous nanoparticles and nanocrystals composed of metal, metal oxide or semiconductor.

In this thesis, we focus on inorganic nanocrystals for their biomedical applications. Typically, these inorganic nanocrystals present two key properties that can be harnessed to design novel diagnostic and therapeutic agents. Firstly, the large surface-to-volume ratio of inorganic nanocrystals allows for efficient and facile surface modification. By attaching rationally designed ligands, active agents, or antibodies to the nanoparticle surface, their behavior *in vivo* can be regulated, enabling targeted imaging and therapy. Secondly, as the nanoparticle size decreases to nanometer scale, their intrinsic physical or chemical properties differ from what are observed in bulk materials. Examples include the surface

plasmonic resonance exhibited by metal nanoparticles, the superparamagnetism displayed by magnetic nanoparticles, and the luminescence of quantum dots. These intrinsic properties can be tuned by the shape, size and composition of the nanocrystals and make these nanocrystals promising candidate in preclinical or clinical settings. Therefore, in the following section, we will present these three aforementioned nanocrystals, discussing their nature, properties, and applications in the fields of bio-imaging and therapy.

a. Semiconductor quantum dots

Semiconductor nanocrystals, also called quantum dots (QDs), are fluorescent nanoparticles. As shown in **Figure.I.2. a**, a QD typically contains an emissive semiconductor core covered by one or several shells of different semiconductors that protect the core from oxidation, improve the quantum yield by passivating the core surface and modulate the emission properties of QDs[13,14]. In the visible range, QDs can be composed of II-VI elements from the periodic table such as CdSe/ZnS core/shell heterostructure or III-V elements like InP. QDs can absorb photons at energies larger than the bandgap, by transferring electrons in the valence band to the conduction band, leaving behind a positively charged hole in the valence band. This electron-hole pair is known as an exciton. Recombination of excitons through radiative processes results in the emission of photons, with the energy of the emitted light depending on the band gap of the semiconductors. This mechanism is responsible for the fluorescence exhibited by QDs. The decrease of QD size to the nanoscale leads to quantization of energy levels within nanoparticles due to the emergence of quantum confinement. The size-dependent quantum confinement increases the effective band gap energy as QDs become smaller, resulting in a blue-shifted absorption and emission spectra (**Figure.I.2. b**)[15].

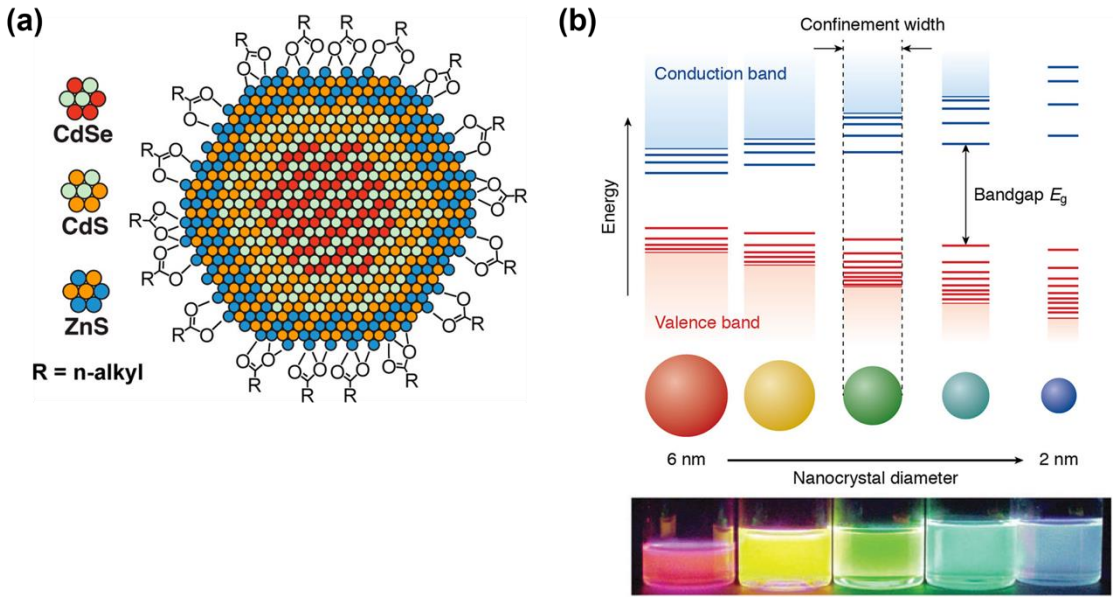

Figure.I.2. (a). Illustration of the heterostructure core-shell-shell quantum dot[16]. (b). Schematic representation of quantum confinement effect & colloidal suspensions of CdSe QDs size-dependent fluorescent emissions[17].

Because of their brightness and photostability, QDs have been widely used in bioimaging and detection. NIR-emitting QDs (typically 700-900 nm wavelength) made of materials with relatively low toxicity such as $CuInS_2$ or $CuInSe_2$ have been developed for fluorescence-guided surgery[18,19]. These QDs are also utilized to visualize tumors[20] or intratumoral blood vasculatures[21] and detect regional and

sentinel lymph nodes through fluorescence[19,22]. In addition, QDs composed of InAs, PbS and Ag_2S are widely studied and applied in bioimaging owning to their strong emission in the short-wave infrared range (SWIR, typically 1000-1500 nm wavelength) where light absorption and scattering by tissues is minimal. Since few conventional organic dye molecules are emissive in the SWIR, these QDs are considered as a good alternative imaging agents and thus become promising in whole body imaging. In comparison to other modalities such as Magnetic Resonance Imaging (MRI) or Positron Emission Tomography (PET), they have unique advantages such as high spatial resolution, ease of use and high sensitivity of fluorescence[23–25]. (**Figure.I.3**) Apart from bioimaging, QDs can also be used as a photosensitizer for photodynamic therapy due to their strong absorbance in visible or NIR light[26].

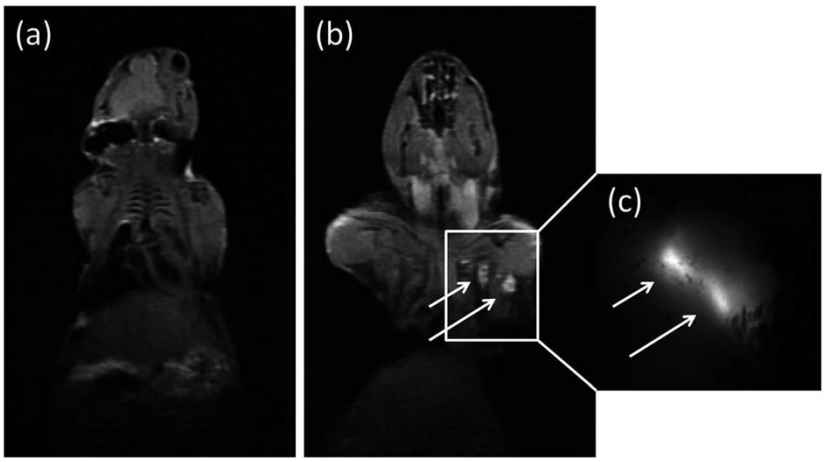

Figure.I.3. Detection of lymph nodes of a mouse by T1-weighted MRI before (a) and after (b) injection of Mn^{2+} doped CuInSe QDs and the corresponding NIR fluorescence image (c)[25].

b. Magnetic nanocrystals

Magnetic nanocrystals can be composed of various types of materials, including metals, metal oxides, and magnetic nanocomposites. Among them, iron oxide nanoparticles (IONPs) (Fe_2O_3 and Fe_3O_4) have gained significant popularity for biomedical applications due to their comparatively lower toxicity and better biocompatibility[27]. Unlike bulk iron oxide materials, IONPs with sizes of 20 nm and below exhibit a unique superparamagnetic property. Within a single small magnetic nanoparticle, the magnetic dipoles are aligned parallel to each other, within a single magnetic domain. As a result, each nanoparticle possesses a magnetic moment that is the sum of its individual magnetic dipoles. In the absence of an external magnetic field, the magnetization of a collection of magnetic nanoparticles appears to be zero because the magnetic moments of the nanoparticles are randomly oriented. In addition, the collective orientation of magnetic dipoles in a single nanoparticle undergoes fast reorientation, with a characteristic time called the Néel relaxation time in the ns-µs range. However, when an external magnetic field is applied, all the nanoparticles become magnetized and their magnetic moments align in the same direction as the applied field[28]. These superparamagnetic IONPs can be selectively accumulated at a desired location in human body by an applied external magnetic field, which is valuable for target drug delivery[29]. In addition, IONPs can be used as contrast agent in magnetic resonance imaging by interacting with local magnetic field, changing the relaxation time of hydrogen nuclei (**Figure.I.4**)[30,31]. IONPs also can be applied as magnetic thermal agents that are able to produce heat under external magnetic field, elevate the temperature of their surrounding environment and eventually kill tumor by cell apoptosis[32,33].

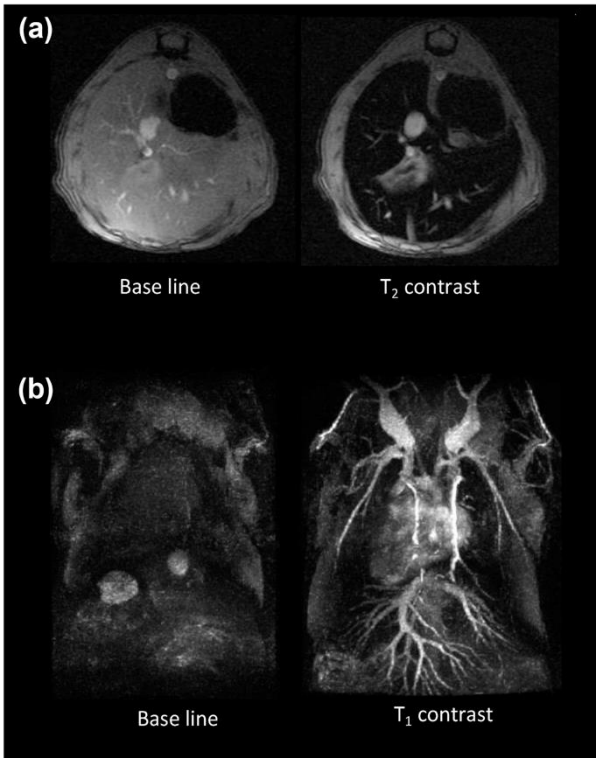

Figure.I.4. Examples of MRI with IONP with different sizes. (a). Mouse Liver T_2-MRI with larger IONP. (b). T_1-weighted MR angiography with smaller IONP[34].

I.1.2. Plasmonic nanocrystals

Plasmonic nanocrystals refer to nanoparticles made of metals (e.g. Au, Ag, Al and Pt), doped semiconductors (e.g. Cu_2S, ZnS) or doped dielectric materials (e.g. Aluminum-doped zinc oxide[35], Indium-doped cadmium oxide[36]). The unique and attractive optoelectronic properties of plasmonic nanocrystals derive from the localized surface plasmonic resonance (LSPR) effect, making them an "antenna" that efficiently concentrates and absorbs incident light energy. Metal plasmonic nanoparticles, particularly gold nanoparticles, have been extensively studied and widely utilized in various fields, including biological diagnostics and therapy. Here, we primarily focus on gold nanoparticles, the details of the physics of surface plasmon resonance effects of bulk materials are presented in the **Annex.V.6**. Plasmon for bulk gold materials. Here we mainly focus on the LSPR effect of gold nanoparticles followed by the related biomedical applications.

As the size of gold materials decreases to the nanoscale, for nanoparticles with size much smaller than the wavelength of incident light (visible or NIR), we can consider that the conduction free electrons at the surface experience the same electric field at each instant with the same phase (**Figure.I.5**). Consequently, this collective interaction causes the conduction electrons to oscillate in phase with the electromagnetic field, so that a resonance arises, leading to field amplification both inside and outside the nanoparticles. This resonance is called localized surface plasmon resonance.

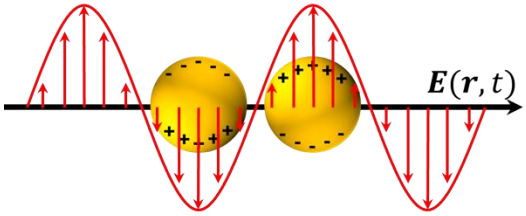

Figure.I.5. Illustration of excited surface plasmons of gold nanoparticles.

We can calculate the spatial field distribution by simply assuming a spherical gold nanoparticle (AuNP) in an electrostatic field, i.e., assuming the electromagnetic field is constant over the particle volume. By solving Laplace equation for the electric field inside and outside the sphere: $E = -\nabla\Phi$, and applying the boundary conditions at the gold nanoparticle surface and $r \to \infty$, we can finally obtain electric field inside and outside the nanoparticle as:

$$\boldsymbol{E_{in}} = -\frac{3\varepsilon_d}{\varepsilon_m + 2\varepsilon_d}\boldsymbol{E_0} \tag{I. 1a}$$

$$\boldsymbol{E_{out}} = \boldsymbol{E_0} + \frac{\boldsymbol{p}\cdot\boldsymbol{r}}{4\pi\varepsilon_0\varepsilon_d r^3} \tag{I. 1b}$$

$$\boldsymbol{p} = 4\pi\varepsilon_0\varepsilon_d a^3\frac{\varepsilon_m - \varepsilon_d}{\varepsilon_m + 2\varepsilon_d}\boldsymbol{E_0} \tag{I. 1c}$$

where E_0 is the incident electric field, $\boldsymbol{p}$ is the dipole moment, ε_d, ε_m and ε_0 are electric permittivity of the surrounding medium, of the gold nanoparticle and in vacuum, respectively, a is the radius of the nanoparticle. Therefore, we notice that both $\boldsymbol{E_{in}}$ and $\boldsymbol{E_{out}}$ are enhanced. Particularly, when $\varepsilon_m + 2\varepsilon_d \to 0$, $\boldsymbol{E_{in}}$ and $\boldsymbol{E_{out}}$ reach the maximum that is called the Fröhlich condition. For a typical Drude metal nanosphere located in the air, when the Fröhlich condition is satisfied, with equation (V.11), we have:

$$\omega_{LSP} = \frac{\omega_p}{\sqrt{3}} \tag{I. 2}$$

From an optical point of view, this resonantly enhanced polarization of a gold nanoparticle also leads to an increased efficiency in scattering and absorption of light. The corresponding cross-section for scattering C_{sca} and absorption C_{abs} is calculated according to the Mie's theory:

$$C_{sca} = \frac{k^4}{6\pi}|\alpha|^2 = \frac{8\pi}{3}k^4a^6\left|\frac{\varepsilon_m - \varepsilon_d}{\varepsilon_m + 2\varepsilon_d}\right|^2 \tag{I. 3a}$$

$$C_{abs} = kIm[\alpha] = 4\pi ka^3 Im\left[\frac{\varepsilon_m - \varepsilon_d}{\varepsilon_m + 2\varepsilon_d}\right] \tag{I. 3b}$$

where α is the polarizability that can be defined as $\boldsymbol{p} = \varepsilon_0\varepsilon_d\alpha\boldsymbol{E_0}$. For a sphere nanoparticle with volume V and dielectric function $\varepsilon = \varepsilon_1 + i\varepsilon_2$, we can calculate the extinction cross section since $C_{ext} = C_{sca} + C_{abs}$:

$$C_{ext} = 9k{\varepsilon_d}^{3/2}V\frac{\varepsilon_2}{(\varepsilon_1 + 2\varepsilon_d)^2 + {\varepsilon_2}^2} \tag{I. 4}$$

Again, the extinction reaches its maximum when Fröhlich condition is met, i.e., $\varepsilon_1 + 2\varepsilon_d \to 0$. Notably, when irradiated under light at plasmon resonant frequency, the cross section of gold nanoparticle is

larger than the physical size. (**Figure.I.6. a, b**) In **Figure.I.6. c**, extinction cross sections of plasmonic nanoparticles, organic fluorophores, semiconductor QDs and atoms/ions are compared against their physical sizes. Only plasmonic nanoparticles exhibit an extinction cross section superior to their physical sizes. Typically, AuNPs exhibit a plasmon absorbance peak at around 520 nm, as calculated from the Mie's theory. This absorbance band can be influenced by several factors such as size, shape and surface environment. **Figure.I.6. d** illustrates an example of sized dependent plasmon absorption of AuNPs.

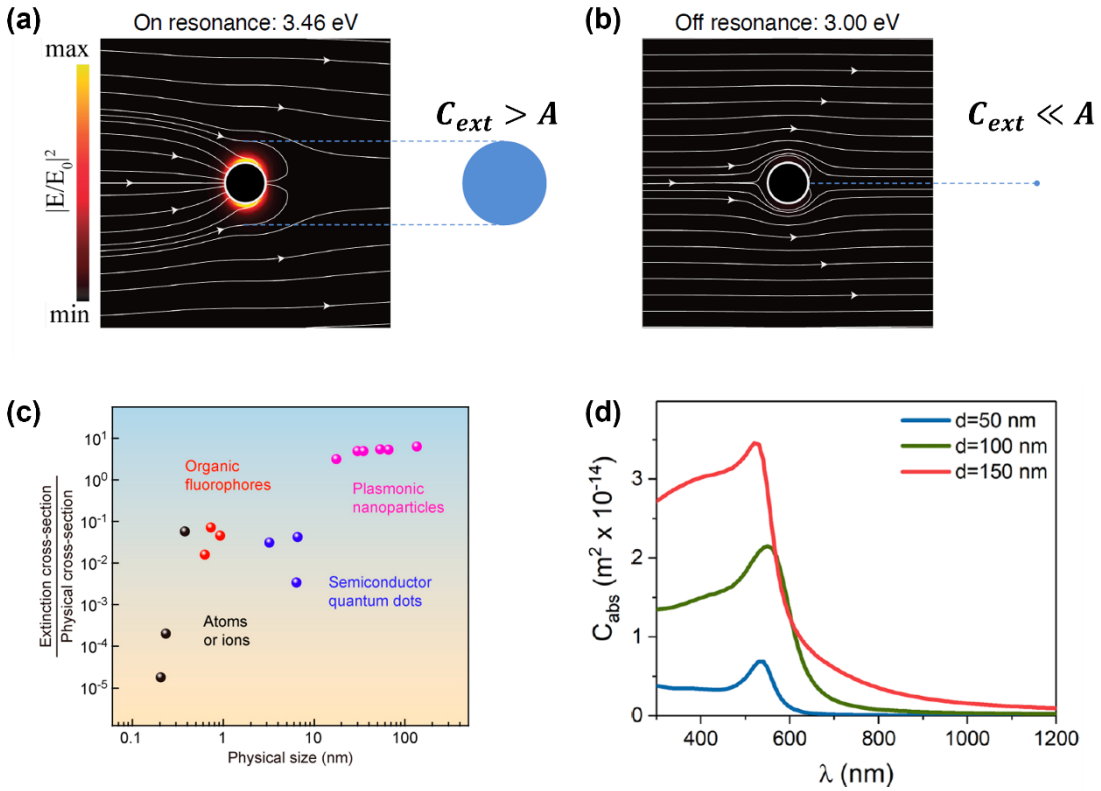

Figure.I.6. Illustration of extinction cross section of gold nanoparticle illuminated by light on (a) and off (b) resonance, A is the cross section of gold nanoparticles. (c). Optical extinction cross sections of various optical nano species. (d). Calculated absorption cross section of AuNPs with diameters of 50, 100 and 150 nm, as a function of wavelength[37,38].

With the extinction cross section, it is possible to calculate the molar extinction coefficient, ε_{ext}, as $\varepsilon_{ext}\ (L \cdot mol^{-1} \cdot cm^{-1}) = 2303 N_A * C_{ext}\ (cm^2)$. Then the absorbance A of a colloidal gold nanoparticle solution with concentration $c\ (mol \cdot L^{-1})$ with optical path $L\ (cm)$ can be deduced:

$$A = \varepsilon_{ext} c L \qquad (I.5)$$

To summarize, the LSPR effect enables gold nanoparticles to absorb electromagnetic field at a range even surpassing their physical size. Besides, since the LSPR peak of a gold nanoparticle depends on its dielectric function, it can be further tuned by the geometry, the size, the surface nature, and the surrounding environment of gold nanoparticles, making gold nanoparticles a promising and versatile optical nanomaterial for biosensing and therapy applications.

I.1.3. Biomedical applications of spherical gold nanoparticles

Due to the high Au^{+}/Au^{0} redox potential (E^{0} = 1.69 V), it is hard to oxidize gold nanoparticles, they thus possess a notable characteristic of being chemically inert, resulting in their high biocompatibility. This property has propelled their advancements in various applications as diagnostic and therapeutic agents for *in vivo* use[39,40].

Gold nanoparticles possess a distinct red-to-pink color in the visible light range due to their plasmon absorption. This unique optical property is advantageous as it allows for easy observation of the nanoparticles, even at low concentrations, using either spectroscopy or the naked eye. This characteristic makes gold nanoparticles well-suited for various applications in biosensing, where the color change can serve as a visual indicator for the presence of specific target analytes or biological interactions. One common technique is the lateral-flow immunochromatographic assay, which involves selectively depositing gold nanoparticles functionalized with antibodies at a specific zone through their interaction with target analytes. These immobilized gold nanoparticles form a colored band, indicating the presence of target analytes. Different formats can be employed based on the nature of the analytes. For analytes with multiple epitopes, such as viruses, a sandwich format is used (**Figure.I.7. a**), where gold nanoparticles with antibodies first bind to the analytes and then the captured analytes further bind to pre-immobilized antibodies at the test zone. In the absence of analytes, no gold nanoparticles will be retained at the test zone. For analytes with a single antigenic determinant and lower molecular weights, a competitive format can be utilized (**Figure.I.7. b**), where target analytes are pre-immobilized at the test zone and gold nanoparticles with antibodies are incubated with the sample solution. If the concentration of target analytes is high enough, the antibodies on the gold nanoparticles will be saturated and no binding will occur at the test zone, resulting in a blank appearance. Conversely, if the concentration is insufficient, the gold nanoparticles with non-conjugated antibodies will be retained at the test zone, forming a colored band indicating a negative result. **Figure.I.7. c** and **d** depict a typical sandwich format-based paper chip device.

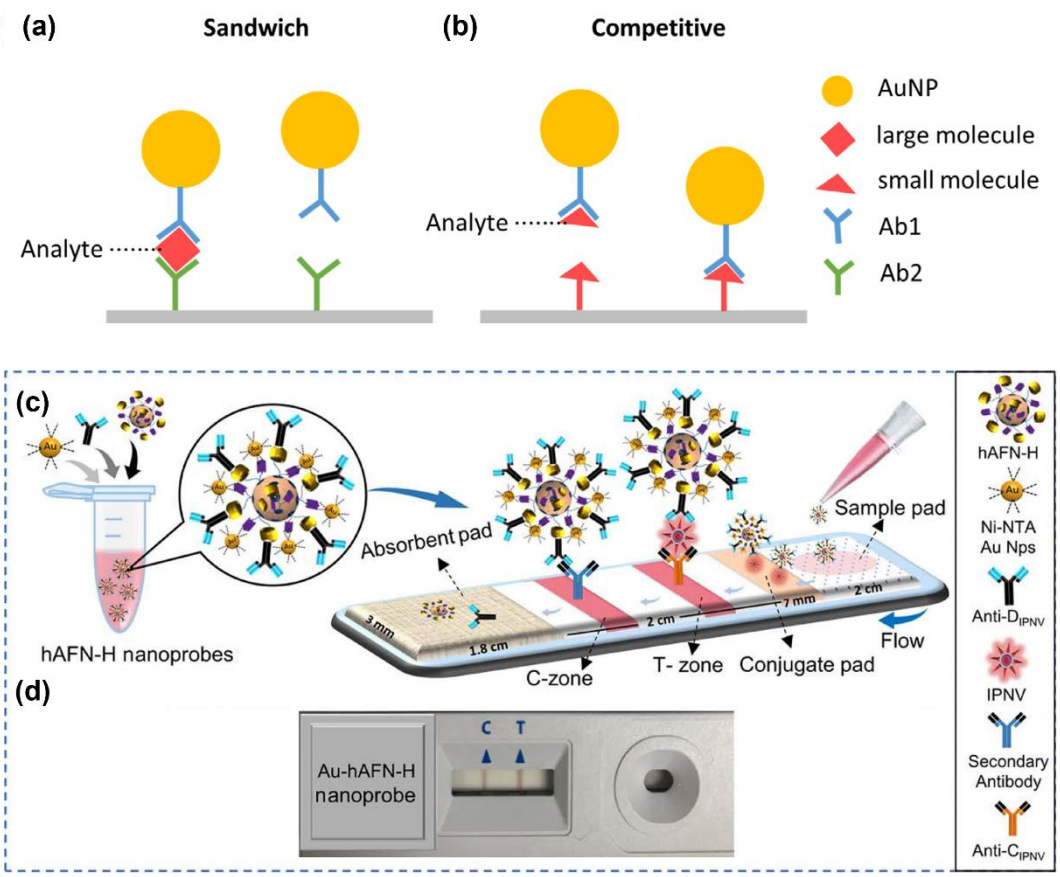

Figure.I.7. Illustration of a gold nanoparticle based lateral-flow immunochromatographic assay with (a). sandwich or (b). competitive format. And an example of paper chip-based detection of the infectious pancreatic necrosis virus. (c). Gold nanoparticles and antibodies are firstly assembled and mixed with the sample solution. In the presence of virus, gold nanoparticles are immobilized at the T(test)-zone by forming a sandwich structure; the gold nanoparticles in excess continue to immigrate and finally retained at the C(control)-zone via direct bounding with fixed secondary antibody. (d). Real image of fabricated paper chip device[41,42].

Apart from deposition of gold nanoparticles, since the LSPR peak of gold nanoparticles depends on the local refractive index, alterations made to the surface of gold nanoparticles, such as polymer or antibody conjugation, coating with other materials, or nanoparticle aggregation, can modify the refractive index and thus induce a shift in the LSPR peak. These changes can be visually observed or detected using spectroscopic techniques. For example, the combination between antibodies and targeted antigens can also modify the refractive index of gold nanoparticles solutions[43], reflected by changes of the absorbance spectrum or even a color change of the colloidal solution. These LSPR-based biosensors can provide quantitative, highly sensitive and selective detections towards biotoxins[44], antigens[45] and viruses[46].

In addition, the LSPR effect of gold nanoparticles can lead to a remarkable amplification of Raman scattering signals. This phenomenon results in a significant enhancement of approximately 100 times compared to the original non-conjugated organic substance when molecules are attached to the surface of gold nanoparticles[47]. While Raman spectroscopy is a valuable nondestructive technique for elucidating molecular structure and vibrations with high sensitivity and speed, its applications have traditionally been limited by low signal intensity, a scarcity of suitable probes, and the potential for detector photobleaching[48]. Due to the unique surface-enhanced Raman scattering (SERS) effect, gold

nanoparticles combined with specific immune probes or antibodies significantly increase sensitivity and contrast of detection, which provides a method to improve the sensitivity of traditional Raman spectroscopy. Furthermore, their ability to extend the irradiation range to the NIR region, coupled with their stability during repetitive diagnostics, renders them crucial imaging agents for the identification and imaging of bacteria and cells[49,50].

I.2. Gold nanorods and their plasmonic properties

Sphere gold nanoparticles have a size dependent LSPR peak in the visible light range, roughly between 500 and 600 nm. However, visible light suffers from a strong absorption by skin, tissues, and blood, resulting in a poor depth of penetration into the human body, eventually limiting their *in vivo* biomedical applications. Indeed, there are two distinct spectral ranges where the absorption of biological tissues is minimum: the first NIR window at 650 – 900 nm and the second NIR window at 1000 – 1300 nm. (**Figure.I.8**) To optimize the light penetration, anisotropic gold nanoparticles such as gold nanostars[51], gold nanocages[52] and gold nanorods have been synthesized with LSPR absorbances in NIR range. Among various anisotropic gold nanoparticles, AuNRs have attracted much more attention and have been widely studied for decades. Since AuNRs are the main object studied in this work, here we give a brief introduction to physical and chemical properties of AuNRs, as well as their applications as therapeutic agents.

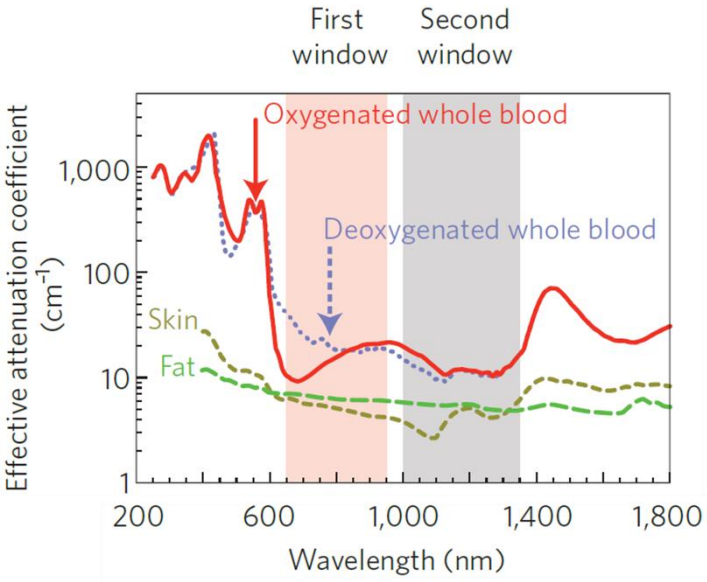

Figure.I.8. Optical windows in biological tissues[53].

I.2.1. Plasmonic properties of gold nanorods

AuNRs are cylindrical rod-like gold nanocrystals characterized by their elongated morphology, with distinct dimensions in terms of length and width. The aspect ratio, defined as the ratio of the length to the width, determines the shape and optical properties of the nanorods. Due to their anisotropic shape, AuNRs possess two different LSPR modes as shown in **Figure.I.9**, the longitudinal plasmon band and the transverse plasmon band, corresponding to electron oscillation along the long and short axes of the AuNR, respectively.

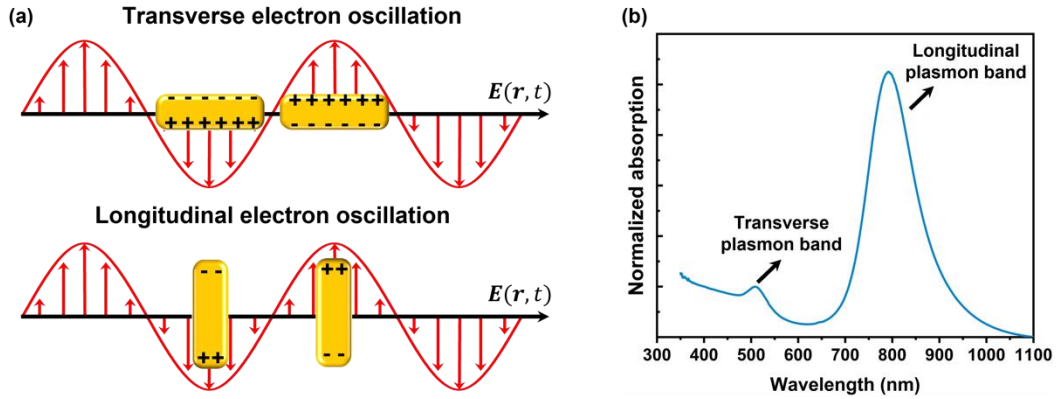

Figure.I.9. (a). Illustration of two distinct modes of LSPR in AuNRs. (b). UV-vis absorption spectrum of a typical AuNRs colloidal solution with transverse plasmon band at around 500 nm and longitudinal plasmon band at around 800 nm.

The transverse plasmon band is less sensitive to the change of AuNR size or the surrounding refractive index. On the contrary, the absorption intensity and wavelength of the longitudinal plasmon band are highly dependent on factors such as the aspect ratio, nanoparticle size, and the properties of the local environment. (**Figure.I.10. a, b**) This unique property enables precise tuning of the longitudinal plasmon band across a wide spectral range, covering both the visible and NIR regions. In addition, this longitudinal LSPR band exhibits a high absorption efficiency, making AuNR among the best plasmonic absorbers of light[38].

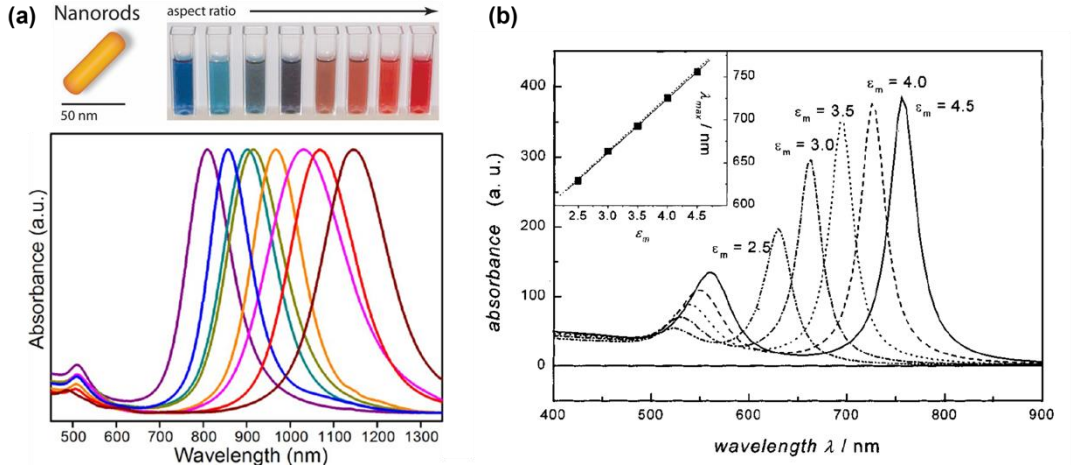

Figure.I.10. (a). Longitudinal absorption band of AuNRs red shifted as the aspect ratio of AuNR increased[54,55]. (b). Simulated longitudinal plasmon band of AuNRs with fixed aspect ratio in the medium with varying dielectric constant[56].

Therefore, when compared to traditional AuNPs, AuNRs offer two main advantages. Firstly, the longitudinal plasmon band of AuNRs is highly sensitive to changes in the refractive index of the surrounding environment, as evidenced by variations in the peak wavelength or absorbance. This property is highly appreciated in biosensing applications. Secondly, the longitudinal absorption of AuNRs can be adjusted to the NIR region with a strong absorption of light. This allows for excitation of AuNRs using NIR light, making them promising photosensitizers for *in vivo* diagnostic and therapeutic applications.

I.2.2. Synthesis of gold nanorods

Due to the distinctive tunable longitudinal LSPR band, AuNRs have captured the attention of scientists for several decades, leading to the development of various synthesis methods. In the early stages, AuNRs were synthesized through electrochemical reduction of a gold anode[57] or electrochemical deposition of gold in polycarbonate or alumina membrane templates[58]. It wasn't until 2003 that the seeded growth synthesis method for AuNRs was introduced, offering a convenient and versatile wet chemistry approach[59]. Since then, research on AuNRs has surged, accompanied by refinements and modifications of the seed growth synthesis method. Presently, the seed growth method, also known as the seed-mediated method, has become the most widely used approach for AuNR synthesis due to its simplicity, high yield, and precise control over particle size[60].

In a typical seed growth synthesis[61–64], (**Figure.I.11**) the chloroauric acid ($HAuCl_4$) is used as the source of gold, with which two different solutions are prepared: seed solution and growth solution. In the seed solution, Au^{3+} ions are directly reduced to Au^0, forming small spheric gold nanoparticles with diameters below 5 nm, which provides a solution of seeds with a brownish color[65]. These small gold nanospheres serve as starting points for the growth of AuNRs and catalyze the reduction of Au^+ to Au^0 in the growth solution. To obtain gold seeds with limited size and good homogeneity, a strong reductant such as $NaBH_4$ is necessary for the simultaneous and instantaneous production of all the nuclei. A surfactant is also needed to stabilize the generated seeds. In addition, seeds capped with different surfactant can finally yield AuNRs with different morphologies. Typically, cetyltrimethylammonium bromide (CTAB)-capped seeds lead to single-crystal nanorods, whereas citrate-capped seeds result in pentatwined nanorods[66]. In terms of the growth solution, the gold precursor $HAuCl_4$ is mixed with the CTAB surfactant, organic additives, a weak reductant, and the silver ions. These components, as well as their concentration in the growth solution can affect the anisotropic growth of AuNRs, which will be discussed in detail in Chapter II. The weak reductant such as ascorbic acid utilized here is a key factor in this seed growth method. The Au^{3+} is reduced first to Au^+, evidenced by the change of solution color from orange yellow to colorless. This step prevents the possible disproportionation reaction between Au^{3+} and Au^0.[67,68] However, the reducing agent should not be able to reduce directly Au^{3+} to Au^0, so that the final reduction of Au^+ to Au^0 only takes place on the added seed nuclei, avoiding secondary nucleation during the growth step.

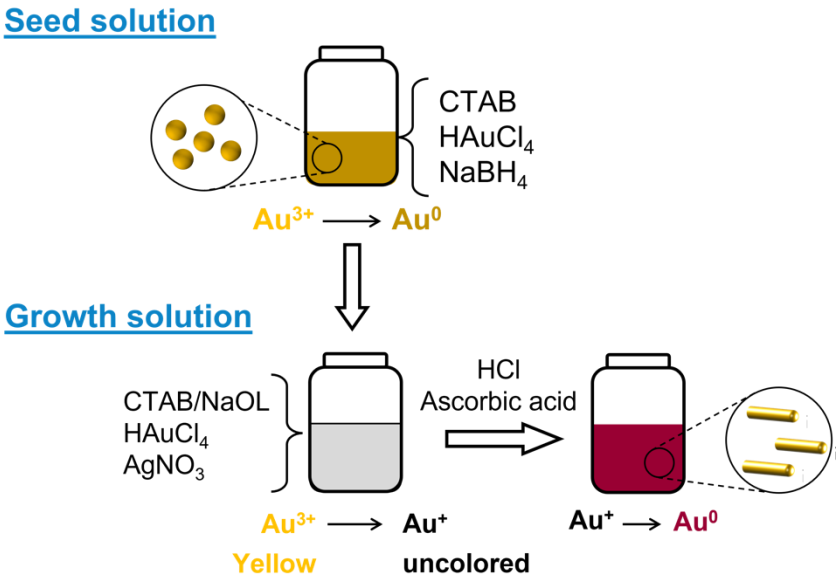

Figure.I.11. Illustration of a typical seed growth synthesis of AuNRs.

The yield of AuNRs can be determined by UV-vis absorption spectroscopy and transmission electronic microscope (TEM). The absorbance of AuNR at wavelength of 400 nm is due to interband transitions in metallic gold, which is independent on the size or shape of gold nanoparticles. With the absorbance at 400 nm measured by UV-vis spectrometer, Au^0 concentration in the solution can be calculated based on a linear relation between Au concentration and absorbance at 400 nm. Particularly, an absorbance of 1.2 cm^{-1} corresponds to $[Au^0] = 0.5\ mM$ [69]. The dimensions of synthesized AuNRs can be determined from TEM images. Finally, the concentration of AuNRs in the solution can be calculated by the following equation:

$$[AuNR] = \frac{[Au^0] \times M_{Au}}{N_A \times \pi l (d/2)^2 \times \rho_{Au}} \quad (I.6)$$

where M_{Au}, ρ_{Au} are the molar mass and the volume mass of gold, respectively; N_A is the Avogadro constant; l, d are the length and diameter of AuNRs.

Based on the seed growth methods, Jana first proposed to synthesize AuNRs in a single step, where seeds in the growth solution are generated in situ by adding strong reductant $NaBH_4$ [70]. This method is thus called seedless AuNR synthesis. One of the remarkable advantages of this seedless method is that it allows for preparing AuNRs with dimensions much smaller than those prepared by classic seed growth methods[71,72]. These miniaturized AuNRs with dimensions of $\sim 25 \times 6\ nm^2$, demonstrate more efficient light absorption than those large AuNRs. Furthermore, their smaller size enables easier distribution within biological systems. Therefore, the higher absorption efficiency and improved bio-transport make them effective phototherapy agents[73].

I.2.3. Surface functionalization of gold nanorods

The presence of CTAB is crucial for the synthesis of AuNRs as it enables the anisotropic growth and provides stability to the nanoparticles in aqueous solutions. However, CTAB-capped AuNRs are not suitable for direct biological applications. Firstly, CTAB-capped AuNRs exhibit instability under certain

conditions, including high salt content, low CTAB concentration, and the presence of organic solvents[74]. Additionally, *in vitro* studies have shown that free CTAB molecules have a cytotoxic effect on human cells[75]. Moreover, the dense CTAB layers hinder the further functionalization of AuNRs with specific ligands or biomolecules, resulting in limited applications of AuNRs[76]. Different strategies have been thus developed to modify the surface of AuNRs to get rid of CTAB and render AuNRs more colloidally stable and easier for further surface decoration.

A common strategy of surface functionalization is the ligand exchange. Various ligands such as polyethylene glycol (PEG) can be prepared with one or several thiol groups at the end of the molecule chain[77,78]. These thiol-terminated ligand molecules can be firmly grafted to the surface of AuNRs through Au-S covalent bonds, thus the CTAB layers can be replaced by designed ligands. However, the direct ligand exchange between CTAB and thiol-terminated ligands often results in an incomplete exchange or is accompanied by unexpected AuNR aggregation[76]. This problem can be addressed by a stepwise ligand exchange process[79]. As shown in **Figure.I.12**, the CTAB-capped AuNRs are in prior exchanged with sodium polystyrene sulfonate (Na-PSS), an anionic polyelectrolyte that binds to positively charged CTAB molecules by electrostatic interaction and serves as a mild detergent to remove CTAB. Afterward, the Na-PSS stabilized AuNRs are further exchanged with sodium citrate. The eventually citrate-capped AuNRs are highly stable in neutral pH value and low salinity solution, and thus they are ready for further functionalization with thiolated ligands.

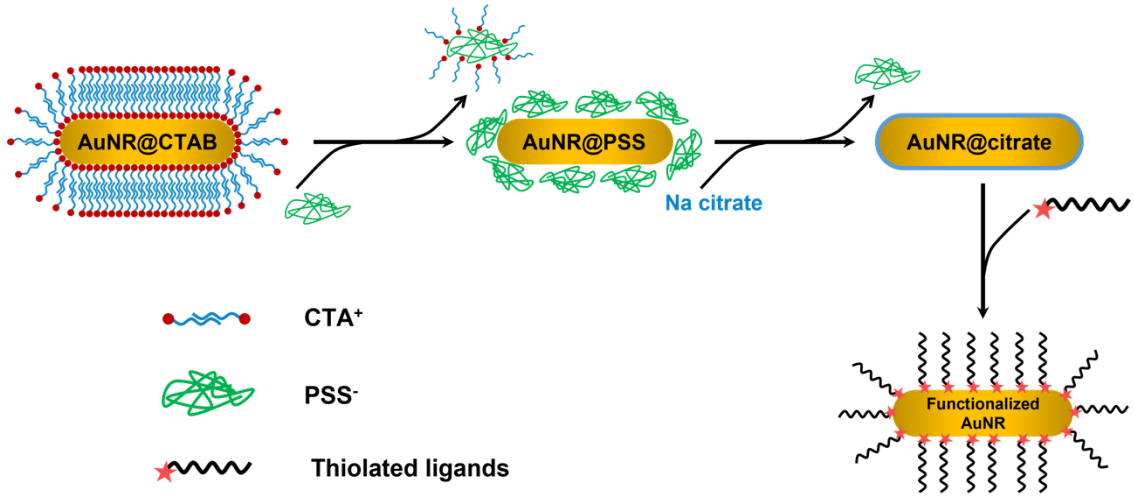

Figure.I.12. Schematic illustration of the stepwise ligand exchange process.

Apart from the ligand exchange method, another strategy to functionalize the AuNR surface is to introduce an additional coating that totally covers the surface of CTAB-capped AuNRs. With the strong electrostatic adsorption between polyelectrolytes, we can consecutively deposit layers of polyanion and polycation onto the surface of AuNRs (**Figure.I.13**), resulting in a complex with high stability[65]. This polyelectrolyte coating method relies on electrostatic interactions between different layers. Despite its simplicity of fabrication, there are always questions on the stability of these multilayers in physiological environment[60].

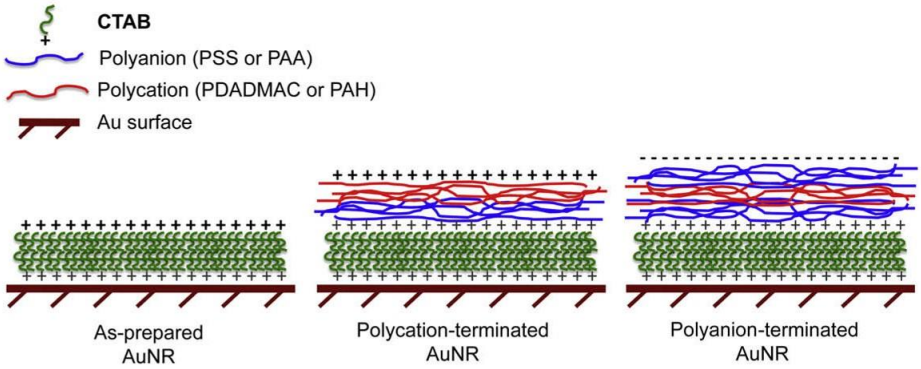

Figure.I.13. Illustration of AuNR surface covered by the CTAB bilayer (left), by 2-layer (polycation terminated, middle), by 3-layer (polyanion terminated, right) polyelectrolyte coatings[80].

Finally, the surface of AuNRs can also be covered by a silica shell. Silica is a commonly used coating material for AuNRs due to its numerous advantages. One of the key benefits is the improved colloidal and thermal stability of silica coated AuNRs, ensuring the stability of the AuNRs in various environments. Additionally, the silica coating increases the surface area of the rods while maintaining the optical properties of the gold core, allowing for enhanced interactions with surrounding molecules. The controllable porosity of silica also offers opportunities for further functionalization and drug loading, as the reactive surface silanols enable the attachment of functional ligands or biomolecules. This enables efficient and selective probing of targeted molecules. Another important aspect is that the silica shell influences the refractive index of the surrounding environment of the AuNRs, making thickness control a critical parameter that affects the LSPR response and sensitivity of the nanoparticles[81].

I.3. Phototherapy based on gold nanorods

AuNRs can efficiently absorb light thanks to its longitudinal LSPR effect. The light energy absorbed by AuNRs can be further harnessed for therapeutic purposes, especially in the treatment of cancer. Phototherapy methods for cancer treatment can be broadly classified into two categories: (1) Photothermal Therapy (PTT), where cancer cells are targeted and destroyed by the localized increase in temperature caused by irradiation; and (2) Photodynamic Therapy (PDT), where cancer cells are eliminated through the generation of reactive oxygen species (ROS) by photosensitizers upon illumination. In this section, we will explore how light energy is absorbed, converted, and dissipated within AuNRs, and discuss the applications of AuNRs as agents for PTT and PDT.

I.3.1. Hot electrons: generation and relaxation

When gold nanoparticles are exposed to light at their plasmon resonance frequency, the LSPR is triggered, causing the electrons to oscillate in synchronization with the incident electromagnetic field. This coherent electronic oscillation is damped very fast as the electronic cloud decouples from the oscillating electric field within a timeframe of approximately 10 fs[82]. The decay of LSPR (Γ) is composed of several different channels[83], as illustrated in **Figure.I.14**, (1) Radiation dumping (Γ_{rad}): LSPR energy decays through scattering a photon; (2) Direct bulk-contribution decay which contains two contributions: the energy loss due to the electron-phonon scattering, i.e. electron gas frictions (Γ_{Drude}), as explained by the aforementioned Drude Model (Annex V.10), and the interband transition of electrons

($\Gamma_{interband}$) from 5d band to 6sp band of gold atom. (3) Damping due to electron-surface collisions (Γ_{surf}), which represents the electronic collisions with the surface of gold nanoparticles. This damping term is size-dependent and becomes increasingly significant as the nanoparticle size decreases. This relaxation, known as Landau damping, is particularly interesting because the surface scattering provides an additional pathway to excite electrons through intraband transition, leading to the generation of high energy electron-hole pair, commonly referred to as hot carriers.

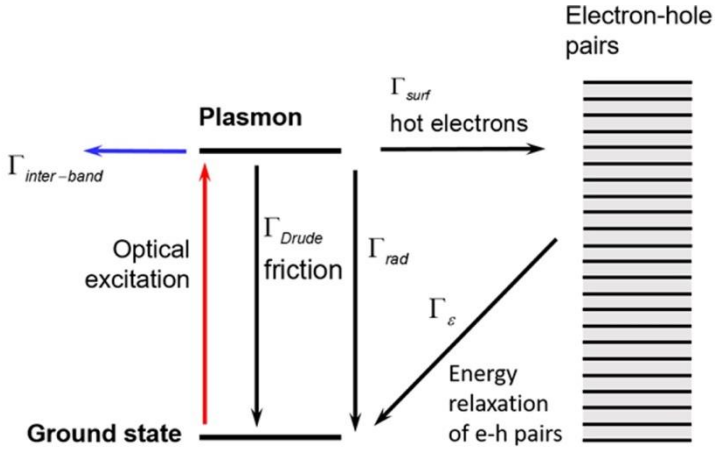

Figure.I.14. Plasmon decay within a gold nanoparticle including both classical (Drude friction) and quantum (hot electron) mechanisms[83].

In **Figure.I.15**, the distribution of excited electron-hole pairs is plotted according to the energy gained from LSPR decay. The Fermi level is set as the reference, the electrons are on the right side while the holes are on the left side. We can easily identify two different types of electrons and holes. Those electrons/holes with high energy correspond to hot electrons/holes generated by Landau damping, whose energy can achieve up to $E_F \pm \hbar\omega$, where $\hbar\omega$ is the energy of LSPR[84]. The other electrons/holes with energy relatively low and close to the Fermi level consist of Drude electrons/holes generated by phonon-assisted intraband electron transition and thermalized hot electrons/holes through electron-electron scattering relaxation.

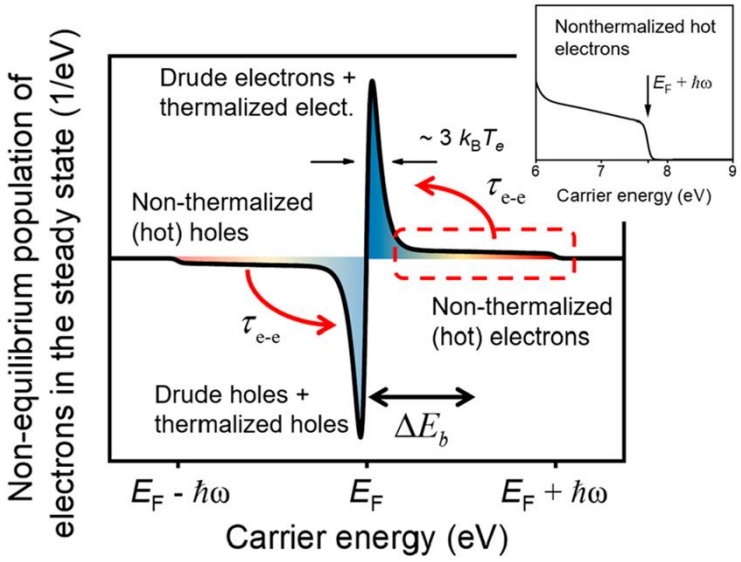

Figure.I.15. Distribution of excited electrons in plasmonic nanoparticles under steady state (continuous wave excitation)[85].

Indeed, this non-equilibrium distribution of hot electrons/holes is highly unstable. These hot carriers will rapidly redistribute their energy with many lower-energy electrons via electron-electron scattering process within a time scale ranging from 100 fs to 1 ps, resulting in a Fermi-Dirac-like electron energy distribution. In this state, the effective electron temperature is much higher than that of the lattice. These thermalized electrons further interact with phonons and finally achieve equilibration where the effective electron temperature is equal to that of the lattice over 0.1-1 ns. Eventually, heat is transferred from nanoparticles to its surrounding environment, leading to a photothermal effect[82]. (**Figure.I.16**)

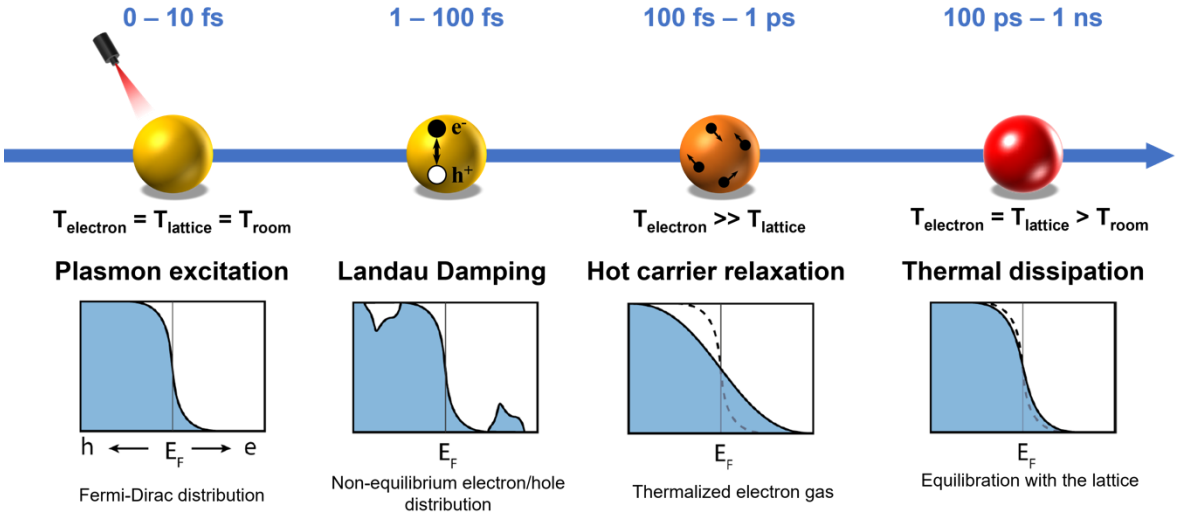

Figure.I.16. Photoexcitation, hot electron generation, relaxation, and thermo-dissipation of gold nanoparticles[86].

I.3.2. Photothermal therapy with gold nanorods

The localized overheating can be applied for cancer cell destruction and is called as hyperthermia. Indeed, irreversible tissue damage occurs when the temperature is increased to 42 °C; further heating tissues to 42-46 °C leads to cell necrosis characterized by the disruption of the plasma

membrane, resulting in the cellular components to leak out and eventually causing inflammation[87,88]. At 46-52 °C, cells die rapidly owing to microvascular thrombosis and ischemia. Finally, when tissue temperature exceeds 60 °C, cell death occurs instantaneously due to protein denaturation and the plasma membrane destruction[89]. Traditionally, hyperthermia methods rely on utilizations of microwave, ultrasound, or magnetic fields. These irradiation methods are nonselective and can cause severe damage to the surrounding normal tissues. Photothermal therapy (PTT) utilizes heat generated by illumination of a laser to kill cancer cells, demonstrating a better local selectivity. Nevertheless, in the case of PTT without photosensitizers, extremely high irradiation power (up to hundreds of watts) is typically required, which raises safety and logistical concerns[90].

The non-radiative relaxation of excited hot electrons leads to the elevation of temperature within the AuNRs, as well as in the surrounding environment, making AuNR a potential photosensitizer for PTT. Compared with other types of photosensitizers, AuNRs possess several advantages such as higher light absorption efficiency, excitation within NIR range where a deeper light penetration is allowed, no significant short- nor long-term toxicity (from 1 month[91] to 15 months[92]). In *in vitro* studies, with optimized size (28 nm in length) and dose (optical density = 0.5), AuNRs under irradiation of an 808 nm NIR light at 5.8 W/cm^2 can lead to a temperature increase of 35 °C in cell culture media within 2 min, resulting in a significant cell viability decrease over 80%[93]. In the context of *in vivo* applications, various strategies have been employed to improve the accumulation of AuNRs in tumors. These approaches include surface functionalization techniques[94–96] and direct intratumoral injection methods[92,97]. In a typical *in vivo* PTT experiment, functionalized AuNRs were injected into mice bearing xenografted tumors followed by irradiation with a continuous wave laser at around 800 nm, at 2 W/cm^2 for 5 min on the tumor zone. The elevation of temperature during the irradiation and the volume of tumor can be assessed by thermal imaging to evaluate the photothermal effect and efficiency. It should be noted that the evaluation of temperature elevation discussed in this context is limited to the skin surface of mice. The measurement of in situ temperature in real-time remains a challenge at present. As shown in **Figure.I.17**, the AuNRs do exhibit an effective photothermal effect under irradiation of NIR light, tumor cells were ablated without regrowth over 20 days.

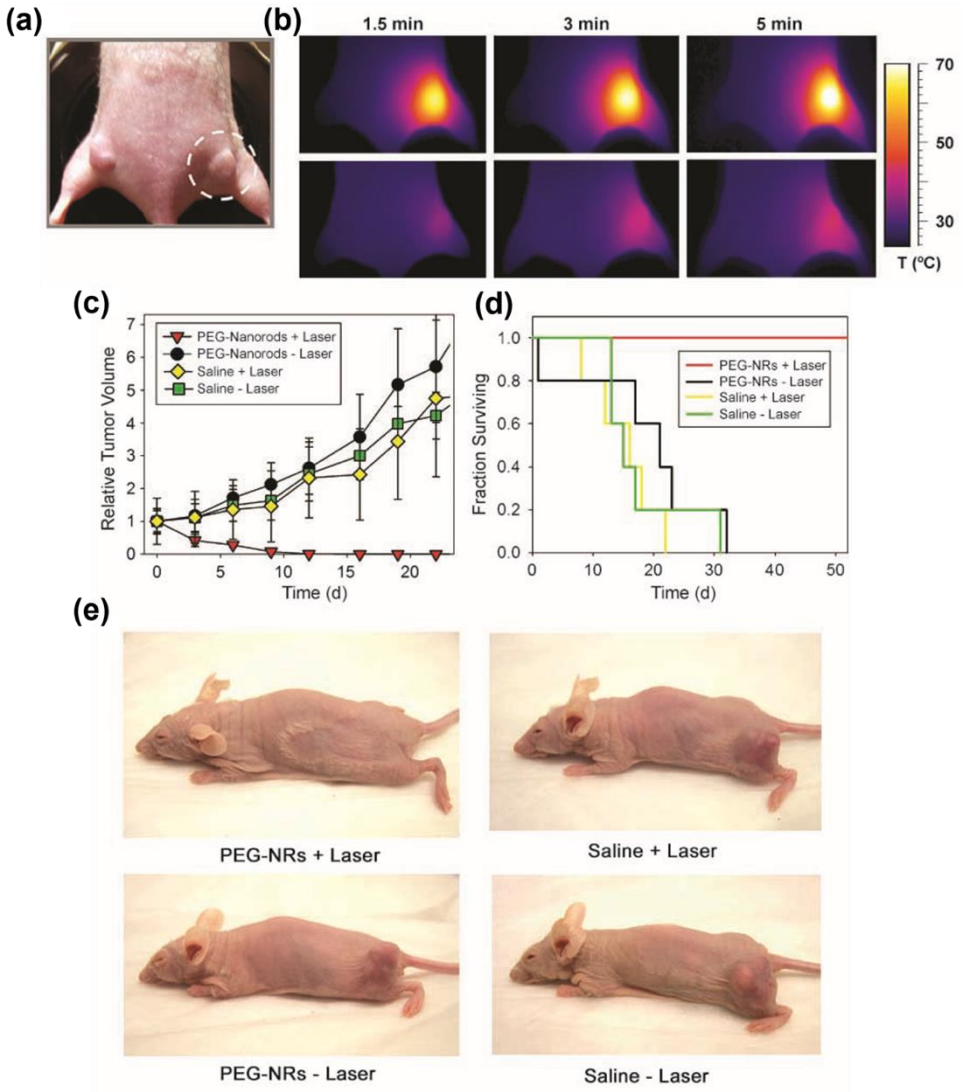

Figure.I.17. PTT on human tumors in mice with PEGylated AuNRs. (a). Mice bearing MDA-MB-435 tumors on opposing flanks, the right flank was irradiated with 810 nm diode laser (2 W/cm^2). (b). Thermographic surveillance of photothermal heating in PEG-AuNRs-injected (top) and saline-injected (bottom) mice. (c). Volume changes in tumor sizes plotted over time after irradiation. (d). Survival of mice after irradiation plotted over time after irradiation. (e). 20 days after irradiation, mice injected with PEG-AuNR, irradiated showed no evidence of tumor regrowth, while the other treatment groups showed thriving tumors[98].

Although tumor ablation was observed in mice, the intense laser irradiation (2 W/cm^2) used during the treatment also resulted in skin wounding effects[92]. This indicates that for *in vivo* applications, it is preferable to use modest irradiation with lower laser power. To achieve more efficient phototherapy, improvements in the phototherapy efficiency of AuNRs are necessary.

I.3.3. Hot electron transfer: Photodynamic therapy

a. Hot electron transfer to adsorbates: AuNR mediated PDT

The previous discussion has shown that upon excitation, the hot electrons in AuNRs can dissipate absorbed light energy as heat through electron-phonon scattering. Alternatively, these hot electrons can engage in photochemical reactions by transferring from the AuNRs to an electron-

accepting orbital of a nearby adsorbate (e.g., H_2 and O_2), thanks to their relatively high energy. As shown in **Figure.I.18. a**, two pathways are proposed for the mechanism of the transfer of hot electrons to adsorbates, namely, the indirect transfer and the direct transfer. For indirect electron transfer, the LSPR decay firstly generates a hot carrier at the surface of the gold nanoparticle. Then this excited hot electron with sufficient energy is injected into the Lowest Unoccupied Molecular Orbital (LUMO) of adsorbate. For direct electron transfer, the decay of LSPR directly create an electron in the LUMO of adsorbate or the conduction, and a hole in the gold nanoparticle[99]. In particular, the processes of thermalization and back-transfer often compete with the transfer processes at similar time scales (**Figure.I.18. b**), presenting significant challenges for the efficient utilization of hot electrons in plasmonic photochemistry[100].

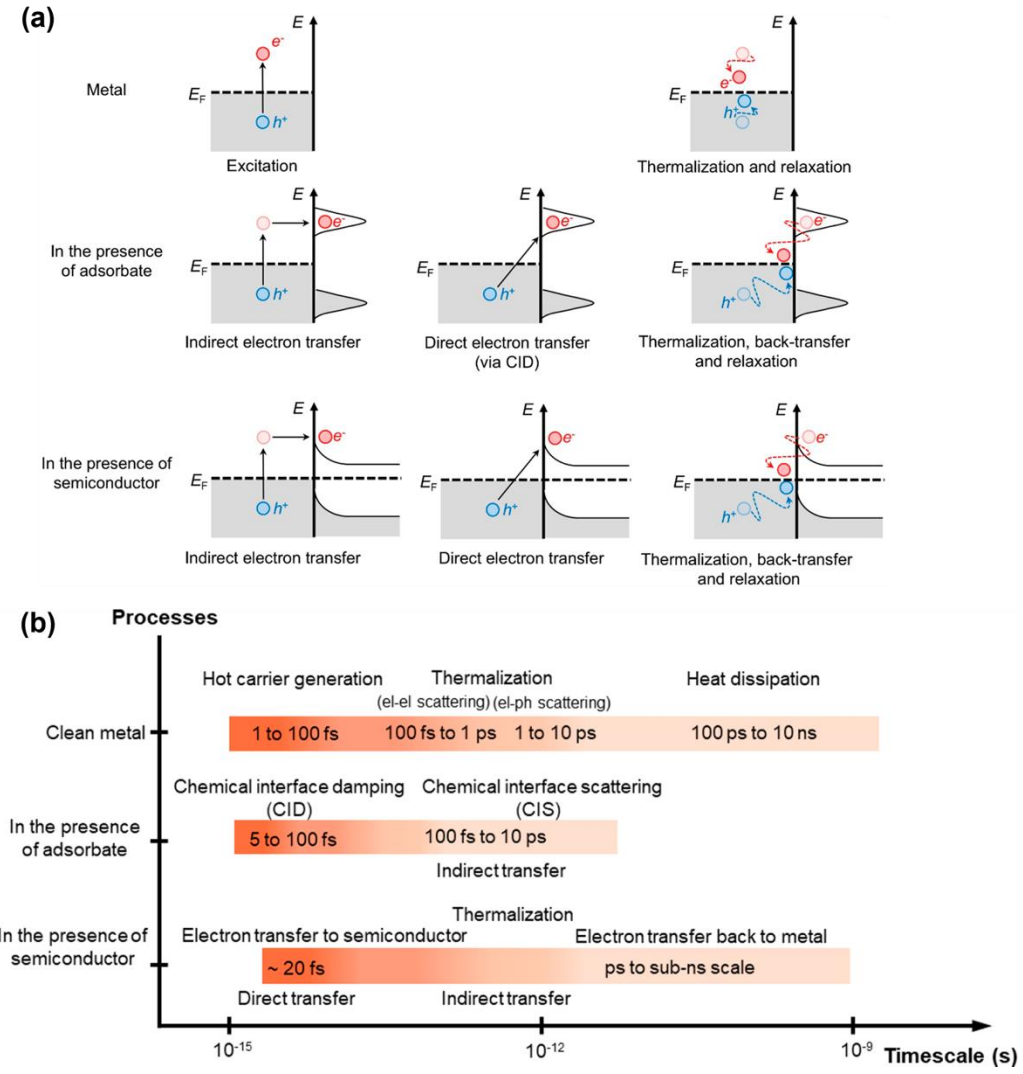

Figure.I.18. (a). Illustration of LSPR induced hot carrier generation and hot electron transfer/back-transfer process in metal, metal/absorbate, and metal/semiconductor systems. (b). Time scales of LSPR induced hot carrier generation, hot electron transfer, and thermalization process with/without absorbate or a semiconductor[100].

Thanks to the hot electron transfer process, it is possible that these hot electrons generated at the surface of gold nanoparticles transfer to the electron-acceptable orbitals of adsorbates such as dioxygen or water molecules in the surrounding environment, leading to the generation of ROS such as

superoxide radicals ($\cdot O_2^-$), hydroxyl radicals ($\cdot OH$) and singlet oxygen ($^1O_2$). These ROS can trigger cell oxidative injury, ultimately inducing cell necrosis and apoptosis, a treatment known as photodynamic therapy (PDT)[101]. Different from the aforementioned cell necrosis, cell apoptosis refers to a programmed cell death pathway that regulates and attenuates inflammatory activities, making it a controlled and cleaner process of cell elimination[102].

AuNRs have been proved to be able to produce different types of ROS when exposed to NIR light. Vankayala et al.[103] reported for the first time that AuNRs can induce tumor cell death both *in vitro* and *in vivo* by producing singlet oxygen under illumination. Importantly, the laser intensity required for this PDT approach was much lower (<130 mW/cm^2) compared to the power levels typically used for PTT (1-48 W/cm^2). Additionally, in a study of Labouret et al.[104], the generation of hydroxyl radicals mediated by AuNRs upon illumination of NIR pulsed laser was observed in a hydrogel film. A multiphoton excitation pathway is attributed to the excitation of hot electrons within AuNRs, leading to dissociation of water molecules and eventually to the generation of hydroxyl radicals. Moreover, Feng et al.[105] compared the photoactivity of gold nanoparticles with various shapes including AuNR, gold nanoshells, and gold nanocages. With the same optical density, these three different gold nanoparticles exhibit the similar photothermal activities while AuNRs were found to be the less effective in producing ROS molecules.

b. Hot electron transfer to semiconductors: hybrid AuNR/semiconductor mediated PDT

The hot electron transfer from AuNRs to adsorbates may suffer from a low efficiency because the transferred electrons can easily back transfer to AuNRs. Energy of these hot electrons can rapidly dissipate through thermalization or recombination with hot holes within AuNRs. To further improve the efficiency in utilizing the hot electrons and prolong their life time, AuNRs can be combined with semiconductors and thus hot electrons produced by AuNRs can transfer to the conduction band of semiconductors, as shown in **Figure.I.18. a**.

Compared to gold/adsorbate electron transfer system, the gold/semiconductor electron transfer system possesses a unique Schottky barrier at the interface of gold and semiconductor. This Schottky barrier plays an important role in the efficiency of harvesting hot electrons from AuNRs. A well-adapted Schottky barrier can effectively avoid the back transfer of hot electrons, reduce the recombination of electron-hole pairs and thus extend the lifetime of hot electrons within semiconductors. However, despite that a low Schottky barrier allows more hot electrons to be injected to the conduction band of semiconductor, this low Schottky barrier cannot effectively delay these transferred hot electrons from transferring back to the gold surface and recombining with the remaining holes. On the other hand, a high Schottky barrier will totally block the electron transfer from AuNR to the semiconductor. For an optimal electron transfer efficiency, a balance between these two effects should be considered[106].

Hot electrons transferred to the conduction band of semiconductors are found to be able to diffuse to the defect states in the semiconductors[107]. For instance, within Au/TiO_2 heterostructures, hot electrons can be trapped either in oxygen vacancies or Ti sites[108]. Additionally, thanks to the Schottky barrier at the Au/TiO_2 interface and the fact that there are no recombination with hot holes in the valence band of TiO_2 [109], hot electrons transferred to TiO_2, trapped at oxygen vacancies show an extremely long lifetime (~10 min)[108], enabling further photochemical reactions to take place.

One potential approach to enhance the efficiency of PDT using AuNRs is to extend the lifetime of the excited hot electrons, thereby increasing the probability of their interaction with oxygen or water

molecules. As previously discussed, the incorporation of semiconductors with gold nanoparticles has been shown to significantly prolong the lifetime of hot electrons due to the reduced recombination of generated hot electrons with hot holes. One of this hybrid Au/semiconductor systems that has been well developed and studied is the combination of gold nanoparticles with TiO_2 substrate. As is shown in **Figure.I.19**, under plasmon resonance excitation, the excited hot electrons are injected into the conduction band of TiO_2, and further displace to the surface of TiO_2, where they can induce photocatalytic reactions such as the reduction of protons in the aqueous solution to produce dihydrogen molecules[110] or synthesis of organic molecules[111].

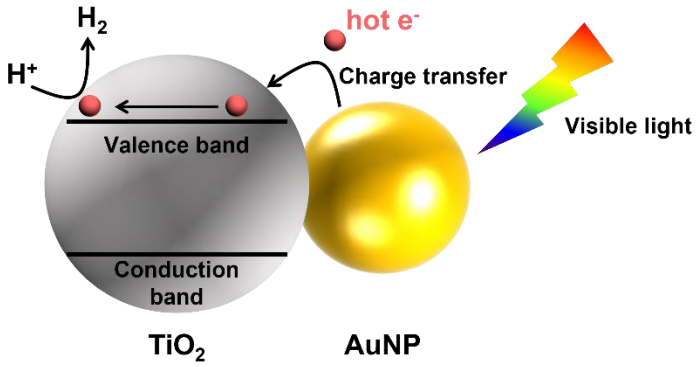

Figure.I.19. Schematic illustration of proposed mechanism of plasmonic photocatalysis realized by Au-TiO_2 hybrid system[110].

Therefore, in terms of AuNR-based PDT agents, by coupling AuNRs with semiconductors, the opportunities for electron to participate in photochemistry reactions can be enhanced, leading to improved ROS production and higher PDT efficacy. (**Figure.I.20. a**) For example, Wang et al.[106] reported the synthesis of hybrid plasmonic Au/$CdSe_xS_y$ nano-dumbbells with efficient hot electron injection from AuNR into the semiconductor tips and subsequent ROS production. (**Figure.I.20. b**) These as-synthesized Au/$CdSe_xS_y$ nano-dumbbells are integrated into a biofilm for antibacterial applications. Besides, Wang et al.[112] synthesized AuNR/CeO_2 core-shell heterostructures. Similarly, the presence of CeO_2 shell significantly enhanced the photocatalytic activity of this hybrid nanostructure with an increase of hydroxyl radical production observed under irradiation. (**Figure.I.20. c**)

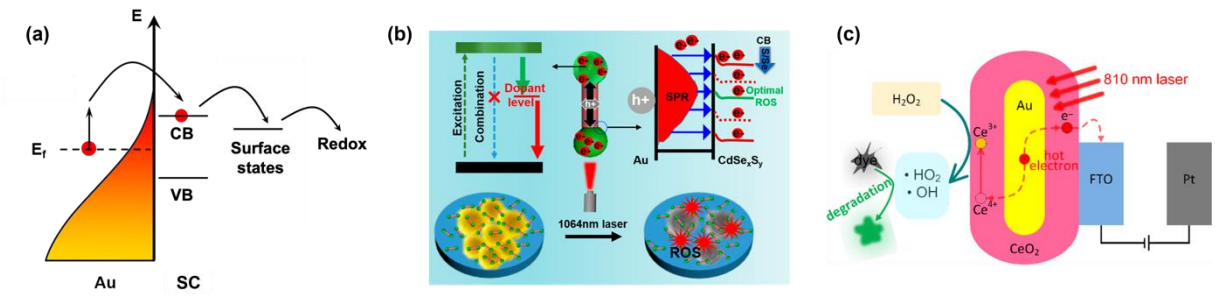

Figure.I.20. (a). Hot electrons excited at the surface of AuNR, transfer to the conduction band (CB) of semiconductor (SC), trapped in the surface defects and participate in Redox reactions. (b). Au/$CeSe_xS_y$ nano-dumbbells with optimized ROS generation efficiency for antibacterial application[106]. (c). AuNR/CeO_2 core-shell heterostructure catalyzed production of hydroxyl radicals under NIR illumination[112].

I.3.4. Energy transfer: Alternative pathway for photodynamic therapy

The LSPR effect is responsible for the excitation of hot electrons. Additionally, this coupling of electromagnetic field with the collective electron oscillation also leads to the enhancement of local electromagnetic field within and around the gold nanoparticles, as described in Equations.I.1 and shown in **Figure.I.21**.

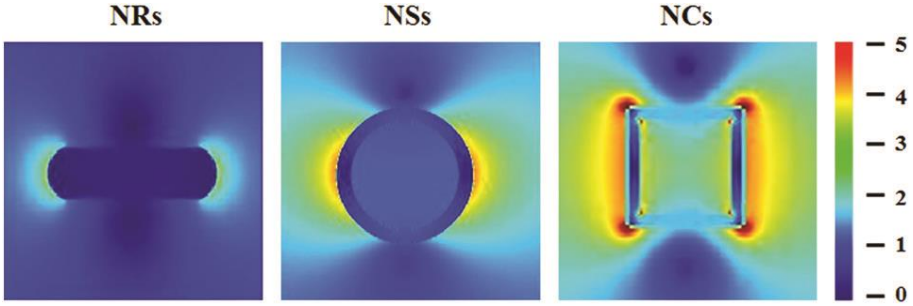

Figure.I.21. FDTD calculations for the Electromagnetic field distribution and enhancement contours of AuNRs (left), gold nanoshells (NSs, middle), and gold nanocages (NCs, right) under 808 nm excitation[105].

As for AuNR-semiconductor heterostructure, when a semiconductor material is attached to the surface of AuNR, under LSPR illumination, it can also be influenced by this local enhanced electromagnetic field. If the energy of the enhanced electromagnetic field is high enough to excite an electron from the valence band of semiconductor to the conduction band, an electron-hole pair can be generated in the semiconductor. In this case, electrons in conduction band of semiconductor are generated by the radiative plasmon energy, instead of hot electrons transferred from AuNRs. Indeed, in the near-field case, which means that the semiconductor component is close enough to the AuNR (~25 nm)[113], the plasmon energy can be transferred through a non-radiative process, namely plasmon-induced resonance energy transfer (PRET): the generation of electron-hole pairs in semiconductor is induced by the localized surface plasmon dipole, similar to Förster resonance energy transfer (FRET), where the LSPR dipole replaces the fluorescent donor system. (**Figure.I.22**)

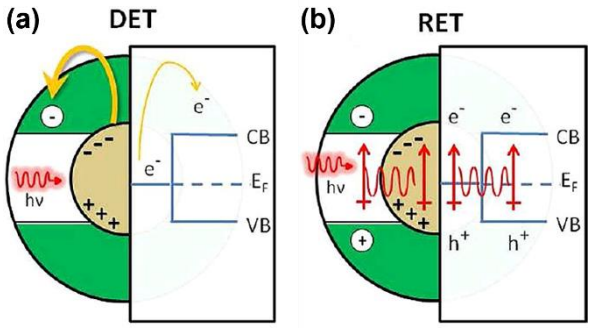

Figure.I.22. Different processes of electron generation in conduction band (CB) of semiconductor assisted by plasmonic nanoparticles. (a). Direct electron transfer (DET) of hot electrons from plasmonic nanoparticles to semiconductor; (b). Resonant energy transfer (RET) from the LSPR dipole to the electron hole pair in the semiconductor[114].

Therefore, the energy transfer process, particularly the PRET process, offers an alternative approach to harness plasmonic energy. Unlike charge transfer, the energy transfer pathway does not necessitate the alignment of electronic band structures between semiconductors and metal materials. This characteristic significantly expands the range of applicable materials. However, for efficient energy

transfer, a substantial spectral overlap between the plasmon band of the metal and the band gap energy of the semiconductor is crucial.

Based on this PRET process, Cushing et al.[114] studied the Au@SiO_2@Cu_2O sandwich structure, where spheric gold nanoparticle core converts the energy of incident visible light photons into LSPR oscillations and transfers the plasmonic energy to the Cu_2O semiconductor shell. (**Figure.I.23. a**) The photocatalytic activity of this Au@SiO_2@Cu_2O sandwich structure is evaluated by the degradation of methyl orange. They found that the photocatalysis efficiency of this energy transfer based Au@SiO_2@Cu_2O sandwich structure is much higher than that of Cu_2O alone (**Figure.I.23. b, c**). Additionally, Chang et al.[115] synthesized a AuNR core@void@CuS shell yolk-shell heterostructures (Au-CuS YSNPs). (**Figure.I.23. d**) Under NIR light illumination, these Au-CuS YSNPs are proved to induce both photothermal and photodynamic effect to kill cancer cells *in vivo*. (**Figure.I.23. e, f**) Particularly, the generation of hydroxyl radicals due to the PRET process was verified.

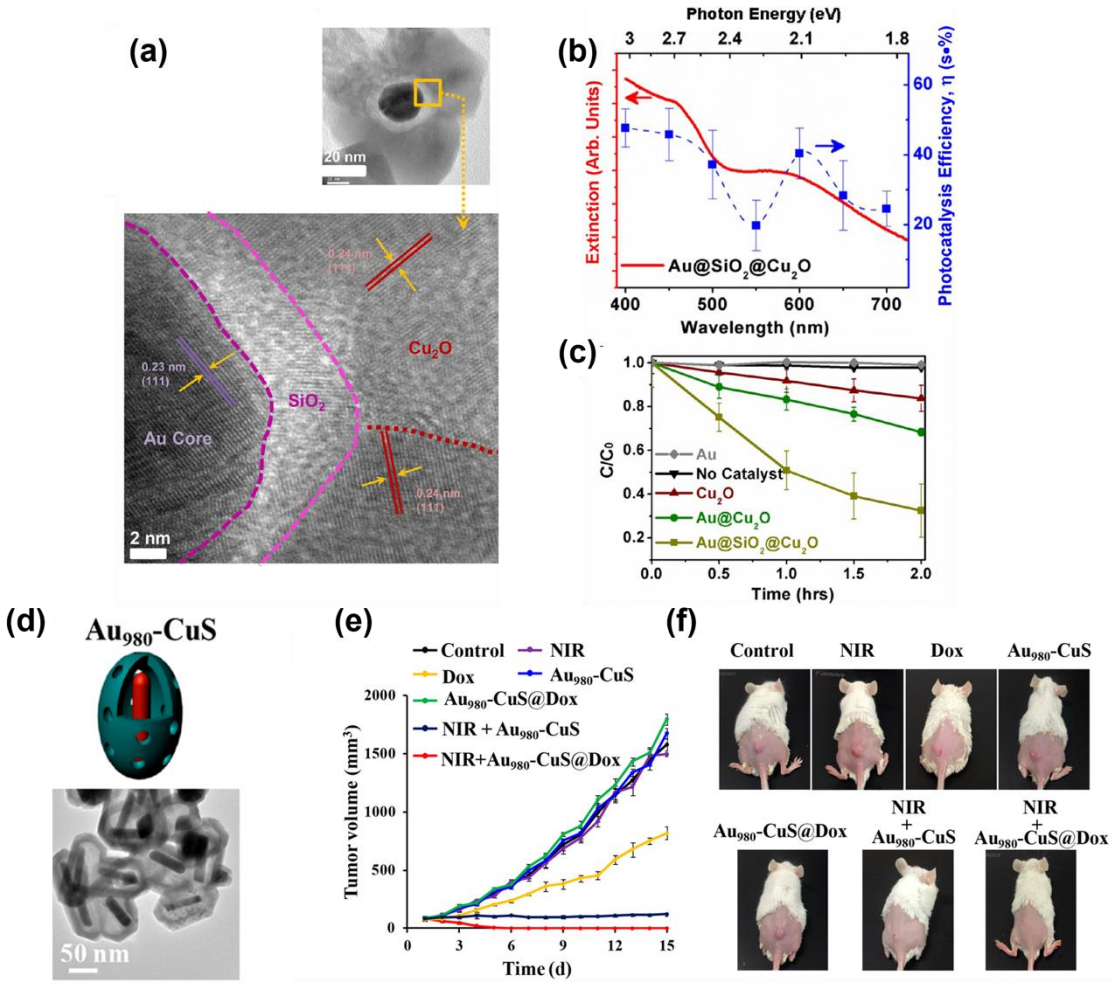

Figure.I.23. Examples of Au-semiconductor heterostructures based on PRET process. (a). TEM images of Au@SiO_2@Cu_2O. (b). UV-visible spectrum and photocatalytic action spectrum for Au@SiO_2@Cu_2O. (c). Visible light photodegradation of methyl orange versus time in comparison between no catalyst, Au, Cu_2O, Au@Cu_2O, and Au@SiO_2@Cu_2O[114]. (d). TEM images of Au-CuS YSNPs. (e, f). tumor growth curves/pictures of 4T1tumor-bearing mice intravenously administered with PBS, Dox, Au-CuS YSNPs, Au-CuS YSNPs-Dox under 980 nm laser irradiation (0.9 W/cm^2, 5 min), Dox is doxorubicin, a chemotherapy drug[115].

I.4. Summary: Significance and objectives of the study

To summarize, this chapter discussed various types of inorganic nanoparticles, including semiconductor quantum dots, magnetic nanoparticles, and plasmonic nanoparticles, and their potential for biomedical applications in sensing, imaging, and therapies. Among these nanoparticles, plasmonic gold nanoparticles, particularly AuNRs, were highlighted.

Gold nanoparticles, due to their localized surface plasmon resonance effect, can interact with light through absorption or scattering. By controlling the shape and size of gold nanoparticles, AuNRs with a strong and tunable plasmon band in the NIR region can be achieved, which aligns well with the optimal light penetration range in the human body. This property makes AuNRs suitable as photosensitizers for phototherapies against cancers.

Under NIR laser irradiation, the localized surface plasmon resonance effect in AuNRs can excite hot electrons. These hot electrons convert absorbed light energy into heat, raising the temperature of the nanoparticles and the surrounding environment. This photothermal effect induced by AuNRs can lead to cell death, making photothermal therapy based on AuNRs effective *in vitro* and *in vivo*.

Alternatively, when coupled with a semiconductor, AuNRs can transfer their hot electrons to the conduction band of the semiconductor or directly generate electron-hole pairs within the semiconductor through resonant energy transfer pathway. The prolonged lifetime of hot electrons at the semiconductor surface allows them to reduce dioxygen molecules in the physiological environment, generating reactive oxygen species that can induce cell apoptosis, a programmed cell death pathway. These hybrid AuNR@semiconductor nanostructures have the potential to combine both photothermal and photodynamic effects, resulting in an enhanced efficiency of phototherapy.

Therefore, based on fruitful research advances and achievements in this domain, this thesis is dedicated to developing novel AuNR-based hybrid plasmonic nanostructures for the application in photodynamic therapy against cancers.

Chapter II will focus on the dumbbell shaped AuNR/TiO_2 nanoparticles. We will discuss how these hybrid nanoparticles can be synthesized, why it is important to finely control their morphology, how to verify and evaluate their photocatalytic activity, what is the importance and strategy to functionalize their surface, and how to test their photodynamic effects in presence of cancer cells.

Chapter III will introduce another type of AuNR@semiconductor nanoparticles which utilizes plasmon energy through plasmon resonance energy transfer pathway. The objective is to improve the quantum yield of the hybrid AuNR@semiconductor nanoparticles through optimizing their structure, identifying and understanding the key parameters that influence their photoactivities. Silver sulfide and copper (I) sulfide are selected as semiconductor materials. The synthesis of these hybrid nanoparticles will be explored, along with the evaluation of their photoactivity.

Chapter IV delves into the topic of the interactions of inorganic nanoparticles with immune systems. The importance of ligands on the surface of nanoparticles in determining their interactions with proteins and cells will be explored. The objective of this chapter is to design and synthesize a series of hydrophilic polymer ligands based on various zwitterionic monomers developed in the laboratory LPEM. These ligands will be used to functionalize different types of inorganic nanoparticles, including iron oxide nanoparticles, CdSe quantum dots, and AuNRs. The zwitterionic polymers aim to prevent the formation of protein corona on the nanoparticle surface, imparting antifouling properties to the

nanoparticles. The chapter will cover the synthesis of these polymers, the grafting of the polymers onto the nanoparticle surfaces, the differences between zwitterionic monomers, the response of macrophages to the functionalized nanoparticles, and pharmacokinetic studies conducted on mice. The goal is to provide a comprehensive understanding of how these hydrophilic polymer ligands can modulate the interactions between inorganic nanoparticles and the immune system, leading to potential applications in biomedical research and therapy.

Chapter II. Plasmon-excited charge transfer-based nanohybrids

Résumé

Les nanoparticules d'or, telles que les nano-bâtonnets d'or (AuNRs), présentent des sections efficaces d'absorption exceptionnellement élevées qui peuvent être réglées dans le proche infrarouge (NIR), la fenêtre optimale pour la pénétration de la lumière dans les tissus biologiques. Cela les rend précieuses en tant que photosensibilisateurs pour le traitement du cancer par thérapie photothermique, où l'énergie lumineuse absorbée est convertie en chaleur. De plus, il existe un fort intérêt à utiliser les porteurs d'électrons chauds générés dans les AuNRs par irradiation NIR pour produire des espèces d'oxygène radicalaires cytotoxiques afin d'améliorer l'efficacité de la photothérapie. Dans ce chapitre, nous optimisons la synthèse des AuNRs et les intégrons avec succès à du dioxyde de titane (TiO_2), un matériau semi-conducteur. Nous montrons que les nanoparticules hybrides composées de AuNRs avec du TiO_2 déposé à leurs extrémités sont des sensibilisateurs efficaces pour produire des espèces radicalaires hydroxyle sous irradiation NIR. Nous attribuons ce phénomène au transfert des électrons chauds générés par l'excitation plasmonique dans les AuNRs vers les pointes de TiO_2, suivi de la réduction du dioxygène. La forme en haltère de ces nanoparticules hybrides AuNR/TiO_2 est cruciale pour obtenir une photoactivité optimale. Nous démontrons que la plupart des électrons chauds dans les AuNRs sont produits par excitation à un photon et suivi par l'injection dans la bande de conduction du TiO_2 par transfert de charge. Ensuite, nous fonctionnalisons ces nanoparticules hybrides AuNR/TiO_2 avec des ligands polymères à bloc poly(éthylène glycol)-phosphonate pour les stabiliser en milieu physiologique. Les ligands polymères peuvent affecter considérablement la photoactivité de ces AuNR/TiO_2 nanoparticules hybrides. Le choix de la densité de polymère à la surface des nanoparticules s'avère critique pour maintenir la stabilité colloïdale tout en préservant une photoactivité élevée. Enfin, nous démontrons que l'effet photodynamique induit la mort cellulaire lors de l'irradiation, avec une efficacité supérieure à celle de l'effet photothermique seul.

Abstract

Gold nanoparticles, such as nanorods (AuNRs), present exceptionally high absorption cross-sections which can be tuned to the near infrared (NIR), the optimal window for light penetration in biological tissues. This makes them valuable photosensitizers for the treatment of cancer using photothermal therapy, where the absorbed light energy is converted into heat. In addition, there is a strong interest in using hot electron carriers generated in AuNRs by NIR irradiation to produce cytotoxic radical oxygen species in order to enhance the efficiency of the phototherapy. In this Chapter, we optimize the synthesis of AuNRs and successfully functionalize them with titanium dioxide (TiO_2), a semiconductor material. We show that hybrid nanoparticles composed of AuNRs with TiO_2 deposited at their extremities are efficient sensitizers to produce hydroxyl radical species under NIR irradiation. We attribute this phenomenon to the transfer of hot electrons generated from the plasmon excitation in AuNR to the TiO_2 tips followed by reduction of dioxygen. The dumbbell shape of these hybrid AuNR/TiO_2 nanoparticles is crucial for achieving optimal photoactivity. We demonstrate that most of hot electrons in AuNRs are produced through one-photon excitation, which are then inject into the conduction band of TiO_2 by charge transfer. We then functionalize these hybrid AuNR/TiO_2 nanoparticles with block poly(ethylene glycol)-phosphonate polymer ligands to stabilize them in physiological medium. The polymer ligands can drastically affect the photoactivity of these hybrid AuNR/TiO_2 nanoparticles. The choice of polymer density on the nanoparticle surface is found to be critical in maintaining colloidal stability while preserving high photoactivity. We finally demonstrate that the photodynamic effect induces cell death upon irradiation, with a greater efficiency than the photothermal effect alone.

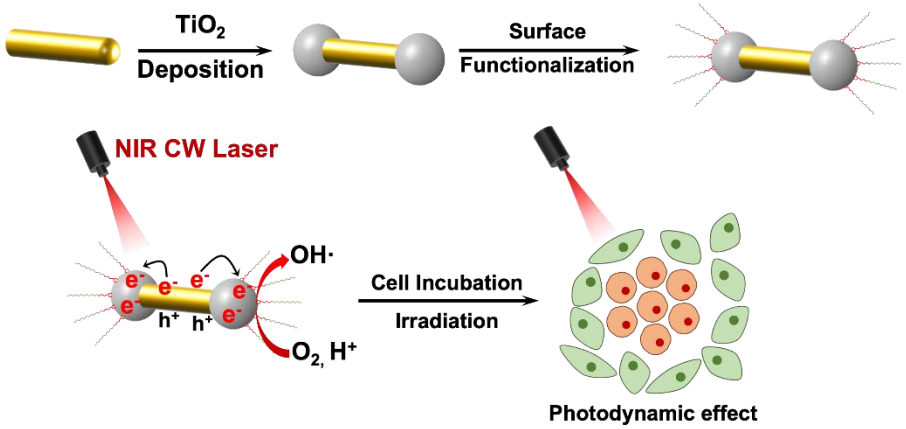

Figure.II.1. Principles of synthesis hybrid dumbbell shape AuNR/TiO_2 nanoparticles and of their application in photodynamic therapy.

Gold/semiconductor heterostructures have been extensively studied and developed for their photocatalytic properties. In these systems, the hot electrons generated in gold nanoparticles are typically injected into the conduction band of the semiconductor material, driving various physical and chemical processes. In the context of photodynamic therapy, the transferred hot electrons need to possess sufficient energy to reduce dioxygen molecules and generate reactive oxygen species. Additionally, the conduction band energy of the semiconductor should align with the energy of the majority of excited electrons to facilitate the hot electron injection process. Wang et al.[106] integrated AuNRs with $CdSe_xS_y$ semiconductors to create a hybrid nanostructure. They demonstrated an optimal photodynamic effect when the conduction band energy of $CdSe_xS_y$ semiconductors was finely tuned to be -0.1V below the surface plasmon resonance (SPR) energy of AuNRs. However, the potential toxicity of cadmium in the semiconductor materials raises concerns regarding their medical safety and limits their *in vivo* applications. Hence, it is desirable to explore more biocompatible semiconductor alternatives.

Among various semiconductor materials, our focus lies on titanium dioxide (TiO_2) due to its suitable conduction band energy that matches the SPR energy of AuNRs, enabling the production of reactive oxygen species. Furthermore, TiO_2 exhibits relatively lower toxicity compared to cadmium, making it more suitable for biomedical applications.

In this chapter, we initiate our exploration by synthesizing hybrid AuNR/TiO_2 nanoparticles. Subsequently, we characterize their photoactivity in generating reactive oxygen species. We then delve into optimizing the surface functionalization of these synthesized hybrid AuNR/TiO_2 nanoparticles. Finally, we evaluate the photodynamic effect of these nanoparticles through *in vitro* experiments.

II.1. Synthesis and characterization of AuNR/TiO_2 nanoparticles

The fabrication of AuNR/TiO_2 nanoparticles involves two successive synthesis steps. The first step is to synthesize AuNRs with an appropriate aspect ratio and size using the well-developed seeded growth synthesis approach. Afterward, a wet-chemistry method developed by Wu's group[116] is used to selectively deposit a TiO_2 layer at the tips of the synthesized AuNRs to form dumbbell-shaped AuNR/TiO_2 nanoparticles. Apart from the dumbbell shape, the TiO_2 layer also can entirely encapsulate the AuNRs, resulting in core-shell-shaped AuNR@TiO_2 nanoparticles. The synthesized nanoparticles were monitored using UV-vis absorption spectroscopy and TEM.

II.1.1. Optimization of seeded growth AuNR synthesis

Seed growth synthesis of AuNRs:

To prepare the seed growth solution for AuNR growth, $HAuCl_4$ solution (25 mM, 200 µL) was mixed with cetyltrimethylammonium bromide (CTAB) solution (0.1 M, 7.5 mL) under stirring in a 20 mL scintillation vial. Then 100 µL of fresh $NaBH_4$ solution (0.1 M) was diluted in 900 µL of Milli-Q® water, and 600 µL of this newly prepared $NaBH_4$ solution (0.01 M) was rapidly injected into the Au(III) – CTAB solution under vigorous stirring (1200 rpm). The stirring was stopped after 2 min, and the seed solution was aged for at least 30 min before use.

To prepare the growth solution, CTAB – Sodium Oleate (NaOL) binary surfactant solution was firstly prepared and heated to 60 °C (CTAB: 37 mM – 85 mM, NaOL 0.008 M). 19.6 mL of this surfactant solution was added to a 20 mL scintillation vial and cooled down to 30 °C. Freshly prepared $AgNO_3$ solution (0.1 M, 20 – 40 µL) was then added, followed by $HAuCl_4$ solution (25 mM, 400 µL). The mixture was kept undisturbed at 30 °C for 90 min and then 50 – 100 µL of HCl (37 wt. % in water, 12 M) was introduced. After 15 min of slow stirring, fresh ascorbic acid solution (0.064 mM, 50 µL) was added to the mixture, followed by 30 s vigorous stirring. Finally, 10 – 20 µL of seed solution was injected. The final mixture was stirred for 30 s and left undisturbed at 30 °C for 17h. The synthesized AuNRs were precipitated under centrifugation (3400 g, 20 min), washed twice with distilled water, and stored in 4 mM CTAB solution.

As discussed in Chapter I, various techniques have been developed for AuNR synthesis. Here, the seeded growth synthesis approach proposed by Ye's group[54] is utilized, a method that provides high reproducibility and allows for the synthesis of AuNRs with diameters ranging from 10 to 40 nm, and longitudinal absorptions between 600 and 1000 nm. Our objective is to synthesize AuNRs with dimensions around 85 * 25 nm² and with a longitudinal absorption at 750 nm. To precisely control and optimize the morphology of the synthesized AuNRs, we adjusted several parameters during the synthesis, including the pH value, surfactant concentration, seed concentration, and silver ion concentration of the growth solution. By fine-tuning these factors, we were able to produce AuNRs with consistent morphology through different syntheses and precisely control their absorption properties by adjusting the shape of the AuNRs. After synthesis, AuNRs were purified and redispersed in 4 mM CTAB stock solution. The lengths and diameters of 50 particles for each synthesis were measured by TEM images, enabling the calculation of the average and distribution of particle size and aspect ratio, the synthesis conditions and results are assembled in Annex. (**Annex.Table.V..1**)

a. Acidity

The pH value of the growth solution is a critical parameter in controlling the growth of AuNRs, as the reactivity of the reductant, ascorbic acid, is dependent on the acidity of the growth solution. As shown in **Figure.II.2**, if the pH value increases, the hydroxyl groups of ascorbic acid will lose protons subsequently, favoring electron transfer and thus increasing the reduction reactivity of the molecule. Adversely, a lower pH can reduce the reactivity of ascorbic acid.

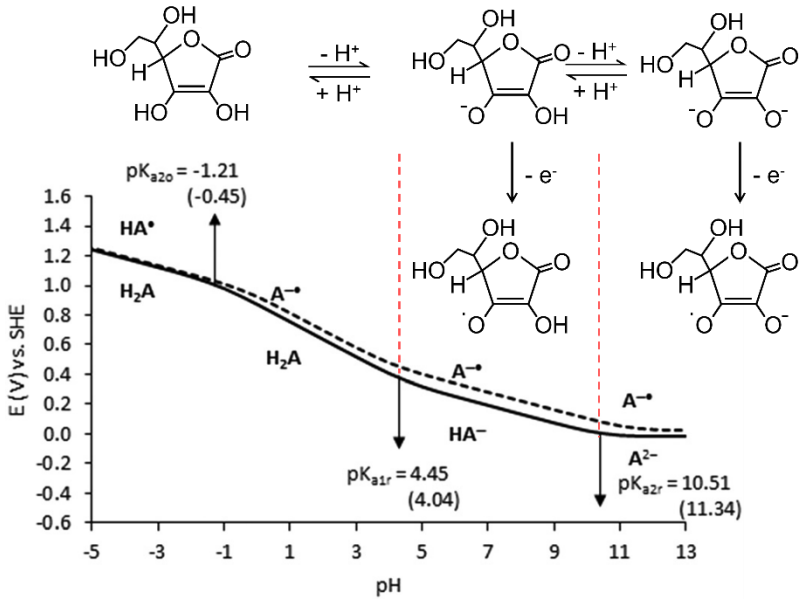

Figure.II.2. Pourbaix diagram for the first $1e^-$ oxidation of ascorbic acid in water. Solid line: The calculated pH-dependent reduction potential Dashed line: The pH-dependent reduction potentials obtained from experiment values[117].

We first adjusted the acidity of the system with fixed CTAB concentration (62 mM), quantity of seeds (10 µL), and $AgNO_3$ concentration (0.15 mM). As shown in **Figure.II.3. a**, by increasing the quantity of HCl in the growth solution, the longitudinal absorbance of synthesized AuNRs shifted to longer wavelength (from 890 nm to 1025 nm), indicating that the aspect ratio of AuNRs has increased, which can be explained by a simultaneous increase in length (from 61.0 to 70.2 nm) and decrease in diameter (from 12.3 to 11.3 nm) (**Figure.II.3. b, c**) measured from TEM images (**Figure.II.3. d – f**). Indeed, if the pH value of the growth solution is below 4, given that the pKa of ascorbic acid is of 4.1, the reduction potential of ascorbic acid in this case will be significantly decreased, resulting in a slower growth rate , thus favoring the anisotropic growth[118].

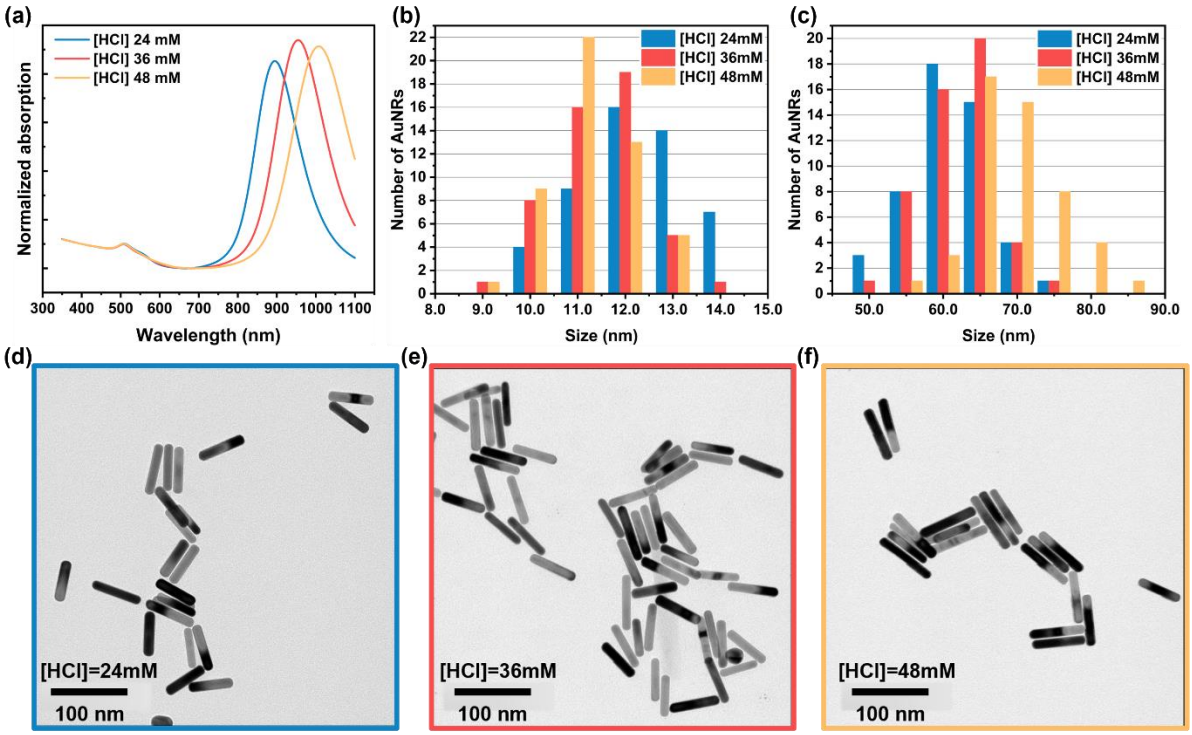

Figure.II.3. Effect of the pH value of growth solution on the morphology and absorption property of synthesized AuNRs. ([CTAB] = 62 mM, V(Seed) = 10 µL, [$AgNO_3$] = 0.15 mM) (a). Normalized UV-vis absorption spectra of AuNRs. (b, c). Size distribution of AuNRs: (b). Diameter; (c). Length. (d – f). TEM images of AuNRs synthesized under different HCl concentrations: (d). 24 mM; (e). 36 mM; (f). 48 mM.

b. Concentration of surfactant CTAB

The molecule CTAB has been widely appreciated and chosen as an indispensable surfactant for synthesizing AuNRs[119–121]. It is believed that CTAB possesses several unique functionalities in the anisotropic growth of AuNR[73,122]. Firstly, CTAB act as an amphipathic molecule, improving the colloidal stability of gold nano-seeds and AuNRs during and after the growth process by forming a hydrophilic bilayer surrounding nanoparticles. Second, the quaternary ammonium surfactant head group forms complexes with the gold precursor salt, modifying its redox potential. Moreover, bromide counterions can selectively deposit on the lateral surface of the nascent AuNRs. The density of CTAB on the lateral surface of AuNRs is higher than that at the tips of AuNRs, rendering the tips of nascent AuNRs more accessible for gold atoms to deposit on promoting symmetry-breaking growth[123].

Here, we synthesized AuNRs using growth solutions with varying concentrations of CTAB while keeping other parameters constant ([HCl] = 30 mM, V(seed) = 10 µL, and [Ag^+] = 0.15 mM). Increasing the CTAB concentration in the growth solution from 48 mM to 82 mM resulted in a red shift of the longitudinal absorption band of AuNRs from 700 nm to 950 nm, meaning that the aspect ratio of AuNRs increased (**Figure.II.4. a**). According to the TEM images (**Figure.II.4. d – f**), as the CTAB concentration increased, the diameter of AuNRs decreased significantly while the length of AuNRs did not change significantly (**Figure.II.4. b, c**). In particular, for AuNRs synthesized with higher CTAB concentrations, from the UV-vis absorption spectra (**Figure.II.4. a**), we observed small "shoulders" appear at around 550 nm near the transverse absorption peaks of AuNRs, which can be attributed to the by-products such as AuNPs generated during the growth process. These small AuNPs were also observed in TEM images (**Figure.II.4. e, f**). The appearance of these small AuNPs is possibly due to the

formation of dense CTAB bilayers at high concentrations, leading to a more difficult diffusion and deposition of Au precursors on the nascent AuNR surface, both at lateral facets and tips, and therefore, a delayed and heterogeneous growth of AuNRs.

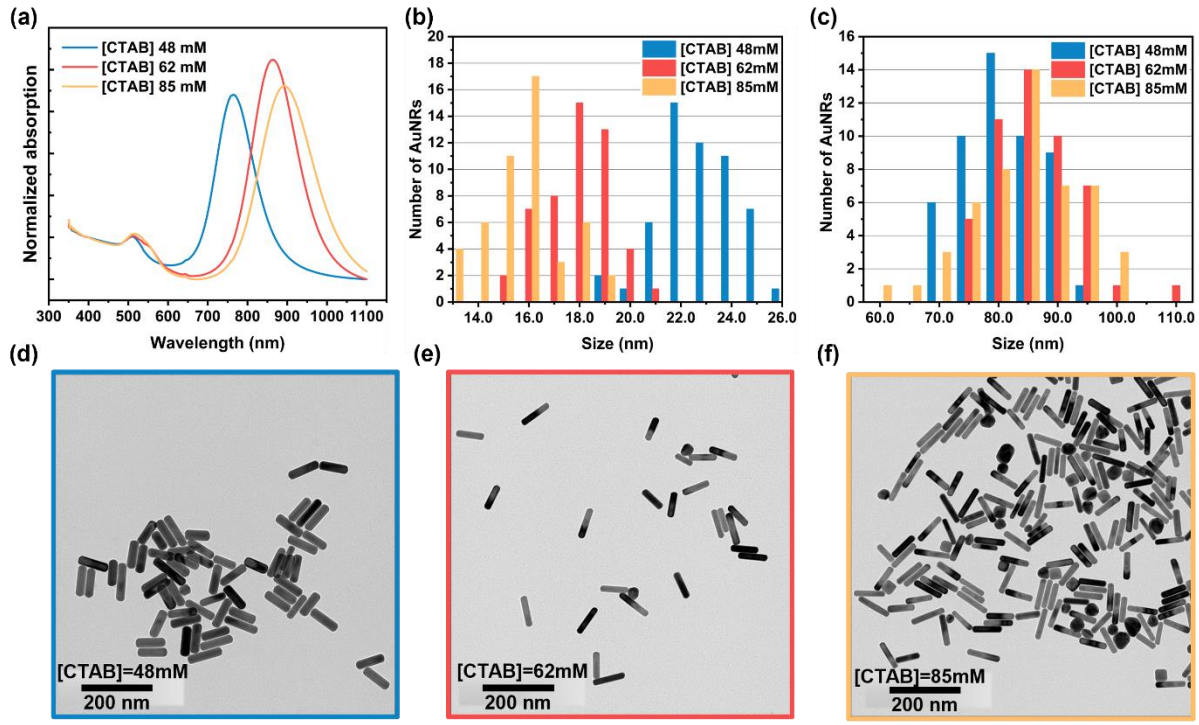

Figure.II.4. Effect of the CTAB concentration in the growth solution on the morphology and absorption property of synthesized AuNRs. ([HCl] = 30 mM, V(Seed) = 10 µL, [$AgNO_3$] = 0.15 mM) (a). Normalized UV-vis absorption spectra of AuNRs. (b, c). Size distribution of AuNRs: (b). Diameter; (c). Length. (d – f). TEM images of AuNRs synthesized under different CTAB concentrations: (d). 48 mM; (e). 64 mM; (f). 85 mM.

c. Concentration of seed particles

In the seed solution, Au (III) ions are rapidly and directly reduced to Au (0) by a strong reductant, such as $NaBH_4$, giving rise to small gold nuclei (diameter < 5 nm). Then the seed solution was added dropwise to the growth solution, where these small gold nuclei serve as the starting point for AuNR growth by catalyzing the reduction of Au (I) to Au (0).

Here, with other parameters fixed ([HCl] = 30 mM, [CTAB] = 48 mM, and [Ag^+] = 0.15 mM), increasing the amount of seed solution (from 10 µL to 20 µL) added into the growth solution results in AuNRs with higher aspect ratio, which is inferred from the red shift (from 763 nm to 797 nm) of longitudinal absorption of AuNRs observed from UV-vis spectra (**Figure.II.5. a**). From TEM images (**Figure.II.5. d – f**), we found that a higher amount of seed leads to smaller AuNRs with reduced diameter (from 22.8 nm to 19.2 nm), and almost unchanged length (**Figure.II.5. b, c**), which also confirms the results of the absorption spectroscopy. These results suggest that every seed in the growth solution has the potential to develop into a nanorod, and thus the presence of more seed particles results in less abundant Au (I) precursors available for each seed nuclei in the growth solution, ultimately leading to the formation of thinner AuNRs.

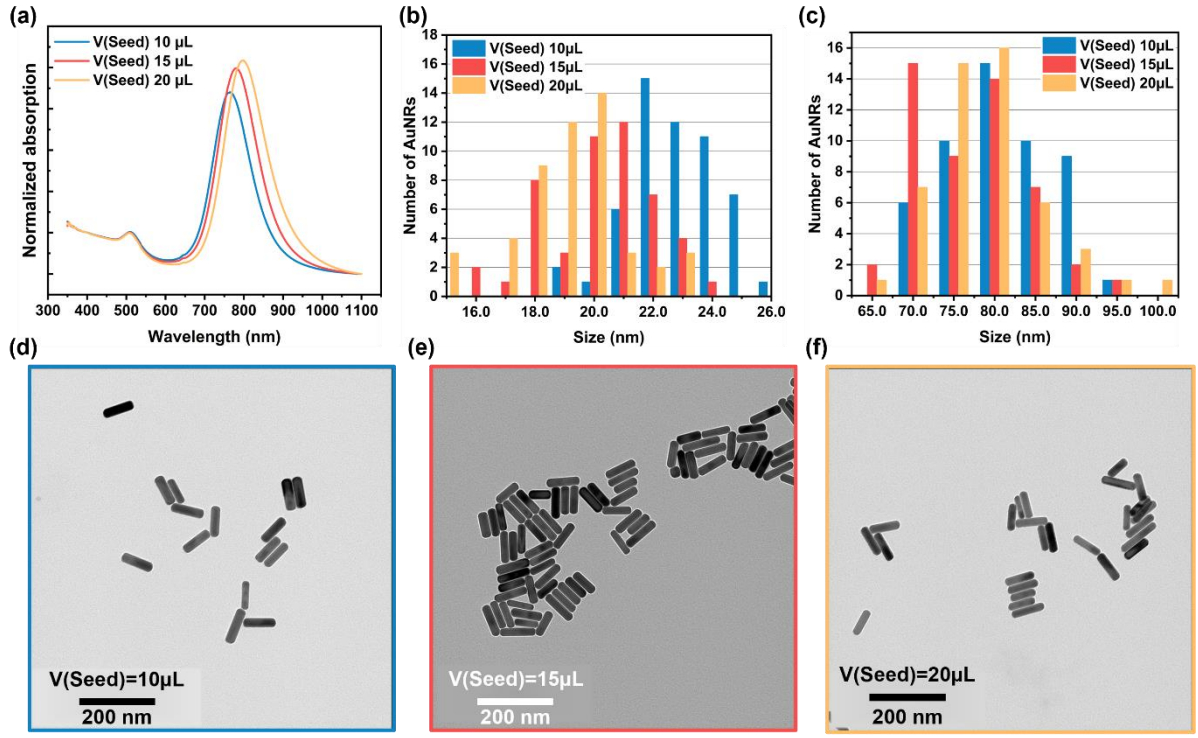

Figure.II.5. Effect of the seed concentration in the growth solution on the morphology and absorption property of synthesized AuNRs. ([HCl] = 30 mM, [CTAB] = 48 mM, [$AgNO_3$] = 0.15 mM) (a). Normalized UV-vis absorption spectra of AuNRs. (b, c). Size distribution of AuNRs: (b). Diameter; (c). Length. (d – f). TEM images of AuNRs synthesized under different seed concentrations: (d). 10 µL; (e). 15 µL; (f). 20 µL.

d. Concentration of silver ions

Although silver ion (Ag^+) has been confirmed to be able to promote anisotropic growth of AuNRs and has been thus widely applied in AuNR synthesis, the exact mechanisms are still under discussion. Generally, three different mechanisms of silver-assisted anisotropic growth have been proposed: (**Figure.II.6**)[59] (1). The formation of the complex CTA-Ag^+-Br^- which selectively caps the lateral face of AuNR; (2). The selective deposition of Ag layer at the lateral surface of AuNR; (3). The deformation of CTAB rod-like micelle due to silver-bromide interaction.

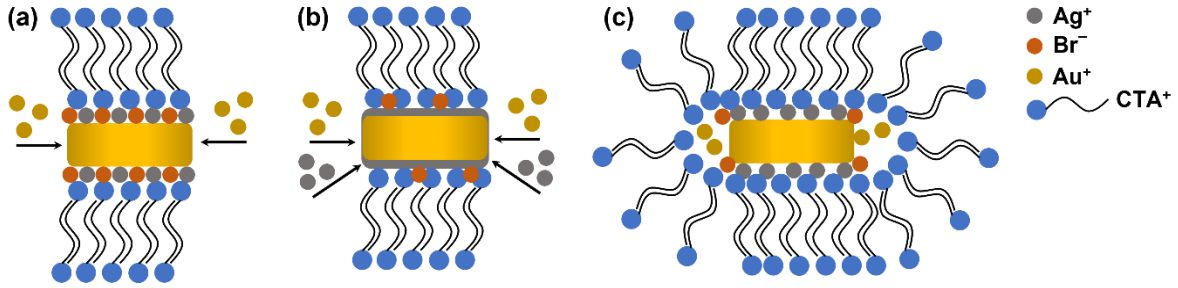

Figure.II.6. Illustration of three proposed mechanism explaining the role of silver ions in the AuNR synthesis. (a). Formation of CTA-Ag^+-Br^- complex; (b). Deposition of Ag layer; (c). Deformed CTAB soft template micelle.

Here, with other parameters fixed (([HCl] = 30 mM, [CTAB] = 48 mM, and V(seed) = 10 µL) by increasing the concentration of Ag^+ in the growth solution (from 0.125 mM to 0.175 mM), we

obtained AuNRs with higher aspect ratio, as shown in **Figure.II.7. a**, the longitudinal absorption peak shifted from 700 nm to 800 nm. From TEM images (**Figure.II.7. d – f**), we also found that the length of AuNRs increased from 74.1 nm to 87.7 nm, while the diameter of the AuNRs remain unchanged (**Figure.II.7. b, c**), which suggests that we could finely modulate the longitudinal absorption of AuNRs by controlling the Ag^+ concentration during the synthesis.

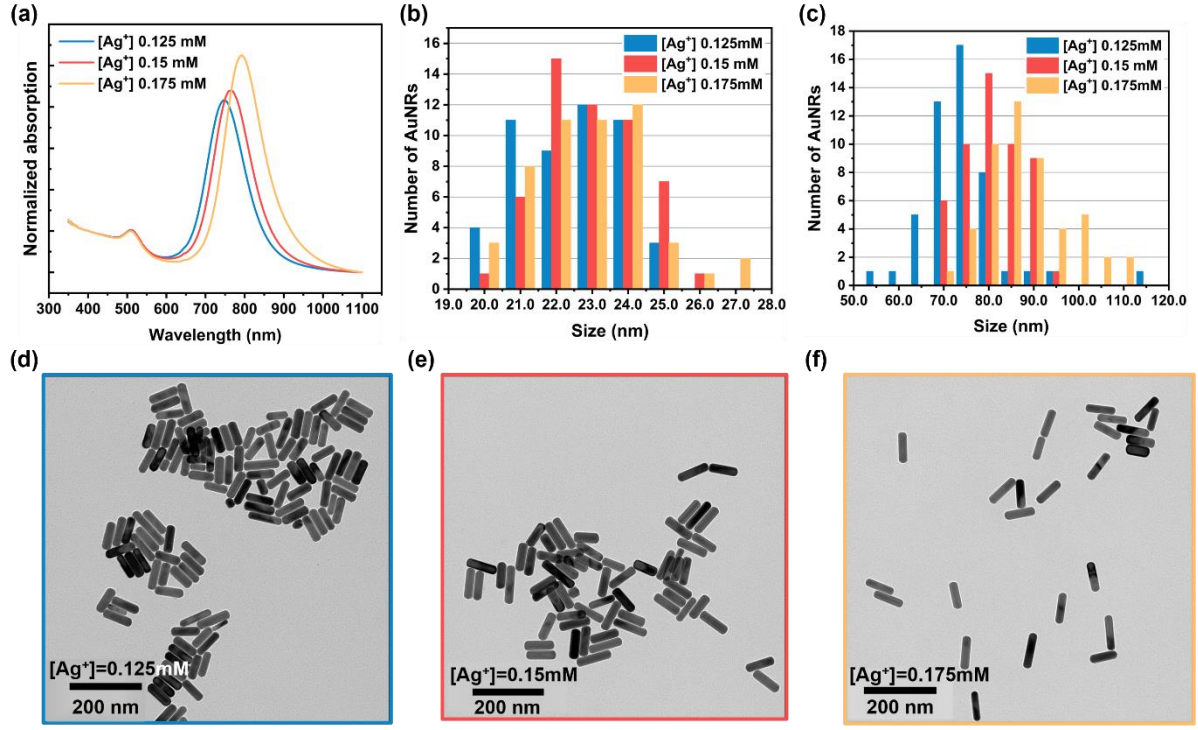

Figure.II.7. Effect of the silver ion concentration in the growth solution on the morphology and absorption property of synthesized AuNRs. ([HCl] = 30 mM, [CTAB] = 48 mM, V(seed) = 10 µL) (a). Normalized UV-vis absorption spectra of AuNRs. (b, c). Size distribution of AuNRs: (b). Diameter; (c). Length. (d – f). TEM images of AuNRs synthesized under different silver ion concentrations: (d). 0.125 mM; (e). 0.150 mM; (f). 0.175 mM.

To summarize, in this section, we studied the influences of different parameters during the synthesis of AuNRs that affect the morphology. Certainly, other factors that are not discussed here such as the temperature, the additives and the nature of reductant can also affect the result of synthesis. The parameters discussed here are sufficient for us to optimize the experimental conditions and to finally synthesize AuNRs with specific size which is 85 nm in length and 25 nm in diameter, with longitudinal absorption at around 750 nm. These AuNRs will be used for the following synthesis of AuNR/TiO_2 nanoparticles.

II.1.2. Synthesis of AuNR/TiO_2 nanoparticles

a. Synthesis of dumbbell-shaped AuNR/TiO_2 nanoparticles

Synthesis of dumbbell-shaped AuNR/TiO_2 nanoparticles:

The previously prepared AuNR solution (0.7 nM, 1 mL) was mixed with CTAB solution (0.2 M, 1 mL) and 2.6 mL of distilled water. Then, in another 20 mL of scintillation vial, $TiCl_3$ solution (12 – 14 wt. %, 400 µL) was added into 8 mL distilled water. A certain quantity of $NaHCO_3$ solution (0.1 M, 900 – 1000 µL) was introduced drop by drop under vigorous stirring. At this step, the color of solution turned from violet to dark blue. The prepared AuNR solution was quickly injected into the dark blue solution. The resultant mixture was kept under stirring (100 rpm) for 20 min under room temperature. The AuNR/TiO_2 nanoparticles were precipitated under centrifuge (3400 g, 10 min), washed with water once and then with ethanol twice, and finally stored in ethanol.

AuNR/TiO_2 dumbbell-shaped nanoparticles were prepared via a wet-chemistry method for the anisotropic growth of TiO_2 layers at the tips of AuNRs reported by Wu et al.[116] The TiO_2 layer was formed through the hydrolysis of $TiCl_3$, catalyzed by the AuNR surface according to the following mechanism (**Figure.II.8. a**):

$$Ti^{3+} + 2H_2O \xrightarrow{Au} TiO_2 + 3H^+ + \frac{1}{2}H_2 \qquad (II.1)$$

The gold surface is believed to help transmit the electrons between Ti^{3+} and H^+. The reduced H^+ form dihydrogen gas and leave the system as the generation of bubbles was observed during the synthesis. The oxidized Ti^{3+} react with water and eventually form TiO_2 depositing on the gold surface. Additionally, in this synthesis, the CTAB surfactant forms a double layer around the AuNR, which enables their colloidal stability and serves as a soft template to control the anisotropic growth of TiO_2. Indeed, as shown in the **Figure.II.8. b**, the CTAB density is higher on the elongated facets and lower near the AuNR tips, which facilitates the deposition of TiO_2 at the tips of the AuNRs.

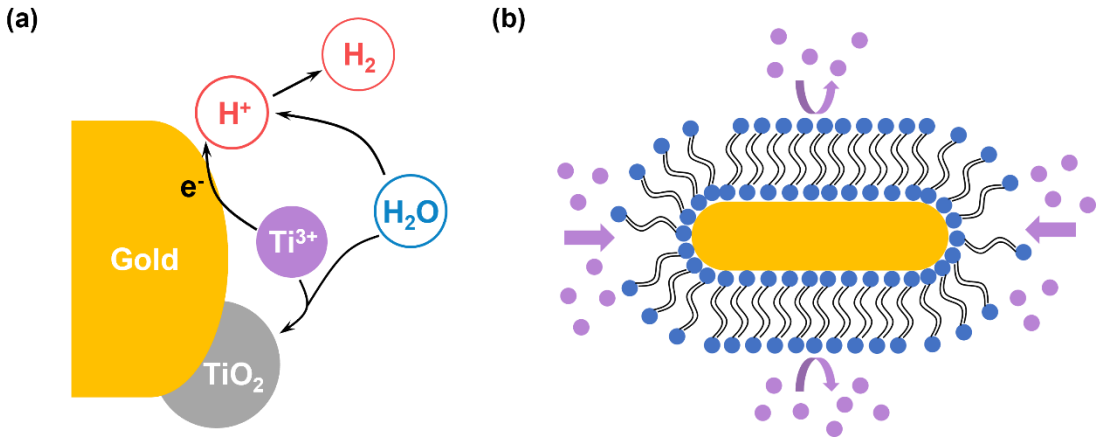

Figure.II.8. Illustration of principles for synthesizing dumbbell-shaped AuNR/TiO_2 nanoparticles. (a). Mechanism proposed for the hydrolysis of $TiCl_3$ catalyzed by gold surface. (b). Anisotropic growth of TiO_2 layers on the tips of AuNR due to lower density of CTAB.

The morphology of the obtained hybrid AuNR/TiO_2 nanoparticles is however very sensitive to the reaction conditions and reproducible syntheses are only obtained under a strict control of the pH

value[116,124]. Indeed, as shown in **Figure.II.9**, slight changes in the pH of the $TiCl_3$ precursor solution may lead to drastic changes in the architecture of the obtained hybrid nanoparticles, ranging from bare AuNR to TiO_2 deposition at the tips or growth of isotropic TiO_2 shells. This control is particularly important since, as we will demonstrate, the efficiency of •OH production depends on the AuNR/TiO_2 morphology. For a successful synthesis with a deposition of TiO_2 only at the tips of the AuNR, the pH value of the solution should be controlled in a narrow range of 2.6 – 2.8. Below this range, most of the Ti(III) ions take the form of $Ti(OH_2)_6^{3+}$ or $Ti(OH)(OH_2)_5^{2+}$, giving the solution a violet color because of a strong absorption band at around 490 nm. The hydrolysis of Ti^{3+} is then very slow, which leads to an incomplete growth of TiO_2 layers. (**Figure.II.9. a**) When the pH is between 2.6 – 3.0, the color of the solution turns to dark blue with the appearance of a new absorption band at around 700 nm observed in the UV-vis spectrum. (**Figure.II.9. f**) This can be attributed to the formation of polynuclear species with a mixed oxidation state, such as $Ti_2O(OH_2)_{10}^{4+}$, and these species are more sensitive to oxidation than Ti^{3+} or $Ti(OH)^{2+}$.[125,126] At this stage, the gold surface can catalytically accelerate the hydrolysis[127], thus avoid the secondary nucleation of small TiO_2 nanoparticles and produce a controlled anisotropic growth of TiO_2 layers at tips of AuNR. (**Figure.II.9. b, c**) When the pH is over 3.0, the polynuclear species transformed to partially oxidized compounds $Ti(OH)_{3+x}$, which are not stable under air and can be rapidly oxidized. The synthesis realized under this condition cannot be well controlled. It results in a much thicker TiO_2 layer within a short reaction time (5 – 10 min) and eventually a complete coating of AuNRs by TiO_2. (**Figure.II.9. d, e**)

The growth of TiO_2 causes a redshift on the longitudinal plasmon resonance of the AuNRs, due to the change in the surrounding refractive index. As shown in the **Figure.II.9. g**, the shift becomes more pronounced as the TiO_2 thickness increases, from 785 nm in the absence of TiO_2 to 870 nm with a thick TiO_2 shell. In addition, the absorbance of the longitudinal plasmon resonance decreases with respect to the lateral one, due to a diminution of the global aspect ratio of the particle[128].

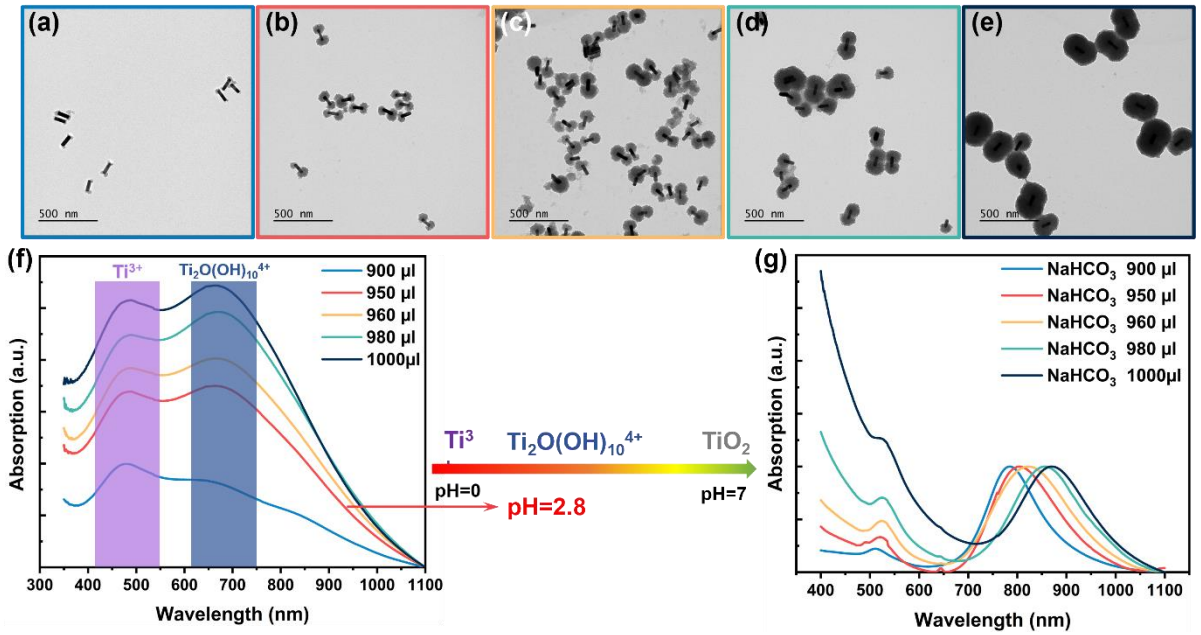

Figure.II.9. Importance of controlling the pH value during the synthesis for AuNR/TiO_2 nanoparticles. (a – e). TEM pictures of synthesized AuNR/TiO_2 nanoparticles at different pH conditions controlled by 0.1 M $NaHCO_3$: (a) 900µl; (b) 950µl; (c) 960µl; (d) 980µl; (e) 1000µl; (f) UV-vis absorption spectra of $TiCl_3$ solution under different pH conditions without AuNR. (g) UV-vis absorption spectra of AuNR/TiO_2 nanoparticles synthesized at different pH conditions, normalized to the peak of the longitudinal plasmon resonance.

When performed at pH 2.6 – 2.8, the synthesis yields homogeneous hybrid AuNR/TiO_2 nanoparticles, with TiO_2 deposited only at the tips (**Figure.II.10. a, b**). The progress of the reaction may be evaluated by monitoring the redshift of the AuNR longitudinal plasmon. A fast red shift of the longitudinal absorption of AuNR was observed and can be attributed to the growth of TiO_2. (**Figure.II.10. c, d**) The hydrolysis of $TiCl_3$ at the beginning is fast because the pH of the system was relatively high; the hydrolysis rate then slows down gradually as a result of the production of H^+, which increases the acidity of the solution. The hydrolysis stops after 30 min to give TiO_2 layers at both tips of AuNRs with a thickness of 27.3 ± 3.7 nm, as shown in TEM pictures. The CTAB surfactant was then removed from AuNR/TiO_2 nano dumbbells by several cycles of centrifugation in ethanol and stabilized in sodium citrate buffer to facilitate access of water or oxygen molecules to the TiO_2 surface. The ratio between Ti/Au was of 2.8, determined by SEM-EDX analysis (**Figure.V.2**).

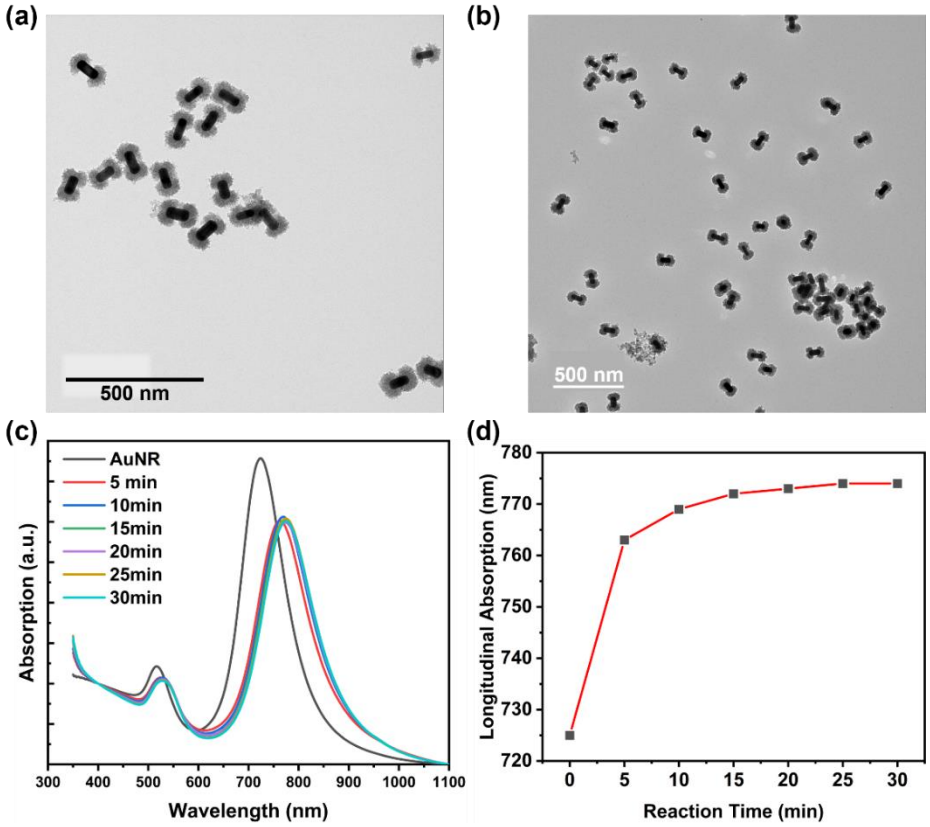

Figure.II.10. Characterizations of synthesized dumbbell-shaped AuNR/TiO_2 nanoparticles. (a – b) TEM image of synthesized AuNR/TiO_2 nanoparticles. (c) UV-vis absorption spectra of AuNR/TiO_2 nanoparticles during the hydrolysis of $TiCl_3$. (d) Red shift of the longitudinal absorption of AuNR/TiO_2 nanoparticles during the hydrolysis reaction.

b. Synthesis of core-shell shaped AuNR/TiO_2 nanoparticles

Synthesis of core-shell shaped AuNR/TiO_2 nanoparticles:

AuNRs separated from the growth solution were dispersed into sodium dodecyl sulfate solution (0.1 M), the suspension was left for over 30 min and then precipitated (3400 g, 10 min) and washed once with distilled water. Then the SDS-stabilized AuNRs were used for the deposition of TiO_2 layers with the same protocol of dumbbell shaped AuNR/TiO_2 nanoparticles, except a longer reaction time for about 2 hours.

Since CTAB surfactant is responsible for the anisotropic growth of TiO_2 layer on the tips of AuNRs, replacing CTAB with another surfactant, such as sodium dodecyl sulfate (SDS), while using the same $TiCl_3$–$NaHCO_3$ system, can result in the random growth of TiO_2 layer on the surface of AuNRs, producing core-shell shaped AuNR/TiO_2 nanoparticles (**Figure.II.11**). In comparison to CTAB, SDS forms a more homogeneous layer on the surface of AuNRs, including the tips, which limits the contact between the AuNR surface and titanium ions, and thus explains the morphology of AuNRs being entirely covered by a TiO_2 layer.

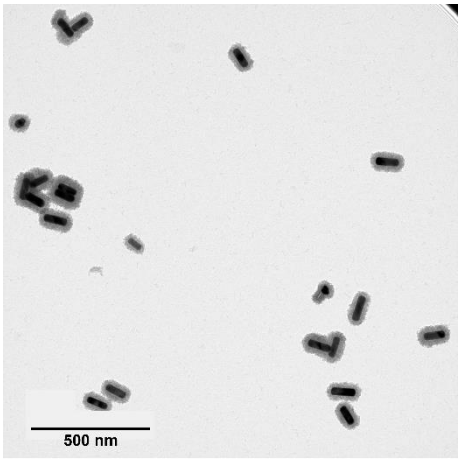

Figure.II.11. TEM image of AuNR@TiO_2 core-shell-shaped nanoparticles.

II.1.3. Characterizations of the photocatalytic activity of AuNR/TiO_2 nanoparticles

The synthesized AuNR/TiO_2 nanoparticles were stored in ethanol solution. To evaluate its ability to produce ROS in physiological environments, the first step is to transfer these nanoparticles into aqueous solution. However, AuNR/TiO_2 nanoparticles cannot maintain their colloidal stability in pure water without ligand functionalization. Although CTAB can stabilize these nanoparticles in aqueous solution, the formation of dense bilayer may also prohibit the reaction between hot electrons and water or dioxygen molecules. Besides, the acute cytotoxicity of CTAB may become troublesome in the future experiments. The citrate ligand, a molecule with smaller size, lower cytotoxicity was finally used to replace CTAB and stabilize the nanoparticles. The citrate anions can adsorb both on the surface of TiO_2 and AuNR through the formation of complexes, turning the entire surface negatively charged[79,129]. As a result, the aggregation of nanoparticles is avoided because of the electrostatic repulsion force. With 5 mM of sodium citrate in the solution, AuNR/TiO_2 nanoparticles were found to be stable under stirring for over 2 hours.

Then we established an optical system to perform irradiation experiments with the solution of AuNR/TiO_2 nanoparticles. As shown in the **Figure.II.12**, a near infrared laser source can be either a femtosecond pulsed laser system or a continuous wave LED; the laser beam is focused by the lens and passes through a diaphragm, with which the laser power can be precisely tuned; finally, the laser beam is directed towards the sample, which consists of a UV quartz cell containing approximately 500 µL of nanoparticle solution and a magnetic stirrer. The nanoparticle solution is kept stirring throughout the entire irradiation process.

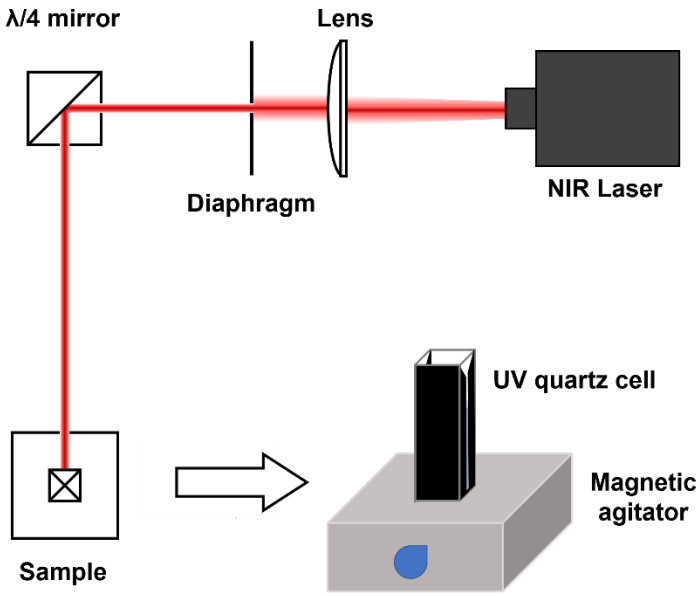

Figure.II.12. Optical structure designed for the irradiation experiments of nanoparticle solutions.

Nosaka et al. summarized the possible photo- oxidation and reduction reactions that take place at the surface of a photocatalyst, such as TiO_2.[130] According to the **Figure.II.13. a**, the successive reductions of dioxygen molecules can finally produce singlet oxygen ($^1O_2$) or hydroxyl radical (·OH). On the other hand, the direct one-hole oxidation of water molecules also generates hydroxyl radicals. Therefore, we decided to mainly focus on detecting OH radicals during the irradiation experiments as it is the common final product of both oxidative and reductive pathways. Additionally, as shown in **Figure.II.13. b**, OH radical exhibits a high reaction constant about 10^{10} M^{-1} s^{-1} for almost all the tested organic or inorganic compounds, making them the most effective reactant in photocatalytic decomposition.

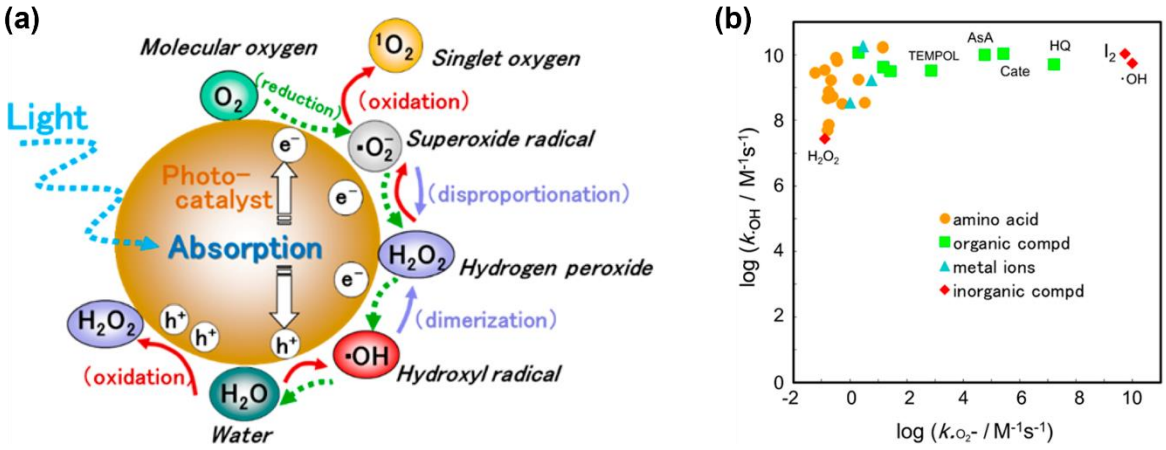

Figure.II.13. (a). ROS generated in the photocatalytic reduction and oxidation steps of oxygen and water. (b). Relationship of bimolecular rate constants of OH radical to those of $\bullet O^{2-}$ for reactions with various molecules: HQ, hydroquinone; Cate, catechol; AsA, aspartic acid[130].

To detect the production of OH radicals during the irradiation, several detection methods have been developed such as laser-induced-fluorescence (LIF) method[131], electron spin resonance spectroscopy[132], and analysis of OH radical reaction products[133,134]. Methylene blue (MB) is reported as a dye molecule that can be decomposed quantitatively by OH radicals while it remains intact with other ROS such as $^1O_2$ and $\cdot O^{2-}$.[135] Additionally, MB is highly sensitive and at a concentration of 0.01 mM in aqueous solution, it can detect the presence of OH radicals by the decrease of absorption band at 664 nm. In contrast, other OH radical sensors such as coumarin or terephthalic acid require a concentration of approximately 1 mM to efficiently detect OH radicals[136,137]. Finally, we conducted an irradiation stability test of MB under a femtosecond pulsed laser for 1 hour. As shown in **Figure.II.14. b**, MB molecules exhibit a good stability when exposed to laser irradiation, with only 3% of MB degraded within 1 hour. Based on these results, eventually we chose MB as sensor to examine the OH radicals produced by AuNR/TiO_2 nanoparticles under irradiation and the degradation of MB can be followed by UV-vis spectroscopy.

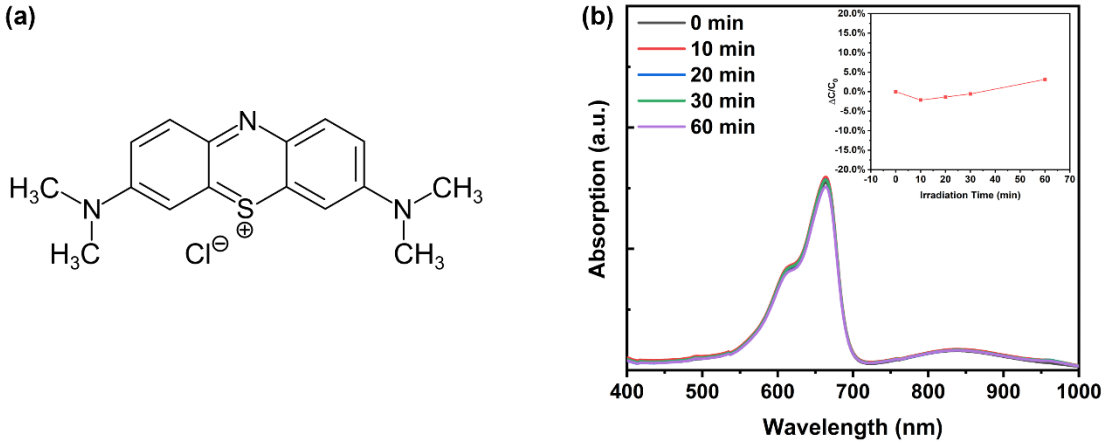

Figure.II.14. (a). Molecule structure of methylene blue. (b). UV-vis absorption spectra of MB 0.01 mM in sodium citrate (5 mM) solution irradiated under pulsed laser at 1.0 W/cm² for 1h; subplot: calculated proportion of degraded MB (ΔC) versus initial MB (C_0).

a. AuNRs irradiated under pulsed laser

Irradiation of AuNRs with NIR laser:

The AuNRs were suspended in a sodium citrate solution (5 mM) to obtain an optical density of 1.0 at 800 nm. Methylene Blue (MB) was added to the nanoparticle solution, resulting in a concentration of 10 µM. A volume of 500 µL from the prepared solution was transferred to a UV quartz cell, and a magnetic stirrer was added. The solution was stirred in the dark for 30 minutes and then exposed to pulsed laser irradiation at 800 nm. Absorption spectra of the solution were recorded at 10-minute intervals during the irradiation process.

To begin with, we performed irradiation experiments with AuNRs alone to evaluate the ability of producing OH radicals. AuNRs synthesized by seeded growth method were irradiated under femtosecond laser beam at 2 W/cm². However, after 10 min's irradiation, a drastic decrease of the longitudinal absorption peak was observed while the absorbance of MB remained unchanged (**Figure.II.15**), indicating that AuNRs cannot remain stable under irradiation. This destabilization may be induced by the photothermal effect of AuNRs under irradiation. The generation of heat can either interfere citrate stabilized AuNR surface, leading to aggregation of AuNRs, or cause damage on AuNR itself by melting or shape transition induced by surface reconstruction[138].

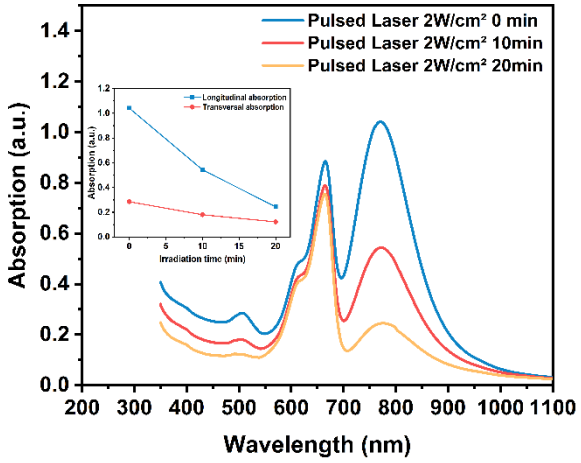

Figure.II.15. UV-vis spectra of AuNRs irradiated with femtosecond pulsed laser at 2 W/cm².

b. Miniaturized AuNR irradiated under pulsed laser

Chen et al.[139] reported that in comparison to large AuNRs with size of 100*20 nm², miniaturized AuNR (AuNRmin) with size of 49*8 nm² exhibited improved photothermal stability under pulsed irradiation. In light of this, we synthesized and irradiated these miniaturized AuNRs under the identical conditions. As shown in **Figure.II.16. a, b**, AuNRmin demonstrated a better stability under irradiation, as evidenced by the unchanged longitudinal absorption peak with or without irradiation. However, the degradation of MB molecules was minimal, which suggests a good thermal stability of MB but a poor efficiency of AuNRs in producing OH radicals. This low efficiency can be attributed to the fast redistribution and equilibrium of hot electron energy (~100 fs), consequently, the lifetime of hot electrons at AuNR surface is too short to enable reactions with water or dioxygen.

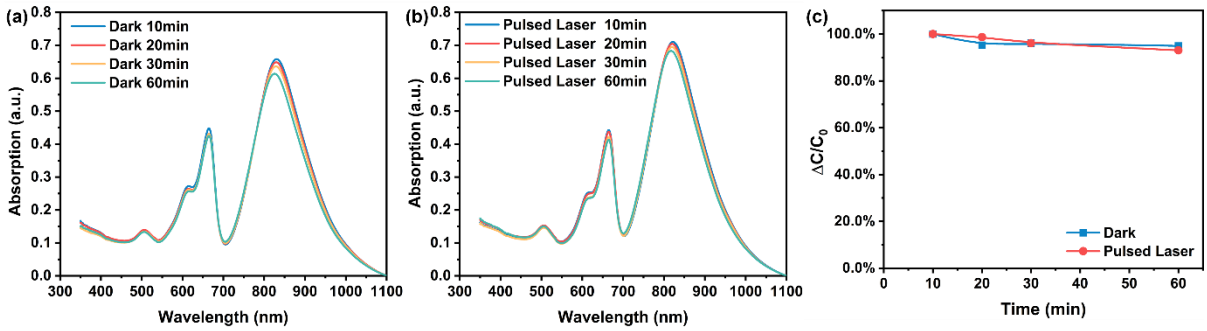

Figure.II.16. Miniaturized AuNRs under femtosecond irradiation. (a). UV-vis absorption spectra of AuNRmin and MB without irradiation. (b). UV-vis absorption spectra of AuNRmin and MB with irradiation. (c). Comparison of MB degradation induced by AuNRmin with or without irradiation.

c. AuNR/TiO_2 nanoparticles irradiated under pulsed laser

Previous irradiation experiments with AuNRs indicate that AuNR alone cannot efficiently generate OH radicals. So next we irradiated the hybrid AuNR/TiO_2 dumbbell-shaped nanoparticles synthesized with 950 µL of $NaHCO_3$ (**Figure.II.10**). Under pulsed laser irradiation at 800 nm (80 fs; 80 MHz; 0.6 W/cm²), in the presence of AuNR/TiO_2, the absorption peak of MB at 664 nm decreased over time (**Figure.II.17. c**), while it remained constant in the dark (**Figure.II.17. a**). This indicates that the MB molecules are progressively degraded by •OH produced by the irradiation of AuNR/TiO_2 nanoparticles. In addition, the absorption peak of AuNR remained constant, which indicates that these AuNR/TiO_2 nanoparticles are photostable under 800 nm light irradiation. Compared with AuNR, the hybrid AuNR/TiO_2 nanoparticles can efficiently utilize light energy to produce OH radicals. Hot electrons generated by light excitation can be injected into the conduction band of TiO_2, where these hot electrons have a prolonged lifetime to further reduce dioxygen molecules and finally produce OH radicals. Then with the same femtosecond laser source, we irradiated AuNR/TiO_2 nanoparticles by changing laser intensity from 0.2 W/cm² to 1.8 W/cm². (**Figure.II.17. b – f**) The UV-vis spectra suggest that the degradation of MB relies on the irradiation time and the laser power. After irradiation at 1.8 W/cm² for 2 hours, the absorption peak of MB at 664 nm totally disappeared, indicating that all of MB in the solution has been degraded.

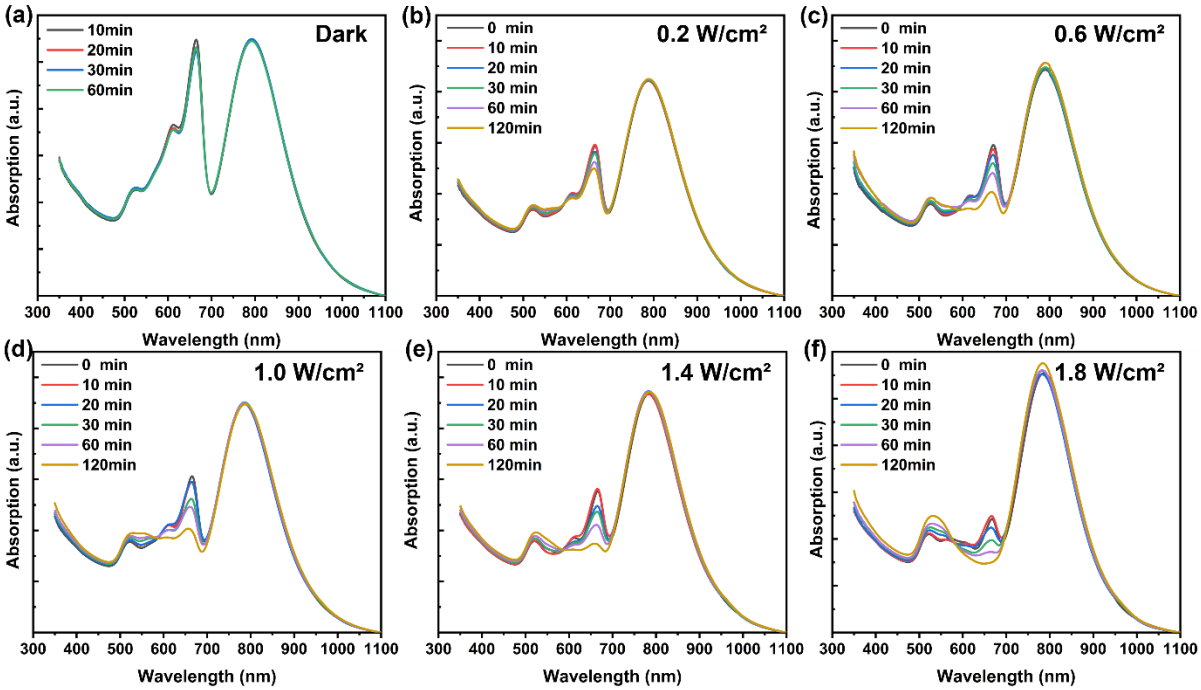

Figure.II.17. UV-vis absorption spectra of AuNR/TiO_2 nanoparticles and MB irradiated with varied laser intensity. (a). 0.0 W/cm²; (b). 0.2 W/cm²; (c). 0.6 W/cm²; (d). 1.0 W/cm²; (e). 1.4 W/cm²; (f). 1.8 W/cm².

d. Mechanism of photo-induced hydroxyl radical generation

Based on the series of irradiation experiments, the quantity of degraded MB molecules can be inferred from the decrease of the absorbance peak at 664 nm and can be used to establish the evolution of the photodegradation reaction with irradiation time. (**Figure.II.18. a**) Since the concentration of MB is initially much higher than that of OH radicals produced by AuNR/TiO_2 nanodumbbells and since the generated OH radicals are rapidly consumed without accumulation during the entire irradiation process, the reaction kinetics is mostly determined by the production rate of OH radicals. The MB degradation then follows a first order reaction and the change in MB concentration over time may be expressed as:

$$\Delta[Methylene\ Blue] = \frac{[MB]_0 - [MB]_t}{[MB]_0} = \frac{1}{[MB]_0} * e^{-kt} \qquad (II.2)$$

where t represents the irradiation time, $[MB]_{0,t}$ represents the concentration of MB initially present or after a time t of irradiation, k is a constant related to the production rate of OH radicals and depends on the laser intensity. As shown in **Figure.II.18. b**, under these conditions, the production rate of OH radicals varies linearly with the irradiation intensity. This linear relation between the production rate of OH radicals and the laser intensity suggests that the production of OH radicals mediated by laser irradiation of AuNR/TiO_2 nanoparticles mainly follows a one-photon excitation pathway. Indeed, if multiphoton processes were responsible for the photo-induced production of OH radicals, the production rate would increase nonlinearly with the irradiation intensity.

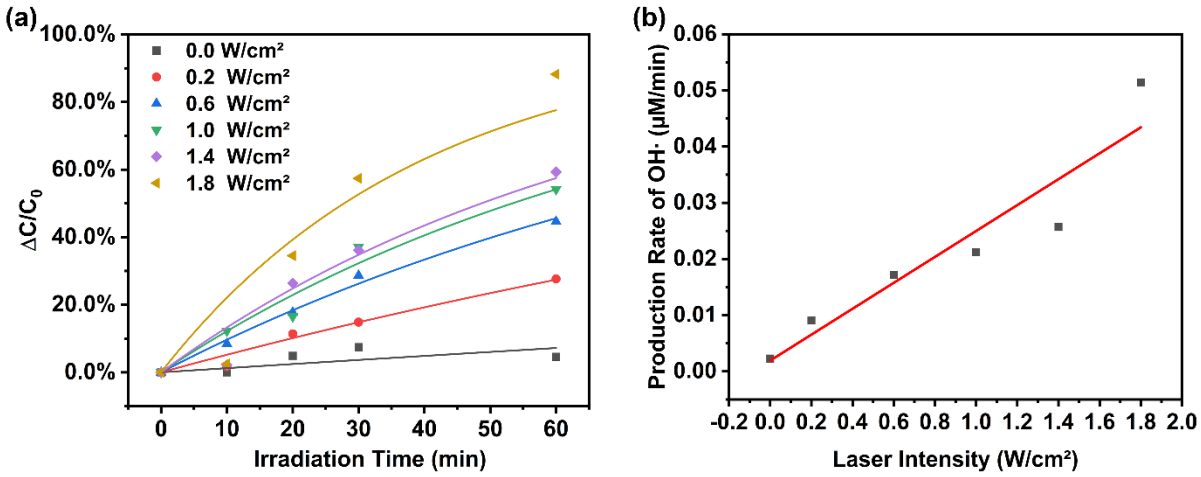

Figure.II.18. (a). Degradation of MB as a function of time induced by AuNR/TiO_2 nanoparticles irradiated under different laser intensity. (b). Calculated production rate of OH radicals as a function of laser intensity.

Based on the previous results, when AuNR/TiO_2 nanoparticles are irradiated under pulsed laser at 800 nm with a power of 300 mW, we have a hydroxyl radical production rate of about 0.017 μM/min. The number of photons absorbed by AuNR/TiO_2 nanoparticles per minute can be calculated as:

$$n_{photon} = P * \frac{\lambda}{1240 * N_A * e} * (1 - 10^{-O.D.}) * 0.5 = 5 \times 10^{-5}\ mol/min \qquad (II.3)$$

where P is the laser power, 300 mW; $\lambda = 800\ nm$ is the wavelength of incident light; N_A, e are the Avogadro constant and elementary charge, respectively. Therefore, the quantum yield of AuNR/TiO_2 nanoparticles can be computed as:

$$\Phi = \frac{n_{OH\cdot}}{n_{photon}} = \frac{0.017 \times 10^{-6} * 500 \times 10^{-6}}{5 \times 10^{-5}} = 1.57 \times 10^{-7} \qquad (II.4)$$

Despite a relatively low quantum yield of AuNR/TiO_2 nanoparticle, the molar extinction coefficient of AuNR/TiO_2 nanoparticles turns out to be approximately $1.1 \times 10^{10}\ L \cdot mol^{-1}cm^{-2}$, a value that is $10^4 - 10^5$ times higher than those conventional organic photosensitizers such as porphyrin, hypercin, and indocyanine green[140,141]. It indicates that AuNR/TiO_2 nanoparticles have a significantly higher photon absorption efficiency compared to these mentioned photosensitizers. As a result, a moderate dose of AuNR/TiO_2 nanoparticles may be sufficient to achieve effective PDT treatment.

Apart from altering the irradiation intensity, another way to verify this one-photon excitation assumption is to modulate the shape of the laser pulse. As illustrated in Equation.II.3, under two photon absorption circumstance, the number of absorbed photons per unit time $\frac{\partial N_{abs}}{\partial t}$ is proportional to the square of the incident laser intensity I^2, where V represents the illuminated volume, C represents the concentration of absorbent and δ represents the two-photon absorption cross-section. For the femtosecond pulsed laser, the average of the square of the intensity of incident light is typically specified as $< I^2 >_t$, instead of the intensity measured in the experiment, which is indeed the average intensity $< I >$. With the Equation.II.4 we can estimate $< I^2 >_t$ based on the measured $< I >$, where f_{rep} represents repetition rate and τ is the time measured across a pulse width, often at its full width half maximum. Therefore, if the two-photon absorption is the main cause of electron excitation, by changing

the pulse width τ, we can regulate $< I^2 >_t$ and thus change the number of absorbed photons N_{abs}, which can finally result in different MB degradation behavior.

$$\frac{\partial N_{abs}}{\partial t} = < \int_V dV \times \delta \times C(r,t) \times I^2(r,t) >_t \rightarrow \frac{\partial N_{abs}}{\partial t} \propto I^2 \quad \text{(II. 5)}$$

$$< I^2 >_t \left(\frac{W}{cm^2}\right) = \frac{< I >^2 \left(\frac{W}{cm^2}\right)}{f_{rep}\ (Hz) \times \tau\ (s)} \quad \text{(II. 6)}$$

Figure.II.19. a illustrates a possible way to modify the pulse width using a laser pulse compensator. Indeed, as the laser beam passes through the optical elements, the pulse width broadens, because each laser pulse is composed of light with a wide range of frequencies, and each frequency travels at a different velocity in the glass. This effect can be mitigated by incorporating a dispersion compensation system adapted with the optical elements, which adjusts the dispersion of light with different frequencies within the laser pulse. By using this compensated laser pulse, the original pulse shape can be restored with a width as short as the pulse emitted by the laser. By controlling the insertion of a prism into the beam, we can apply either low or high compensation for the laser pulse, leading to a respectively more or less broadened laser pulse absorbed by the sample.

Another approach to modify the laser pulse is to replace the pulsed laser by a continuous wave laser. As shown in **Figure.II.19. b**, instead of emitting bursts of light spaced in time, continuous was laser produces steady emission. In this case, the I_{peak} and the $I_{average}$ are identical. Therefore, based on Equation.II.5 and Equation.II.6, compared with a femto-second pulsed laser (80 fs, 80 MHz), two-photon process rates should be reduced by a factor of approximately 10^5 under continuous wave irradiation, due to the homogeneous repartition of photons in time, and any multiphoton processes should likely become undetectable.

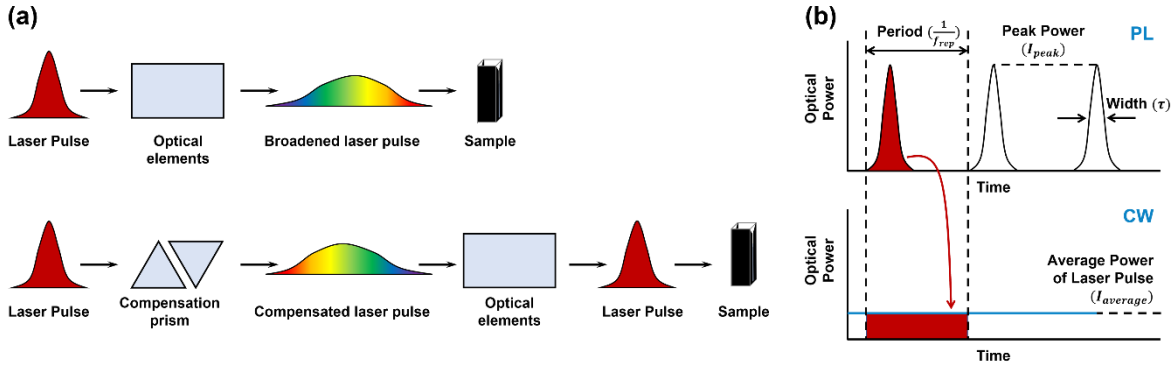

Figure.II.19. Principles of methods used for modifying the laser pulse. (a). Change of laser pulse width by adding a set of compensation prisms. (b). Comparison between the pulsed laser and continuous wave laser with the same average power.

Our experiment shows that, under irradiation with the same average laser intensity, neither the pulsed laser dispersion compensation nor the replacement of the pulsed laser by a continuous wave laser result in different MB degradation performance. (**Figure.II.20**) This confirms that, in this range of intensity (< 2 W/cm²), in contrast to the case of bare AuNRs irradiated under 3.7 W/cm²,[104] photo-production of ROS originates from one-photon absorption processes, which facilitates their biological application.

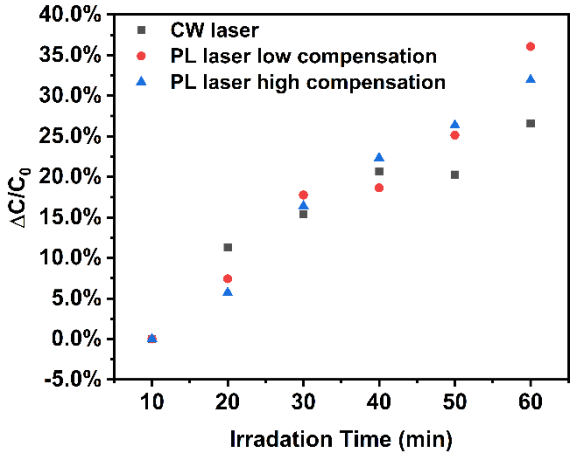

Figure.II.20. Comparison of MB degradation induced by AuNR/TiO_2 nanoparticles irradiated under pulsed laser with compensation and continuous wave laser.

In order to confirm that the photodegradation of MB is induced by OH radicals, rather than through the direct reduction of MB by electrons at the surface of TiO_2 or by hydrogen generated from the reduction of water, a series of irradiation experiments were realized in the presence of DMSO, a molecule known as OH radical scavenger[142]. As is shown in **Figure.II.22. a**, by increasing the concentration of DMSO in the solution, the photodegradation rate of MB indeed strongly decreased, with much less MB degraded within 2 hours of irradiation. This result proves that the photodegradation of MB in the presence of AuNR/TiO_2 nanoparticles is mainly caused by production of OH radicals.

A single photon with a wavelength in NIR region does not have enough energy to directly excite electrons at the valence band to the conduction band of TiO_2 because of the wide band gap of 3.14 eV. Therefore, neither AuNRs alone nor TiO_2 nanoparticles alone are able to produce OH radicals under 800 nm laser irradiation. This suggests that the absorption of 800 nm photons by the AuNR creates hot electrons which can transfer to the conduction band of TiO_2, and ultimately be trapped at the surface of TiO_2. Therefore, there are two possible pathways that can explain the AuNR/TiO_2 nanoparticles mediated production of OH radicals, (**Figure.II.21**) either via the oxidation of water molecules at the lateral surface of AuNR by h^+ (Equation.II.7), or via the successive reduction of oxygen molecules at the surface of TiO_2 by transferred hot electrons (e^-) (Equations.II.8 – 10).

$$H_2O + h^+ \rightarrow H^+ + \cdot OH \quad (II.7)$$

$$O_2 + e^- \rightarrow \cdot O_2^- \quad (II.8)$$

$$\cdot O_2^- + e^- + 2H^+ \rightarrow H_2O_2 \quad (II.9)$$

$$H_2O_2 + H^+ + e^- \rightarrow H_2O + \cdot OH \quad (II.10)$$

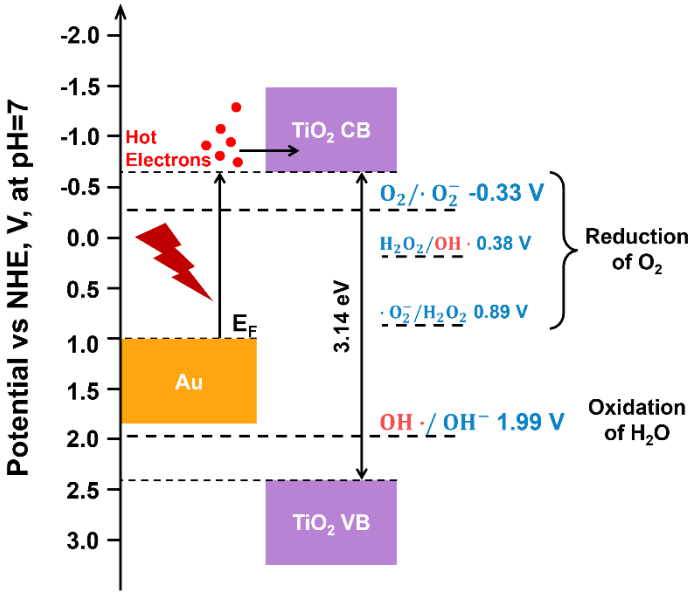

Figure.II.21. Energy diagram for energy band gap of Au and TiO_2 and one electron redox potentials of O_2, H_2O and H_2O_2 at pH=7.

Therefore, to distinguish which pathway, (II.7) or (II.8 – 10), contributes the most to the generation of OH radicals, the AuNR/TiO_2 nanoparticles solution was degassed under argon flux to eliminate O_2 from the solution for 30 min before irradiation, and the photodegradation behavior of MB under argon was compared with results obtained in air in the presence of O_2. As shown in **Figure.II.22. b**, the photodegradation of MB was slowed down in the absence of O_2, with eventually four times less of MB molecules degraded within 1 hour, which suggests that the photogeneration of OH radicals mainly takes place by reduction of dioxygen by hot electrons transferred to the surface of TiO_2.

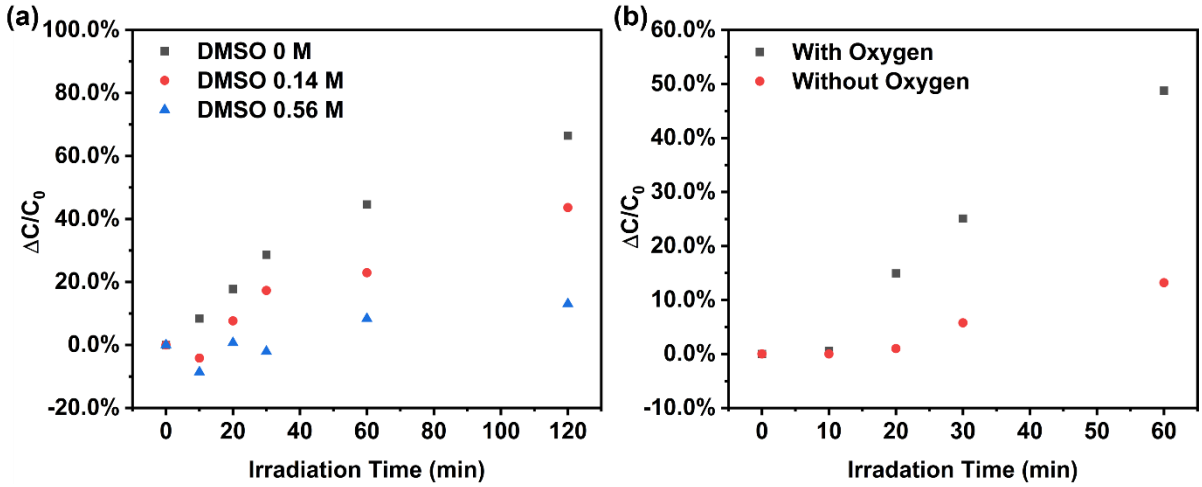

Figure.II.22. (a) AuNR/TiO_2 nanoparticles assisted photodegradation of MB in the presence of DMSO, a OH radical scavenger. (b) Comparison of AuNR/TiO_2 nanoparticles assisted photodegradation of MB with or without oxygen.

e. Shape-determined photoactivity of AuNR/TiO_2 nanoparticles

We also compared the photoactivity of core-shell-shaped AuNR/TiO_2 nanoparticles with that of dumbbell-shape AuNR/TiO_2 nanoparticles. AuNRs completely surrounded by a continuous shell of TiO_2

did not show any photocatalytic activity either (**Figure.II.23**). This might be related in this case to the progressive loss of electrons from the AuNRs in the TiO_2 and the lack of compensating electron transfer into the AuNR from reducing species in the solution, or from the poor electron transport through the thick and porous TiO_2 shell, which may prevent trapped electrons to access to the TiO_2/solution interface. This emphasizes the importance of precisely controlling the AuNR/TiO_2 architecture.

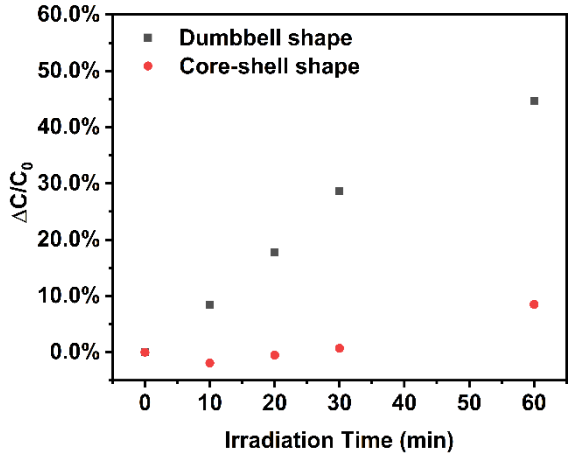

Figure.II.23. Comparison of photoactivity of core-shell-shaped AuNR/TiO_2 nanoparticles with dumbbell-shaped AuNR/TiO_2 nanoparticles.

f. Detection of Singlet Oxygen by SOSG

The hot electrons transferred into the TiO_2 conduction band firstly reduce dioxygen molecules to superoxide anion radicals ($\cdot O^{2-}$), which can be further reduced to produce OH radicals as discussed above. Alternatively, these intermediate radicals can also undergo oxidation to generate singlet oxygen ($^1O_2$). (**Figure.II.24**) It is possible to detect $^1O_2$ by a specific molecule, singlet oxygen sensor green (SOSG), that can form a fluorescent endoperoxide with $^1O_2$ while it shows no response to OH radicals or $\cdot O^{2-}$. The increase of fluorescence intensity can be measured by fluorescence emission spectroscopy[130].

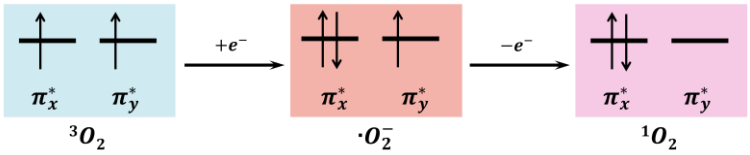

Figure.II.24. Illustration of generation of $^1O_2$ by photochemical reactions with molecular π* orbitals of O_2, $\cdot O^{2-}$ and $^1O_2$.

Since $^1O_2$ is not stable in aqueous solution with a very short lifetime of 3 µs, prior to irradiate nanoparticles, we first utilized indocyanine green (ICG) as reference, a molecule that can be excited at 780 nm to generate $^1O_2$. To extend the lifetime of the produced $^1O_2$, samples were prepared with D_2O. The ICG solution was irradiated under pulsed laser for 30 min, and the fluorescence intensity revealed a net 20% increase compared with the non-irradiated ICG solution. (**Figure.II.25. a, b**) Then dumbbell-shape AuNR/TiO_2 nanoparticles were added into the ICG solution and irradiated, however, no evident fluorescence increase was observed, (**Figure.II.25. c, d**) suggesting that few $^1O_2$ were produced by AuNR/TiO_2 nanoparticles. It is reported that the generation of $^1O_2$ is strongly dependent on the heat effect. The production rate of $^1O_2$ with a pulsed laser can be up to 5 times higher than with a continuous wave laser, which is attributed to the faster temperature increase and better heat confinement achieved

by pulsed laser[137]. For hybrid AuNR/TiO_2 nanoparticles, since TiO_2 layer grows at the tips of AuNR where photothermal effect should be the highest, the TiO_2 layer may hinder the generation or diffusion of heat, eventually leading to a low production of $^1O_2$.

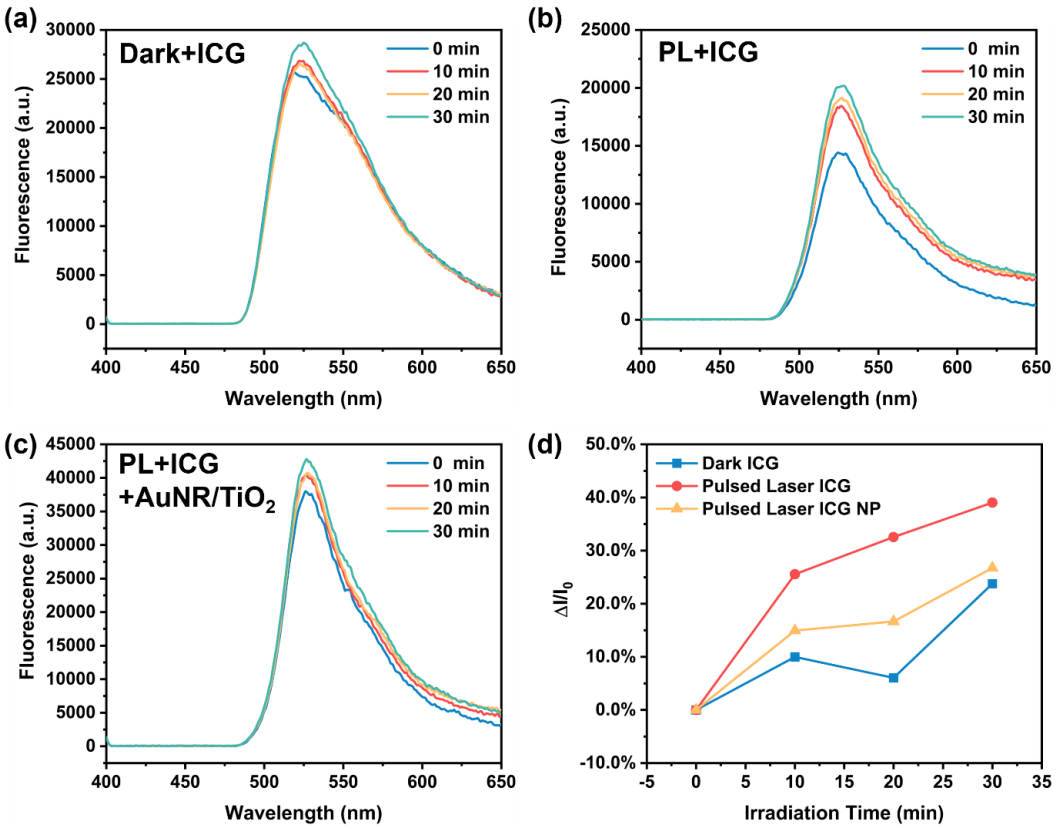

Figure.II.25. Evaluation of $^1O_2$ generation by AuNR/TiO_2 nanoparticles under irradiation of pulsed laser (a). Fluorescence emission spectra of ICG solution without irradiation. (b). Fluorescence emission spectra of ICG solution with irradiation. (c). Fluorescence emission spectra of ICG solution with AuNR/TiO_2 nanoparticles under irradiation. (d). Summary of fluorescence increase of different samples with/without irradiation.

II.2. Surface functionalization of AuNR/TiO_2 nanoparticles

The biological application of these hybrid AuNR/TiO_2 nanoparticles requires their colloidal stability in saline solutions. While AuNR/TiO_2 nanoparticles can form stable colloidal suspension in citrate solution, they tend to rapidly aggregate and precipitate once dispersed in phosphonate-buffered solution (PBS) (**Figure.II.26. b**). The citrate stabilization for AuNR/TiO_2 nanoparticles is not sufficient to maintain colloidal stability in physiological environment due to the relatively high saline concentration, which reduces the electrostatic repulsion force provided by citric ligands through screen effect (**Figure.II.26. a**). Therefore, it is necessary to design and perform rational surface functionalization for AuNR/TiO_2 nanoparticles.

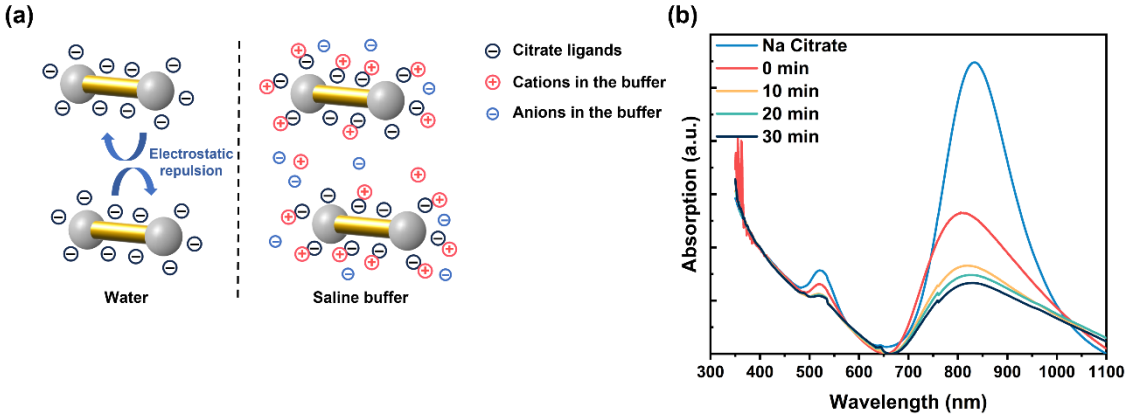

Figure.II.26. (a). Schematic illustration of screen effect induced by charged ions in the saline buffer solution. (b). UV-vis absorption spectra of AuNR/TiO_2 nanoparticles dispersed in Na citrate solution and in PBS.

II.2.1. Colloidal stability of AuNR/TiO_2 nanoparticles in different solvents

The surface of hybrid dumbbell shape AuNR/TiO_2 nanoparticles is composed of the gold surface and the TiO_2 surface. The surface functionalization strategy for these two materials is different, especially in terms of the anchor groups used. To understand the colloidal stability of AuNR/TiO_2 nanoparticles and determine whether it is influenced by one or both materials, their stability is compared with that of individual AuNRs and TiO_2 nanoparticles in various solutions. AuNRs, TiO_2 nanoparticles and AuNR/TiO_2 nanoparticle separately suspended in different solutions and stirred for 30 min. As shown in **Table.II.1**, under acidic condition (pH = 2) or in non-polar solvents (ethanol), both TiO_2 and AuNR/TiO_2 nanoparticles remained stable while AuNRs precipitated, indicating that the surface property of AuNR/TiO_2 nanoparticle are more similar to that of TiO_2. Indeed, for a single AuNR/TiO_2 nanoparticle, the surface area of gold is approximately 3000 nm², and the surface area of TiO_2 is four times larger than that of gold, amounting to about 12,000 nm². And because of the dumbbell shape, geometrically, it is difficult to have gold-gold interactions (**Figure.II.27**) while the TiO2 surface is more exposed to the environment, dominating the interparticle interactions. Therefore, TiO_2 dominates the colloidal stability of AuNR/TiO_2 nanoparticles and specific functionalization method for TiO_2 is developed.

Table.II.1. Colloidal stability of AuNR, TiO_2 and AuNR/TiO_2 nanoparticles dispersed in different solutions and solvents. ✗ suggests precipitation; ✓ suggests stable suspension.

	AuNR	**TiO_2**	**AuNR/TiO_2**
Pure water	✗	✗	✗
PBS (pH = 7)	✗	✗	✗
Water (pH = 2)	✗	✓	✓
EtOH	✗	✓	✓
CTAB solution	✓	✓	✓
Na citrate solution	✓	✓	✓

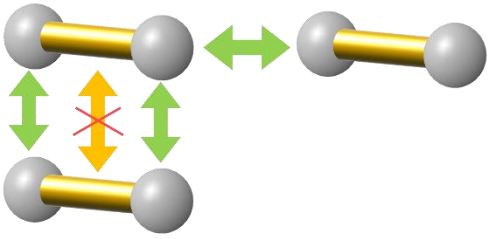

Figure.II.27. Schematic illustration of possible surface interactions of AuNR/TiO_2 nanoparticles in the solution.

II.2.2. Design and synthesis of polymer ligands

Ligands utilized to functionalize TiO_2 surface contain a hydrophilic polymer chain and an anchoring group at the end of polymer chain with several hydroxyl groups. The hydrophilic polymer chain forms a stretched conformation in aqueous solution due to its affinity to water molecules, providing steric effect to prevent nanoparticles from aggregating. The anchoring group grafts ligand molecules onto the surface of TiO_2 by forming covalent or coordinal bonds with titanium, as shown in **Figure.II.28. a**. Anchoring groups reported in the literature include catechols[143], silanes[144] and phosphonic acids[145]. We also tested these mentioned anchoring groups. Besides, polyethylene glycol (PEG) and poly(sulfobetaine) were chosen as the hydrophilic polymer chains. (**Figure.II.28. b, c**)

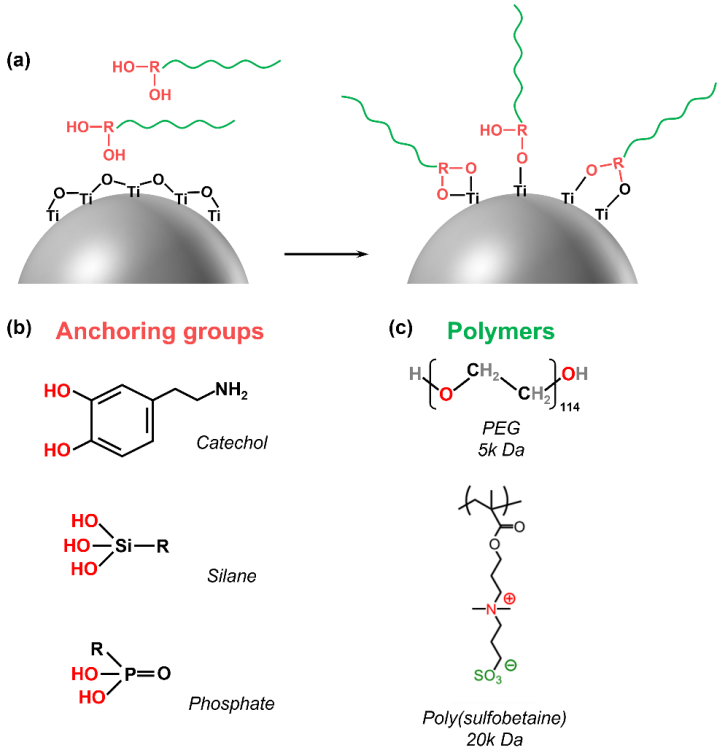

Figure.II.28. (a). Schematic representation of ligands grafting onto TiO_2 surface and principal bonding modes of different types of anchoring groups. (b). Molecule structure of anchoring groups. (c). Molecule structure of hydrophilic polymers.

Different strategies were used to synthesize and couple the polymer chain with anchoring groups. Eventually, four different ligands were successfully synthesized, and their structures are shown in

Figure.II.29. The details of each synthesis are presented in **V.2. Ligand synthesis**. Here, synthesis routes of each ligand are briefly summarized:

For the ligand Caffeic acid-PEG, the commercially available NH_2-PEG-OCH_3 reacted directly with caffeic acid through amide coupling (**Figure.II.29. a**).

For the ligand Silane-SPP, the synthesis route is inspired by the work of Estephan[146] as is realized through a ring-opening addition of propane sultone by aminoalkylsiloxane. (**Figure.II.29. b**).

For the ligand Phosphonate acid-PEG ligand, we first modified a primary-amine terminated PEG polymer with a chain transfer agent (CTA), CADB, using amide coupling. Then this modified CADB-PEG polymer is used as a CTA for the polymerization of (methacryloyloxy)methyl phosphonic acid (PA) monomers by controlled radical polymerization (RAFT). The resulting copolymer, PEG-pPA contains eventually two blocks (**Figure.II.29. c**), the PEG polymer with a molar mass around 5,000 g/mol, and a second block containing 6 – 7 PA monomers.

For the ligand Phosphonic acid-pSPP, we first polymerized poly(sulfobetaine) (pSPP) block through RAFT polymerization, in the presence of CADB. Then, since the pSPP block is still living, we subsequently added the second block of poly(phosphonic acid) by RAFT polymerization. Finally, a copolymer consists of 45 SPP monomers and 10 PA monomers is obtained (**Figure.II.29. d**).

All the synthesized ligands were characterized by NMR ^{1}H spectrum.

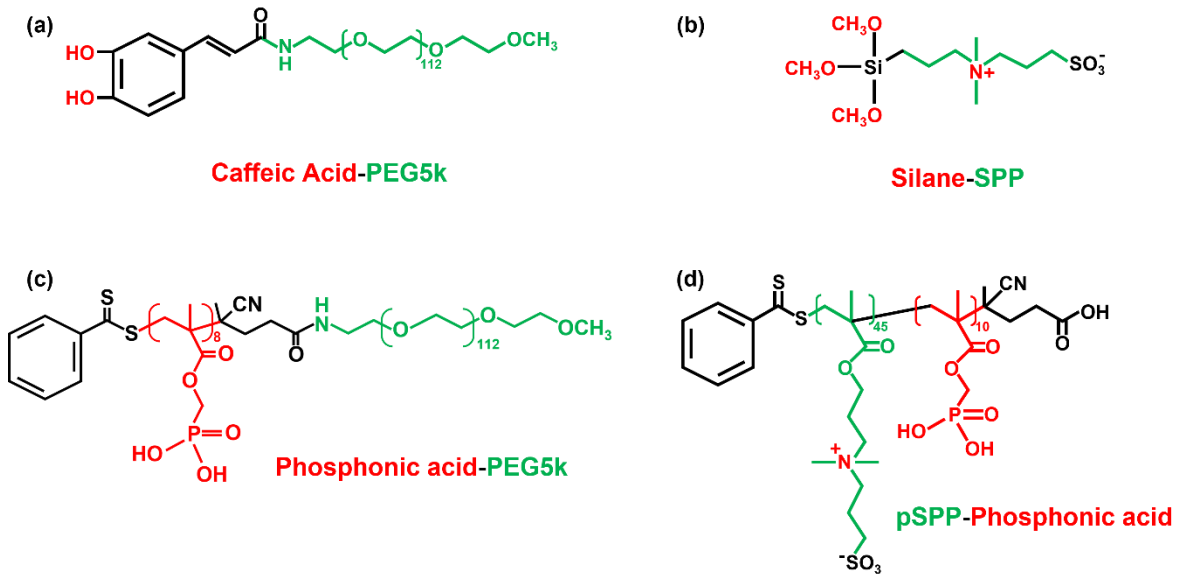

Figure.II.29. Molecule structure of synthesized ligands.

II.2.3. Colloidal stability of functionalized AuNR/TiO_2 nanoparticles

Ligand exchange of citrate capped AuNR/TiO2 nanoparticles:

In a 2 mL scintillation vial, 10 mg (1.5 µmol) PEG5k-pPA polymer were dissolved in 1 mL distilled water under stirring. 2 mL AuNR/TiO_2 stock solution (0.1 nM) was centrifuged (3400 g, 10 min) and redispersed in 50 µL ethanol, then this nanoparticle solution was added into the polymer solution. After 10 min of stirring, the pH of the mixed solution was adjusted to 7.5 – 8 with 0.2 M NaOH solution. The final mixture was kept under gentle stirring overnight. Then the exchanged nanoparticles were collected by centrifugation (3400 g, 10 min), washed twice with sodium citrate solution (5 mM) and three times with HBS buffer solution (pH = 7.5).

The citrate-stabilized AuNR/TiO_2 nanoparticles went through ligand exchange process with as-synthesized ligands in neutral or basic aqueous solution (pH = 8). Then these functionalized AuNR/TiO_2 nanoparticles were washed twice and dispersed in PBS buffer and stirred for 60 min. The absorption spectra of the supernatant were taken, as shown in the **Figure.II.30**. Firstly, for AuNR/TiO_2 nanoparticles exchanged with pure PEG without anchoring groups, more than 80% of nanoparticles aggregated and were lost during the washing process (**Figure.II.30. a**), indicating that the nanoparticle surface was poorly functionalized. In fact, without anchoring groups, polymers cannot adsorb on the nanoparticle surface and can be easily washed away. Secondly, AuNR/TiO_2 nanoparticles exchanged with Phosphonic acid-pSPP also exhibit a drastic quantity diminution after washing process (**Figure.II.30. d**). This may be attributed to the unexpected electrostatic interaction between the zwitterion polymer and the TiO_2 surface, resulting in aggregation of nanoparticles. Thirdly, for AuNR/TiO_2 nanoparticles functionalized with caffeic acid-PEG ligands, half of the nanoparticles were lost after washing process (**Figure.II.30. b**), indicating a low exchange efficiency. Next, for AuNR/TiO_2 nanoparticles functionalized with SPP-silane, since the hydrophilic part of the ligand contains only one sulfobetaine monomer, the electrostatic interaction between sulfobetaine and TiO_2 is much less important compared with long polymer chain, eventually, most of the nanoparticles remain stable in PBS buffer (**Figure.II.30. c**). Finally, for AuNR/TiO_2 nanoparticles functionalized with phosphonic acid-PEG, few nanoparticles were lost during the washing process, suggesting a good exchange efficiency. Besides, nanoparticles can remain stable in PBS buffer for over 60 min with less than 10% of loss, revealing a good colloidal stability ensured by phosphonic acid-PEG ligands (**Figure.II.30. e**).

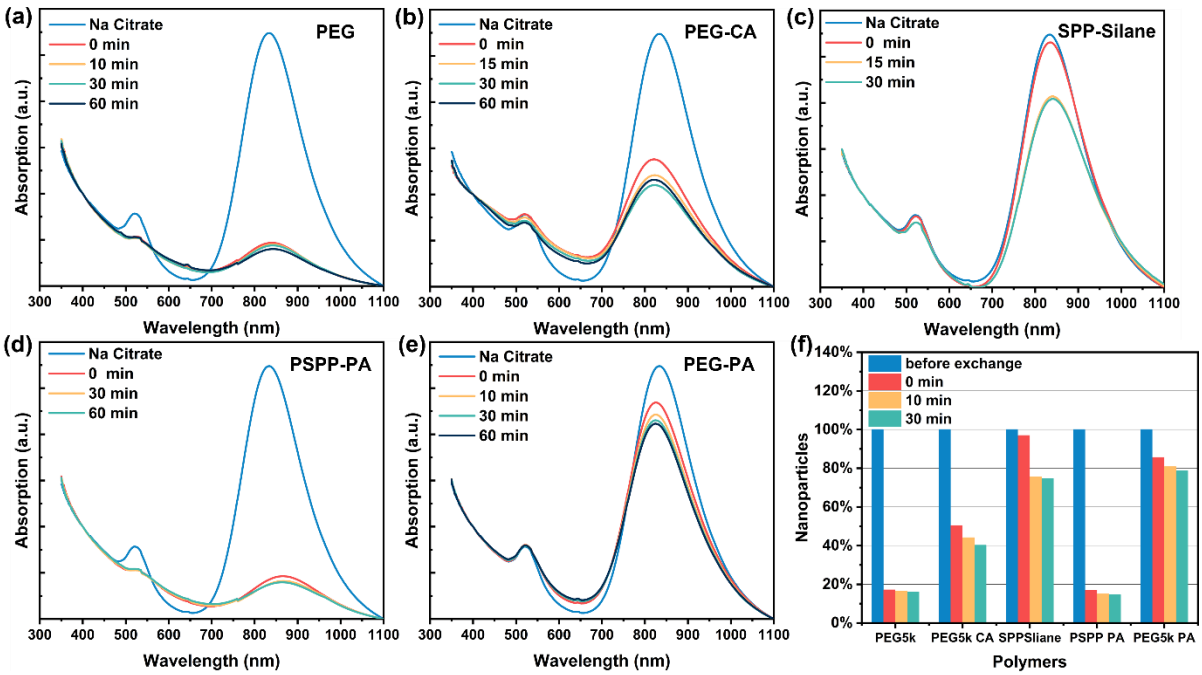

Figure.II.30. (a – e). UV-vis absorption spectra of AuNR/TiO_2 nanoparticles dispersed in PBS solution functionalized with different ligands: (a) PEG without anchoring group; (b). Caffeic acid-PEG; (c). SPP-Silane; (d). Phosphonic acid-pSPP; (e). Phosphonic acid-PEG. (f). Comparison of colloidal stability of functionalized nanoparticles with different ligands.

Based on the exchange efficiency and colloidal stability of AuNR/TiO_2 nanoparticles functionalized with these four ligands, we finally chose the AuNR/TiO_2 nanoparticles functionalized with phosphonic acid-PEG for the following experiments.

II.2.4. Photoactivity of functionalized AuNR/TiO_2 nanoparticles

Since the electron transfer from AuNR/TiO_2 nanoparticles to solution-phase oxygen species is expected to occur at the surface of TiO_2, the presence of polymer ligands on the surface of nanoparticles could influence this electron transfer. Polymer layers may slow down the diffusion of oxygen molecules to the surface of the nanoparticles. Additionally, polymer ligands can occupy the reactive spots on the surface of nanoparticles, which also hinders adsorption of O_2 on Ti surface atoms and electron transfer. These two factors were examined in this section.

First of all, we investigated whether the surface functionalization of the nanoparticles by the PEG5k-pPA polymer modified the production rate of OH radicals under laser irradiation in PBS. As shown in **Figure.II.31. a**, degradation of MB was drastically reduced for PEG5k-pPA functionalized nanoparticles, suggesting that the production of OH radicals was totally suppressed. We firstly assumed that this suppression of photoactivity to the bulky PEG layer formed at the surface of nanoparticles which prevents the contact between dioxygen molecules with hot electrons at the surface of nanoparticles by a limited diffusion of oxygen species from the solution phase to the TiO_2 surface. So, we functionalized AuNR/TiO_2 nanoparticles with a shorter PEG chain (2k Da). Under irradiation, however, no production of OH radicals was detected neither (**Figure.II.31. b**), while the colloidal stability is no longer ensured due to a reduced steric effect with shorter polymer chains. Therefore, the photoactivity of AuNR/TiO_2 nanoparticles cannot be retrieved by simply reducing polymer size.

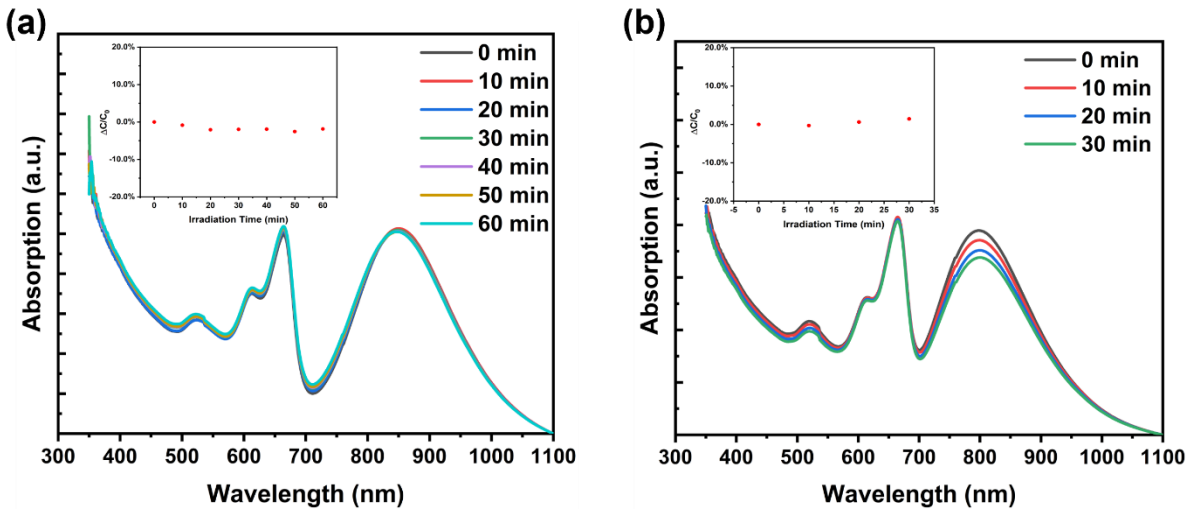

Figure.II.31. UV-vis absorption spectra of AuNR/TiO_2 nanoparticles functionalized with (a). PEG5k-pPA; (b). PEG2k-pPA, irradiated under continuous wave laser at 1 W/cm².

On the other hand, since the phosphonic acid groups of the ligands graft on nanoparticle surface by forming covalent bonds with titanium atoms[145], the chemical environment of the TiO_2 surface is different before and after the ligand exchange. For example, the ligands may induce the passivation of sites at the surface of TiO_2, which prevents electron trapping and/or O_2 adsorption and thus hinder the photocatalytic activity. As illustrated in **Figure.II.32**, without ligands, the positively charged titanium atoms can attract and capture electrons and are exposed to dioxygen molecules, which enables photocatalytic reductions to happen, while once bonded with phosphonic acid groups, titanium atoms can no longer attract electrons causing a limited contact between O_2 and electrons.

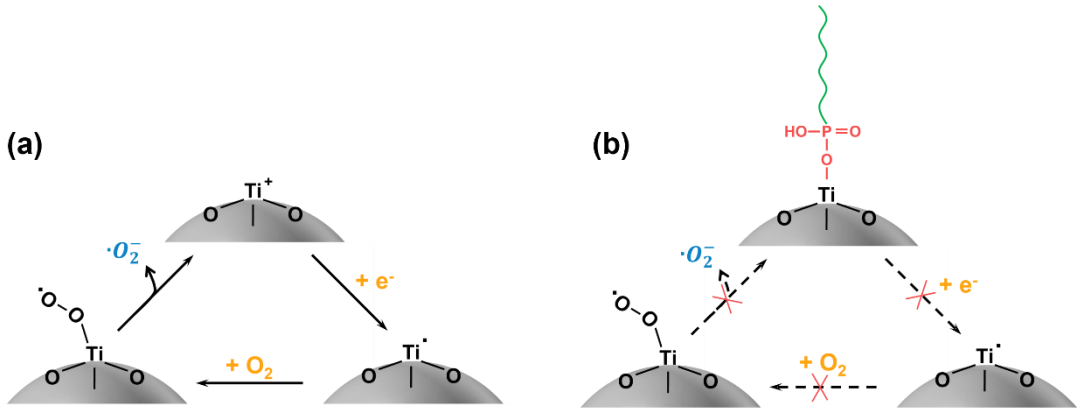

Figure.II.32. (a). Plausible photocatalytic mechanism of O_2 reduction mediated by TiO_2. (b). Passivation of active sites of TiO_2 induced by ligands.

Considering these possible factors, we decided to reduce the polymer density that graft on the TiO_2 surface so that we liberate some accessible titanium atoms for photocatalysis. We synthesized a PEG based polymer with a block of about 5 methacrylic acids, as shown in **Figure.II.33. a**. Unlike phosphonic acid group, which can form bidentate bonds with TiO_2, each methacrylic acid monomer can only bond to one titanium atom, meaning that the methacrylic acid-PEG5k ligands bind with TiO_2 much more loosely than phosphonic acid-PEG5k ligands. After ligand exchange, these methacrylic acid-PEG5k functionalized AuNR/TiO_2 nanoparticles were retro-exchanged with sodium citrate, in order to

partially replace methacrylic acid-PEG5k by small citric molecules. The irradiation of these partially exchanged AuNR/TiO_2 nanoparticles were performed, and we found that the photocatalytic activity of AuNR/TiO_2 nanoparticles was gradually recovered during a successive back-exchange with Na citrate. (**Figure.II.33. b**)

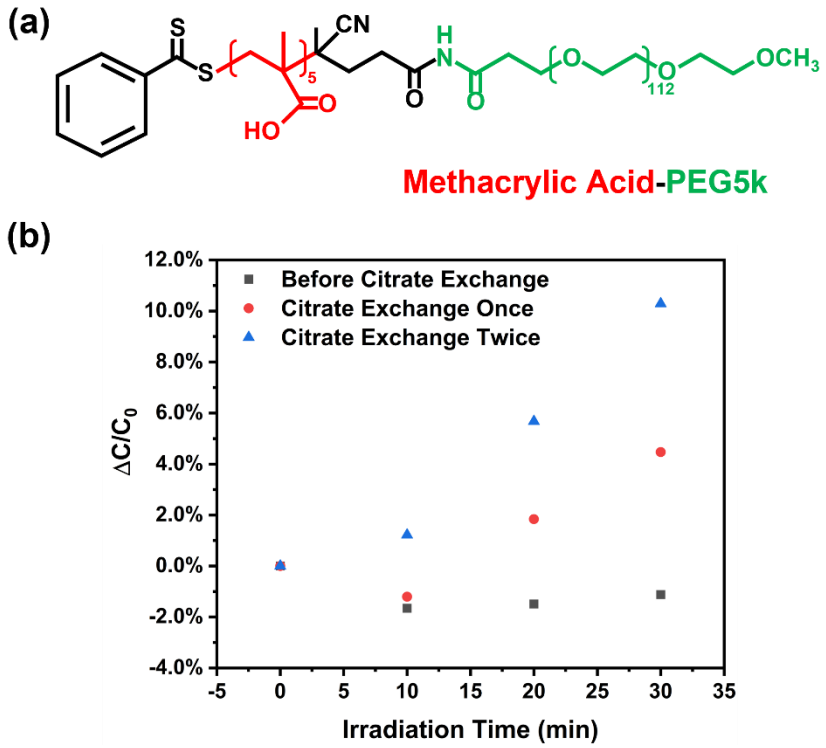

Figure.II.33. (a). Molecule structure of Methacrylic acid-PEG5k ligands. (b). Retrieved photocatalytic activity of AuNR/TiO_2 nanoparticles functionalized with Metacrylic acid-PEG5k through retro-exchange with citrate ligands.

In light of these results, we also performed the similar back-exchange process with AuNR/TiO_2 nanoparticles functionalized with PEG5k-pPA ligands. As shown in **Figure.II.34. a**, this partial exchange enables partial recovery of the AuNR/TiO_2 photoactivity. The resulting nanoparticles are about half as efficient as the original citrate coated AuNR/TiO_2, but remain colloidally stable in saline and cell culture medium. This was confirmed by dynamic light scattering (DLS) analysis, with a measured hydrodynamic radius of PEG-pPA AuNR/TiO_2 nanoparticles in PBS which remains constant before (R = 92.9 nm) and after (R = 94.7 nm) partial exchange with citrate ligands (**Figure.II.34. b**) and is similar to the hydrodynamic radius of bare AuNR/TiO_2 in citrate buffer.

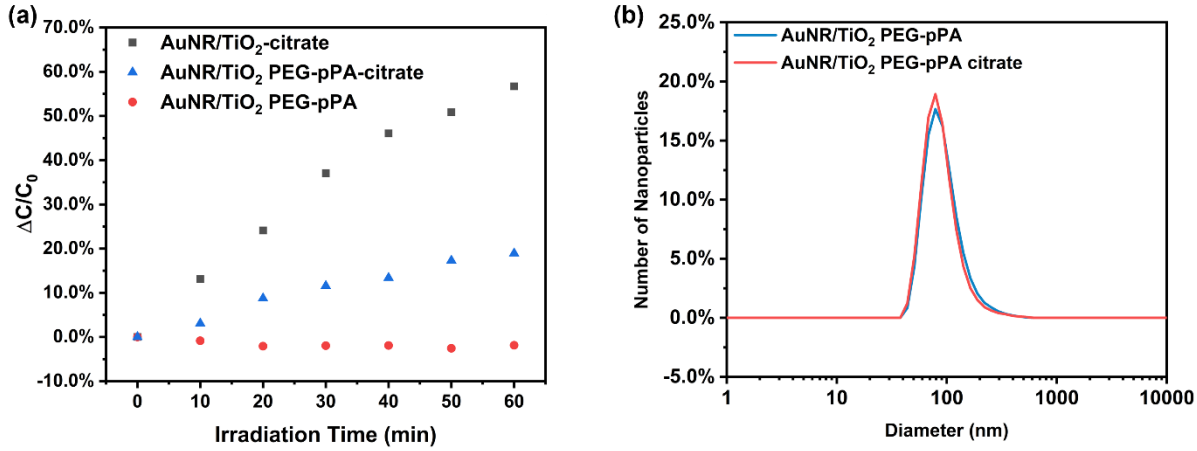

Figure.II.34. (a). Comparison of photodegradation behavior of AuNR/TiO_2 nanoparticles between non functionalized/partially functionalized/completely functionalized TiO_2 surface. (b). Hydrodynamic radius of partially/completely functionalized AuNR/TiO_2 nanoparticles measured by DLS.

To summarize, in this section, we evaluated several possible methods to improve the colloidal stability of AuNR/TiO_2 nanoparticles by functionalizing TiO_2 surface of nanoparticles with hydrophilic polymer ligands. Among these methods, the use of PEG5k-pPA ligands demonstrated the most favorable outcomes in terms of ligand exchange efficiency and nanoparticle stabilization. However, it was observed that functionalized AuNR/TiO_2 nanoparticles may experience a reduction in their photoactivity due to the presence of the dense polymer ligand layer, which may also occupy the reactive sites on the nanoparticle surface. Therefore, it is crucial to strike a balance by finely adjusting the polymer density on the nanoparticle surface. This balance ensures both the colloidal stability of nanoparticles in physiological environments and the preservation of high photoactivity that is not hindered by ligand functionalization.

II.3. Photodynamic effect of AuNR/TiO_2 nanoparticles: *in vitro* test

For the following *in vitro* cellular experiments, AuNR/TiO_2 nanoparticles were functionalized with the PEG-pPA copolymer, then partially ligand exchanged with citrate before being transferred into cell culture media. To test their PDT efficacy under NIR irradiation, AuNR/TiO_2 nanoparticles were incubated with HeLa cells for 6h, followed by irradiation under a continuous wave laser at 800 nm for 10 min. The photodynamic effect of AuNR/TiO_2 nanoparticles can be evaluated by measuring cell viability after irradiation.

II.3.1. Evaluation of cell viability by cell staining

To test cell viability, HeLa cells were stained with fluorescent dyes after irradiation. Calcein green AM, a dye molecule with excitation/emission of 495/515 nm, can be transported into live cells where it can be converted into fluorescent calcein green after intracellular esterase removes the acetoxymethyl (AM) esters[147]. Propidium iodide, another dye molecule with excitation/emission of 535/617 nm, can bind to double stranded DNA but is not membrane permeable[148]. When observed under a fluorescent microscope, green cells are live cells whose cytoplasm is stained by calcein green AM (**Figure.II.35. a**), whereas red cells are dead cells whose nucleus is stained by propidium iodide (**Figure.II.35. b**)

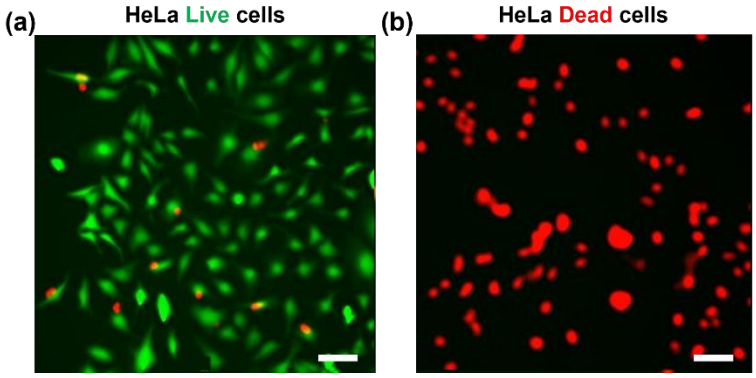

Figure.II.35. Images of HeLa cells stained by calcein green AM and propidium iodide. Scale bar = 100 µm.

II.3.2. Irradiation of HeLa cells incubated with AuNR/TiO_2 nanoparticles

a. Nanoparticles remain in cell culture media during the irradiation

As shown in **Figure.II.36. a**, laser irradiation at 7.5W/cm² in the absence of AuNR/TiO_2 or incubation with AuNR/TiO_2 without laser irradiation did not lead to significant changes in cell viability. However, when cells were irradiated in the presence of a solution of 0.15 nM AuNR/TiO_2 nanoparticles, over 90% of cells in the irradiation zone are dead for laser intensities above 6.3 W/cm^2. (**Figure.II.36. b, c**) The photo-induced cell death was dependent on the AuNR/TiO_2 concentration, as shown in **Figure.II.36. d** and **e**: cell viability decreased from 95% to 40% as the concentration of AuNR/TiO_2 nanoparticles in the culture medium increased from 0 nM to 0.25 nM, for a laser intensity of 3.8 W/cm². These results show the effectiveness of AuNR/TiO_2 nanoparticles to kill cancer cells under moderate NIR irradiation, which is dependent on the laser intensity and quantity of AuNR/TiO_2 nanoparticles.

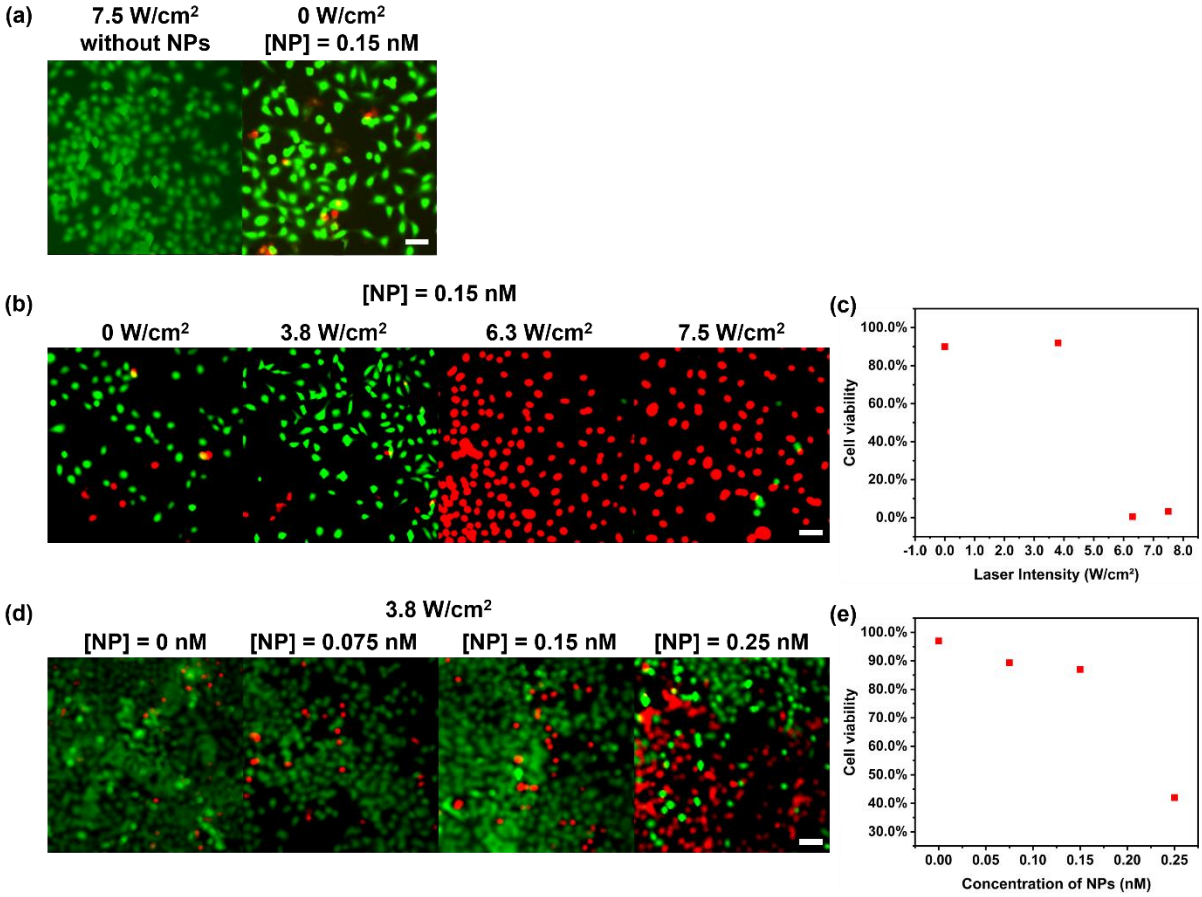

Figure.II.36. Live/dead images of HeLa cells incubated with/without AuNR/TiO_2 nanoparticles after irradiation of 800 nm continuous wave laser. (a). Control group: left: HeLa cells irradiated without AuNR/TiO_2 nanoparticles, right: HeLa cells incubated with AuNR/TiO_2 nanoparticles in dark. HeLa cells irradiated in the AuNR/TiO_2 nanoparticle solution (b). under varied laser intensity (d). with different concentration and (c, e). calculated cell viability. Scale bar = 100 µm.

b. Nanoparticles removed from cell culture media before the irradiation

In order to discriminate the effects of extracellular and intracellular AuNR/TiO_2 nanoparticles on photo-induced cell death, we repeated the same protocol but replaced the AuNR/TiO_2 containing medium with fresh cell culture medium after 6h incubation. As shown in **Figure.II.37. b, c**, above 3.8 W/cm², the fraction of live cells drastically decreases from 95% to 60%. At 3.8 W/cm², increasing the nanoparticle concentration seems to have no evident influence on cells (**Figure.II.37. d, e**). A significant portion of cells have detached from the substrate after laser irradiation, so that the actual cellular toxicity is probably underestimated. Overall, this shows that internalized AuNR/TiO_2 play a major role in the photo-induced toxicity. Here, AuNR/TiO_2 are functionalized with PEG, which minimizes cellular internalization. Improving cell internalization, e.g., by targeting cell surface receptors, would certainly improve the efficiency of the photoinduced cellular death and enable efficient cell killing at lower irradiation intensity.

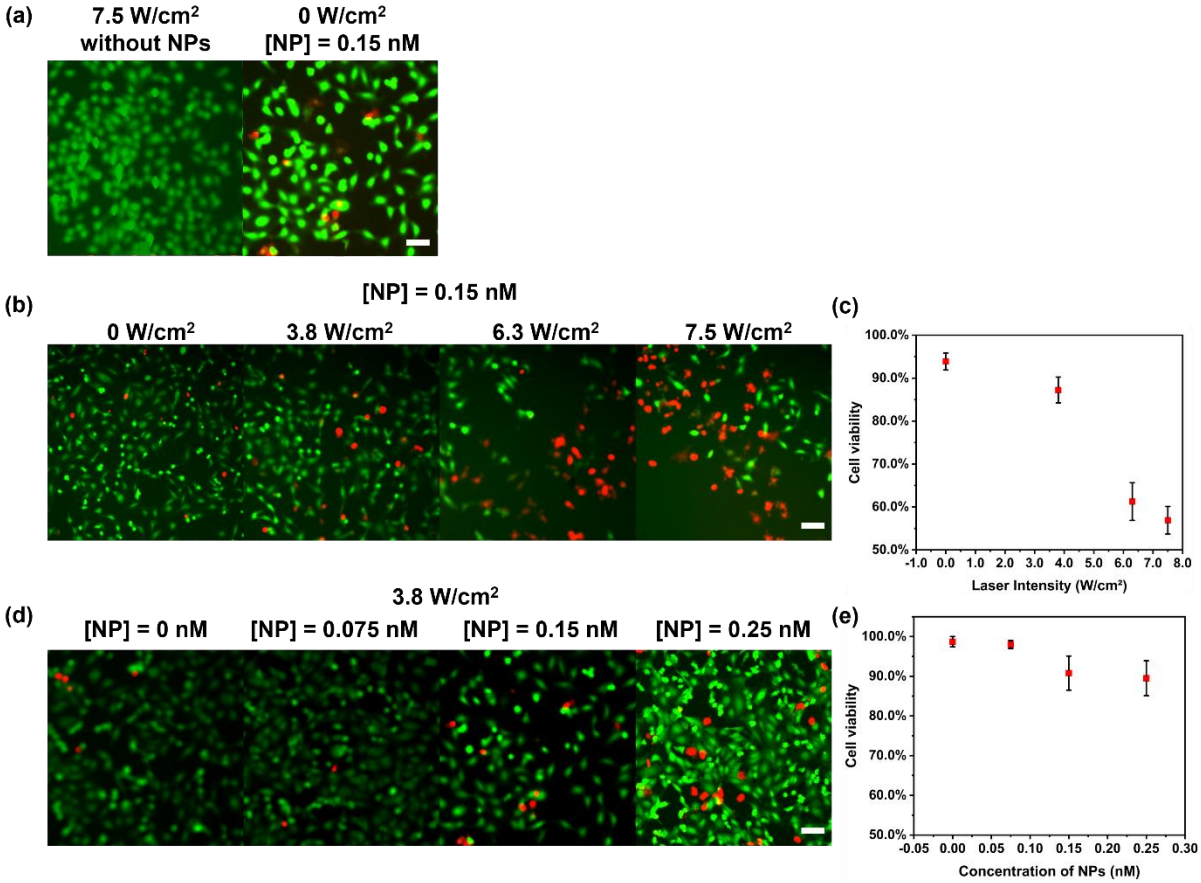

Figure.II.37. Live/dead images of HeLa cells incubated with/without AuNR/TiO_2 nanoparticles after irradiation of 800 nm continuous wave laser. (a). Control group: left: HeLa cells irradiated without AuNR/TiO_2 nanoparticles, right: HeLa cells incubated with AuNR/TiO_2 nanoparticles in dark. HeLa cells irradiated in fresh culture media (b). under varied laser intensity (d). with different concentration and (c, e). calculated cell viability. Scale bar = 100 μm.

c. Irradiation in the presence of DMSO

So far, the reported experiments proved the efficiency of photo-induced cell death mediated by the presence of AuNR/TiO_2 nanoparticles, without discriminating between photothermal (local temperature increase) and photodynamic (ROS production) effects. In order to separate these two effects, cells were incubated with AuNR/TiO_2 nanoparticles, and the irradiation was performed in the presence of increasing concentration of DMSO, which efficiently captures photo-produced OH radicals. As shown in **Figure.II.38. a**, in the dark, the presence of up to 1% of DMSO in the culture media didn't lead to noticeable changes in cell viability. After irradiation for 10 min at 6.3 W/cm^2, cell survival progressively increases with the concentration of DMSO in the medium, going from 60% in the absence of DMSO to a virtual full recovery of 100% in the presence of 1% DMSO in the culture medium. We attribute this effect to efficient OH radicals scavenging by DMSO, which totally suppresses the toxicity of AuNR/TiO_2 nanoparticles. This result demonstrates that the photodynamic effect, i.e., the photo-induced production of OH radicals by AuNR/TiO_2 nanoparticles, is more efficient to kill cells than the photothermal effect alone.

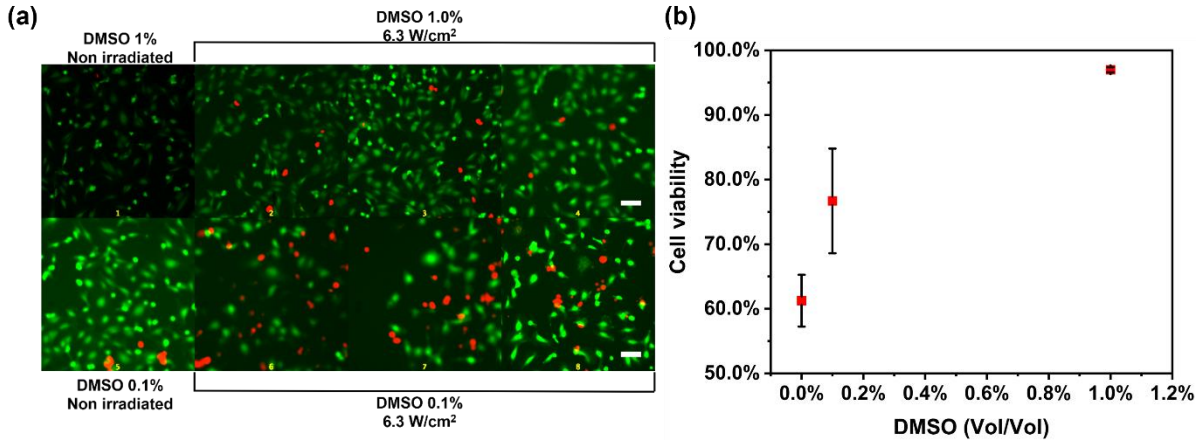

Figure.II.38. (a). Images of HeLa cells incubated with AuNR/TiO_2 nanoparticles irradiated with different concentration of DMSO in the cell culture media. (b) Cell viability after irradiation in the presence of different concentration of DMSO.

II.4. Conclusion and perspective

Gold nanoparticles, such as AuNRs, have been reported to efficiently induce cell death due to the photothermal effect. In this chapter, in an effort to further improve the efficiency of gold-based nanoparticles as photosensitizers, we sought to harness the large absorption cross-section of AuNRs to produce radical oxygen species. First, we optimized the synthesis of AuNR/TiO_2 hybrid nanoparticles. Fine tuning the pH is key to controlling the rate of oxidation of the Ti precursors and enable the growth of TiO_2 tips at the extremities of AuNRs, without complete encapsulation. We demonstrated the shape-dependent generation of hydroxyl radicals by AuNR/TiO_2 nanoparticles under irradiation by NIR light. The rate of photoproduction of hydroxyl radicals depends linearly on the laser intensity and is as efficient under continuous-wave and femtosecond-pulsed irradiation. We have shown that the generation of radicals is mainly due to transfer of hot electrons generated by plasmon excitation to the TiO_2 tips, followed by reduction of dioxygen molecules. Interestingly, a residual photogeneration of OH radicals remains even in the absence of O_2, which could prove beneficial for PDT in O_2-depleted tissues. We have designed a hydrophilic block copolymer ligand to provide colloidal stability of AuNR/TiO_2 nanoparticles in physiological environments. We optimized the polymer density at the surface of AuNR/TiO_2 nanoparticles to ensure a good colloidal stability with preserved high photoactivity. While NIR irradiation or incubation with functionalized AuNR/TiO_2 nanoparticles alone did not affect the viability of HeLa cells, NIR irradiation in the presence of the hybrid nanoparticles led to efficient cell death. The cell survival was recovered in the presence of radical scavengers, which demonstrates that the photodynamic toxicity was superior to the photothermal toxicity in these conditions. This suggests the high potential of these AuNR/TiO_2 for photodynamic therapy applications, which should be confirmed in small animal models in further studies.

Furthermore, the utilization of plasmonic hot charge carriers for photocatalysis in AuNR/TiO_2 nanoparticles exhibits a limited quantum efficiency, where less than 0.1% of the incident photons from the laser are ultimately absorbed and employed in the generation of hydroxyl radicals. Several factors may contribute to this low efficiency. Firstly, at the plasmon resonance frequency, only a small fraction of electrons within the AuNRs are excited and become hot electrons. Among these, only a subset of electrons with suitable characteristics, such as energy and direction, can effectively transfer to the conduction band of TiO_2. Additionally, the presence of a Schottky barrier at the AuNR-TiO_2 interface

can further hinder the efficiency of electron transfer. Secondly, the transferred electrons must migrate to the surface of the TiO_2, where they can react with oxygen molecules. A thick TiO_2 layer may limit the number of electrons that successfully reach the surface and participate in the desired reactions. Thirdly, the ligands present at the surface of the TiO_2 can influence the probability of electron-oxygen reactions. The availability of reactive sites and the nature of the ligands can affect the chances of electron interactions with oxygen molecules, thereby impacting the overall photochemical efficiency.

To overcome these limitations and enhance the utilization of plasmonic energy, the subsequent chapter will explore alternative hybrid gold-semiconductor structures that leverage energy transfer pathways rather than direct electron injection into the semiconductor's conduction band.

Chapter III. Plasmon energy transfer-based nanohybrids

Résumé

Dans le chapitre précédent, nous avons démontré que les nanostructures hybrides de nano-bâtonnets d'or (AuNRs) et de dioxyde de titane peuvent générer des espèces réactives de l'oxygène (ROS) par processus de transfert de charge. Cependant, ce processus a des limites et seule une petite fraction des photons absorbés peut être utilisée pour des réactions photochimiques. Les AuNRs peuvent également fonctionner comme des antennes qui concentrent le champ électromagnétique incident dans leur environnement proche. Lorsqu'un matériau semi-conducteur doté d'une bande interdite appropriée est placé dans ce champ électromagnétique renforcé, les électrons de sa bande de valence peuvent être excités vers la bande de conduction, qui ensuite participent aux réactions photochimiques. Ce processus, connu sous le nom de transfert d'énergie, transfère directement l'énergie absorbée des AuNR aux électrons du semi-conducteur. Dans ce chapitre, nous nous concentrons sur la conception et la fabrication de nanostructures hybrides or-semiconducteur qui exploitent l'énergie plasmonique par la voie du transfert d'énergie. Nous évaluons leur photoactivité par la dégradation de molécules de bleu méthylène et discutons de l'importance de la structure et de la composition de ces nanoparticules hybrides par rapport à leur activité photocatalytique. En outre, nous observons que le faible rendement quantique des nanoparticules hybrides or-semiconducteur est probablement attribué à la dissipation thermique dominante des électrons excités. Trouver des moyens de guider ces électrons excités pour qu'ils participent à des réactions chimiques peut être crucial pour obtenir un rendement quantique plus élevé et une utilisation plus efficace de l'énergie plasmonique.

Abstract

In the previous chapter, we demonstrated that the hybrid nanostructures of gold nanorods (AuNRs) and titanium dioxide can generate reactive oxygen species (ROS) through a charge transfer pathway. However, this process has limitations, and only a small fraction of absorbed photons can be utilized for photochemical reactions. Alternatively, AuNRs can function as antennas that concentrate the incident electromagnetic field in their surrounding environment. When a semiconductor material with an appropriate band gap energy is placed in this enhanced electromagnetic field, the electrons in its valence band can be excited to the conduction band, enabling further photochemical reactions. This process, known as the energy transfer pathway, directly transfers the absorbed energy from AuNRs to the electrons of the semiconductor. In this chapter, we focus on designing and fabricating hybrid gold-semiconductor nanostructures that leverage plasmon energy via the energy transfer pathway. We evaluate their photoactivity through the degradation of methylene blue molecules and discuss the significance of the structure and composition of these hybrid nanoparticles in relation to their photocatalytic activity. Additionally, we observe that the low quantum yield of the hybrid gold-semiconductor nanoparticles is likely attributed to the dominant thermal dissipation of excited electrons. Finding ways to guide these excited electrons to participate in chemical reactions may be crucial for achieving a higher quantum yield and more efficient utilization of plasmon energy.

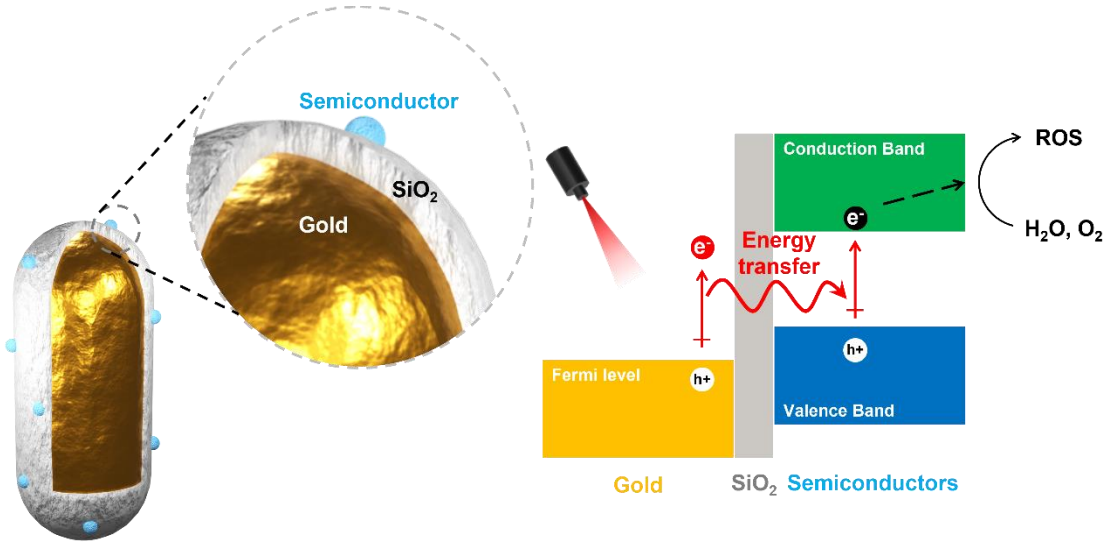

Figure.III.1. Gold nanorod@silica shell@semiconductor hybrid nanoparticles produce reactive oxygen species under near infrared irradiation via energy transfer pathway.

In the previous chapter, we discussed the ability of AuNRs to generate hot electrons when excited at their plasmonic resonance frequency. These hot electrons can be harnessed through charge transfer pathways when combined with semiconductor materials, enabling further photocatalytic reactions. This phenomenon has been demonstrated in the AuNR/TiO_2 dumbbell nanostructure. In this chapter, our objective is to explore the use of plasmon energy transfer to improve the quantum efficiency of ROS production of AuNR/semiconductor heterostructures. Indeed, when illuminated at their plasmon resonance frequency, AuNRs can also act as nanoantennas, resulting in a large exaltation of electromagnetic field near their surfaces. By placing a suitable semiconductor material in this enhanced electromagnetic field region, the electrons in the valence band of the semiconductor could be excited to the conduction band. This energy transfer occurs through dipole-dipole interactions between the AuNRs and the semiconductor material.

In comparison with the charge transfer pathway, the energy transfer pathway exhibits several differences. Firstly, the charge transfer requires an intimate interface between AuNRs and semiconductors while it is not necessary for the energy transfer. Secondly, for the charge transfer, the hot electrons injected to the semiconductors should possess appropriate momenta and energy to overcome the Schottky barrier at the interface of AuNR and semiconductors. For energy transfer, the efficiency of energy transfer is dependent on the spectral overlap between the plasmon absorbance of AuNR and the absorbance of semiconductors. Thirdly, during the charge transfer process, the charge neutrality must be maintained. As illustrated in chapter II, core-shell AuNR/TiO_2 nanoparticles exhibit a much lower photocatalytic activity than the dumbbell AuNR/TiO_2 nanoparticles which can be explained by the fact that for core shell shape AuNR/TiO_2 nanoparticles it is more difficult to consume the generated hot holes with species in the solution as hot electrons are continuously consumed for photocatalytic reactions. However, core-shell nanostructures are widely used in energy transfer processes, which are not limited by the requirements of charge neutrality and the core-shell structure provides a larger contact area between plasmonic nanoparticles and semiconductors, improving the energy transfer efficiency. In a second step, the electron-hole pairs generated in the semiconductor could be used to generate radical oxygen species, for example, by O_2 reduction or by water oxidation.

The semiconductor materials used here include silver sulfide (Ag_2S) and copper(I) sulfide (Cu_2S). Unlike TiO_2, these two semiconductor materials possess a narrower band gap (1 – 2 eV) and absorption in the near infrared range. This absorption overlaps with the longitudinal absorption of AuNR (700 – 1200 nm), which allows efficient energy transfer from AuNRs to these semiconductor materials.

In the first part of this chapter, we develop the synthesis of AuNR/silver sulfide core/shell nanoparticles and examine their plasmonic and photocatalytic properties. In the second part, we synthesize AuNR/silver or copper sulfide nano-hybrids containing a silica spacer between these two components. Indeed, it has been proved that an insulator layer such as SiO_2 between gold and semiconductor can further improve the photocatalytic efficiency by preventing charge transfer back to the gold nanoparticle[99].

This project has been completed in collaboration with Beatrice Jeffries, a Master I intern student in the laboratory.

III.1. Gold nanorods – silver sulfide core-shell nanoparticles

III.1.1. Synthesis of gold nanorod core – silver shell nanoparticles

Synthesis of AuNR@Ag core-shell nanoparticles:

To a 20 mL scintillation vial was added subsequently cetyltrimethylammonium chloride solution (CTAC, 10 mL, 80 mM), AuNR stock solution (500 µL, 1 nM), ascorbic acid solution (1 mL, 0.1 M), $AgNO_3$ (10 µL, 0.1 M), and NaOH solution (400 µL – 700 µL, 0.2 M). Then the resulting solution was sonicated for 2 min to homogenize the mixture and placed in a water bath at 30 °C. The formation of Ag shells at the surface of AuNRs takes 2 – 3 hours. Afterwards, the AuNR@Ag nanoparticles were collected by centrifugation (4500 g, 10 min), washed twice with distilled water, and stored in CTAC solution (80 mM).

The growth of silver shells at the surface of AuNRs is realized based on the protocol reported by Xiang et al with slight modifications[149]. As discussed in Chapter II, the CTAB ligands pack more densely on the lateral surface of the AuNRs, leaving the tips of the AuNRs more accessible for precursor deposition. This preferential binding results in the formation of a dumbbell-shaped hybrid nanostructure. To achieve a uniform core-shell structure, it is necessary to replace the CTAB ligands on the surface of the AuNRs with a ligand that does not exhibit surface binding preference. Therefore, the CTAB-stabilized AuNRs are subjected to ligand exchange with the surfactant cetyltrimethylammonium chloride (CTAC). CTAC also forms double layers to stabilize the AuNRs, but the bilayer formed by CTAC is more homogeneous compared to that formed by CTAB. Silver nitrate ($AgNO_3$) is used as precursor in this synthesis.

Ag^+ ions are reduced to Ag (0) in the solution by anionic ascorbic acid. Similar to the synthesis of AuNRs, the redox potential of ascorbic acid determines the speed of Ag deposition and can be adjusted by the acidity of the solution. Indeed, ascorbic acid in an acidic environment cannot reduce the Ag^+ ions, a basic environment with a pH value between 9 and 10 is necessary for an appropriate reaction rate. The acidity of the solution is therefore tuned by the quantity of NaOH added into the system. As depicted in **Figure.III.2**, we conducted experiments with fixed quantities of $AgNO_3$, ascorbic acid, and AuNRs, while varying the volume of NaOH solution (0.2 M) from 400 µL to 700 µL. By doing so, we successfully synthesized AuNR@Ag nanoparticles with a range of silver shell thicknesses measured by TEM, from 0.5 nm to 7 nm. (**Figure.III.2. d**) The formation of the silver shell resulted in a blue shift of the longitudinal absorption of AuNRs, where a thicker silver shell led to a greater blue shift (from 800nm to 650 nm). (**Figure.III.2. a**) This blue shift in longitudinal absorption can be attributed to a decrease in the aspect ratio of the AuNR@Ag nanoparticles compared to the initial AuNRs. Additionally, the color of the AuNR@Ag solution changed from pale red to yellow and green. (**Figure.III.2. c**) In addition to changes in longitudinal and transverse absorbance, a new absorption peak gradually emerged at approximately 400 nm and became more pronounced with increasing thickness of the silver shell. This new absorption band can be attributed to the octupolar plasmon mode associated with the Ag shell, as it is also observed in pure silver cubes[150].

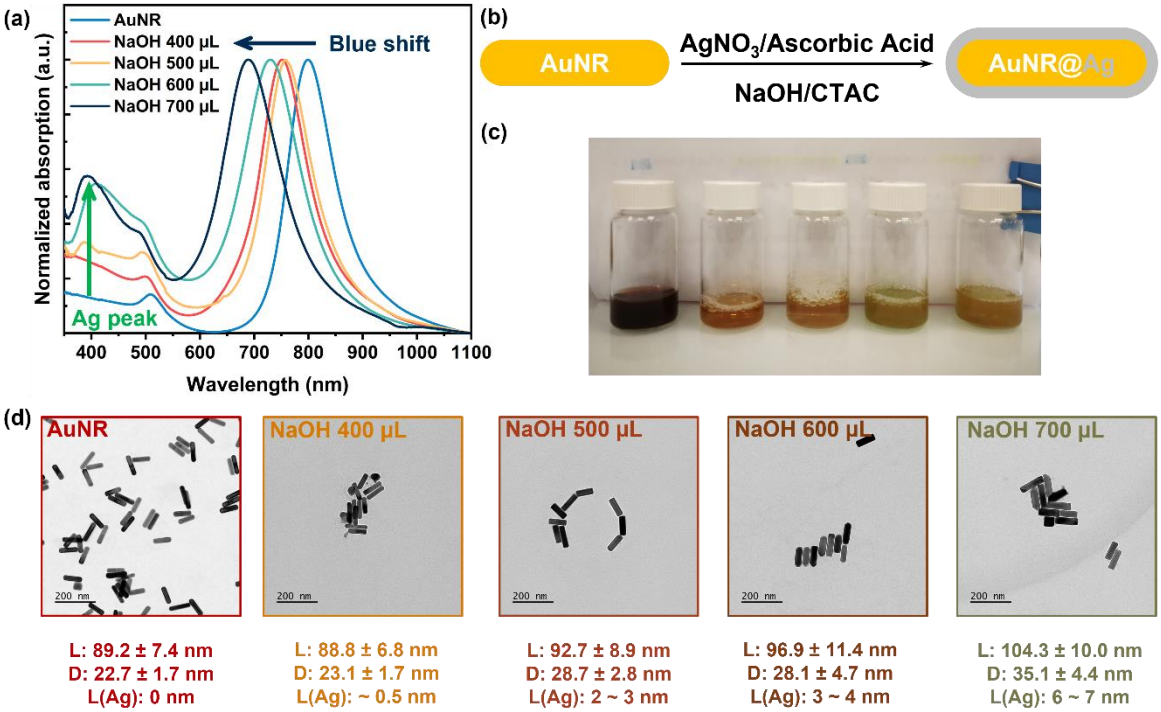

Figure.III.2. (a) UV-Vis absorption spectra of AuNR@Ag core-shell nanoparticles synthesized with increased volume of NaOH solution. (b). Illustration of synthesis condition of AuNR@Ag core-shell nanoparticles. (c). The color of the solution of AuNR@Ag core-shell nanoparticles with increased thickness of Ag shells. (d). TEM images of synthesized AuNR and AuNR@Ag nanoparticles with measured length (L), diameter (D) and thickness of Ag (L(Ag)).

In addition, the thickness of Ag shells can also be modified by the quantity of $AgNO_3$. As shown in **Figure.III.3**, by increasing the concentration of $AgNO_3$ from 0.1 mM to 0.4 mM with volume of NaOH fixed at 500 µL, we can obtain AuNR@Ag nanoparticles with thickness of Ag shells ranging from 5 nm to 20 nm.

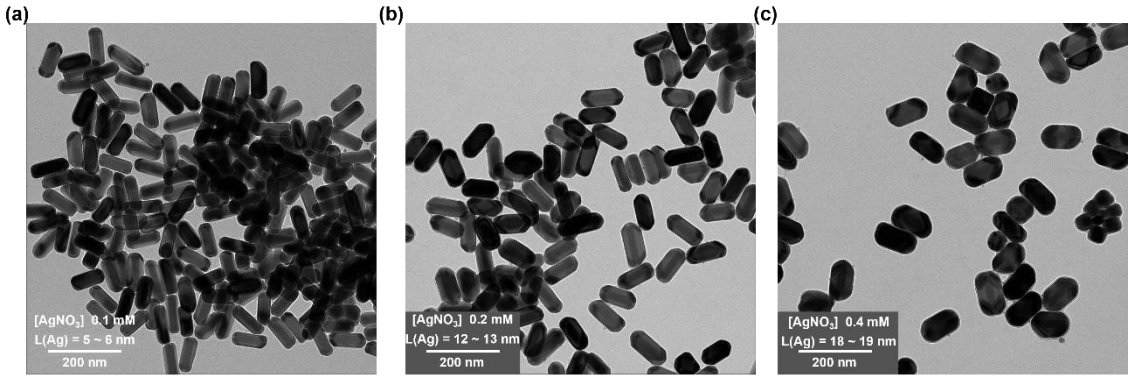

Figure.III.3. TEM images of AuNR@Ag synthesized with fixed volume of NaOH (500 µL) and varied concentrations of $AgNO_3$: (a). 0.1 mM; (b). 0.2 mM; (c). 0.4 mM.

III.1.2. Synthesis of gold nanorod core – silver sulfide shell nanoparticles

Synthesis of AuNR@Ag_2S core-shell nanoparticles:

To a 20 mL scintillation vial was added subsequently 1 mL of as-synthesized AuNR@Ag nanoparticle solution ([AuNR@Ag] = 1 nM, stabilized in CTAC 80 mM), 2 mL of distilled water. The solution was kept under stirring at 500 rpm. A solution of sodium sulfide was prepared (Na_2S, 1 mM). This Na_2S solution was added to the solution of AuNR@Ag via programmed injection with syringe at a rate of 1 µL/min for 5 hours. Afterwards, the nanoparticles were collected by centrifugation (4500 g, 10 min) washed with distilled water twice and stored in CTAC solution (80 mM).

The as synthesized AuNR@Ag nanoparticles with a silver shell thickness of 3 nm, were reacted with sodium sulfide. The silver shell can be oxidized by the oxygen in the air in the presence of S^{2-} ions and eventually forms silver sulfide shell at the surface of AuNRs.

$$4Ag + 2S^{2-} + O_2 + 2H_2O \rightarrow 2Ag_2S + 4OH^- \quad \text{(III. 1)}$$

To ensure a gradual and complete oxidation of the silver shell, the sodium sulfide solution (1 mM) was injected at a rate of 1 µL/min. The progression of this reaction was monitored using UV-Vis absorption spectroscopy. As shown in **Figure.III.4. a**, upon the introduction of Na_2S solution, the longitudinal absorbance of AuNR@Ag nanoparticles exhibited a decrease in intensity and a shift towards longer wavelengths (from 700 nm to 900 nm). This attenuation in absorption intensity and the red shift of the longitudinal absorption peak can be attributed to the higher refractive index of Ag_2S (~ 2.2) compared to Ag (~ 0.1), indicating the progressive formation of an Ag_2S shell on the surface of the AuNRs. Furthermore, as the Ag_2S shell formed, the plasmon peak at 400 nm rapidly diminished and became no longer observable. The TEM images (**Figure.III.4. b**) show that with the conversion of Ag shell to Ag_2S shell, the thickness of the shell increased progressively from 3 nm to 6 nm. The interplanar distance measured from high resolution TEM images (**Figure.III.4. c**) gives an average value of 0.343 nm, which corresponds to the distance between two $(11\bar{1})$ planes of Ag_2S, reported in the literature[151].

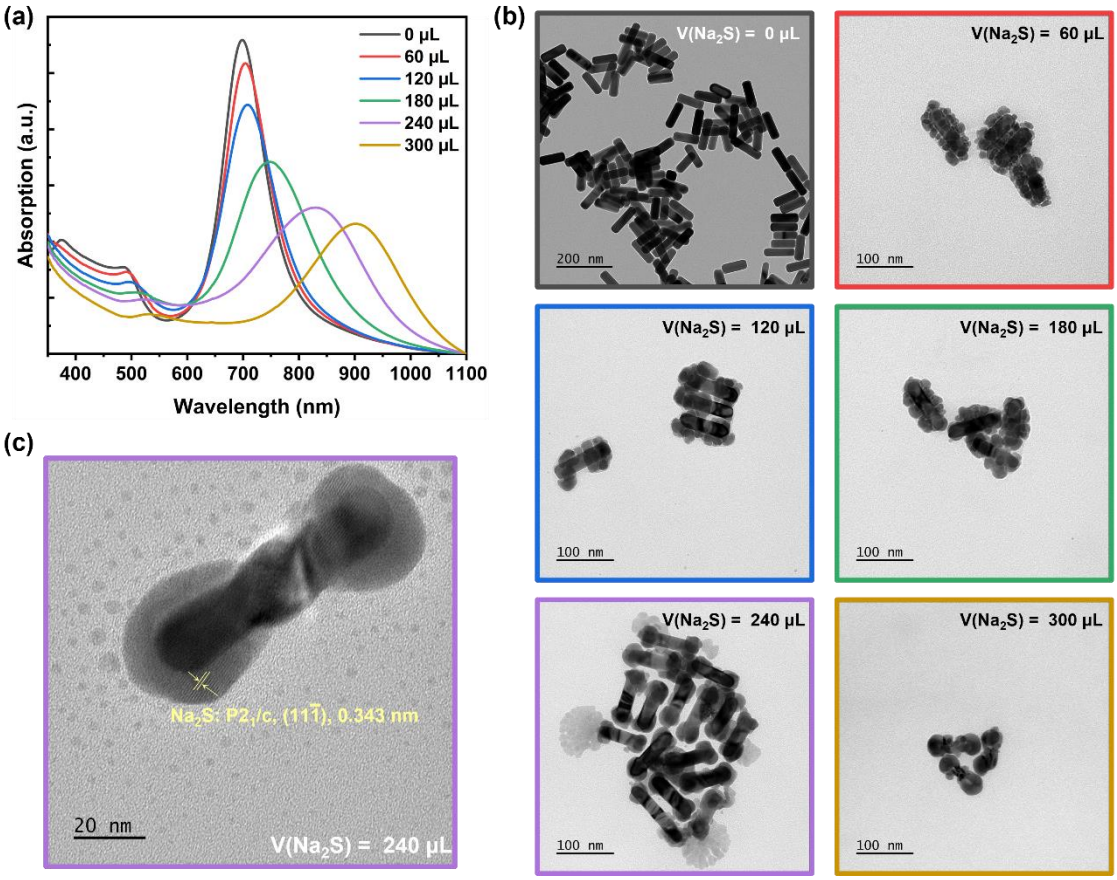

Figure.III.4. (a). UV-Vis absorption spectra of the conversion from AuNR@Ag nanoparticles to AuNR@Ag_2S nanoparticles with the injection of Na_2S solution (1 mM). (b). TEM images of the conversion from AuNR@Ag nanoparticles to AuNR@Ag_2S nanoparticles with the injection of Na_2S solution (1 mM). (c). High resolution TEM image of AuNR@Ag_2S nanoparticles, after injection of 240 µL of Na_2S solution.

III.1.3. Photoactivity of AuNR@Ag_2S in producing hydroxyl radicals

Irradiation experiments with AuNR@Ag_2S nanoparticles:

The AuNR@Ag_2S nanoparticles synthesized by adding successively 240 µL of Na_2S with a longitudinal absorption band at 800 nm were selected for irradiation experiments. They were redispersed in sodium citrate solution (5 mM), with an optical density adjusted to 1.0 at 800 nm. Methylene blue (MB) was then introduced to the solution, reaching a concentration of 10 µM. A volume of 500 µL from the resulting solution was transferred to a quartz cuvette and stirred in the dark for 30 minutes. Subsequently, the solution of AuNR@Ag_2S nanoparticles was irradiated using a NIR continuous wave (CW) laser, while being stirred with a magnetic bar. The laser intensity was set to approximately 1.0 W/cm². UV-Vis absorption spectra of the solution were recorded at 10-minute intervals during the irradiation process.

We also irradiated these AuNR@Ag_2S nanoparticles with an 800 nm NIR laser to study their photocatalytic property. However, as shown in **Figure.III.5**, no remarkable MB degradation was observed, suggesting that these AuNR@Ag_2S nanoparticles are not capable of producing hydroxyl radicals under irradiation.

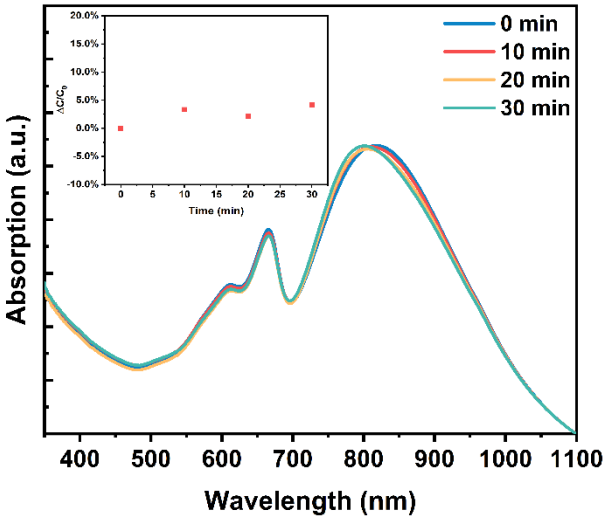

Figure.III.5. UV-vis absorption spectra of AuNR@Ag_2S and MB under irradiation of a CW NIR laser at 1.0 W/cm².

We suppose that the low photocatalytic activity of AuNR@Ag_2S is because it is possible for electrons that are excited to the conduction band of Ag_2S to transfer back to the gold conduction band. (**Figure.III.6**) Then these back-transferred electrons return to the Fermi level through energy relaxation process. Consequently, these back-transferred electrons can no longer be used for photocatalytic reactions and produce ROS.

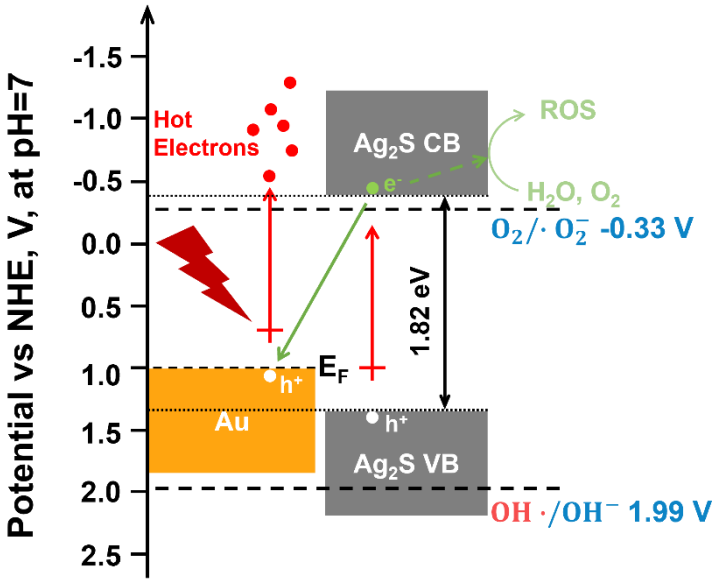

Figure.III.6. Illustration of possible back transfer of excited electrons in Ag_2S to the conduction band of AuNRs.

III.2. Gold nanorod@silica shell@silver/copper(I) sulfide nanoparticles

Based on our previous results and the hypothesis that most of the excited electrons in the conduction band of Ag_2S relax to the conduction band of AuNRs, hindering the production of ROS, we have decided to introduce an insulator layer between the AuNRs and Ag_2S in order to prevent this

electron transfer. In this regard, a silica (SiO_2) layer is a suitable choice for the following reasons: (1) Transparency: SiO_2 is transparent in the NIR range, which allows the unattenuated propagation of the electromagnetic field around the nanoparticles. This transparency ensures that the interaction between incident light and AuNRs is not hindered. (2) Stability: The presence of a SiO_2 layer provides thermal, structural, and colloidal stability for the AuNRs. This stability is crucial for further synthesis in organic solvents and at high temperatures, ensuring the robustness of the nanoparticles. (3) Insulating properties: SiO_2 has been widely used as an insulator to separate gold nanoparticles from semiconductors. It effectively prevents direct hot electron transfer from gold nanoparticles to semiconductors, as supported by previous studies[114,152]. By incorporating a SiO_2 layer, we anticipate that electrons in the conduction band of Ag_2S will be prevented from reaching the surface of AuNRs. As a result, they would remain longer in Ag_2S, leading to more favored ROS production.

III.2.1. Synthesis of AuNR@SiO_2 core shell nanoparticles

Synthesis of AuNR@SiO_2 core-shell nanoparticles:

*AuNRs prepared via seed growth methods (30*95 nm^2, 1.2 nM, 4 mL) were precipitated by centrifugation and redispersed in CTAB solution (1.6 mM, 1.0 mL). The pH value of the resulting AuNR solution was adjusted to 4.0 with HCl or NaOH solution (0.1 M). A 15 µL of (3-mercaptopropyl)trimethylsilane (MPTMS) solution (100 mM) in EtOH was added and the solution was stirred for 3 hours (400 rpm) at room temperature. Next, 7 µL of tetraethyl orthosilicate (TEOS) solution (40 wt.%) in methanol was added (Au/TEOS = 1/1.8), the suspension was stirred for 1 hour. Then the pH of the system was brought back to 8 by addition of NaOH solution (0.2 M) and was kept undisturbed at 30 °C for 24h. The resulting AuNR@SiO_2 nanoparticles were collected by centrifugation and washed twice with EtOH.*

The growth of a silica (SiO_2) shell on the surface of AuNRs follows the method reported by Pellas et al.[153] with slight modifications. As shown in **Figure.III.7**, the initial step involves replacing the CTAB stabilizing bilayer on the AuNRs with MPTMS ligands. The MPTMS ((3-mercaptopropyl)trimethylsilane) ligands bind to the AuNR surface through the formation of Au-S bonds. And the three methoxy groups of MPTMS undergo hydrolysis under weakly acidic conditions (pH = 4), resulting in the production of silanol groups on the AuNR surface. Then, TEOS (tetraethyl orthosilicate) is introduced to the solution. The TEOS serves as a source of silica, leading to the formation of silica shells on the surface of the AuNRs through hydrolysis and condensation reactions. Finally, the pH of the system was gradually increased to facilitate the condensation reaction of SiO_2, allowing for the growth of a stable and homogeneous silica shell around the AuNRs.

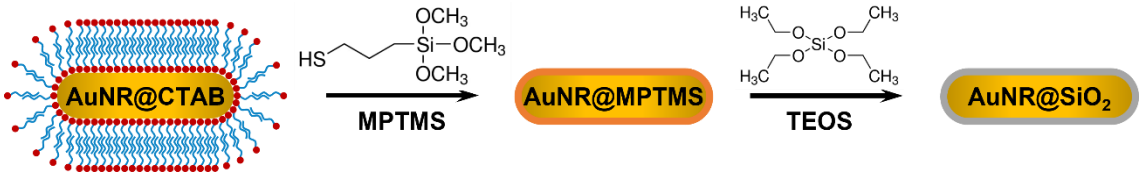

Figure.III.7. Illustration of synthesis of AuNR@SiO_2 core-shell nanoparticles.

The absorption spectrum of synthesized AuNR@SiO_2 was taken after purification. A blue shift of the longitudinal plasmon absorbance from 770 nm to 753 nm was observed, which can be attributed

to the removal of CTAB from the surface of AuNRs (**Figure.III.8. a**). When the ratio of Au and TEOS is set to 1.8, the TEM images of AuNR@SiO_2 demonstrate a homogenous formation of silica shell with an average thickness of 6.0 ± 0.8 nm (**Figure.III.8. b, c**). Therefore, the calculated yield of this synthesis is 77 ± 10%. On the other hand, below this ratio (Au/TEOS = 1.2), the formed silica shell is less homogenous and exhibits a rugged surface (**Figure.III.8. d**), while at a higher Au/TEOS ratio, the condensation of TEOS take place not only at the surface of AuNRs, but also in the solution, resulting in the formation of core free silica nanoparticles (Figure.III.8**. e**).

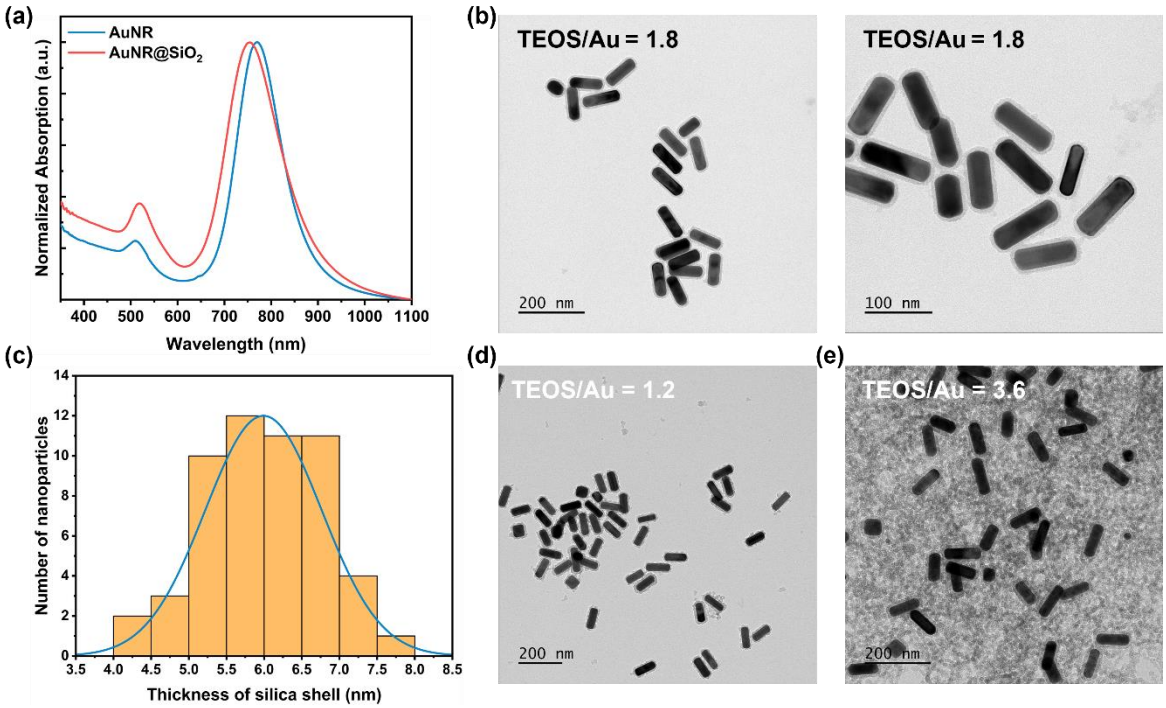

Figure.III.8. (a) UV-Vis spectra of CTAB-capped AuNR and AuNR@SiO_2 after purification. (b). TEM images of AuNR@SiO_2 synthesized at an Au/TEOS ratio of 1.8. (c). The distribution of silica shell thickness of AuNR@SiO_2 measured from TEM images. (d, e). TEM images of AuNR@SiO_2 synthesized at an Au/TEOS ratio of 1.2 or 3.6.

III.2.2. Synthesis of AuNR@SiO_2@Ag_2S core-shell nanoparticles

Synthesis of AuNR@SiO_2@Ag core-shell nanoparticles:

AuNR@SiO_2 nanoparticles were in prior dispersed in EtOH. To a 20 mL scintillation vial was added subsequently 2 mL of AuNR@SiO_2 solution (1 nM) and 30 µL of MPTMS. The resulting solution was kept stirring (200 rpm) for 2 days. The MPTMS capped AuNR@SiO_2 nanoparticles were collected and washed twice with EtOH.

The MPTMS capped AuNR@SiO_2 nanoparticles were redispersed in 6 mL of EtOH. Next, 165 mg of polyvinylpyrrolidone (PVP, M_W =55 000 g/mol) was added in the solution, followed by the addition of 200 µL of nitrate silver(I) diamine ($Ag(NH_3)_2)NO_3$) solution (0.01 M). The resulting solution was sonicated for 2 min and kept undisturbed for 6 hours at 70 °C. The as-synthesized AuNR@SiO_2@Ag nanoparticles were collected and washed twice with EtOH.

Synthesis of AuNR@SiO_2@Ag_2S core-shell nanoparticles:

2 mL of solution of AuNR@SiO_2@Ag nanoparticles (EtOH) was added to a 20 mL scintillation vial. An aqueous solution of sodium sulfide ($Na_2S \cdot xH_2O$, 1 mM) was added to the solution at a rate of 5 µL/min for 1h under vigorous stirring at room temperature. Then the nanoparticles were collected by centrifugation and washed 3 times with EtOH.

Huang et al.[154] proposed a protocol to deposit silver layer on the surface of silica nanoparticles. To graft silver nanoparticles on the surface of the silica shell of AuNR@SiO_2 nanoparticles, we adapted Huang's protocol. Initially, the silica surface was activated using MPTMS. The MPTMS molecules attached to the silica surface through hydrolysis/condensation reactions, forming Si-O-Si bonds with SiO_2. The thiol groups of MPTMS improved the affinity between the silica surface and silver nanoparticles by capturing silver nuclei during their formation. This facilitated the deposition of silver nanoparticles onto the surface of AuNR@SiO_2. Without the presence of MPTMS, it would be difficult for silver nanoparticles formed in the solution to attach to the surface of AuNR@SiO_2 nanoparticles. The reduction of the silver precursor was assisted by PVP, a polymer that also acted as a stabilizer for the nanoparticles. The nanoparticle solution was heated at 70 °C for 6 hours. After the reaction, the initial dark red solution transformed into a bright ruby red solution.

As shown in **Figure.III.9. a**, the UV-Vis absorption spectra of purified AuNR@SiO_2@Ag nanoparticles were checked. A new absorption band appears at around 430 nm indicating the formation of Ag nanoparticles. The longitudinal absorption band show a red shift from 753 nm to 786 nm, which can be attributed to the enhanced plasmon coupling between silver nanoparticles and AuNRs. The SEM-EDX analysis (**Figure.III.9. b**) confirms the formation of silver nanoparticles at the surface of silica shell and according to the Au/Ag ratio we can estimate the yield of this reaction is about 80 – 90%. According to the TEM images shown in **Figure.III.9. c**, the formed silver nanoparticles distribute homogeneously at the surface of silica shell, with an average size of 5.4 ± 1.0 nm in diameter. Additionally, during the synthesis process, the AuNR@SiO_2 nanoparticles were subjected to heating at 70 °C for 6 hours. It has been previously reported by Zou et al.[155] that bare AuNRs can undergo shape deformation when exposed to temperatures exceeding 60 °C, transforming from a rod-like shape to a spherical shape, resulting in a blue shift in the plasmon absorption band. However, in our case, no evidence of shape deformation of AuNR@SiO_2 was observed in either the TEM images or the absorption spectra. This result suggests that the silica shell surrounding the AuNRs effectively enhances their stability.

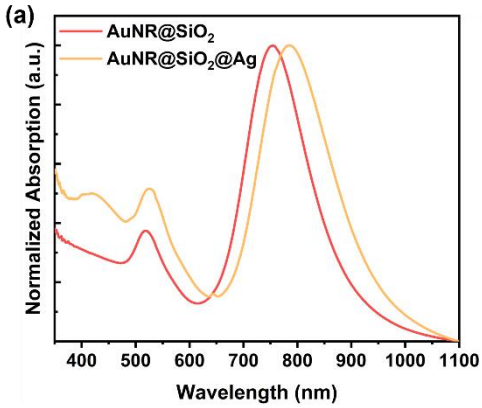

(b)

Elements	Atom %
Au	75.9 ± 7.2 %
Ag	24.1 ± 2.8 %

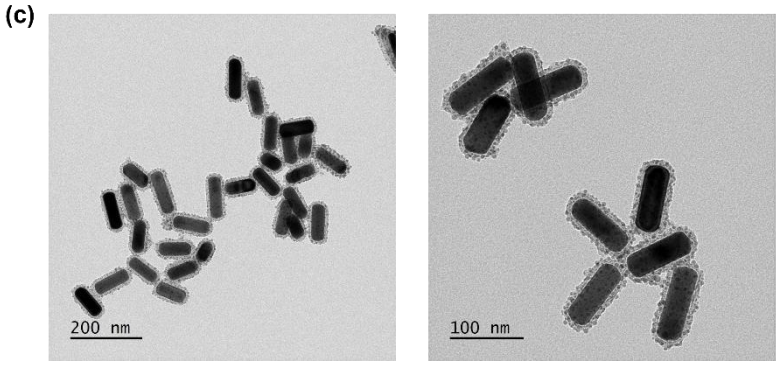

Figure.III.9. (a). UV-Vis spectra of AuNR@SiO_2 and AuNR@SiO_2@Ag after purification. (b). SEM-EDX analysis results. (c). TEM images of as-synthesized AuNR@SiO_2@Ag nanoparticles.

The oxidation process of silver nanoparticles to silver sulfide nanoparticles on the surface of the silica shell was performed using a similar protocol to the preparation of AuNR@Ag_2S from AuNR@Ag nanoparticles. The oxidation was achieved by successive injections of Na_2S solution, which ensured a gradual and uniform transformation of the Ag nanoparticles into Ag_2S nanoparticles. This oxidation process was visually observed through a change in the solution color from bright ruby red to violet red, indicating the successful conversion of the silver nanoparticles to silver sulfide nanoparticles. UV-Vis absorption spectra shown in **Figure.III.10. a** reveal a slight red shift of the longitudinal plasmon band from 786 nm to 797 nm. Besides, the disappearance of absorption band at around 400 nm indicates the transformation of Ag to Ag_2S nanoparticles at the surface silica shell. The SEM-EDX analysis confirms the conversion from Ag to Ag_2S, by the observed increased S/Ag ratio (2/1). (**Figure.III.10. b**) It should be noted that during the synthesis, the MPTMS ligands also introduce a small quantity of sulfur at the nanoparticle surface, leads to an initial S/Ag ratio of 1.5/1 before introduction of Na_2S, as determined by the SEM-EDX measurement. The TEM images of the synthesized AuNR@SiO_2@Ag_2S nanoparticles are shown in **Figure.III.10. c**. The Ag_2S nanoparticles remain at the silica surface after purification: no unbound Ag_2S nanoparticles are observed and the density of Ag_2S nanoparticles at the silica surface is roughly similar to that of the initial Ag nanoparticles. The average size of the Ag_2S nanoparticles measured from TEM images is 6.2 ± 0.9 nm in diameter. As the conversion from Ag to Ag_2S should lead to an inflation of crystal size, we can calculate the ratio of radius between Ag and Ag_2S nanoparticles at the same quantity of silver as:

$$\frac{r_{Ag}}{r_{Ag_2S}} = \left(\frac{V_{Ag}}{V_{Ag_2S}}\right)^{\frac{1}{3}} = \left(\frac{2 * M_{Ag} * \rho_{Ag_2S}}{\rho_{Ag} * M_{Ag_2S}}\right)^{\frac{1}{3}} = 0.84 \qquad \text{(III. 2)}$$

where $M_{Ag} = 108\ g/mol$ is the molar mass of Ag, $\rho_{Ag} = 10.49\ g/cm^3$ is the density of Ag, $M_{Ag_2S} = 247.8\ g/mol$ is the molar mass of silver sulfide, and $\rho_{Ag_2S} = 7.23\ g/cm^3$ is the density of silver sulfide. Finally, given that the initial silver nanoparticles have an average size of 5.4 nm, the expected average size of Ag_2S nanocrystals is thus 6.4 nm, a value that corresponds to the value measured from TEM images.

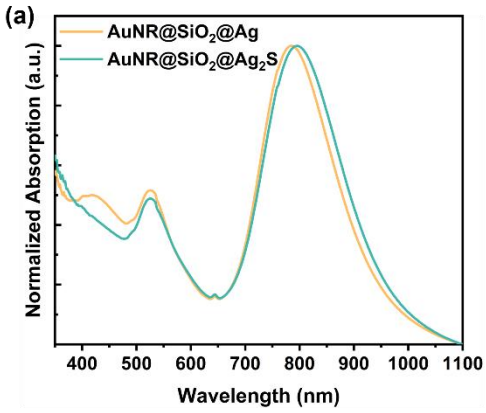

(b)

Elements	Atom %
Au	56.5 ± 2.3 %
Ag	14.3 ± 0.9 %
S	29.2 ± 1.1 %

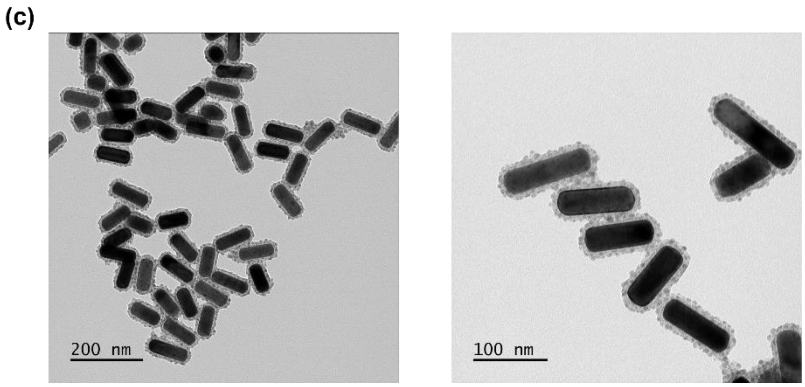

Figure.III.10. (a). UV-Vis spectra of AuNR@SiO_2@Ag and AuNR@SiO_2@Ag_2S after purification. (b). SEM-EDX analysis results. (c). TEM images of as-synthesized AuNR@SiO_2@Ag_2S nanoparticles.

III.2.3. Photoactivity of AuNR@SiO_2@Ag_2S nanoparticles in producing hydroxyl radicals

The Ag_2S nanoparticles with an average size of 5 nm were synthesized in citrate solution. (**Annex.V.1.3**. Synthesis of Cu2S/Ag2S nanoparticles) Under NIR irradiation, these Ag_2S nanoparticles cannot induce the degradation of methylene blue (MB). (**Annex.V.4.2**. Irradiation experiments with Cu2S/Ag2S nanoparticles) The negative variation of MB intensity during the irradiation can be attributed to the adsorption-desorption of MB on the surface of Ag_2S nanoparticles. Therefore, Ag_2S nanoparticles alone exhibit no photocatalytic activity at 800 nm.

The solution of AuNR@SiO_2@Ag_2S nanoparticles with an optical density of 0.7 cm^{-1} at 800 nm was subjected to NIR continuous wave laser irradiation (average intensity 1.0 W/cm^2) in the presence of 10 µM of MB. As a control, the same irradiation experiments have been performed with the solution of AuNR@SiO_2 nanoparticles. As shown in **Figure.III.11. a, b**, the absorption spectra of the nanoparticle solution show fluctuations during the irradiation process, together with an increase of the extinction spectrum at low wavelengths. This may indicate partial agglomeration of nanoparticles leading to increased scattering, or to changes in the optical properties of the nano hybrids. It is therefore

difficult to directly compare the absorption intensity of the MB between each measurement. Nevertheless, as a substitute we use the difference in absorption between the value of the MB peak at 664 nm and the value at 705 nm, where MB does not contribute to the total absorption. This difference is less influenced by the fluctuation of the nanoparticle contribution, since the absorbance of AuNR@SiO_2@Ag2$_S$ is similar at these two wavelengths. The obtained values enable tracking the quantity of MB that remain in the solution. In **Figure.III.11. c**, we plot the variation of MB absorbance as a function of irradiation time. Clearly, the AuNR@SiO_2@Ag_2S nanoparticles exhibit a higher MB degradation rate than AuNR@SiO_2 and AuNR@Ag_2S nanoparticles. The better photocatalytic performance of AuNR@SiO_2@Ag_2S nanoparticles compared to the AuNR@SiO_2 nanoparticles confirms that the energy transfer from AuNRs to the Ag_2S is necessary for an efficient production of hydroxyl radicals that further lead to MB degradation.

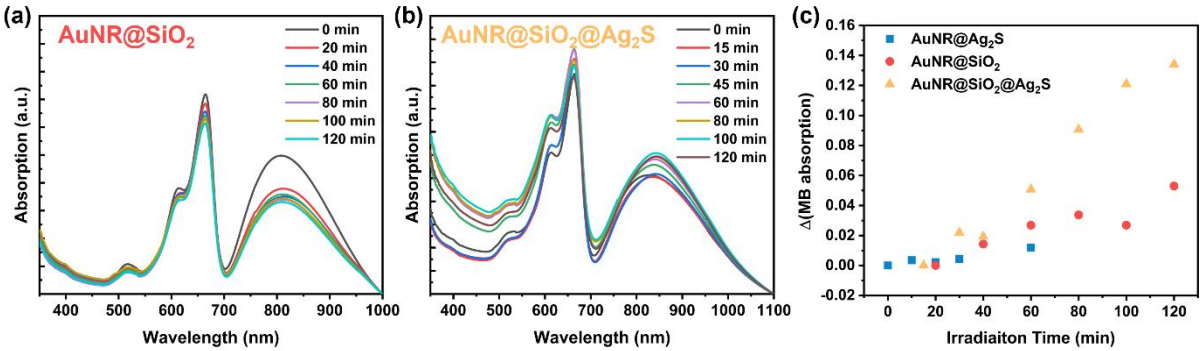

Figure.III.11. UV-vis absorption spectra of (a). AuNR@SiO_2 and (b). AuNR@SiO_2@Ag_2S nanoparticles in the presence of MB irradiated by a CW NIR laser at 1.0 W/cm² for 2 hours. (c). Comparison of MB degradation induced by AuNR@SiO_2@Ag_2S, AuNR@SiO_2, and AuNR@Ag_2S nanoparticles.

In addition, the presence of insulator, the silica shell, does improve the photocatalytic activity of AuNR@Ag_2S nanostructure. As the silica shell prevent the back transfer of electrons to the AuNRs, electrons in the conduction band of Ag_2S can no longer to the conduction band of AuNRs. (**Figure.III.12**) As a result, there are more chances for electrons to react with dioxygen molecules in the environment, and eventually lead to a higher production rate of hydroxyl radicals.

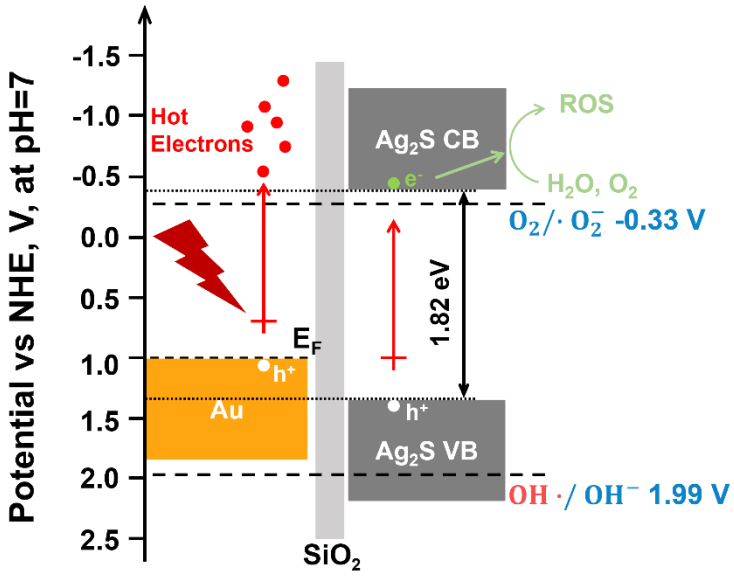

Figure.III.12. Illustration of the elimination of electron-hole recombination at the interface of AuNR and Ag_2S owning to the insertion of silica shell as an insulator.

Based on the previous results, we calculated the quantum yield of AuNR@SiO_2@Ag_2S, as illustrated in Equation.III.3

$$\Phi = \frac{Quantity\ of\ Decomposed\ MB}{Quantity\ of\ absorbed\ photons} = \frac{\frac{\Delta(A_{MB})}{\varepsilon_{MB} * l} * V(solution)}{\frac{\lambda}{I * t * \frac{1240}{N_A * e}} * (1 - 10^{-O.D.}) * 50\%} \quad (III.3)$$

where Φ is the quantum yield defined as the ratio between the total number of decomposed MB and the total number of absorbed photons by nanoparticles within 2h of irradiation; $\Delta(A_{MB}) = 0.134\ cm^{-1}$ is the total variation of absorption intensity of the MB peak; $\varepsilon_{MB} * l = 7.4 \times 10^4\ mol \cdot L^{-1} \cdot cm^{-1} * 1.0\ cm$ is the molar extinction coefficient of MB multiplied by the length of cuvette; $V(solution) = 500\ \mu L$ is the volume of the prepared nanoparticle solution; $I * t = 700\ mW * 7200\ s = 5040\ J$ represents the total energy that produced by the light source; $\lambda = 800\ nm$ is the wavelength of incident light; $e = 1.6 \times 10^{-19} J/ev$; the term $(1 - 10^{-O.D.}) * 50\% = (1 - 10^{-0.7}) * 50\% = 0.4$ calculates the proportion of photons absorbed by nanoparticles. And finally, we have:

$$\Phi = \frac{9.1 \times 10^{-10}\ mol}{0.013\ mol} = 6.7 \times 10^{-8} \quad (III.4)$$

The value of calculated quantum yield of AuNR@SiO_2@Ag_2S seems to be very low. Next, we compare this value to the other similar systems. Gao et al.[137] performed a similar irradiation experiment with gold nanocages. According to the experiment conditions provided in the article, we can calculate the quantum yield of gold nanocages in producing hydroxyl radicals, which is approximately 6.0×10^{-7}, 10 times higher than that of AuNR@SiO_2@Ag_2S.

III.2.4. Synthesis and photoactivity of AuNR@SiO_2@Cu_2S nanoparticles

Synthesis of AuNR@SiO_2@Cu_2S nanoparticles:

To a 20 mL scintillation vial was added subsequently 3 mL of AuNR@SiO_2 solution (1 nM) and 27 µL of (3-aminopropyl)trimethoxysilane (APTMS). The resulting solution was heated to 60 °C and kept stirring for 1 h. Then the solution was left undisturbed overnight at room temperature.

The APTMS activated AuNR@SiO_2 solution was purified and redispersed in 6 mL of water. To the solution was added 100 µL of $CuCl_2$ (200 nM, Au/Cu=1/2), followed by 1 mL of Na_2S (20 nM) injected by a syringe pump at a rate of 2 mL/h while stirring and heating at 90 °C. Then the resulting solution was washed 3 times with water.

In addition to silver sulfide, another semiconductor material, the copper(I) sulfide was also integrated in this AuNR@SiO_2@semiconductor structure and their photoactivity was investigated. In comparison with Ag_2S, the copper atom in Cu_2S can afford multiple oxidation degrees (Cu^+/Cu^{2+}). The hole trapping on a Cu(I) site may favor charge separation and reaction of the remaining electron with adsorbed dioxygen molecules to produce radicals.[156–158] These changes in oxidation states also create vacancies within the nanoparticles. These vacancies serve several purposes: they can trap specific molecules on the nanoparticle surface, facilitating electron contact with targeted molecules, promote electron excitation, and lead to a large absorption band in the NIR range due to the plasmonic resonance. (**Figure.V.3. a**)

Similar to the process of growing silver nanoparticles at the surface of silica shell, to grow copper sulfide nanoparticles on the surface of SiO_2, the surface of silica shell needs to be activated by specific ligands that enable capture of formed Cu_2S nanoparticles from the solution. Next, following the exact same protocol as above for silver sulfide did not result in deposition of copper sulfide at the surface of the silica shell. Firstly, since copper is not reduced as easily as silver, we chose to perform the oxidation reaction of copper ions by sodium sulfide directly without going through the intermediate formation of copper particles. In accordance with the Hard-Soft-Acid-Base (HSAB) theory, it is known that the affinity between thiol groups and Cu(I) is relatively weaker compared to that with silver (Ag), as Cu(I) is considered a harder acid than Ag. Indeed, deposition of copper sulfide was not observed on MPTMS-functionalized AuNR@SiO_2.To address this, we have chosen to replace the thiol group of MPTMS with the amine group of APTMS. The amine group of APTMS is a harder base than thiols and exhibits a higher affinity towards Cu(I), making it more suitable for capturing and facilitating the growth of Cu_2S nanoparticles on the silica shell surface.

The **Figure.III.13** shows the characterizations of the AuNR@SiO_2@Cu_2S nanoparticles. According to the UV-vis spectra, a broadened longitudinal absorption band is observed, which can be attributed to the formation of Cu_2S nanoparticles which exhibit a broad absorption band from 800 nm to 1100 nm. The TEM image shows that unlike the silver forming independent nanoparticles, the Cu_2S tends to form a shell on the surface of silica shell. The successive injection of the Na_2S precursor led to the slow but more homogeneous deposition of Cu_2S on silica shell and eventually produce a Cu_2S layer. It should be noted that from the TEM image, the secondary nucleation of Cu_2S can be observed, meaning that we can still improve the synthesis quality by adjusting the ratio of Au/Cu in the system and also the injection rate. The SEM-EDX analysis give a ratio of Au/Cu=4/1, indicating the Cu_2S yield of approximately 15%.

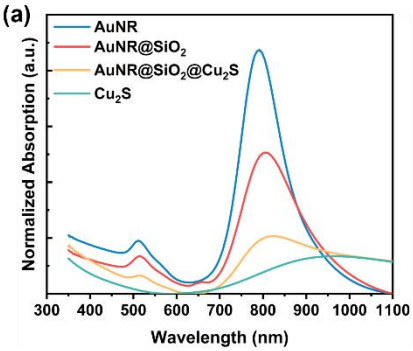

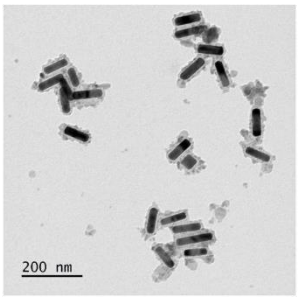

(c)

Elements	Percentage
Au	62 ± 4 %
Cu	15 ± 2 %
S	23 ± 2 %

Figure.III.13. (a). UV-Vis spectra of AuNR, AuNR@SiO_2, AuNR@SiO_2@Cu_2S and Cu_2S nanoparticles. (b). TEM image of synthesized AuNR@SiO_2@Cu_2S nanoparticles. (c) SEM-EDX analysis result of synthesized AuNR@SiO_2@Cu_2S nanoparticles.

Then the irradiation experiment was performed with the solution of AuNR@SiO_2@Cu_2S nanoparticles. However, we did not observe evident photocatalytic activity induced by these nanoparticles. (**Figure.III.14**) Indeed, the MB degradation rate of AuNR@SiO_2@Cu_2S nanoparticles is almost the same as that of AuNR@SiO_2 nanoparticles. This could be due to a low energy transfer efficiency, or to a low ROS production quantum yield after absorption by the Cu_2S nanoparticles. In order to test these hypotheses, we first synthesized Cu_2S nanocrystals of sizes similar to those deposited on AuNR@SiO_2. Their optical and morphological properties were characterized by UV-vis absorption spectra and TEM, as shown in **Annex.V.1.3**. Synthesis of Cu2S/Ag2S nanoparticles. Then we performed the irradiation experiment on the solution of Cu_2S nanoparticles. Despite a broad absorption peak at NIR range (800 – 1000 nm), these Cu_2S nanoparticles did not lead to MB degradation under irradiation. (**Annex.V.4.2**. Irradiation experiments with Cu2S/Ag2S nanoparticles) In order to evaluate the energy transfer efficiency from AuNR@SiO_2 to the surrounding Cu_2S nanoparticles, we measure the thermal photoconversion efficiency of these particles in the following section.

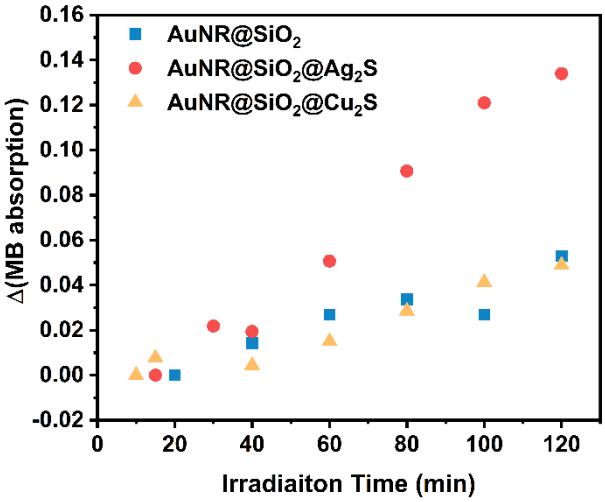

Figure.III.14. Comparison of MB degradation induced by AuNR@SiO_2@Cu_2S, AuNR@SiO_2, and AuNR@SiO_2@Ag_2S nanoparticles.

III.3. Study on photothermal effect

As the recombination between excited electrons and hot holes is prohibited by the insulating SiO_2 layer, if the excited hot electrons were not to react with oxygen molecules, the energy stored in these electrons is likely to be transformed to heat through an electron-phonon relaxation pathway. To assess the extent of energy conversion to heat, we monitored the temperature changes in the nanoparticle solution during irradiation. By measuring the evolution of temperature, we can gain insights into the amount of absorbed light energy that is ultimately transformed into heat.

Temperature profile measurement:

The temperature profile was measured by a thermocouple inserted into 2 mL of nanoparticle solution (optical density at 800 nm ≈ 1.0 cm^{-1}) loaded in a plastic cuvette (length = 1 cm). The solution was kept stirring to achieve a uniform temperature distribution during the irradiation. a continuous wave laser at 800 nm (700 mW) was used to irradiate the nanoparticle solution. The temperature of the solution was measured at an interval of 200 seconds.

Three different types of nanoparticle solution were tested, including AuNR@SiO_2, AuNR@SiO_2@Ag_2S, and AuNR@SiO_2@Cu_2S. As shown in **Figure.III.15. b**, the increase of solution temperature was observed in all these three samples upon irradiation and achieve a plateau after 10 min. Additionally, in the presence of semiconductor nanoparticles at the silica surface, the nanoparticle solution containing AuNR@SiO_2@Ag_2S and AuNR@SiO_2@Cu_2S exhibit a higher temperature increase (ΔT = 16.5 – 17.0 °C) than that containing AuNR@SiO_2 nanoparticles (ΔT = 14.5 °C).

To calculate the light-to-heat conversion efficiency, we adapted a collective heating model proposed by Jiang et al.[159] Briefly, the variation of thermal energy of the nanoparticle solution can be described as:

$$m_{solution} C_{solution} \frac{dT}{dt} = Q_{in} - Q_{out} \quad \text{(III. 5)}$$

where $m_{solution}$ and $C_{solution}$ are the mass and the specific heat capacity of the solution, respectively. Here, we take the values of water: $m_{solution} = 2\ g$ and $C_{solution} = 4.18\ J \cdot g^{-1} \cdot K^{-1}$. Q_{in} represents the input heat transformed from laser energy absorbed by nanoparticles while Q_{out} represents the heat dissipation to the environment, they are expressed as:

$$Q_{in} = (I_0 - I_{tr})\eta \quad \text{(III. 6)}$$

$$Q_{out} = b(T_t - T_0) \quad \text{(III. 7)}$$

where I_0 is the incident laser power, I_{tr} is the power of laser that transmits through the solution. η is the light-to-heat conversion efficiency, T_t is the temperature of the nanoparticle solution during the irradiation measured by the thermocouple, the T_0 is the temperature of the environment, which is set to 25 °C, and b is the constant rate of heat dissipation from the nanoparticle solution to the environment, which can be measured by the decrease temperature profile after irradiation (**Figure.III.15. c**). Finally, we can obtain the relation between the variation of temperature of solution and irradiation time as:

$$\Delta T = A\left(1 - e^{-bt}\right) \quad \text{(III. 8)}$$

with

$$A = \frac{I_0(1-10^{-O.D.})}{m_{solution}C_{solution}b}\eta \qquad (III.9)$$

therefore, by fitting the temperature elevation profile with Equation (III.8), we can get the value A of each sample, and eventually calculate the light-to-heat conversion efficiency η (**Figure.III.15. d**).

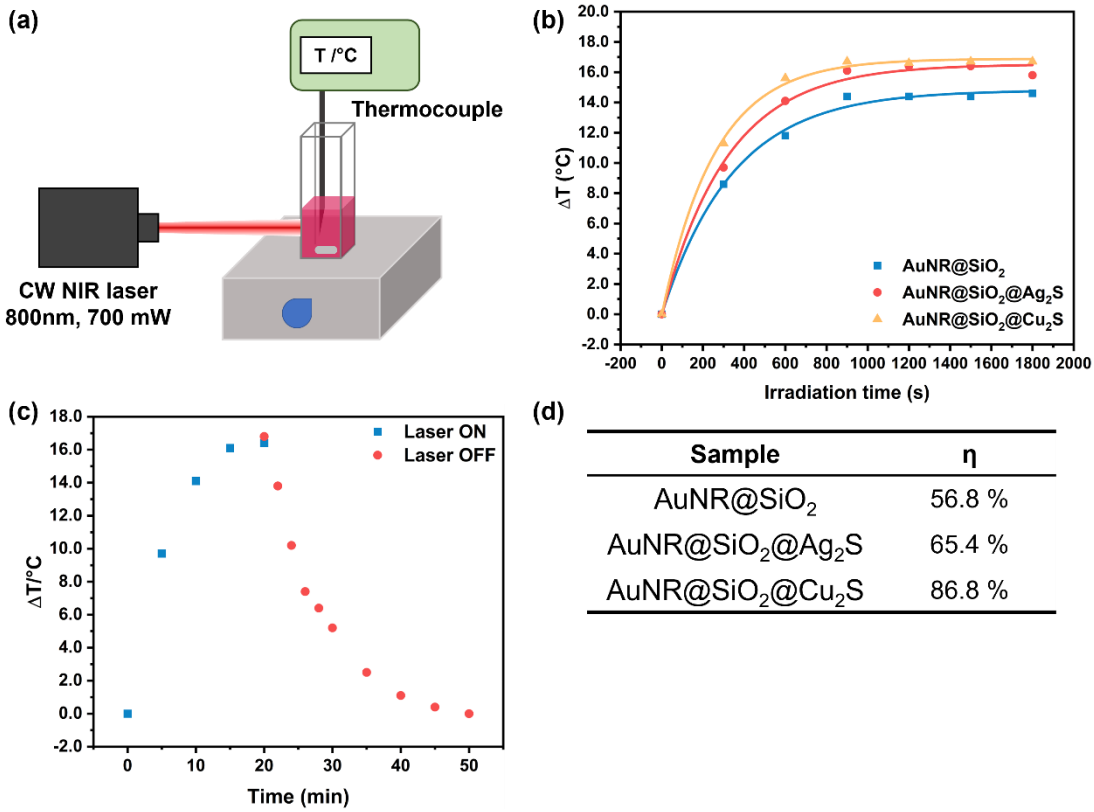

Sample	η
$AuNR@SiO_2$	56.8 %
$AuNR@SiO_2@Ag_2S$	65.4 %
$AuNR@SiO_2@Cu_2S$	86.8 %

Figure.III.15. (a). Schematic illustration of experimental setup for measuring temperature of nanoparticle solution. (b). Temperature evolution of nanoparticle solution under irradiation and the corresponding fitting curves. (c). Temperature evolution of $AuNR@SiO_2@Ag_2S$ nanoparticle solution under and after irradiation. (d). calculated light-to-heat conversion efficiency of different nanoparticles.

Eventually, for nanoparticles without coupling with semiconductors ($AuNR@SiO_2$) the light-to-heat conversion efficiency is 57±10%. This efficiency is in accordance with the values reported in the literature for AuNRs of similar size[160]. In comparison, nanoparticles coupled with semiconductors show a higher light-to-heat conversion efficiency, with 65±10% for $AuNR@SiO_2@Ag_2S$ and 87±10% for $AuNR@SiO_2@Cu_2S$. The findings suggest that in the AuNR/semiconductor hybrid nanostructure, a significant portion of the absorbed light energy is dissipated as heat instead of being utilized for photochemical reactions. Furthermore, it is observed that the coupling of AuNRs with semiconductors leads to a higher efficiency of converting light into heat compared to AuNRs without semiconductors. Taking into account the direct light absorption by Cu_2S and the thermal photoconversion efficiency of Cu_2S nanoparticles alone (measured at 90±10%), we can estimate that the energy transfer efficiency is on the order of 80±20%. This implies that despite the majority of the transferred energy being transformed into heat, the energy transfer process within these hybrid nanostructures is effective.

III.4. Conclusion and perspectives

In this chapter, our objective was to combine AuNRs with semiconductors that have a band gap energy overlapping the longitudinal plasmon absorption band of AuNRs. The aim was to enable the transfer of light energy absorbed by AuNRs to the semiconductors through a dipole-dipole interaction. This energy transfer process would then excite electrons from the valence band to the conduction band of the semiconductors. The semiconductors selected for this purpose were Ag_2S and Cu_2S, both of which have a band gap energy of 1 – 2 eV, corresponding to the energy of a photon with wavelength at NIR region (700 – 1200 nm).

In our initial experiments, we synthesized core-shell nanoparticles consisting of AuNRs coated with Ag_2S semiconductor. However, when we put these nanoparticles to NIR laser irradiation, we observed that the direct combination of AuNRs with the semiconductor did not result in efficient production of hydroxyl radicals. We suppose that the low photoactivity is attributed to the quick back transfer of excited electrons from the conduction band of the semiconductors to the AuNRs, instead of participating in reactions with oxygen molecules, leading to a diminished photochemical response.

By introducing an insulating silica layer between AuNRs and semiconductors, the photoactivity of these AuNR@SiO_2@Ag_2S nanoparticles were successfully observed. Therefore, an insulator that separates AuNRs and semiconductors can effectively improve the amount of electrons available for photoreaction by suppressing the possible charge recombination. Besides, AuNR@SiO_2@Ag_2S nanoparticles possess a higher photoactivity than AuNR@SiO_2 nanoparticles, suggesting an effective energy transfer from AuNRs to semiconductors can eventually lead to production of hydroxyl radicals. Since AuNR@SiO_2@Ag_2S nanoparticles can be excited in NIR light region, they are a promissing candidate for photodynamic therapy.

We also synthesized a different heterostructure, AuNR@SiO_2@Cu_2S, and evaluated its photoactivity. However, the addition of Cu_2S to the AuNR@SiO_2 nanoparticles did not improve their photoactivity. In fact, by monitoring the temperature changes in the solution during irradiation, we observed that the presence of Cu_2S on the surface of AuNR@SiO_2 nanoparticles significantly increased the conversion efficiency of light to heat. This suggests that a majority of the energy stored in the excited electrons is dissipated as heat, rather than being utilized for photochemical reactions.

Based on these results, a possible energy transfer pathway is explored to utilize plasmon energy with the AuNR/semiconductor hybrid nanostructure. To further improve the efficiency in utilizing plasmon energy for ROS production, several factors that are not be discussed in this project could be tested and improved.

To begin with, the thickness of insulator layer can be optimized. Simulation of the electromagnetic field distribution surrounding the AuNRs has been performed via Discrete Dipole Approximation using the ddscat software developed by Draine et al.[161]. As shown in **Figure.III.16**, at the plasmon resonance frequency, the localized electric field exponentially decreases from the surface of the AuNRs, with over 50% of loss at approximately 5 nm of distance. Therefore, a thick insulator layer may cause a diminished energy transfer capacity. On the other hand, if the insulator layer is too thin, the electron-hole recombination may not be sufficiently avoided.

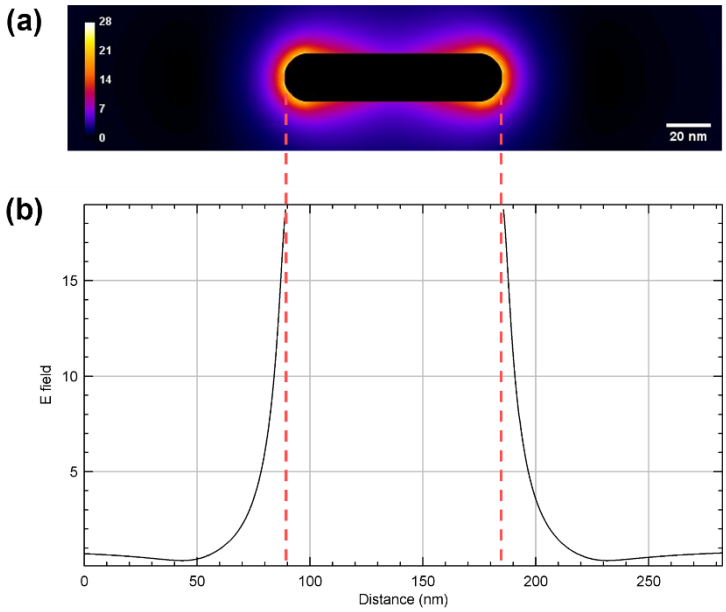

Figure.III.16. (a). Simulated electric near field of around an AuNR (90 * 20 nm²); (b). Corresponding electric field intensity a function of distance plotted from simulation.

Next, the band gap energy of semiconductor is crucial in this energy transfer process. First of all, a maximized energy overlap with the plasmon absorbance band of AuNR ensures an optimal energy transfer efficiency. Secondly, electrons excited to the conduction band should possess a redox potential higher enough to reduce oxygen molecules. The band gap energy depends on the size and composition of the semiconductor, and fine-tuning these parameters or exploring alternative semiconductors can potentially improve the quantum yield of AuNR/semiconductor nanoparticles.

Finally, the surface of AuNR/semiconductor nanoparticles should be optimized to enhance photocatalytic activity. Ligands are necessary for colloidal stability, but bulky ligands can hinder the contact between electrons and oxygen molecules, thus inhibiting photochemical reactions. Moreover, certain functional groups, particularly electron-withdrawing groups, on the ligands may react with electrons or produced radicals, leading to a lower efficiency of ROS production. Therefore, careful selection and modification of ligands is important to improve the ROS production efficiency and overall photocatalytic activity of AuNR/semiconductor nanoparticles.

Chapter IV. Interactions between polyzwitterion functionalized nanoparticles and macrophages

Résumé

Dans ce chapitre, notre recherche s'oriente vers la fonctionnalisation de surface de nanoparticules inorganiques, plus précisément les quantum dots (QDs), les nanoparticules d'oxyde de fer (IONPs) et les nanobâtonnets d'or (AuNRs), avec des ligands polyzwitterioniques. Nous visons à améliorer la stabilité colloïdale de ces nanoparticules dans les environnements physiologiques et à prolonger leur temps de circulation sanguine. Pour ce faire, en nous basant sur les travaux précédemment réalisés en laboratoire, nous avons développé des méthodes pour fonctionnaliser chaque type de nanoparticule avec des polymères de zwitterions, et avons étudié leurs propriétés physico-chimiques. Nous examinons ensuite l'interaction entre les nanoparticules fonctionnalisées et les macrophages ou les cellules cancéreuses *in vitro*, en utilisant diverses techniques d'analyse telles que la microscopie de fluorescence, la cytométrie en flux et la spectrométrie de masse à plasma couplé par induction (ICP-MS). Nos résultats révèlent que les macrophages présentent une efficacité plus élevée pour capturer des nanoparticules par rapport à d'autres types de cellules. L'interaction entre les ligands polymères et les macrophages est identifiée comme le principal mécanisme responsable de la reconnaissance et de la capture des nanoparticules. De plus, nous observons que la composition des monomères de zwitterion dans les ligands influence le taux de capture des nanoparticules par les macrophages. Dans certains cas, l'introduction de ligands polymères libres dans le système entre en compétition avec la capture des nanoparticules par les macrophages, entraînant une réduction des taux de capture. Pour valider nos résultats *in vitro*, nous menons des expériences *in vivo* en utilisant des AuNRs fonctionnalisés avec des polyzwitterions pour étudier leur cinétique de circulation sanguine et leur biodistribution. Les résultats obtenus à partir de ces expériences *in vivo* concordent avec les observations de nos études *in vitro*. Dans l'ensemble, ce chapitre offre un aperçu de la fonctionnalisation de surface de nanoparticules inorganiques avec des ligands polyzwitterioniques et met en lumière leurs interactions avec les macrophages, en soulignant l'impact de la composition des ligands et le potentiel de modulation de la capture des nanoparticules.

Abstract

In this chapter, our research focuses on the surface functionalization of inorganic nanoparticles, specifically quantum dots (QDs), iron oxide nanoparticles (IONPs), and gold nanorods (AuNRs), with polyzwitterion ligands. We aim to improve the colloidal stability of these nanoparticles in physiological environments and extend their blood circulation time. To achieve this, based on the previous work done in the laboratory, we developed methods to functionalize each type of nanoparticle with polyzwitterion polymers, and investigated their physicochemical properties. We then examine the interaction between the functionalized nanoparticles and macrophages or cancer cells *in vitro*, utilizing various analysis techniques such as fluorescence microscopy, flow cytometry, and inductively coupled plasma mass spectrometry (ICP-MS). Our findings reveal that macrophages exhibit higher efficiency in capturing nanoparticles compared to other cell types. The interaction between the polymer ligands and macrophages is identified as the main mechanism responsible for nanoparticle recognition and capture. Additionally, we observe that the composition of zwitterion monomers in the ligands influences the uptake rate of nanoparticles by macrophages. Furthermore, the introduction of free polymer ligands into the system competes with nanoparticle uptake by macrophages, resulting in a reduction of uptake rates. To validate our *in vitro* findings, we conduct *in vivo* experiments using polyzwitterion-functionalized AuNRs to investigate their blood circulation kinetics and biodistribution. The results obtained from these *in vivo* experiments align with the observations from our *in vitro* studies. Overall, this chapter provides insights into the surface functionalization of inorganic nanoparticles with polyzwitterion ligands and sheds light on their interactions with macrophages, highlighting the impact of ligand composition and the potential for modulating nanoparticle uptake.

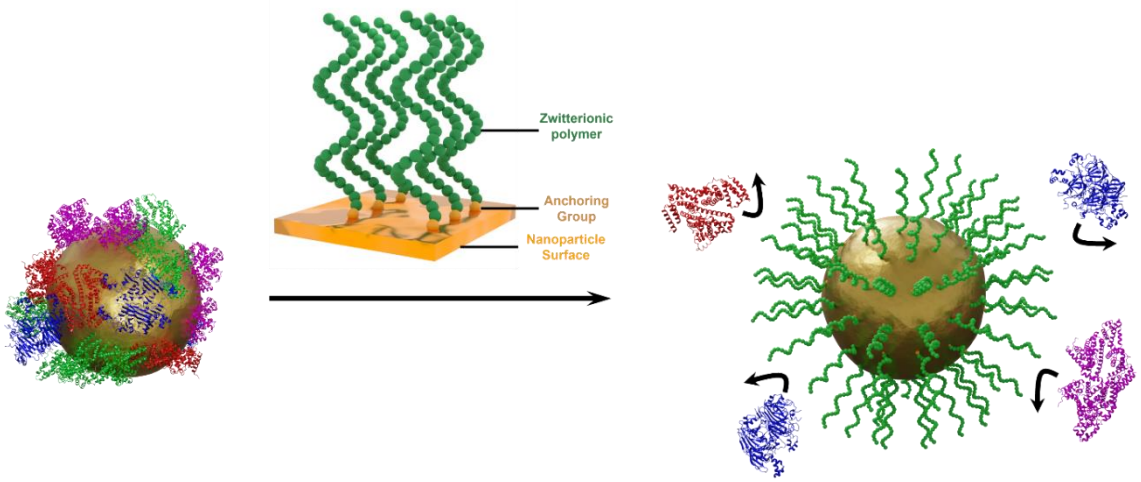

Figure.IV.1. Utilization of hydrophilic polyzwitterions to functionalize the surface of inorganic nanoparticles for the purpose of avoiding protein adsorption during blood circulation.

The first two chapters are focused on the phototherapy assisted by gold/semiconductor nanoparticles. Same as any other inorganic nanoparticles used for imaging and therapy *in vivo*, these hybrid nanoparticles would eventually be applied in a physiological environment. Therefore, understanding and controlling the interactions between these nanoparticles with the complex biological environment is crucial for an optimized distribution and functionality of nanoparticles *in vivo*, this, however, currently remains a challenge.

Typically, for *in vivo* applications, nanoparticles are administered by intravenous injection, then they are transported by the blood circulation. Ideally, nanoparticles are expected to reach the whole body through the blood circulation and accumulate at the target tumor zone. However, upon injection, the nanoparticles start to interact with a wide range of biomolecules such as lipids, peptides, and proteins, leading to nonspecific and complex interactions with the nanoparticle surface. These interactions play a crucial role in determining the fate of the nanoparticles and can have significant adverse effects, including nanoparticle agglomeration and rapid uptake by immune cells. As a result, their ability to reach the target tissue is drastically impaired. In the literature, it is reported that the dose of injected nanoparticles that can eventually reach the tumor zone is only about 0.7%, a median value[162]. Consequently, imaging or therapeutic capabilities of nanoparticles are greatly hindered.

In our laboratory LPEM, we have previously developed polymer ligands based on betaine zwitterions[163–165] for QDs and IONPs. Debayle et al. showed that the nature of the zwitterion influences the non-specific interaction with proteins. Here, we will investigate the interaction of the different nanoparticles coated with different zwitterions and macrophage cells in culture and see if there is a correlation between *in vitro* and *in vivo* behaviors.

In this section, we will first provide an introductory overview that includes the nature of nanoparticle surfaces, where a variety of interactions occur, as well as different strategies employed to enhance the biodistribution of nanoparticles. It is important to note that the scope of nanoparticles discussed in this chapter is not limited to plasmonic gold nanoparticles. Rather, we will expand the topic to encompass a broader range of inorganic nanocrystals commonly used in biomedical applications, such as IONPs and semiconductor QDs, in order to test the possible role of the composition of the inorganic NP on their interaction with macrophages.

Following the introduction, we will discuss the surface functionalization strategies applied to each type of nanoparticles, along with the physical and chemical characterizations conducted on the nanoparticles after their functionalization with polyzwitterions.

To assess the anti-fouling properties of these polyzwitterion-capped nanoparticles, we will present a series of experiments conducted *in vitro* and *in vivo*. Our focus will primarily be on examining the uptake of nanoparticles by macrophages during their incubation *in vitro*. We will then conduct pharmacokinetics studies to see if trends observed *in vitro* on macrophage uptake correlate with *in vivo* blood circulation time of nanoparticles after intravenous administration.

IV.1. Introduction of Nano/bio interface

When nanoparticles enter the biological environment, at their surface exists a layer composed of various organic molecules which contacts and interacts with various substances. The influences of these interactions can be classified into categories: (1) interactions that affect the colloidal stability, which describes the aggregation and dispersion behavior of nanoparticles; or (2) interactions that induce

the adsorption of biomolecules especially proteins at the surface of nanoparticles. The formation of protein corona at the surface is responsible for the uptake of nanoparticles by immune cells.

IV.1.1. Colloidal stability of nanoparticles

In aqueous solution, the colloidal stability of charged nanoparticles can be described by the Derjaguin–Landau–Verwey–Overbeek (DLVO) theory[166]. According to the DLVO theory, the interparticle interaction in a liquid system can be divided into two main components: the electrostatic repulsion and the Van der Waals attraction:

$$G = G_{van\ der\ Waals} + G_{electrostatic} \quad (\mathrm{IV}.1)$$

where G is the total free energy of interparticle interaction. The electrostatic repulsion prevents particles from coming too close to each other due to the electrostatic forces of the charged surfaces, therefore, the $G_{electrostatic}$ is usually positive. A higher surface charge at the surface will increase the electrostatic repulsion while a high concentration of electrolyte in the system can screen these surface charge and thus decreases this repulsive force. On the other hand, the Van der Waals attraction arises from the fluctuations in electron distribution within the particles, leading to temporary dipole moments. These temporary dipoles induce attractive forces between the particles, which can lead to their aggregation and thus $G_{van\ der\ Waals}$ is always negative. Finally, the stability of colloidal systems depends on the balance between the repulsive electrostatic forces and the attractive Van der Waals forces. If the repulsion dominates ($G > 0$), the particles remain dispersed and stable. If the attraction dominates ($G < 0$), particle aggregation and flocculation can occur.

Furthermore, surface functionalization introduces additional factors to the interparticle interaction. In the case of polymer-functionalized nanoparticles, the polymer ligands on the nanoparticle surface contribute to the interparticle forces, including steric repulsion and hydration force, in addition to electrostatic repulsion and van der Waals attraction. When two polymer-covered surfaces come close to each other, they experience a repulsive force once the polymer ligands start to overlap. This so-called steric repulsion is attributed to the fact that, in a good solvent, the polymer ligands always adopt a stretched conformation that is entropically favorable and is resistant to compression. Conversely, in a poor solvent, these polymer ligands tend to collapse and van der Waals force dominates, leading to aggregation of nanoparticles[167]. Additionally, when the polymer ligands are electrically charged or are highly hydrophilic, water molecules tend to form a quasi-discrete layer at the vicinity of the polymer layer. This organized and oriented water layer give rise to a repulsive force, namely, hydration force[168]. This repulsive hydration force can be enhanced by the addition of electrolyte, which reduce the net charge on the surfaces but also lead to the formation of additional ion pairs. The presence of ion pairs with dipole moments polarizes the surrounding water molecules, resulting in the induction of a hydration force[169]. Since either steric effect or hydration force contributes to the repulsion force in interparticle interaction, the functionalization of nanoparticle surface with adequate polymer ligands can improve the colloidal stability of nanoparticles in biological environment.

IV.1.2. Protein corona

Blood contains a wide variety of proteins that play crucial roles in various physiological functions. Once intravenously injected, nanoparticles begin to interact with these proteins during their entire blood circulation process. Proteins can interact with the surface of nanoparticles if the ligand coating is loose or not dense enough to prevent protein access. Additionally, proteins can interact with the surface chemistry coating through hydrophobic, electrostatic, or hydrogen bonding interactions. The strength of the interaction between nanoparticles and proteins depends on their respective chemical and

physical properties. Proteins that are weakly bound exhibit a dynamic equilibrium between bound and unbound states, forming what is known as the "soft corona." In contrast, proteins that are strongly bound and resist washing and purification procedures form the "hard corona." (**Figure.IV.2**) This protein corona plays a major role in the biological fate of the nanoparticles, as it determines the interaction of nanoparticle with other biomolecules and cells[170,171].

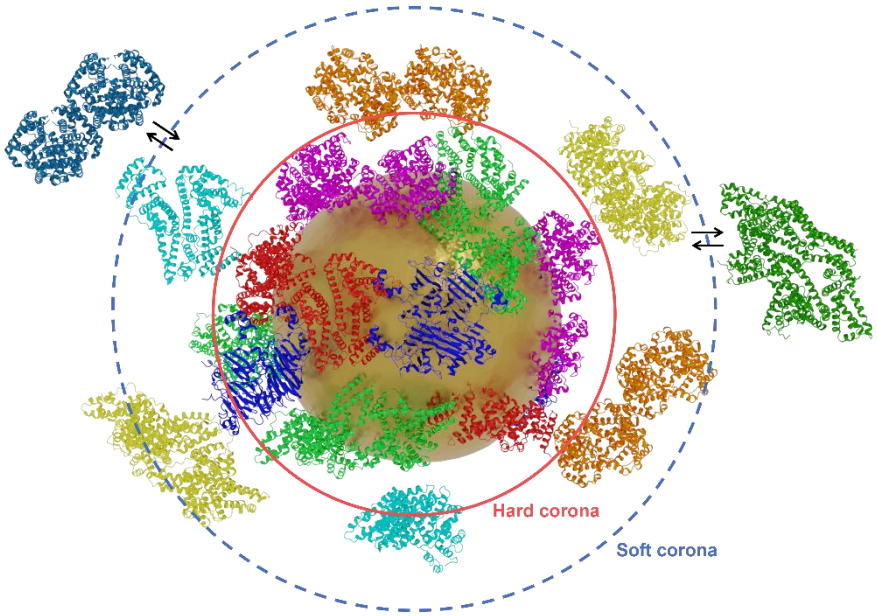

Figure.IV.2. Schematic illustration of a nanoparticle surrounded by surface organic ligands and coated with a combination of strongly bound proteins, forming the hard corona (inside red circle), and weakly bound proteins that are in equilibrium with proteins present in the surrounding solution, forming the soft corona (between red and blue circles).

The composition of the protein corona is dynamic and undergoes changes over time, a phenomenon referred to as the Vroman effect[172]. Initially, proteins that are more concentrated and/or diffuse faster tend to access the surface of the nanoparticle first, forming the initial protein corona. However, these proteins may subsequently be replaced by proteins with higher affinities, which are more stably anchored on the nanoparticle surface. When a protein is anchored on the surface of a nanoparticle, it can undergo conformational changes to optimize its interaction with the nanoparticle. This denaturation process may expose previously hidden hydrophobic segments, which can then interact with other proteins or the nanoparticle surface. These conformational changes can result in the formation of stronger protein-protein interactions, leading to cooperative nanoparticle-protein and protein-protein interactions, the formation of protein multilayers, or even nanoparticle aggregation. The structure of the nanoparticle-protein complexes is also influenced by the relative and absolute concentrations of nanoparticles and proteins. If a protein is present in large excess, strong interactions between the nanoparticle and the protein can lead to the formation of a nanoparticle surrounded by a protein corona. However, when the concentration of these proteins is low, they may bind to multiple nanoparticles, resulting in the formation of large nanoparticle clusters coexisting with protein-free nanoparticles. The presence of the protein corona significantly impacts the physicochemical and colloidal properties of the nanoparticles. It can alter their colloidal stability, hydrodynamic size, and zeta potential, thereby influencing their behavior in biological systems[173].

IV.1.3. Recognition and uptake of nanoparticles by macrophages

During the blood circulation, most nanoparticles are detected and captured by phagocytic cells, known as the "eating cells" of the immune system. They filter the blood to remove debris, bacteria, viruses, or foreign particles from the body. The main cells involved in the detection and capture of nanoparticles are macrophages, phagocytic cells located in the tissues, interacting with nanoparticles injected in bloodstream. The most important population of macrophages is the Kupffer cells, located in the liver. There are also macrophages in the spleen, lymph nodes, and all tissues. Liver and spleen macrophages are primarily responsible for the detection and capture of nanoparticles[174]. They are attached to the walls of blood vessels in these organs. The capture of nanoparticles by macrophages prevents them from reaching the desired target organ or the tumor. A critical parameter for nanoparticles to reach their target is their circulation time in the bloodstream. The longer the circulation time, the higher the chances for nanoparticles to reach their target. Therefore, increasing this circulation time is a major goal in nanomedicine. To achieve this, it is necessary to understand the phenomena that cause the capture of nanoparticles by macrophages.

The macrophages can detect nanoparticles by their size and shape, but more commonly through the surrounding protein corona[175,176]. The protein corona may contain certain types of so called opsonin protein (immunoglobulins, complement proteins, and blood clotting factors) that are bound to the nanoparticle surface and can be recognized by macrophages. The clearance of these recognized nanoparticles by macrophages is quite efficient: up to 95% of nanoparticles can be finally captured regardless of nanoparticle nature[177]. There are several mechanisms explaining the recognition and internalization of nanoparticles by macrophages, as shown in **Figure.IV.3**: the phagocytosis (d), the macropinocytosis (e) and the endocytosis with (a, b) or without (c) receptor.

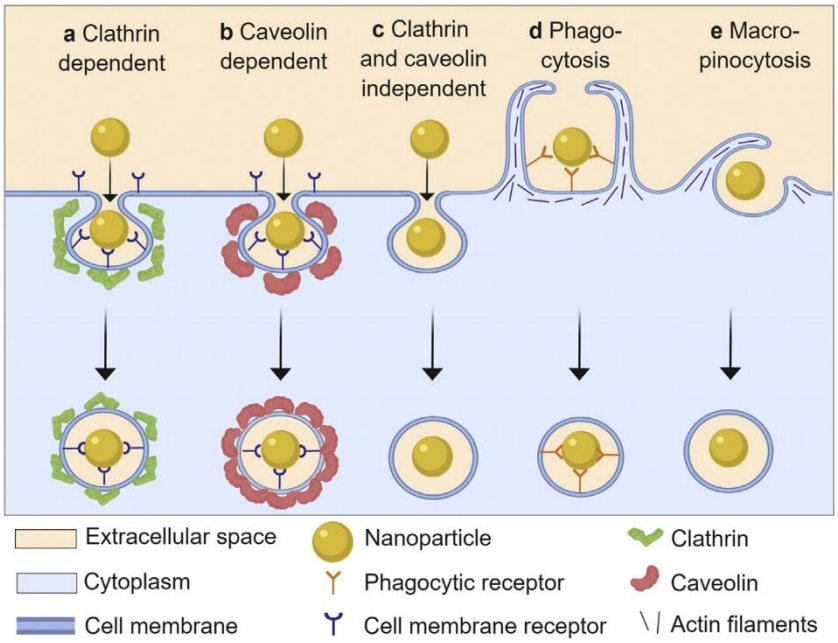

Figure.IV.3. Schematic overview of nanoparticle uptake pathways via endocytosis. Multiple different pathways exist for cellular entry of nanoparticles via endocytosis mechanisms: (a) clathrin- dependent; (b) caveolin-dependent; (c) clathrin- and caveolin-independent; (d) phagocytosis; and (e) micropinocytosis pathways[178].

Phagocytosis is the process by which a cell engulfs a large solid object, such as a bacterium, that has been marked by opsonins. Macropinocytosis is non-specific, where the cell engulfs a volume

of the surrounding fluid, which forms a vesicle, followed by total internalization. Endocytosis can be triggered by receptors or by the activation of lipid rafts. In this latter case, it is referred to as receptor-independent endocytosis. In receptor-mediated endocytosis, a vesicle is formed following the activation of membrane receptors. The vesicle can be formed with the help of clathrin or caveolin proteins[179]. Nanoparticles interact with several receptors on the surface of macrophages, including scavenger receptors that recognize low-density lipoproteins, Fc receptors that bind to antibodies, complement receptors that recognize complement proteins, as well as sugar receptors such as mannose and galactose, and folate receptors like vitamin B9. It has been suggested that Fc and mannose receptors may play a more important role in particle uptake process than the others[180].

The uptake effectiveness of liver macrophages is also due to their strategic position: on the walls of liver microcapillaries. The microcapillary system allows for a large surface area of contact between the blood and the vessel wall, where macrophages are located. Additionally, blood flow slows down in these microcapillaries, increasing the contact time of nanoparticles in the blood with macrophages. These two phenomena enable macrophages to detect and capture a significant proportion of nanoparticles[181]. Moreover, the recognition of foreign materials can locally activate tissue-resident macrophages, which are normally quiescent. This activation provokes the rearrangement of their surface receptors, making them even more sensitive to nanoparticles and resulting in accelerated internalization and clearance rates[180].

IV.1.4. Strategies used to prolong the blood circulation time of nanoparticles

To extend the blood circulation time of nanoparticles, it is important to reduce the recognition and uptake of nanoparticles by the macrophages. Up to now, several techniques have been developed to overcome this challenge.

Firstly, in most cases, nanoparticles circulating in the bloodstream are coated with a protein corona, therefore, the chances for macrophage surface receptors to interact with the adsorbed proteins are higher than with the bare nanoparticle surface. Opsonin proteins, which have suitable electrostatic or conformational properties for specific cell receptor recognition, can significantly enhance and accelerate nanoparticle uptake and clearance. On the other hand, in some cases, adsorbed proteins known as "dysopsonins" can mask the materials from surface recognition, providing a "bioinvisibility" or stealth effect to nanomaterials[182]. Therefore, one can modulate the composition of protein corona formed at the surface of nanoparticles to avoid the capture of macrophages by excluding the opsonins and favoring the dysopsonins. For example, in various studies, it has been observed that apolipoproteins can coat nanoparticles (NPs) and act as a masking layer, preventing their cellular uptake. For instance, when PEGylated NPs are incubated in serum, they can become coated with different proteins, including apolipoprotein J or clusterin. The presence of these proteins on the NP surface has been found to significantly decrease their uptake by macrophages[183].

Secondly, another possible way to reduce nanoparticle recognition and elimination by macrophages is to saturate the clearance capacity of the macrophage. For instance, in a study where a trillion gold nanoparticles were systematically injected into mice, a dose that surpasses the capacity of Kupffer cells in the liver, there was a significant decrease in nanoparticle clearance. As a result, up to 12% of the injected nanoparticles successfully reached tumor cells[184]. Similarly, instead of saturating macrophages with overdosed nanoparticles, an alternative approach is to stimulate the macrophage to enhance the clearance of the body's own intact blood cells, such as erythrocytes, by injecting allogeneic

anti-erythrocyte antibodies, resulting in the nanoparticle clearance blockade[185]. However, this strategy may have several possible inconveniences. The higher dose of nanoparticles that is needed to saturate the macrophages could provoke side effects or toxicity for *in vivo* applications. Besides, the long-term effect on organs or immune systems induced by this macrophage saturation strategy is still not clear and need to be studied.

In addition, nanoparticles can be encapsulated within red blood cells, taking advantage of the biocompatible nature of the red blood cell membrane. This encapsulation allows the nanoparticles to be concealed from macrophage detection, and this strategy is commonly referred to as "cell hitchhiking"[186].

Furthermore, macrophages possess signaling pathways that inhibit the phagocytosis of cells expressing the membrane protein CD47. CD47 acts as a "marker of self," with which a cell signals its identity to macrophages and prevents clearance from the bloodstream. Leveraging this natural mechanism, nanoparticles functionalized with a minimal CD47-based "self" peptide exhibit prolonged circulation compared to non-functionalized nanoparticles[187].

Despite the development of various strategies over the past years to prolong the blood circulation time of injected nanoparticles, very few methods have demonstrated sufficient effectiveness. This may be due to the fact that macrophage uptake is still too high for clinical use or because the toxicity and adverse effects associated with these methods are significant and cannot be overlooked.

IV.1.5. Surface functionalization of nanoparticles by hydrophilic ligands

The strategy we will adopt to overcome the aforementioned challenges is to limit and eventually eliminate the interaction between the nanoparticle surface and opsonin proteins. Macrophages primarily recognize nanoparticles through the protein corona, so by preventing the formation of a protein corona on the nanoparticle surface and by limiting interactions between nanoparticles and biomolecules, we could render these nanoparticles "invisible" to macrophages and ultimately prolong their circulation time in the bloodstream. Achieving this would require carefully designed surface ligands to coat the nanoparticles.

Polymer ligands on the nanoparticle surface must fulfill two primary requirements. Firstly, the polymer ligands should react with the nanoparticle surface to form stable covalent or complex bonds, ensuring a strong attachment of the ligands to the nanoparticle surface and preventing the loss of surface functionalization during circulation in the bloodstream. Secondly, the polymer ligands need to be hydrophilic to promote good water solubility of the nanoparticles in physiological environments. Therefore, a typical polymer ligand consists of two parts: an anchoring group and a hydrophilic group.

a. Anchoring group

The type of anchoring group used in polymer ligands should be adapted according to the nature of nanoparticle surface. Several most frequently used anchoring groups are listed in **Table.IV.1**, along with their appliable nanoparticles. In general, for IONPs, anchoring groups such as phosphonate, carboxylate can react covalently with the hydroxyl groups present at the surface of nanoparticles, the formed P(C) – O – Fe bond are stable in most of the physiological environment. And for QDs and gold nanoparticles, thiolates are almost the most popular anchoring groups utilized for the good stability of formed Zn-S or Au-S covalent bonds.

Table.IV.1. Name, structure and material compatibility of the main anchoring function using in the surface chemistry of nanoparticles (NPs)[173].

Name	Structure	Applicability
Carboxylate		Iron Oxide NPs
Phosphonate		Iron Oxide NPs
Thiol/thiolate	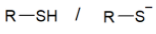	AuNPs, QDs
Imidazole		QDs
Catechol	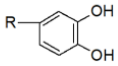	Iron Oxide NPs
Aryldiazonium	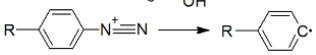	AuNPs
N-heterocyclic carbene	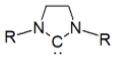	AuNPs
Silane	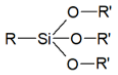	All NPs

The affinity between the anchoring groups and the nanoparticle surface is indeed a crucial factor for successfully immobilizing polymer ligands on the nanoparticle surface. However, it is important to consider other parameters as well. One such parameter is the multiplication of anchoring groups within a single polymer chain, which can lead to improved functionalization outcomes including higher ligand exchange efficiency and enhanced stability of the graft. For example, multiplication of thiol groups in the same polymer molecule is found to increase the ligand stability and limit the desorption of ligands *in vivo* in cases of both QDs[188–191] and gold nanoparticles[192]. Additionally, the anchoring groups can also influence the physical and chemical properties of nanoparticles. Anchoring groups containing carboxylates such as citric acid, can efficiently bind to the surface of IONPs, while these carboxylate groups are reported to reduce the relaxivity and saturation magnetization of IONPs, thereby making them less interesting for applications[193]. The conditions of ligand exchange process should also be considered when choosing appropriate anchoring groups. Thiolate groups are found to be inactive in acid conditions and are prone to be oxidized, resulting in their loss of affinity to the nanoparticles[194].

b. Hydrophilic group

The hydrophilic groups consist of monomers with high polarity. They enhance solubility of nanoparticles in the aqueous solution. As previously mentioned, to maintain the colloidal stability of nanoparticles and prevent aggregations, the surface ligands should be capable of enhancing repulsive interparticle interactions either via electrostatic force, steric effect or hydration force to counteract the attractive van der Waals force.

Charged groups such as carboxylate groups in citrate acid molecules can provide repulsive electrostatic repulsion for nanoparticles in low salinity aqueous solution. Therefore, citrate ligands are widely used to functionalize the surface of gold and IONPs. However, the high salinity of physiological media provides counterions to screen this repulsion, making it ineffective. Additionally, pH changes can alter the charge of the ligands based on the pKa of the ionizable groups. Furthermore, charged

nanoparticles are more prone to nonspecific interactions with proteins, result in even more rapid protein corona formation at the surface of functionalized nanoparticles than non-functionalized nanoparticles. Therefore, it is preferable for nanoparticles to remain overall neutral to avoid these nonspecific interactions.

Polyethylene glycol (PEG) is a group of polymers consisting of ethylene glycol monomers (-O-CH_2-CH_2-O-) with different molecular weights. It is widely used as a stabilizing ligand for inorganic nanoparticles in biological media. PEG ligands can stabilize nanoparticles in aqueous solution due to the steric effect. Besides, the partial negative charge located on the oxygen atoms of ethylene glycol monomers attract the partially positively charged hydrogen atoms from water, which enhances the water solubility of PEG ligands[195]. Thanks to its hydrophilic nature, when PEG is grafted onto the surface of inorganic nanoparticles, it forms a hydrated cloud due to interactions with surrounding water molecules via hydrogen bond. This cloud prevents the aggregation of nanoparticles and reduces the adsorption of proteins onto their surface[196]. The molecular weight of PEG is considered a crucial factor in determining the effectiveness of the PEGylation layer in preventing protein adsorption. A suitable range for achieving the desired antifouling property is typically between 1500 and 5000 Da. In addition to molecular weight, the surface density of the PEG layer plays a crucial role in preventing protein adsorption. As shown in **Figure.IV.4**, when the surface PEG density is low, individual PEG molecules do not overlap and tend to adopt a "mushroom" conformation. As the surface PEG density increases, adjacent PEG chains start to overlap and are compelled to extend away from the NP surface, resulting in a "brush" conformation[197]. The brush conformation is associated with a higher resistance to protein adsorption.

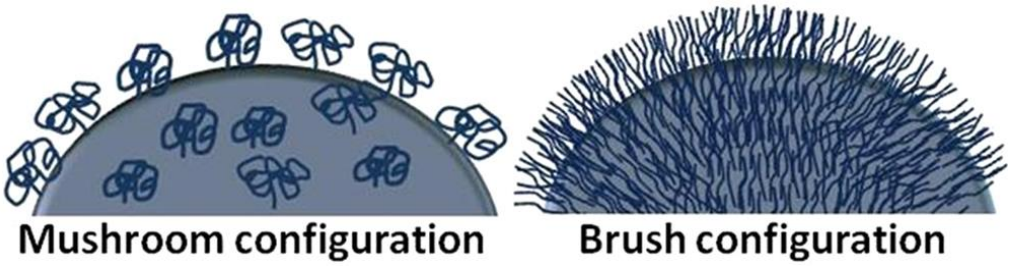

Figure.IV.4. Schematic illustration of the PEG configurations at low and high surface coverage densities[197].

Despite the anti-fouling properties of PEGylated NPs, it is important to note that the hydrophobic blocks present in PEGs, such as the backbone (-CH_2CH_2-) and methoxy terminal (-OCH_3), can still contribute to nonspecific interactions and potentially trigger an immune response. This immune response may result in the production of anti-PEG antibodies, which can impact the effectiveness of PEGylation and the overall stability of the NPs in biological systems[198]. As a consequence, repetitive injection of PEGylated nanoparticles can eventually lead to accelerated blood clearance as a result of their rapid recognition by these anti-PEG antibodies. This phenomenon can ultimately result in a poor biodistribution of the NPs within the body[199].

Apart from PEG ligands, other types of hydrophilic ligands that take advantage of steric effect to stabilize nanoparticles and offer anti-fouling properties, such as pHPMA, Peptoids and Dextran are also developed (**Figure.IV.5**)[200–202]. However, studies on these ligands are limited both in width and depth, compared to PEG ligands.

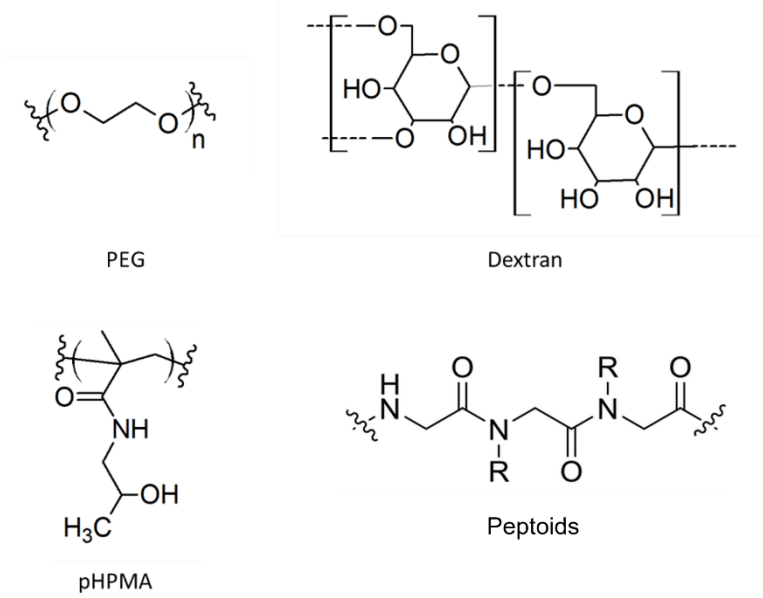

Figure.IV.5. Molecule structures of several representative hydrophile groups utilized in inorganic nanoparticle functionalization.

IV.1.6. Nanoparticle functionalized with zwitterionic polymers

Here, we aim to develop hydrophilic polymer ligands based on polyzwitterions, to functionalize the surface of nanoparticles. Zwitterion molecules consist of positively and negatively charged groups linked by a small alkyl chain. Consequently, despite the separated charged groups, the overall charge of a zwitterion molecule remains neutral. The most used three zwitterion molecules are sulfobetaines (SBs), carboxybetaines (CBs) and phosphorylcholine (PCs), as shown in **Figure.IV.6**. Each zwitterionic monomer contains a common quaternary ammonium cation group and a different anion group: SBs contain a sulfonate anion, CBs have a carboxylate anion, and PCs have a phosphonate anion. After polymerization, the polyzwitterions composed of SBs and CBs have anion groups distal to the backbone, while for PC based polyzwitterions, anion groups are at the proximal of backbone.

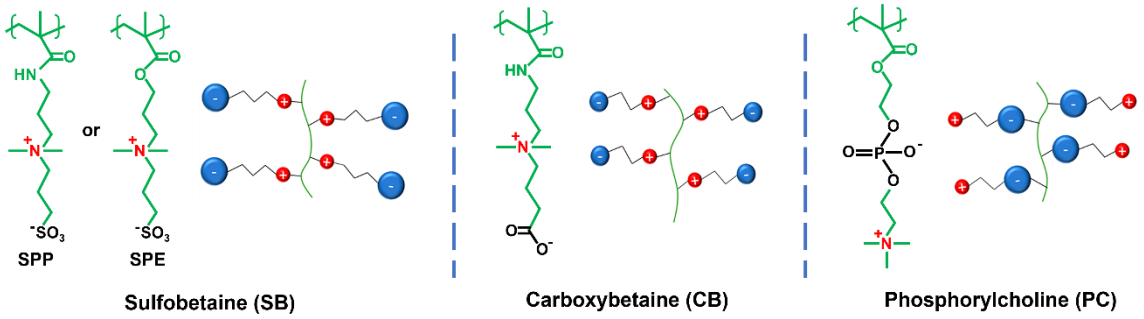

Figure.IV.6. molecular structures of three different polyzwitterions: polysulfobetaine (left), polycarboxybetaine (middle), polyphosphorylcholine (right)[203].

The separated positive and negative charges within the polyzwitterions form electrical dipole moments, which depends on the distance between opposite charges. Water molecules are attracted by these charged functional groups, forming a hydration shell surrounding the polyzwitterions. (**Figure.IV.7**) This hydration shell forms a barrier that prevents adsorption of biomolecules, and is responsible for the antifouling properties of polyzwitterions[204]. In contrast, the energy barrier provided

by PEG ligands is much lower since the hydration shell formed by PEG is based on hydrogen bond, a type of interaction weaker than ionic solvation. This hydration induced energy barrier is dependent on several factors such as molecular weight, surface density, chain conformation and concentration of electrolyte in the solution[205].

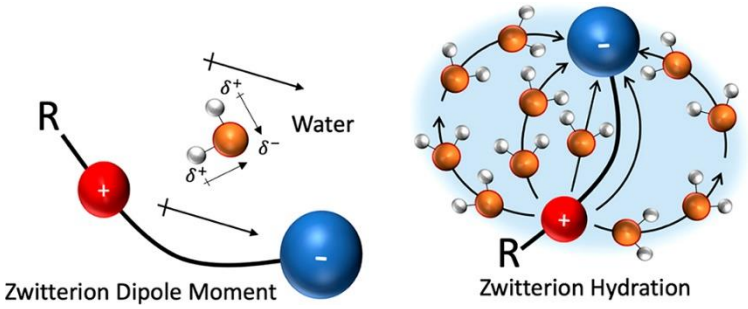

Figure.IV.7. Schematic illustration of zwitterion dipole moment arises from separated positive and negative charges (left). Alignment of water molecules around zwitterions under ionic solvation induced by zwitterionic molecule dipole moment (right)[203].

The physiological environment is known for its relatively high electrolyte concentration. In this context, polyzwitterions offer unique advantages due to their antipolyelectrolyte effect. Poly-zwitterions tend to adopt an expanded conformation in high salt concentration solutions (**Figure.IV.8**)[206]. Unlike other types of polymer ligands such as PEG and polyelectrolytes, which may aggregate in saline physiological environments, polyzwitterions demonstrate enhanced stability and solubility. Therefore, polyzwitterions are considered highly suitable for various biological applications.

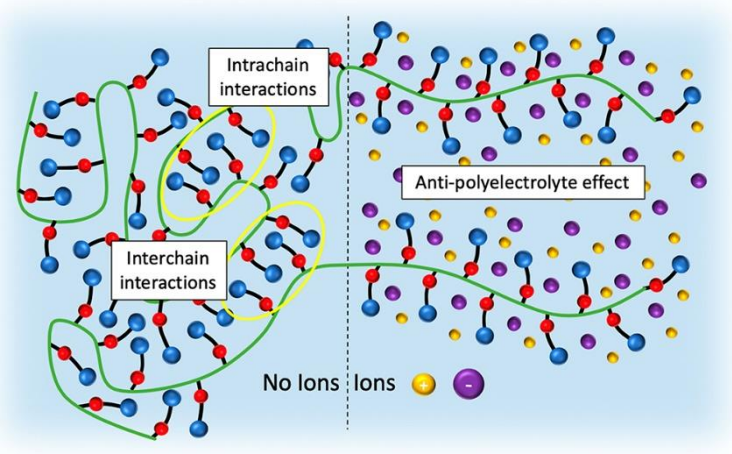

Figure.IV.8. Schematic illustration of antipolyelectrolyte effect within polyzwitterions. Left: without extra ions in the system, polyzwitterion chain tend to take a compressed conformation because of the inter- and intrachain dipole-dipole interactions. Right: in the presence of extra ions, the charged groups in the polyzwitterion chains are screened, reducing dipole-dipole interactions, favoring a stretch conformation[203].

In our laboratory, Debayle et al.[164] investigated the formation of hard and soft protein corona around QDs coated with SB, PC and CB polyzwitterion ligands in bovine serum albumin (BSA) solutions and in whole human serum. The albumin protein is considered as a main component in the hard protein corona due to its abundancy in human blood and affinity to nanoparticle surfaces. As shown in **Figure.IV.9**, they found a complete absence of protein corona on the surface of SB-coated nanoparticles, demonstrated by a undetectable BSA quantity at the surface of QDs (**Figure.IV.9. a (ii)**)

and a constant hydrodynamic radius of functionalized QDs in BSA solutions with various concentrations (**Figure.IV.9. a (iii)**), while PC- and CB-coated QDs undergo reversible BSA adsorption or partial aggregation. These results indicate that polyzwitterions have the potential to totally prohibit the protein corona formation and thus help nanoparticles evade detection and capture by macrophages. In particular, SB-based polyzwitterions could be the best antifouling candidate for nanoparticle functionalization.

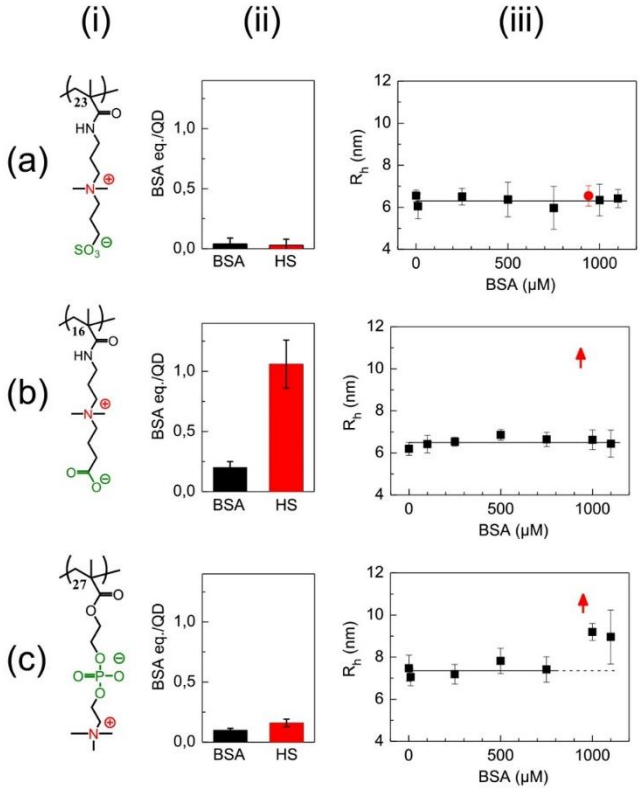

Figure.IV.9. Influence of polyzwitterions grafted on the surface of QDs on protein adsorption and cytoplasmic diffusion. From left to right, (i) structure of the SB (a), CB (b) and PC (c). (ii) Average number of BSA equivalents adsorbed per QD within the hard corona, determined by fluorescamine. (iii) QD hydrodynamic radius determined by fluorescence correlation spectroscopy (FCS) as a function of BSA (black squares) concentration and whole human serum (red circle, placed at 950 μM equivalent BSA concentration). Red arrows reflect an aggregation of the QDs[164].

Based on the favorable results obtained so far, indicating the potential of polyzwitterions for extending the blood circulation time of nanoparticles, our research in this chapter aims to further explore the use of SB-based polyzwitterions for functionalizing various types of nanoparticles. In addition to QDs, are polyzwitterions also capable of protecting other types of nanoparticles such as IONP and gold nanoparticles? How to design and adapt these polyzwitterionic ligands to optimize the surface functionalization on different nanoparticles? Can we further study the interactions between these functionalized nanoparticles and cells, particularly macrophages, to gain insights into the mechanisms underlying nanoparticle capture *in vivo*? Finally, is the *in vivo* blood circulation time correlated to observations of nanoparticle *in vitro* uptake by macrophages?

IV.2. Preparation of polyzwitterion coated nanoparticles

All three types of nanoparticles in our study are functionalized using sulfobetaine-based polyzwitterions. These block copolymer ligands consist of two blocks: a sulfobetaine block and a block of anchoring groups. (**Figure.IV.10**) Two different sulfobetaine monomer is utilized: the 3-[3-methacrylamidopropyl-(dimethyl)-ammonio]propane-1-sulfonate (SPP), and the [2-(methacryloyloxy)ethyl]dimethyl-(3-sulfopropyl)ammonium hydroxide (SPE). Specific choice of anchoring groups depends on the surface characteristics of the nanoparticles being targeted. For QDs, we utilize imidazole groups as anchoring groups in the polymer ligands[163,164]. These imidazole groups enable the strong attachment of the ligands to the QD surface. For IONPs, a block of phosphonate groups is integrated into the polymer ligands[165]. These phosphonate groups facilitate the stable attachment of the ligands to the surface of IONPs. For gold nanoparticles, thiol groups are employed as anchoring groups to graft the ligands onto the surface of the nanoparticles. Thiol groups have a strong affinity for gold surfaces, allowing for efficient and stable binding.

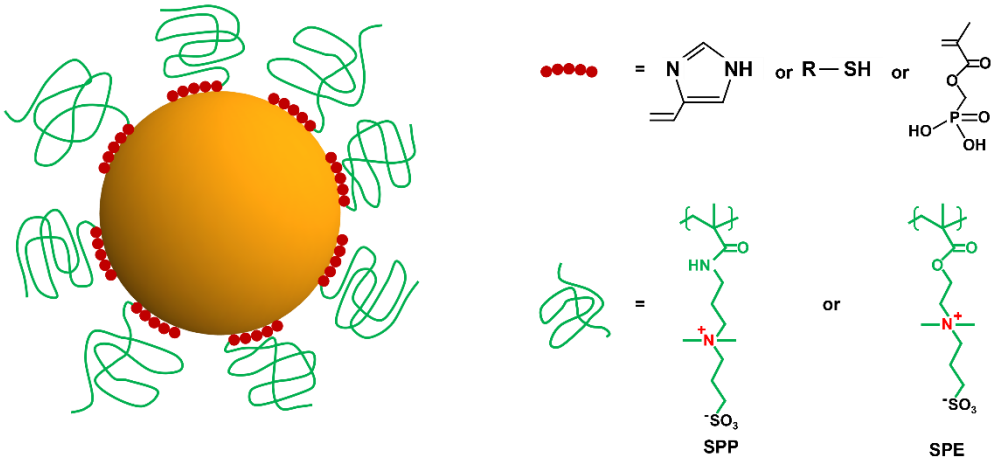

Figure.IV.10. Schematic illustration of polyzwitterions designed for nanoparticle functionalization.

The synthesis of these polymer ligands is carried out stepwise using a technique called Reversible Addition-Fragmentation Chain Transfer (RAFT) polymerization. (**Annex.V.7**. RAFT polymerization) This polymerization method enables precise control over the polymer chain length and composition, ensuring the desired structure and properties of the resulting polymer ligands.

In the following sections, we will begin by presenting the typical RAFT polymerization method used for preparing polyzwitterionic ligands. This polymerization technique serves as a general preparation approach for ligands that are applied to all the three types of nanoparticles (QDs, IONPs, AuNRs). We will then delve into the specific ligand preparation and functionalization strategies for each type of nanoparticle, which will include the integration of anchoring groups, the ligand exchange process, and purification methods. Additionally, we will present the physical and chemical characterizations performed on the functionalized nanoparticles to assess their properties and confirm successful functionalization.

IV.2.1. Synthesis of the poly(sulfobetaine)

Synthesis of poly(sulfobetaine) (pSPP):

To a round-bottomed flask of 250 mL, 3-[3-methacrylamidopropyl-(dimethyl)-ammonio]propane-1-sulfonate (SPP, 9.42 g, 32.4 mmol), and 2,2′-Azobis(2-methylpropionamidine) dihydrochloride (V50, 29.1 mg, 0.1 mmol) were added and dissolved in 150 mL of acetate buffer (pH = 5.2, 0.2 M). Then, to a 20 mL scintillation vial, 4-Cyano-4-(phenylcarbonothioylthio) pentanoic acid (CADB, 150 mg, 0.54 mmol) was added and dissolved in 4 mL NaOH (0.2 M), this resultant solution was rapidly added into the mixture of SPP and V50. The flask was then sealed and degassed under argon flux. After 30 min, the reactive mixture was heated to 70 °C with an oil bath and kept under stirring (400 rpm) for 4 h. The obtained polymer was precipitated in acetone, washed twice with diethyl ether, and finally dried overnight under vacuum.

Polyzwitterion ligands are prepared with the RAFT polymerization of sulfobetaine monomers. (**Figure.IV.11**) Since the zwitterionic monomers have a high polarity and so are the polyzwitterions, this polymerization should be carried out in highly polar solvents such as acetic acid or water, to ensure a good solubility of products. Whereas CADB has a low solubility in water at room temperature, a small quantity of NaOH solution is thus used to dissolve CADB in basic solution in prior to obtain a homogeneous dispersion in final mixture solution. The initiator is also chosen according to their solubility in water. 2,2′-Azobis(2-methylpropionitrile) (AIBN) is an initiator widely used in organic solvents, while in aqueous solution, the 2,2′-Azobis(2-methylpropionamidine) dihydrochloride (V50) exhibits a better solubility. The ratio of initiator and CTA is fixed at 1/5 for an efficient activation of polymerization and limit the number of activated polymer chains non controlled by CTAs.

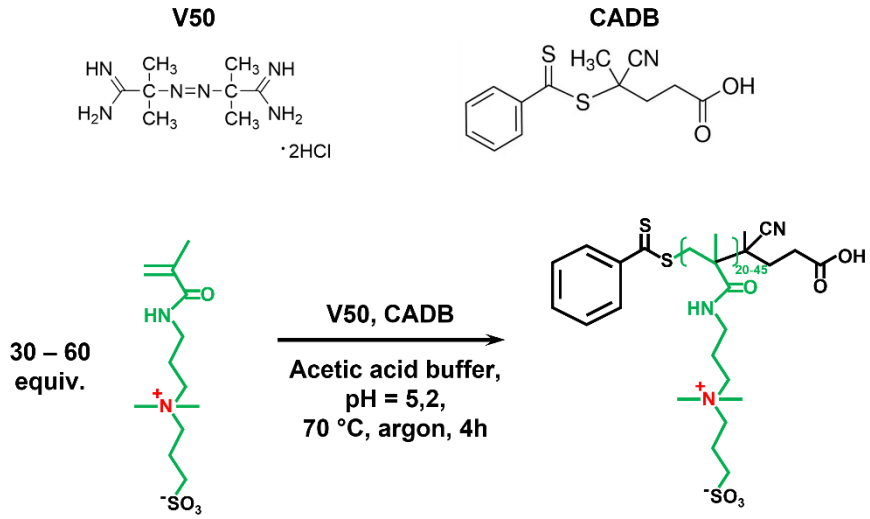

Figure.IV.11. A typical RAFT polymerization of sulfobetaine zwitterions.

The polymerization last for about 4h, a longer reaction time increases the risk of hydrolysis of the CTA groups at the end of polymer chain, resulting in the loss of control in the next polymerization step. A ^{1}H NMR spectrum is taken right after the polymerization, before the purification. As shown in **Figure.IV.12**, the pics at around 5.5 ppm represent alkene hydrogens of the non-reacted monomers. By comparing the integration of these alkene hydrogens with those of other pics in the monomers, we can

finally determine the polymerization yield. Typically, in the experiment shown in **Figure.IV.12**, 30% of monomers remain unreacted after polymerization, thus the yield of polymerization is of 70%. Therefore, in a single polymer chain there are about 45 sulfobetaine monomers. This estimation is confirmed by the integration of the proton peaks in the terminal benzyl group compared to the integration of, for example, the methyl groups on the quaternary ammonium from the sulfobetaine.

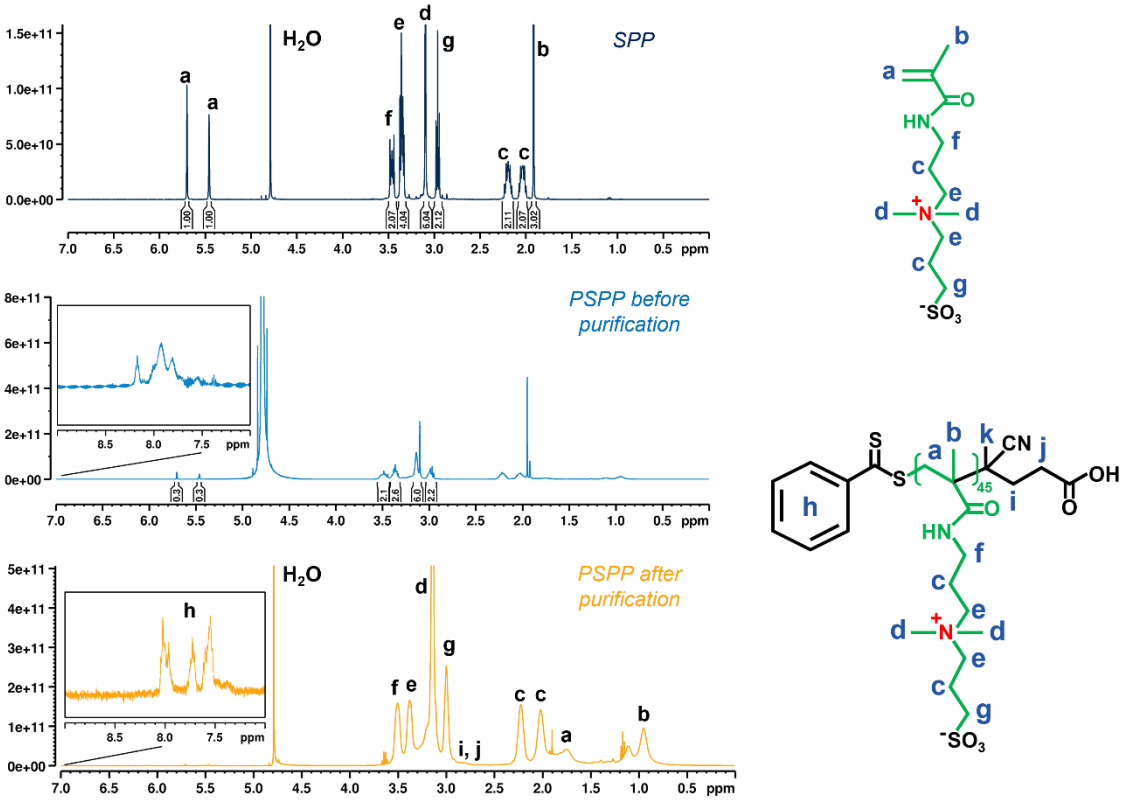

Figure.IV.12. ^{1}H NMR spectra of SPP monomer, pSPP before purification and pSPP after purification. After polymerization, a widening of proton peaks of polymer is observed.

The purified polymer pSPP is further characterized by Gel Permeation Chromatography (GPC), a type of steric exclusion chromatography, carried out by Mohammed Hanafi at the Sciences et Ingénierie de la Matière Molle (SIMM) laboratory. (**Figure.IV.13**) The number average molar mass is determined using GPC, and the results are consistent with that calculated from NMR spectra, using the integration of the benzyl group. Furthermore, due to the RAFT polymerization process, the distribution of polymer chain lengths is observed to be monodisperse. The polydispersity of the synthesized pSPP, as measured by GPC, is approximately 1.14, which is defined as the ratio of number average molar mass and mass average molar mass: $Đ = M_\omega/M_n$.

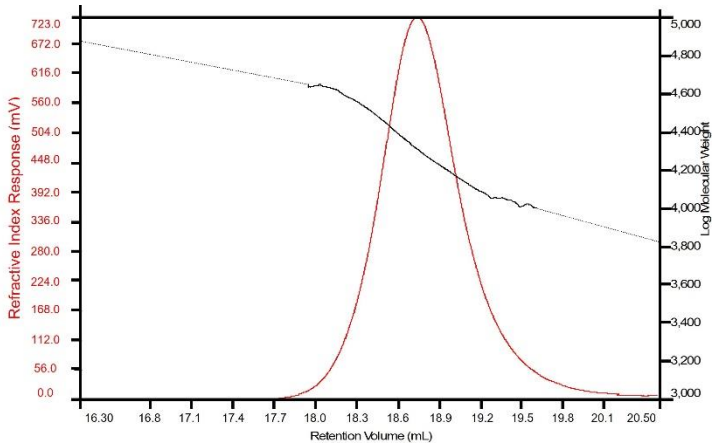

Figure.IV.13. Purified pSPP characterized by GPC.

IV.2.2. Preparation and characterization of polyzwitterion coated quantum dots

a. CdSe/CdS/ZnS core-shell QDs

The QDs utilized in this research project present a core-shell structure, with a CdSe core, a CdS shell in the middle, and a ZnS shell on the outermost layer. These QDs were synthesized by Bainvel-Sato Juichi, an intern in our laboratory. The resulting QDs have an average size of 5 nm in diameter and exhibit a fluorescent emission at approximately 580 nm. (**Figure.IV.14**) The fluorescent characteristics of the QDs facilitate their direct detection and monitoring *in vitro*. As a result, the uptake of QDs by cells can be visualized using widefield microscopy or assessed using flow cytometry techniques.

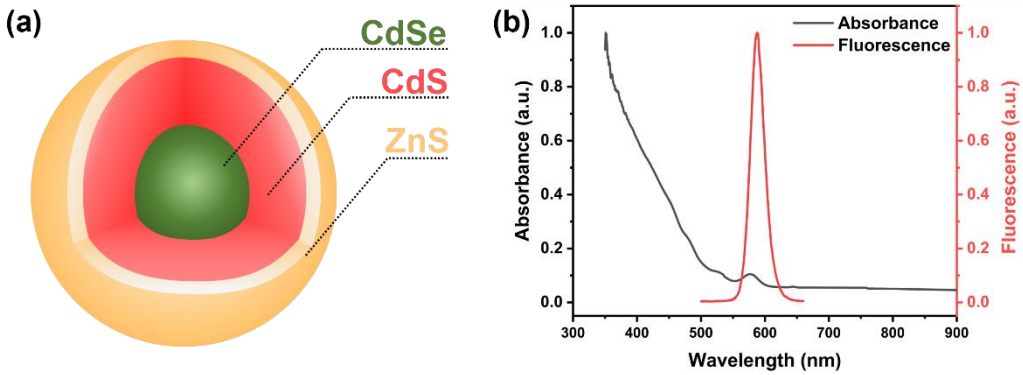

Figure.IV.14. (a). Core-shell structure of CdSe@CdS@ZnS QDs. (b). Normalized absorption and emission spectra of pSPP functionalized QDs.

b. Ligand preparation and exchange for QDs

The monomer vinylimidazole (VIM) was selected as the anchoring group to graft polyzwitterions to the surface of QDs. They can form strong complex bonds with Zn^{2+} at the surface of QDs. These VIM monomers can be integrated in the polyzwitterion chain (M_n = 9000 g/mol) through RAFT polymerization to form a blocked copolymer following the previous work[163,164]. (**Figure.IV.15**)

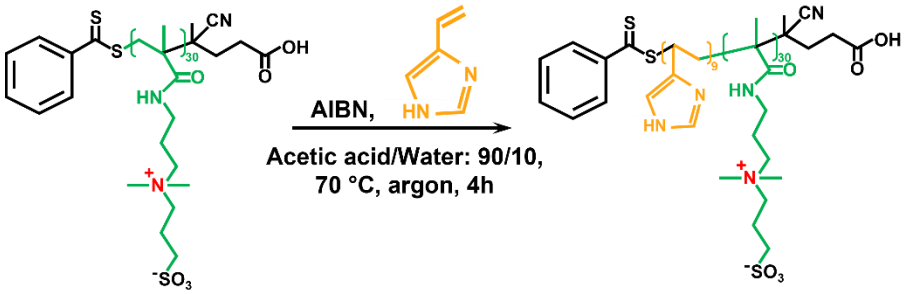

Figure.IV.15. A typical RAFT polymerization of p(SPP-b-VIM) from pSPP.

Two different SB-based polyzwitterions were utilized to functionalize the QDs, the SPP and the SPE as illustrated in **Figure.IV.16**. The difference between them is in the pSPP chain, the zwitterion groups are linked to the backbone via amide bond, while in the pSPE chain, they are linked to the backbone via ester bond. This difference may lead to distinct cell responses. Both synthesized SB polymers have a molar mass around 10k Da.

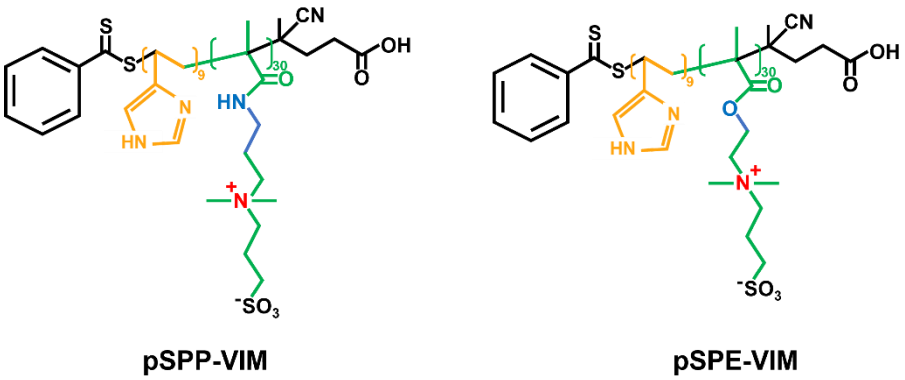

Figure.IV.16. Molecule structures of SB-based polyzwitterions for QD functionalization.

Ligand exchange for QDs

To 200 µL of solution of QD CdSe@CdS@ZnS, 400 µL of 3-Mercaptopropionic acid (MPA) was added. The mixed solution was left at 60 °C overnight. 1 mL of chloroform was then added. QDs were precipitated by centrifugation at 12000 g and the supernatant was discarded. QDs were redissolved in 1 mL of DMF. A few mg of potassium tert-butoxide were added to precipitate the QDs, followed by another round of centrifugation. Next, 1 mL of EtOH was added to remove the remaining free MPA. QDs were collected by precipitation via centrifugation. The obtained MPA-capped QDs were dissolved in 600 µL of $NaHCO_3$ solution (0.1 M), approximately 10 mg of polyzwitterion ligands (M_n = 10,000 g/mol), were added. The mixture was left overnight for ligand exchange. The exchanged QDs were concentrated by centrifugation. To remove the excess polymer ligands and any possible aggregates of nanoparticles, the exchanged QDs went through an ultracentrifugation (268,000 g, 25 min) on a 10-40% by mass sucrose gradient in 100 mM HEPES/Na buffer, 150 mM NaCl, pH=7.5. Non-aggregated nanoparticles formed a band after centrifugation on the sucrose gradient, which was extracted with a BioComp Instruments, Inc, Fredericton, NB, Canada. Excess sucrose was washed by a series of ultrafitration through a Vivaspin 100 kDa membrane. Purified nanoparticles were finally resuspended in 100 mM HEPES/Na, 150 mM NaCl, pH 7.5 buffer and stored at 4°C until use.

The synthesized QDs are initially coated with oleic acid and 1-octanethiol, which are nonpolar ligands that provide stability to the QDs in organic solvents. However, these nonpolar ligands hinder the direct ligand exchange with polyzwitterions, which are only soluble in polar solutions. To make the QDs soluble in water, the oleic acid and 1-octanethiol ligands are first replaced by a more hydrophilic ligand, 3-Mercaptopropionic acid (MPA). Subsequently, the MPA-capped QDs undergo an exchange process with polyzwitterion ligands (M_n = 10,000 g/mol) and are purified for further *in vitro* experiments. The yield of this stepwise ligand exchange is approximately 60%. The exchanged QDs exhibit good stability in water, saline buffers, and cell culture medium. Debayle et al.[164] have found that QDs prepared via this method possess a hydrodynamic radius of 6.8 nm when incubated in serum, indicating a good dispersity and low protein adsorption at the surface of QDs. In addition, their absorption and emission properties remain intact after functionalization.

IV.2.3. Preparation and characterization of polyzwitterion coated iron oxide nanoparticles

a. Iron oxide nanoparticles

The IONPs used in this study are spherical nanoparticles possessing an average size of 8 nm in diameter. (**Figure.IV.17**) The synthesis and characterization were originally developed by Fanny Delille at LPEM and synthesis details can be found in the article of Delille et al.[165]. These IONPs have a strong absorption at around 400 nm.

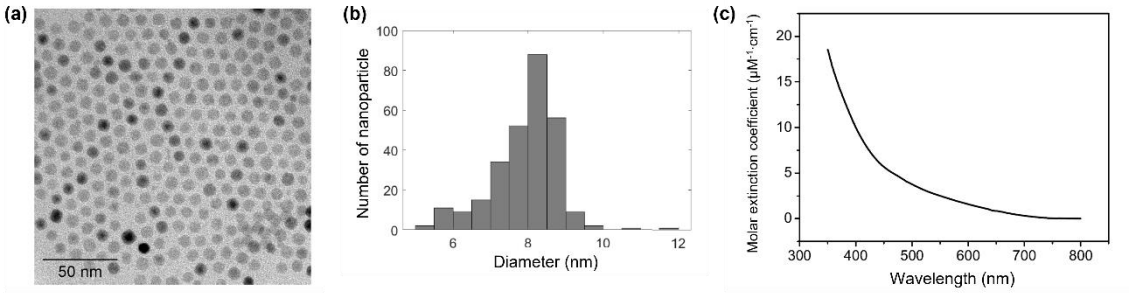

Figure.IV.17. (a). TEM image of synthesized IONP. (b). Size distribution of IONP. (c). UV-vis absorption spectrum of IONP.

b. Ligand preparation and exchange

IONPs are not fluorescent. In order to perform the analysis by flow cytometry, we need to label these IONPs with fluorescent molecules. In terms of preparation of polyzwitterion ligands, the SB monomers (SPP and SPE) are polymerized together with N-(3-aminopropyl)methacrylamide hydrochloride (APMA), a monomer containing a primary amine group which allows further conjugation of polymer ligands with fluorescent groups. The obtained statistical pSPP-s-APMA is further polymerized with (methacryloyloxy)methyl phosphonic acid (PA), the anchoring groups that graft polyzwitterions to the surface of IONPs. The resulting polyzwitterion ligands have a M_n of around 13,000 g/mol. (**Figure.IV.18**)

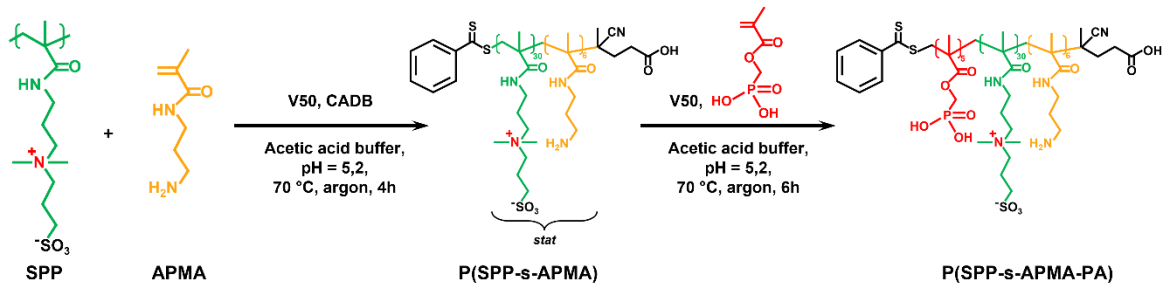

Figure.IV.18. Preparation of SB-based polyzwitterions for IONP surface functionalization.

Ligand exchange for IONPs

4 nM of IONPs in hexane were washed to remove excess oleic acid by addition of 1mL ethanol followed by centrifugation. The nanoparticles were then resuspended in hexane. Next, 500 µL of nitrosonium tetrafluoroborate ($NOBF_4$) solution (25 mg/mL in dimethylformamide (DMF)) was added. Two phases are formed. The mixture is gently stirred for 12h. The nanoparticles move from the upper hexane phase to the lower DMF phase. After three washes with a 50/50 toluene/hexane solution followed by centrifugation, the 4 nM of nanoparticles are resuspended in 100 µL of dimethyl sulfoxide (DMSO), in which they remain stable for several months.

To add the poly(zwitterion-s-APMA-PA) ligand, 10 mg of the previously synthesized polymer (M_n = 13,000 g/mol) was dissolved in 1 mL of ultrapure water. This solution was then added to 4 nM of DMSO-stored nanoparticles. The mixture was cloudy and had a pH around 3.5. It was sonicated for 5 min, then the pH was adjusted to 7.5 by adding tens of microliters of 0.1M NaOH solution. The mixture reacts for 12 hours at room temperature. At the end of the reaction, the solution is translucent.

Then the IONPs were collected by centrifugation. The possible aggregates and excess polymer ligands were removed by the ultracentrifuge process the same as what described in the ligand exchange process for QDs.

After the synthesis of IONPs, they are initially coated with organic hydrophobic ligands and stored in a nonpolar solvent. To functionalize the IONPs with polyzwitterions, a stepwise ligand exchange process is performed to replace the organic ligands on the nanoparticle surface. Subsequently, a fluorescent molecule called FP647 is introduced to the suspension of IONPs. FP647 fluorophores can bind to the amine groups present on the polyzwitterion chains through an amine-acid coupling reaction. It is important to note that not all amine groups can be coupled with FP647. The presence of free amine groups can enhance the uptake of IONPs by macrophages. To quench the remaining active primary amine groups after the fluorophore conjugation, bis(sulfosuccinimidyl)suberate (BS3) is used. BS3 is a molecule that efficiently reacts with amine groups, effectively neutralizing the remaining active amine groups on the IONPs. (**Figure.IV.19**)

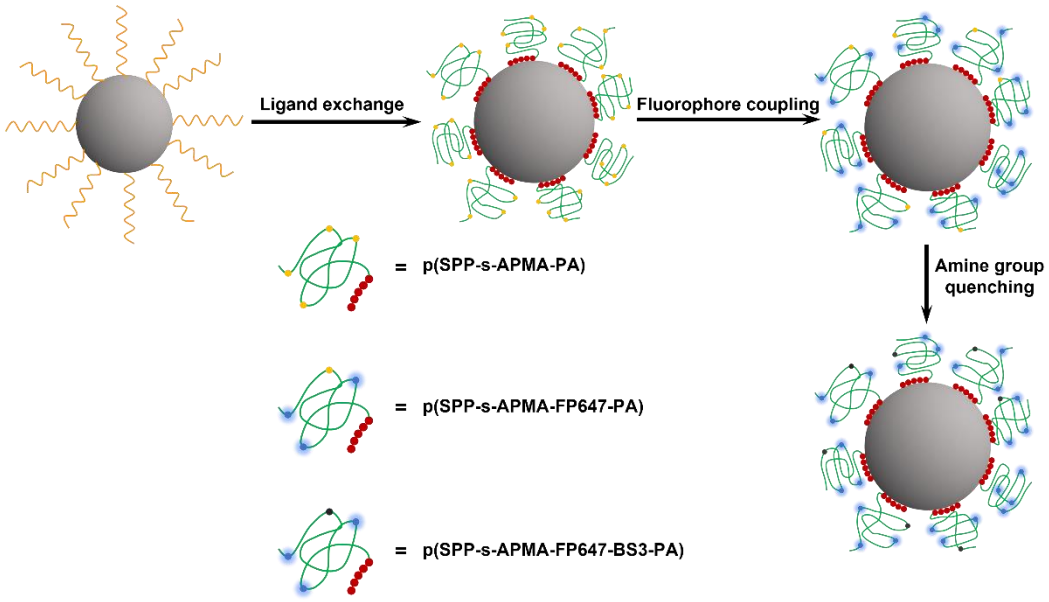

Figure.IV.19. Schematic illustration of ligand exchange process of IONPS and conjugation with fluorophores.

Finally, the IONPs are purified and stored in PBS buffer. **Figure.IV.20** shows the absorption and emission spectra of these nanoparticles. the concentration of IONPs can be estimated by the absorption at 400 nm. The absorbance peak at around 650 nm is attributed to the absorption of fluorophore FP647, with which the concentration of FP647 can be determined. Therefore, with the absorption spectrum we can eventually calculate the ratio between fluorophore and IONPs.

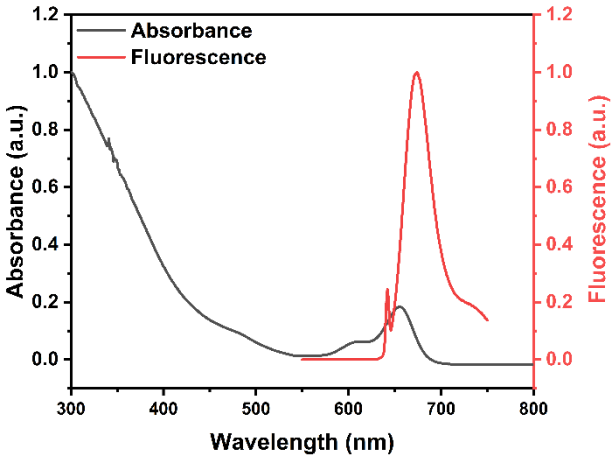

Figure.IV.20. Normalized absorption and emission spectra of pSPP functionalized IONPs.

Delille et al.[165] the hydrodynamic radius of functionalized IONPs was evaluated by incubating them with increasing concentrations of BSA, the major protein in blood. The hydrodynamic radius did not show any significant increase as the concentration of BSA increased up to 1 mM, (**Figure.IV.21**) suggesting the absence of interactions between the proteins and nanoparticles. To further investigate interactions in a more complex biological environment, the nanoparticles were also incubated in a solution containing increasing amounts of mouse plasma. Similar to the results with BSA, there was no visible increase in the hydrodynamic radius, indicating a lack of significant interactions between the nanoparticles and plasma components.

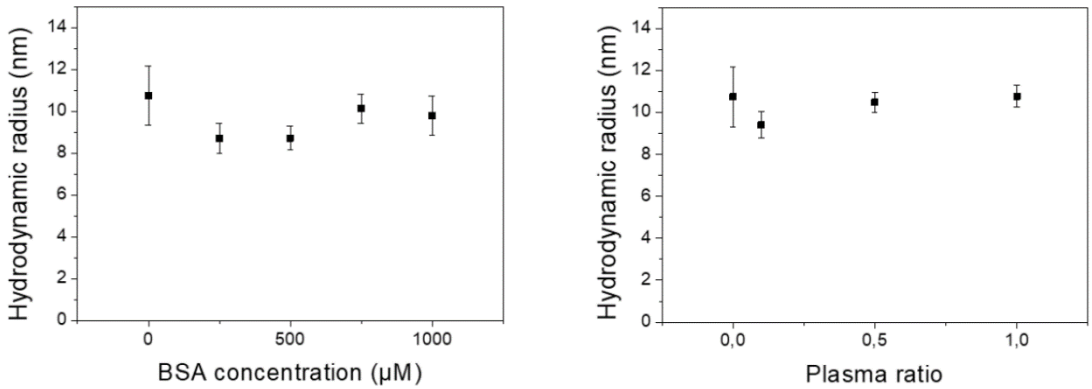

Figure.IV.21. Evolution of the hydrodynamic radius of IONPs as a function of the BSA concentration (left) or the ratio of plasma to buffer (right)[165].

IV.2.4. Preparation and characterization of polyzwitterion coated gold nanorods

a. Miniaturized AuNRs

The size of nanoparticles plays a crucial role in their biodistribution *in vivo*. Smaller nanoparticles have an advantage in being more effectively distributed to the tumor region because they are less likely to be captured by macrophages during circulation in the bloodstream. Additionally, the distribution of small nanoparticles is facilitated by the enhanced permeability and retention effect, which is a characteristic property observed in solid tumors. This effect is due to the leaky vasculature of tumors, which promotes the accumulation of small nanoparticles within the tumor region[207]. Moreover, AuNRs with smaller size have a higher absorption-to-scattering ratio, meaning that they utilize light energy more efficiently to produce heat. Therefore, to achieve an optimal blood circulation time of AuNRs *in vivo,* to minimize cellular uptake caused by the size of the nanoparticles, and finally improve the photothermal effect, the AuNRs used in this section have been miniaturized. The size of these AuNRs is approximately three times smaller in each dimension compared to the AuNRs used in previous chapters. They are referred to as miniaturized gold nanorods (AuNRmins).

Synthesis of AuNRmin:

To a 20 mL scintillation vial was added subsequently 10 mL of cetyltrimethylammonium bromide (CTAB) solution (0.1 M), 200 µL of $HAuCl_4$ solution (25 mM), 20 µL of $AgNO_3$ solution (0.1 M), and 200 µL of HCl (0.1 M). The mixed growth solution is stirred for 5 min. Then 500 µL of hydroquinone aqueous solution (0.1 M) is added to the growth solution under gentle stirring. The color of the resultant solution turns from orange to a very clear yellow. After 15 min of stirring, 18 µL of $NaBH_4$ aqueous solution (0.01 M) is added to the growth solution, followed by a vigorous stirring for 30 seconds. Then the growth solution is kept still overnight under 30 °C. The AuNRmins are precipitated by centrifuge at 12,000 g for 20 min and washed once by distilled water. After washing process, AuNRmins are stored in distilled water for further use.

The seedless growth method enables the synthesis of smaller AuNRs compared to the seed growth method. In the seedless growth method, the nuclei of AuNRs are formed in situ in the growth solution using $NaBH_4$ as the reducing agent. The quantity of $NaBH_4$ used determines the eventual size of the AuNRs. Additionally, the seed growth method utilizes ascorbic acid as the reducing agent, which is replaced by hydroquinone in the seedless growth method. Hydroquinone's reduction potential is more sensitive to the pH of the system, leading to better anisotropic growth of the AuNRs.

The synthesized AuNRmins are characterized using TEM and UV-visible absorption spectroscopy. The results depicted in **Figure.IV.22** show that the AuNRmins have an average length of 32.1 ± 4.6 nm and a diameter of 6.0 ± 0.7 nm. The longitudinal plasmon band of the AuNRmins is observed at 883 nm. Similar to the seed growth method, the shape and optical properties of the AuNRmins synthesized via the seedless growth method can also be tuned by adjusting factors such as acidity, concentration of silver ions, or concentration of CTAB.

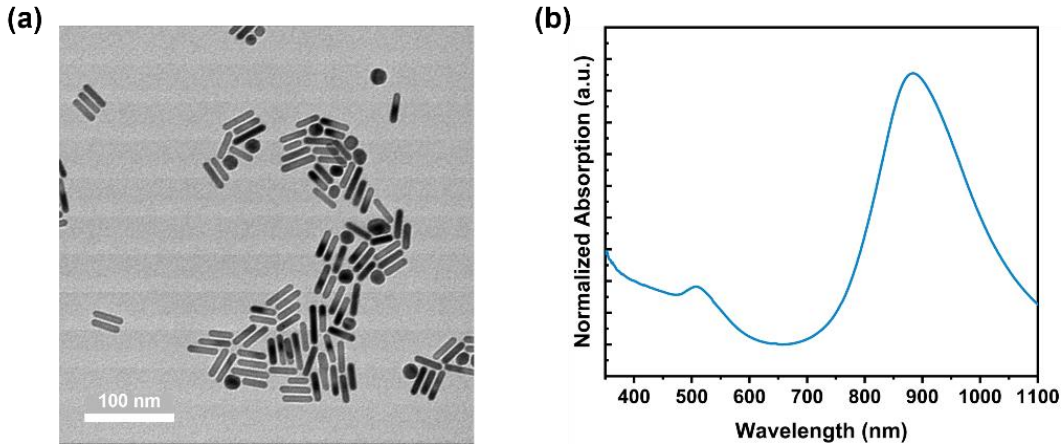

Figure.IV.22. (a). TEM image of AuNRmins. (b). Normalized UV-vis absorption spectra of AuNRmins.

b. Stabilization miniaturized gold nanorods with citrate ligands

Preparation of citrate-capped AuNRmins:

Typically, the stocked AuNRmins ([AuNRmin] = 1 nM) were precipitated by centrifugation (12,000 g, 25 min) and redispersed in Na-PSS solution (0.15 wt %, 70 kDa). After 2 hours, the residual CTAB was depleted by another round of centrifugation and redispersion in Na-PSS solution. The resultant PSS-stabilized AuNRmins were left overnight. Then AuNRmins were subjected to 2 rounds of centrifugation and redispersion in sodium citrate solution (5 mM) to exchange Na-PSS, eventually yielding stable citrate-capped AuNRmins.

As discussed in Chapter I, it is necessary to replace the cytotoxic CTAB with a more suitable ligand before the bio-applications of AuNRs. First, these AuNRmins are treated with sodium polystyrene sulfonate (Na-PSS), a detergent that removes the CTAB bilayer from the surface of the AuNRmins. Subsequently, the Na-PSS-stabilized AuNRmins are further exchanged with sodium citrate, a ligand that provides colloidal stability in low salinity aqueous solutions. The ligand exchange results in a slight blue shift of the longitudinal absorption band of the AuNRmins, as shown in **Figure.IV.23**. This shift is attributed to the replacement of CTAB by citrate ligands on the surface of the AuNRmins.

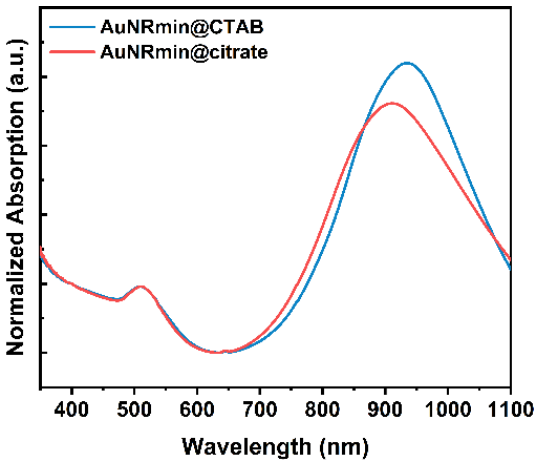

Figure.IV.23. UV-visible absorption spectrum of AuNRmins covered by CTAB and by citrates.

c. Stability of anchoring groups

To attach polymer ligands onto the surface of gold nanoparticles, thiol groups are commonly used as anchoring groups. In a biological environment, there are various proteins and small molecules in the bloodstream that can interact with the gold surface. These species have the potential to displace the polymer ligands from the surface of gold nanoparticles. This displacement can disrupt the colloidal stability of the gold nanoparticles and facilitate their capture by macrophages. One of the solutions is to increase the number of thiol groups on the polymer chain, so that the desorption rate of the ligands is reduced and these ligands can be maintained at the surface of AuNRs as long as possible.

To investigate the impact of the number of thiol groups on binding stability, we synthesized p(SPP-s-APMA) polyzwitterion ligands. These ligands have a chain transfer agent group (dithiobenzoate group) at the end of the polymer chain, which can be reduced to a thiol group in the presence of $NaBH_4$. (**Figure.IV.24**) The reduced p(SPP-s-APMA)-SH ligand was used to functionalize AuNPs with an average diameter of 8 nm. These AuNPs have a plasmon absorbance at 520 nm.

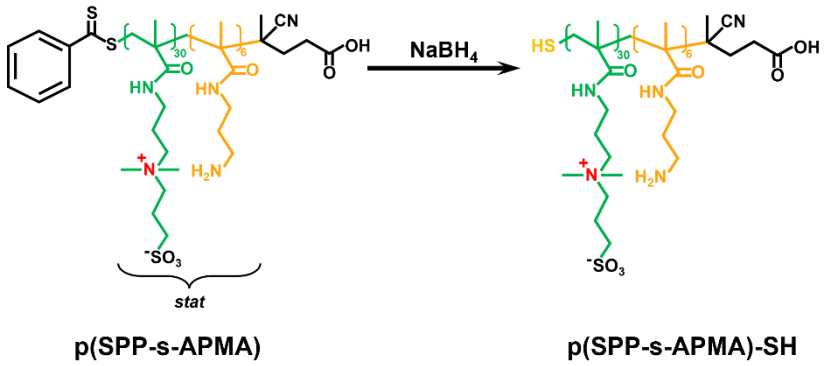

Figure.IV.24. Reduction of chain transfer agent to produce thiol group at the end of p(SPP-s-APMA).

Additionally, the APMA monomers in the polymer chain were able to couple with a dye molecule, Cy5.5-NHS ester, which has an absorption peak at 675 nm. This enabled the tracing of the polymers using absorption spectra. The resulting p(SPP-s-APMA-Cy5.5)-SH polymer-functionalized AuNPs were subjected to a ligand exchange process and dispersed in a physiological solution containing 4% (wt.%) bovine serum albumin. The solution was then incubated at 37 °C for a specific duration, after which a fraction of the solution was centrifuged to separate AuNPs from the supernatant. The absorption spectra of the AuNPs and the supernatant were measured. If the polymer ligands cannot remain attached on the AuNPs, the desorbed ligands will remain in supernatant, and the number of dye molecules on the AuNPs will decrease. As shown in **Figure.IV.25.a**, the absorption spectrum of supernatant exhibit an important increase in the absorption intensity of Cy5.5 during the 6h of incubation, suggesting that monothiol ligands progressively desorbed from the surface of AuNPs and were detected in the supernatant. The concentration of AuNPs can be calculated by the absorbance at 400 nm and the concentration of p(SPP-s-APMA-Cy5.5)-SH ligands can be calculated from the absorption peak at 675 nm. Therefore, we can further calculate the number of ligands grafted on each AuNP. As shown in **Figure.IV.25. c**, at the beginning of incubation, there are about 75 ligands on each AuNPs, however, six hours later, only 35 ligands can remain on the surface of a single AuNPs.

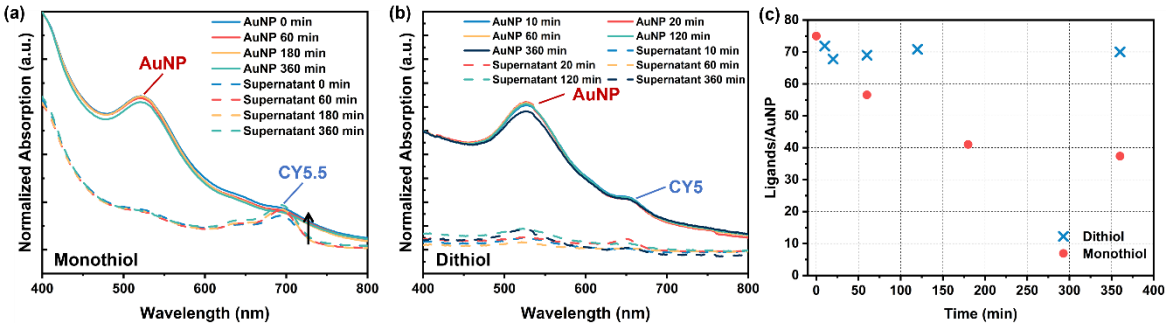

Figure.IV.25. UV-vis absorption spectra of separated AuNPs nanoparticles solution and supernatant with AuNPs functionalized by (a). p(SPP-s-APMA-Cy5.5)-SH monothiol ended ligands and (b). TA-PEG-CY5 dithiol ended ligands. (c). calculated number of ligands per AuNPs as a function of incubation time.

To assess the binding stability of dithiol-ended polymer ligands, we synthesized polymer ligands based on PEG (1000 Da) with dithiol groups at the end of the polymer chain, as depicted in **Figure.IV.26**. To track these polymers, we labeled them by coupling a dye molecule, DBCO-CY5, which has an absorption peak at 646 nm, to the opposite end of the polymer chain using click chemistry. This resulted in the formation of TA-PEG1000-CY5 polymers that could be monitored using absorption spectra. Using similar incubation experiments as before, the supernatant and AuNP solution were separated after centrifugation. The absorption spectra of the supernatant and AuNP solution were then measured and presented in **Figure.IV.25. b**. Based on the absorption spectra, there was no noticeable increase in the absorption peak of Cy5 at 646 nm in the supernatant, nor was there a decrease in the same peak in the AuNP solution, even after 6 hours of incubation. The number of ligands per AuNP (**Figure.IV.25. c**) was also found to be constant all over the incubation period. This observation suggests that the dithiol-ended ligands remained bound to the surface of the AuNPs throughout the incubation period.

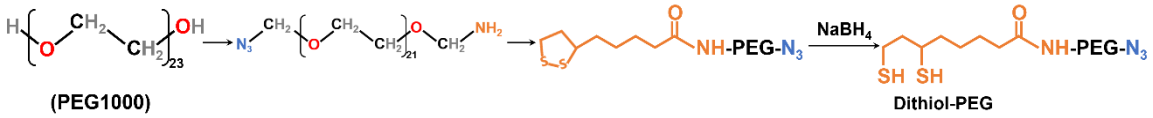

Figure.IV.26. Synthesis of dithiol ended Polyethylene glycol[208].

It should be noted that in these two experiments, the nature of hydrophilic polymer ligand is different. However, the deposition rate is influenced mainly by the nature of the anchoring group, rather than the nature of hydrophilic part.

Therefore, it can be concluded that polymer ligands with dithiol groups exhibit better binding stability to the gold surface compared to those with monothiol groups. Therefore, in the following experiments, we first synthesize zwitterionic polymer ligands with dithiol anchoring end-groups, and these polymers are used to functionalize gold nanoparticles.

d. Gold nanoparticles functionalized with dithiol-ended polyzwitterions

To add dithiol groups at the end of polyzwitterion chain, we designed the synthesis route as shown in **Figure.IV.27**. We start with a thioctic acid (TA) coupled PEG-amine ligand. This ligand is coupled with chain transfer agent CADB via amine-acid coupling. The PEG spacer in the molecule help improve the water solubility of as-synthesized chain transfer agent for further polymerization.

Afterwards, this modified chain transfer agent goes through RAFT polymerization with zwitterionic monomers and finally produce a polyzwitterion polymer with a TA group at the end of polymer chain (M_n ~ 16,000 g/mol). The TA group can be further reduced by $NaBH_4$ to produce two thiol groups.

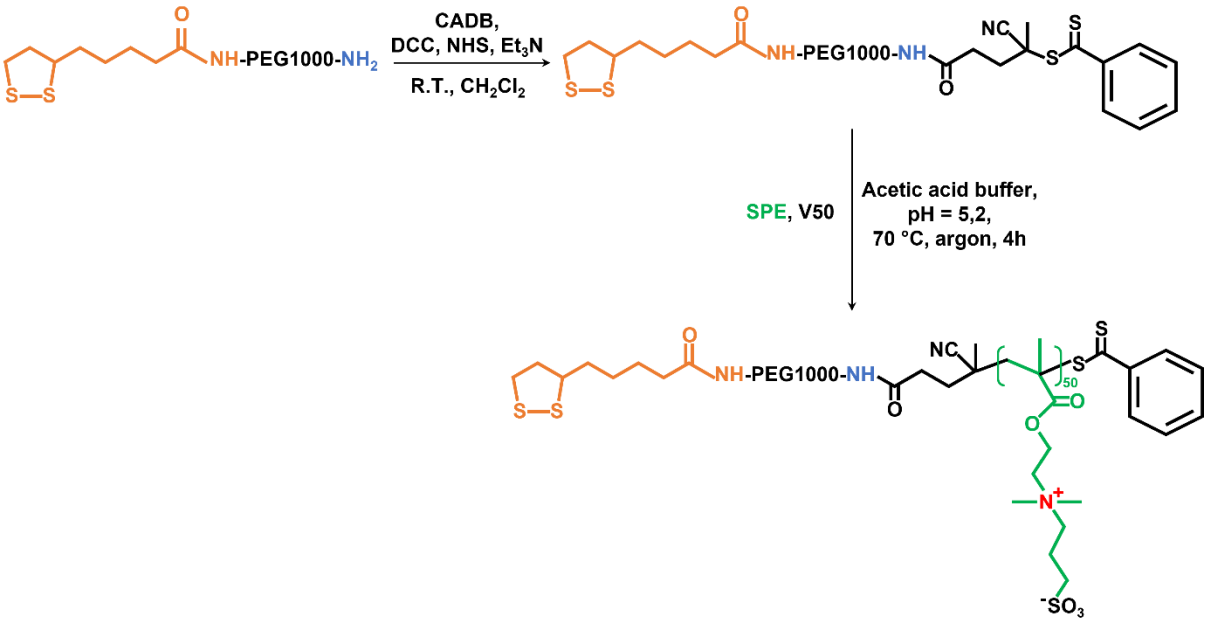

Figure.IV.27. Illustration of synthesis of ligand TA-PEG1000-pSPE-CADB.

We utilized the TA-PEG1000-pSPE-CADB polyzwitterion ligand to functionalize the AuNPs. To evaluate the colloidal stability of the functionalized AuNPs in saline solution and the BSA (4%) solution, we took the absorption spectra of the solution of AuNPs during a specific period of time. Figure.IV.28**. a** and **b** demonstrate that, in both the saline solution and the BSA solution, there was no significant broadening of the absorption bands observed over several hours. Besides, if AuNPs aggregated during the incubation, their absorption intensity in the supernatant would decrease. Therefore, by calculating the absorption intensity of the plasmon peak during the incubation, we can compare the number of AuNPs remaining in the supernatant during the incubation with the number of AuNPs at the beginning. As shown in **Figure.IV.28. c**, no decrease in AuNP numbers was observed for AuNPs incubated in either saline solution or BSA solution. These observations indicate that the AuNPs functionalized with dithiol-ended polyzwitterions possess good colloidal stability in these environments.

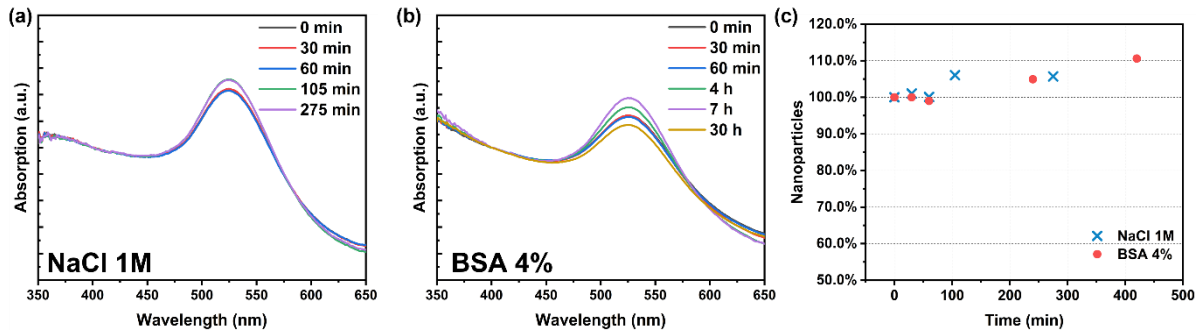

Figure.IV.28. Absorption spectra of AuNPs functionalized with TA-PEG1000-pSPE-CADB ligands incubated in (a). Saline water (NaCl, 1M) and (b). BSA solution. (c). Calculated percentage of AuNPs that remain suspension in the solution of saline water or BSA during the incubation, compared to their initial concentration.

e. Ligand preparation and exchange

The polyzwitterions used to functionalize the AuNRmins in this project include two sulfobetaines (pSPP and pSPE) and one phosphoryl choline (PC). The synthesis of these polyzwitterions follows a similar procedure as described in section IV.2.4.d. Additionally, after the RAFT polymerization, the polyzwitterions undergo an oxidation process in the presence of hydrogen peroxide (H_2O_2). (**Figure.IV.29**) This oxidation step replaces the dithiobenzoate group at the end of the ligand with a hydroxyl group[209]. This modification is necessary to prevent unexpected interactions between the dithiobenzoate group and proteins in the bloodstream. By introducing a polar hydroxyl group, the adsorption and formation of a protein corona at the surface of functionalized AuNRmins can be minimized.

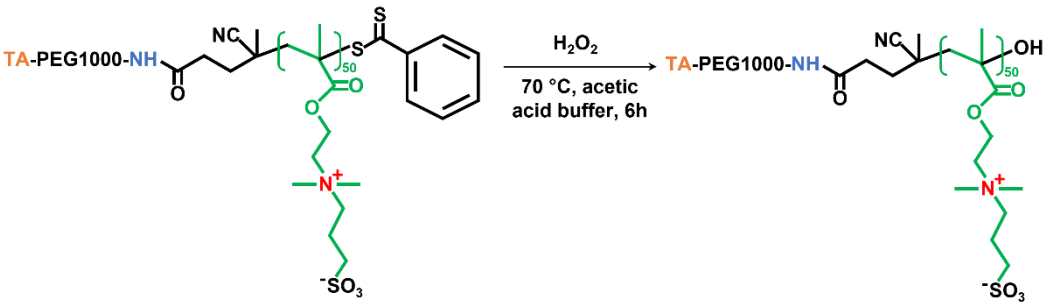

Figure.IV.29. Oxidation of chain transfer agent group by hydrogen peroxide.

After reacting with hydrogen peroxide, the color of the polymer ligand changed from pink to white. This color change is a visual confirmation of the elimination of the dithiobenzoate group. Furthermore, the ^{1}H NMR spectra (**Figure.IV.30**) of the polymer ligand before and after the H_2O_2 treatment confirmed the removal of the dithiobenzoate group. In the spectrum of the polymer before the H_2O_2 treatment, peaks corresponding to aromatic protons of the dithiobenzoate group are observed. However, these peaks are not observed in the spectrum of the polymer after the H_2O_2 treatment. This absence of aromatic proton peaks in the post-treatment spectrum provides further evidence of the successful removal of the dithiobenzoate group.

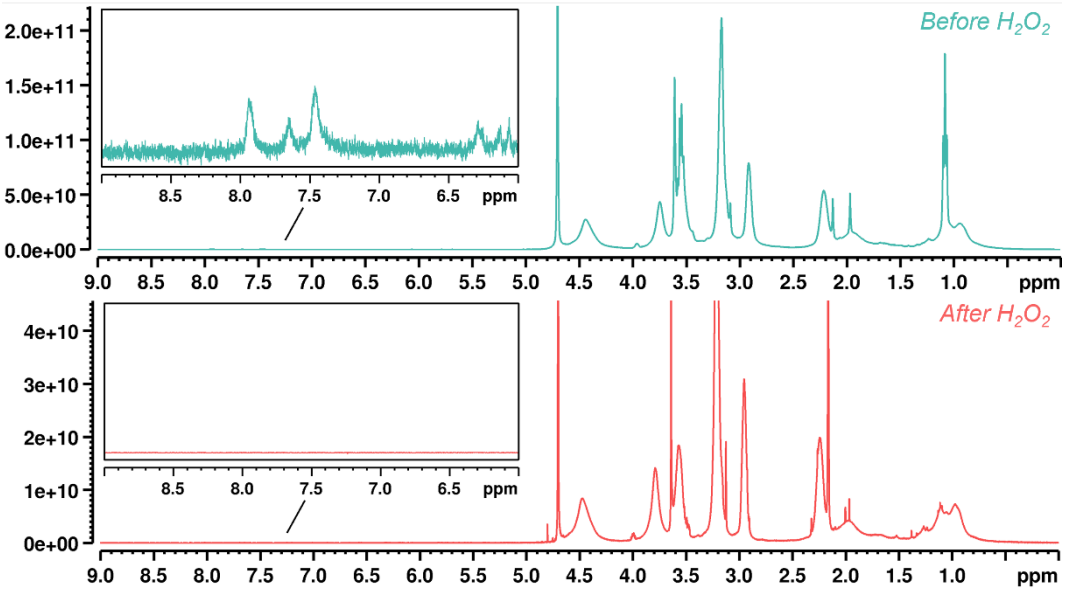

Figure.IV.30. ^{1}H NMR spectra recorded before and after removal of the dithiobenzoate end-group from TA-PEG1000-pSPE-CADB polyzwitterion ligand.

Ligand exchange of AuNRmin:

To a 20 mL scintillation vial was added subsequently 4 mL of sodium citrate solution (5 mM), 40 mg polyzwitterion ligands (approximately 4 µmol), and 330 µL of $NaBH_4$ solution (0.1 M). This mixed solution was kept stirring at room temperature for at least 30 min. Then the citrate capped AuNRmin solution (1.1 mL, 15 nM) was added. The resulting solution was kept stirring overnight for a complete ligand exchange. Afterwards, the exchanged AuNRmins were collected by centrifuge (6000 g, 30 min) and washed with PBS three times.

The thioctic acid group at the end of the polyzwitterion chain is reduced by $NaBH_4$ to produce two thiol groups before the addition of AuNRmins. The exchanged AuNRmins were collected and redispersed in PBS solution. According to the absorption spectra of polyzwitterion-capped AuNRmins (**Figure.IV.31. a**), after ligand exchange, the absorption spectra of AuNRmin slightly broadened, which can be attributed to the partial aggregation of AuNRmins caused by the electrostatic interaction between polyzwitterions. The addition of extra salts or elevation of temperature can reduce this aggregation. From TEM images (**Figure.IV.31. b**) compared with citrate-capped AuNRmins, the morphology and dispersity of polyzwitterion-capped AuNRmins remain unchanged, without important aggregations. Zetametry measurements (**Figure.IV.31. c**) show that before the ligand exchange, the citrate capped AuNRmins are negatively charged, suggesting that the good dispersity of AuNRmins in the citrate solution relies on the electrostatic repulsion. After ligand exchange, all the polyzwitterion coated AuNRmins are nearly neutral at physiological pH, and there is no significant difference between their values. The hydrodynamic radius of nanoparticles was measured by the DLS. Before the ligand exchange process, the citrate-capped AuNRmins exhibited a hydrodynamic radius of 35.0 ± 3.0 nm, which correlated with the length of the AuNRmins as determined from TEM images. Following the ligand exchange, the hydrodynamic radius of AuNRmins coated with pSPE and PC ligands slightly increased. However, for AuNRmins coated with pSPP ligands, the measured hydrodynamic radius exceeded 100 nm. It is important to note that the hydrodynamic radius obtained from DLS measurements is more influenced by the presence of larger particles or aggregations in the sample. Thus, the observation of a larger hydrodynamic radius in the case of pSPP-coated nanoparticles may be attributed to the presence of a small proportion of aggregates in the solution. This aggregation could be attributed to the antipolyelectrolyte effect of polyzwitterions. When the concentration of salts and the temperature of the solution are low, the interaction between polyzwitterion chains could lead to the aggregation of the nanoparticles.

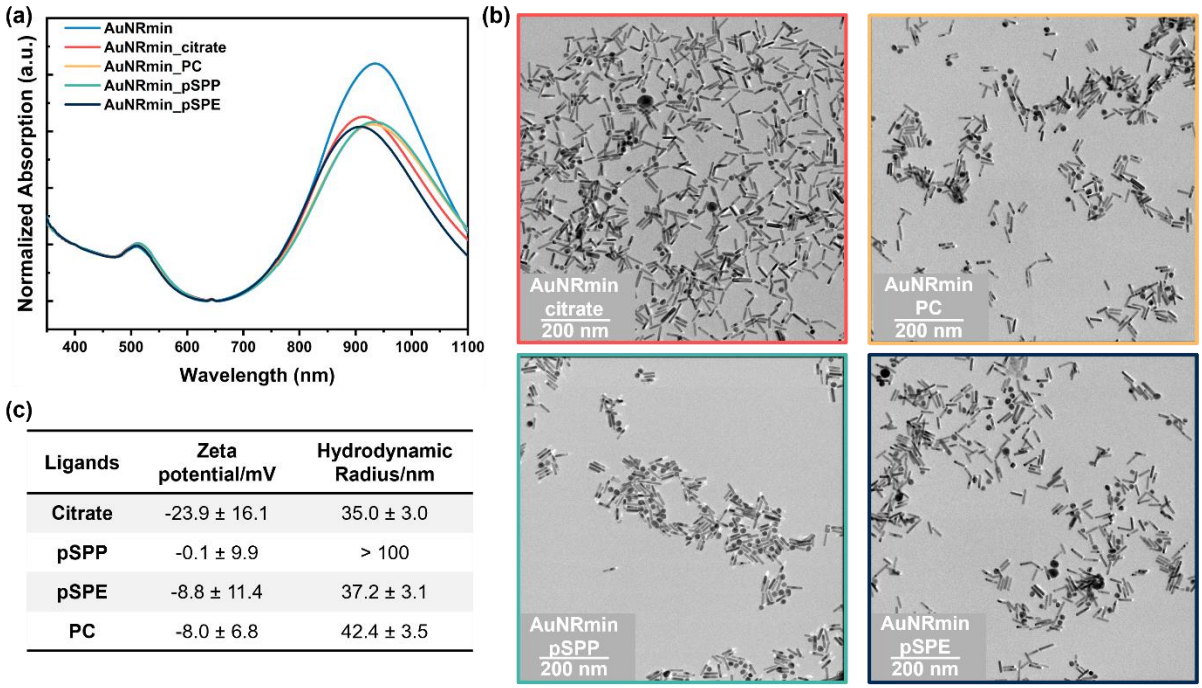

(c)

Ligands	Zeta potential/mV	Hydrodynamic Radius/nm
Citrate	-23.9 ± 16.1	35.0 ± 3.0
pSPP	-0.1 ± 9.9	> 100
pSPE	-8.8 ± 11.4	37.2 ± 3.1
PC	-8.0 ± 6.8	42.4 ± 3.5

Figure.IV.31. (a). UV-visible absorption spectra of AuNRmins after synthesis, capped with citrate, and capped with polyzwitterions. (b). TEM images of AuNRmins before ligand exchange (citrate-capped) and after ligand exchange (polyzwitterion-capped). (c). Characterizations of polyzwitterion coated AuNRmins: Zeta potential and hydrodynamic radius from DLS.

IV.3. Interaction between polyzwitterion-coated nanoparticles and macrophages: *in vitro* experiments

In this section, we conducted *in vitro* experiments to study the interaction of polyzwitterion-coated inorganic nanoparticles with macrophages. The key factor that we quantify and focus on is the uptake rate of nanoparticles by cells. The tumor cells were also incubated with nanoparticles in certain experiments to complete the comparison. The two cell lines that we used in this section are presented in **Figure.IV.32**: the HeLa cells (**Figure.IV.32. a**) an immortalized cell line which is the oldest and most commonly used human cell line; and the macrophages RAW264.7 (**Figure.IV.32. b**), an immortal mouse macrophage cell line, considered to be a good model of macrophage.

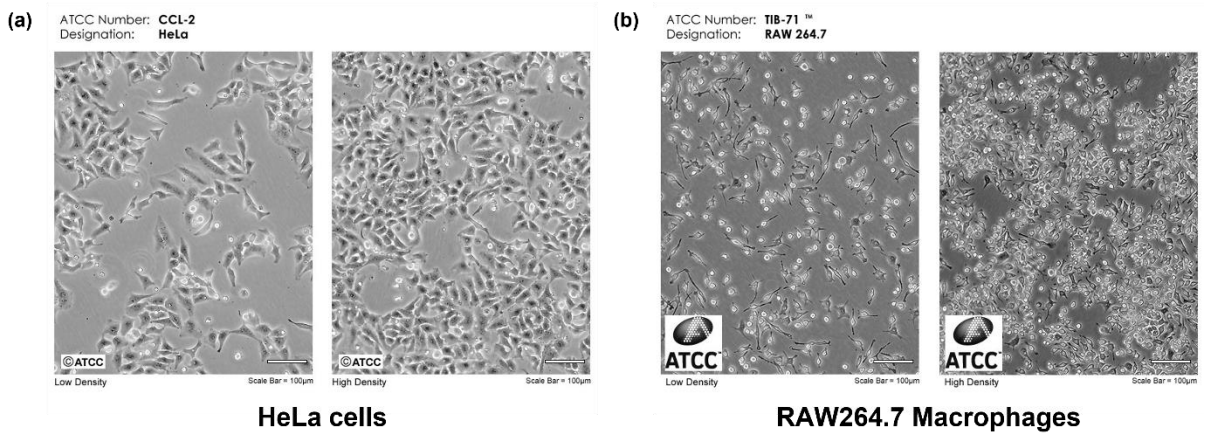

Figure.IV.32. Optical microscope images of (a). HeLa cells (https://www.atcc.org/products/ccl-2); (b). RAW264.7 macrophages (https://www.atcc.org/products/tib-71).

To trace and quantify nanoparticles during and after incubation, several techniques were used according to the nature of nanoparticles. For QDs, these nanoparticles are fluorescent, therefore, we can easily observe these nanoparticles by fluorescence microscopy. Besides, the fluorescence intensity can also be measured by flow cytometry. For IONPs, these nanoparticles are not fluorescent. Therefore, we graft fluorophores onto the surface of nanoparticles to make these nanoparticles detectable by the same modalities. Afterwards, the fluorescent intensity can be quantified by flow cytometry. For AuNRs, these nanoparticles are not fluorescent either. In addition, gold nanoparticles can quench the fluorophores grafted at the surface. Therefore, to trace and quantify gold nanoparticles in cells, the Inductively Coupled Plasma Mass Spectrometry (ICP-MS) was employed to directly quantify the concentration of gold in each sample.

IV.3.1. Interactions between QDs and cells

a. Study via fluorescent imaging

The interactions between QDs and cells were studied by fluorescent imaging. These experiments were conducted by Nicolas Kuszla, an intern of the laboratory. Two different types of polyzwitterions were used to functionalize QDs: the poly(sulfobetaine) (pSPP) and the poly phosphorylcholine (pPC). Polyzwitterion-functionalized QDs were incubated with cells in DMEM or DMEM supplemented with 10% serum during 1h allowing the uptake of QDs by cells. After incubation, cells were washed and fixed with paraformaldehyde, and observed by a wide field microscope. **Figure.IV.33** presents macrophages with internalized QDs in the cytoplasm. The interaction between QDs and macrophages can be thus assessed by the fluorescence intensity of QDs.

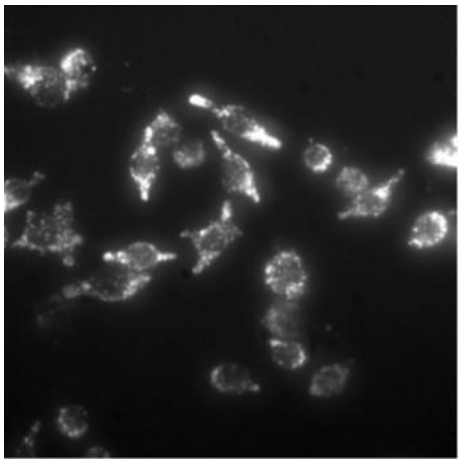

Figure.IV.33. Image of RAW 267.4 macrophages incubated with QDs under fluorescence microscopy.

QDs functionalized with pSPP (10,000 g/mol) and PC (10,000 g/mol) were incubated with HeLa and RAW cells at two different concentrations, 50 nM and 200 nM, which are comparable to the concentration of nanoparticles injected in the blood in typical imaging experiments. Measurements of average fluorescence intensities by fluorescence microscopy (excitation: 425-475 nm; emission: 565-605 nm) on typically 60-100 cells, as shown in **Figure.IV.34. a**, indicate that RAW cells capture more QDs compared to HeLa cells, suggesting that macrophages have a higher uptake efficiency than cancer cells. Furthermore, an increase in nanoparticle concentration leads to an increase in the quantity of QDs captured by the cells. Additionally, QDs functionalized with pSPP show lower cellular uptake compared to QDs coated with PC. It is not clear why this difference exists. It could be associated with the arrangement of the charges, since SPP terminates with the negatively charged sulfonate and PC by the positively charged ammonium. The phosphocholine groups are also known to readily bind to C-reactive protein in the plasma in the presence of calcium ions[210]. And this activates the complement system, promoting phagocytosis by macrophages, which eventually clears the detected PC-coated nanoparticles[211]. Even though no C-reactive proteins are present in the medium, it is possible that similar interactions exist with molecular receptors at the surface of the macrophages.

Afterwards, we aimed to determine whether the interaction between macrophages and nanoparticles is primarily influenced by the polymer coating on the nanoparticles or by the formation of a protein corona on the nanoparticle surface. To investigate this, we conducted an experiment using functionalized QDs incubated with macrophages in the presence of 10% plasma. The uptake of nanoparticles by macrophages was actually decreased in the presence of plasma (**Figure.IV.34. b**). If the protein corona was responsible for the internalization of nanoparticles, we would expect an increase in uptake rate in the presence of plasma, as the formation of a protein corona is facilitated. Therefore, we conclude that the capture of nanoparticles by macrophages is mainly attributed to the direct interaction between the polymer-coated nanoparticles and the macrophages. We hypothesize that macrophages recognize nanoparticles through the polymer ligands on the nanoparticle surface. To further support this hypothesis, we introduced excess free polymer ligands in solution, which could competitively interact with macrophages and subsequently reduce the uptake of polymer-coated nanoparticles. We incubated the pSPP functionalized QDs with free pSPP polymers (10,000 g/mol) at 1 mg/mL. As shown in **Figure.IV.34. b**, the uptake of QDs has reduced by 50% in the presence of free pSPP ligands, indicating that the receptors at the cell membrane of macrophages may be saturated by the free pSPP polymers in solution, which help the QDs to escape from the detection of macrophages.

This result suggests that macrophages recognize nanoparticles mainly through the polymer ligands at their surface.

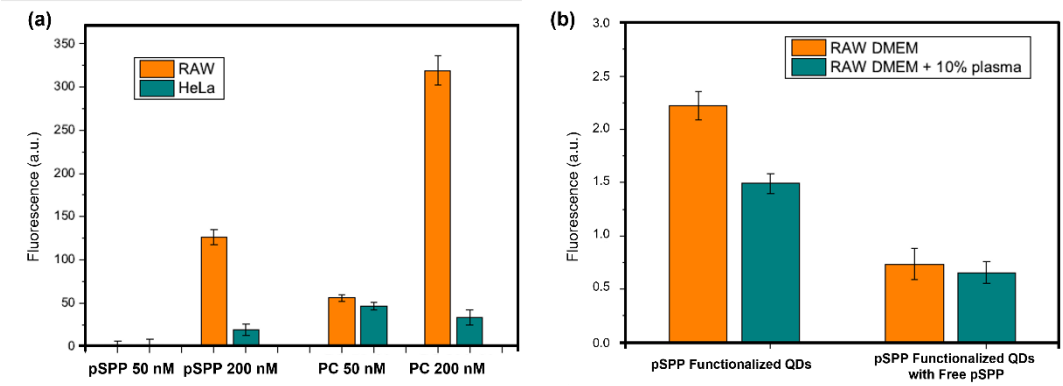

Figure.IV.34. Average cellular QD fluorescence intensity measured on (a). RAW or HeLa cells after incubation with pSPP or PC functionalized QDs at two concentrations, 50 nM or 200 nM. (b). RAW cells after incubation with QDs in DMEM culture medium with or without plasma, and with or without sulfobetaine free polymer.

b. Study via flow cytometry

Imaging analyses require cells to be analyzed one by one and are therefore time-consuming. To complete the study with more precise, rapid measurements that can analyze a larger number of cells, the technique of flow cytometry has been employed. In this process, a fluid containing cells or particles is prepared as a sample and introduced into the flow cytometer instrument. (**Figure.IV.35**) The sample is carefully directed to flow through a laser beam, ideally allowing one cell at a time to pass through. As the cells pass through the laser beam, the light scattered by the cells and their components is measured. Additionally, the fluorescence signal from fluorescent nanoparticles is detected. The flow cytometer can rapidly analyze tens of thousands of cells, and the resulting data are collected and processed by a computer for further analysis and interpretation. In our study, the flow cytometer is capable of measuring the fluorescence intensity of each cell caused by the captured QDs. This allows us to have an idea about the distribution of the number of cells based on their detected fluorescence intensity. By analyzing the average fluorescence intensity determined by the flow cytometer, we can correlate it with the quantity of QDs captured by cells in a specific sample.

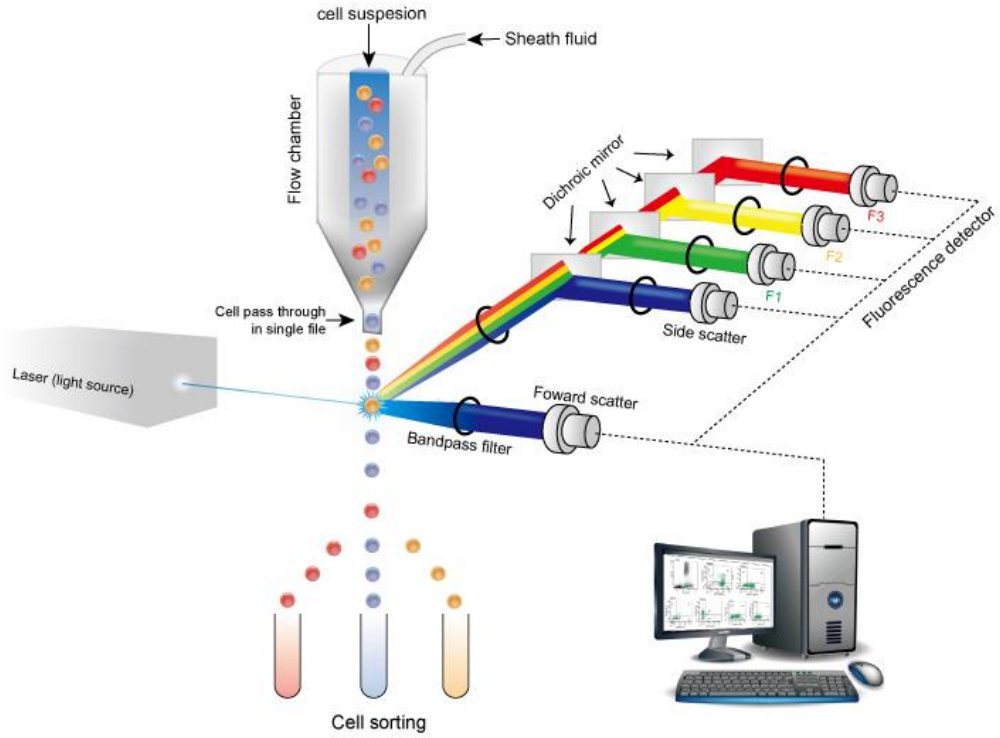

Figure.IV.35. Schematic illustration of the principle of a flow cytometer platform. Adapted from *https://www.creative-bioarray.com/support/principle-of-the-flow-cytometry.htm*

Flow cytometry analysis:

RAW267.4 cells were incubated in a 6-well plate until they covered approximately 60% of the surface of the well. The culture medium is removed and replaced by pure DMEM (without fetal bovine serum) to study the interaction between cells and QDs in the absence of protein. The QDs were then added to the culture medium and the cells were incubated for one hour with the QDs. After one hour, the medium was removed by aspiration, the cells were washed with 1mL of PBS, then 500 µL of PBS was added to each well. The cells were then scraped with a cell scraper. The sample of cells in PBS was pipetted vigorously to disrupt cell aggregates that would distort the fluorescence measurement in cytometry. The absence of cell aggregates was checked under the microscope. The solution of cells in PBS was then placed in special cytometer tubes.

Analysis with the Guava EasyCyte flow cytometer (Merck Millipore):

Each sample was shaken for 3 seconds to ensure homogeneity. The flow in the cytometer was set at 0.6 µL/s. There were approximately 500 cells/µL in the samples. Fluorescence measurement is performed on the "YeL-V" channel, with a laser that excites at 405 nm and an emission measured at 583 nm with a width of 26 nm. Before each series of measurements, the cytometer's gain is set to maximize the difference between the sample with the highest and lowest fluorescence. It is generally around 10, with a maximum of 1000. A threshold is applied to the lateral diffusion value to regulate the detection limit above which a detected signal is considered as a cell. For each sample, the fluorescence of 5,000 or 10,000 cells was measured.

After 1h of incubation with functionalized QDs in different concentrations ranging from 0 to 200 nM, the macrophages were washed and collected in PBS for analysis of flow cytometry.

Approximately 10,000 cells were analyzed using the flow cytometer for each experimental condition. **Figure.IV.36. a** and **b** present the distribution of fluorescence depicting the results for RAW264.7 cells incubated with $pSPP_{10k}$ or $pSPE_{10k}$ functionalized QDs, respectively. The fluorescence intensity of cells is dependent on the quantity of captured QDs. Given that the measured fluorescence intensity values are all positive, a normal distribution may not be suitable for fitting the data. Instead, the logarithm of the measured fluorescence intensity values is expected to follow a normal distribution. Hence, a logarithmic normal distribution model is employed to describe the obtained results:

$$f_{\lg-N}(x;\,\mu,\sigma) = \frac{1}{x\sigma\sqrt{2\pi}} e^{-\frac{(lnx-\mu)^2}{2\sigma^2}} \qquad (IV.2)$$

where μ, σ represent the mean and standard deviation respectively. A high concentration of QDs in the cell culture media can lead to a high fluorescence signal from the cells, resulting in a wide distribution of fluorescence intensities. To compare the results obtained from different measurements, it is important to note that the cytometer gain is adjusted between each series of measurements. Therefore, the measured fluorescence levels should not be directly compared between graphs. To facilitate comparison, the measured average fluorescence intensities are normalized using a reference sample in each measurement. The reference sample consists of cells incubated without QDs, and its fluorescence intensity due to the autofluorescence of cells serves as reference for normalization. **Figure.IV.36. c** compares the uptake quantities of QDs functionalized by pSPP and pSPE: QDs with surface covered by pSPP are more significantly captured than those covered by pSPE, indicating that pSPP may be recognized by macrophages more easily than pSPE.

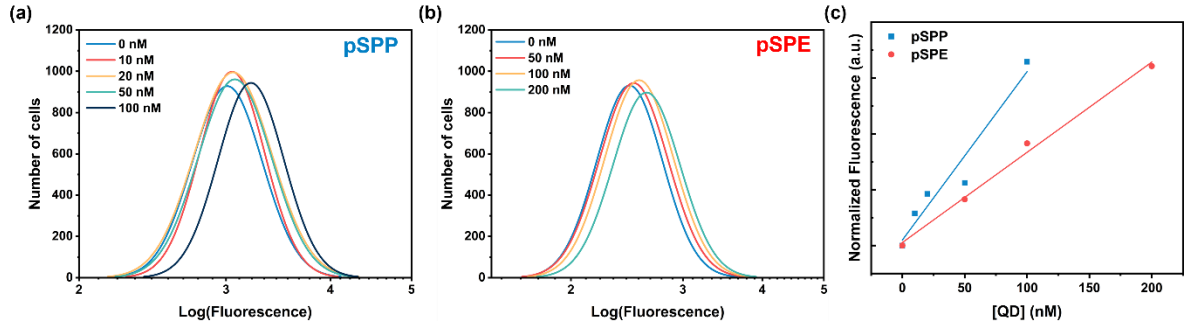

Figure.IV.36. Fluorescence distribution measured for RAW cells incubated with increasing concentration (from 0 to 200 nM) of QDs functionalized by (a). pSPP, and (b). pSPE. (c). Normalized fluorescence intensity of RAW cells as a function of concentrations of QDs added in the cell culture media.

To summarize, in this section, we conducted a series of *in vitro* experiments using polyzwitterion-coated QDs incubated with macrophages and HeLa cells. Based on the results, we have drawn the following conclusions. Firstly, macrophages, which play a key role in the capture and elimination of nanoparticles, exhibited a higher *in vitro* uptake of nanoparticles compared to HeLa cells. Secondly, the presence of plasma or free polymer ligands resulted in a decrease in the uptake rate of nanoparticles. Lastly, we functionalized QDs with three different polyzwitterions. QDs coated with PC demonstrated the highest uptake by macrophages, followed by QDs coated with pSPP, while QDs coated with pSPE exhibited the lowest uptake rate among the three polyzwitterions.

IV.3.2 Interactions between IONPs and cells

Apart from the QDs, the interactions of IONP nanoparticles functionalized by polyzwitterions with macrophages are also studied. This series of studies are carried out in collaboration with Dr. Fanny Delille from our laboratory.

According to the absorption-emission spectrum of functionalized IONPs shown in **Figure.IV.20**, an intense fluorescence emission is observed at around 690 nm, which is due to the coupled fluorophore FP647. Therefore, to optimize the detection sensibility of flow cytometer, the fluorescence channel "Red-R" was chosen to measure the fluorescence intensity of cells, with an excitation at 642 nm and a detection at 661 ± 15 nm.

a. Interaction of fluorophore with macrophages

IONPs are functionalized with pSPP-based polyzwitterion ligands with APMA monomers to enable functionalization with fluorophores, and a block made of typically 5-6 phosphonate monomers (Mn~13,000 g/mol), subsequently conjugated with the fluorophore FP647, with the remaining amines blocked by BS3, as described above. A maximum of 60 fluorophores are successfully grafted onto each IONP. These functionalized IONPs are then incubated with RAW cells at increasing concentrations ranging from 5 nM to 200 nM. To investigate the impact of the number of fluorophore groups on cell uptake behavior, a similar set of experiments is conducted with a reduced number of fluorophores, specifically 30 Fluo/IONP. The results obtained from flow cytometry analysis are presented in **Figure.IV.37**. It can be observed that as the concentration of IONPs increases, the quantity of IONPs captured by macrophages also increases accordingly. In the case of 60 Fluo/IONP, the fluorescence intensity of RAW cells reaches a plateau rapidly once the concentration of IONPs reaches 20 nM. This saturation of fluorescence intensity suggests that macrophages reach their maximum capacity for internalizing nanoparticles. In contrast, in the case of 30 Fluo/IONP, the fluorescence intensity exhibits a linear increase until the concentration of IONPs reaches 50 nM. This difference may be attributed to the enhanced internalization of IONPs assisted by fluorophores.

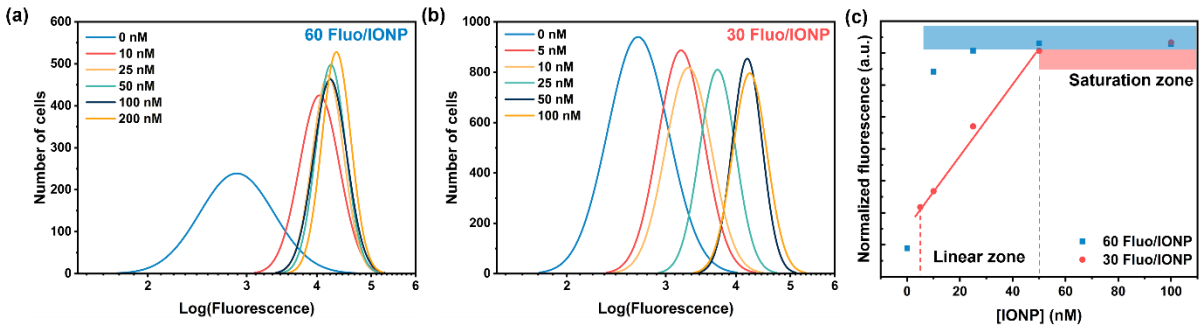

Figure.IV.37. Fluorescence distribution measured for RAW cells incubated with increasing concentration (from 0 to 200 nM) of IONPs with (a). 60 Fluorophores/nanoparticle; (b). 30 Fluorophores/nanoparticle. (c). Normalized fluorescence intensity of RAW cells as a function of concentrations of IONPs added in the cell culture media.

The interactions between fluorophores and macrophages should be minimized or avoided in the following experiments. We further conducted a set of experiments by changing the number of fluorophores on the nanoparticles from 5 Fluo/IONP to 70 Fluo/IONP. The concentration of IONPs

incubated with RAW cells is fixed at 30 nM to avoid possible saturation of macrophages by quantity of nanoparticles. As shown in **Figure.IV.38**, when the number of fluorophore is inferior to 30 Fluo/IONP, the fluorescence intensity of cells is independent of the number of fluorophores on the nanoparticles. When the number of fluorophores increases, the detected fluorescence intensity starts to rise, indicating the interaction between the fluorophores and macrophages is no longer negligible. It should be noted that when the number of fluorophore increases, the average fluorescence intensity detected by the cytometer will naturally increase, therefore, the values of average fluorescence intensity shown in the **Figure.IV.38** have been normalized according to the average fluorescence signal per IONP, measured in solution by spectrofluorometry.

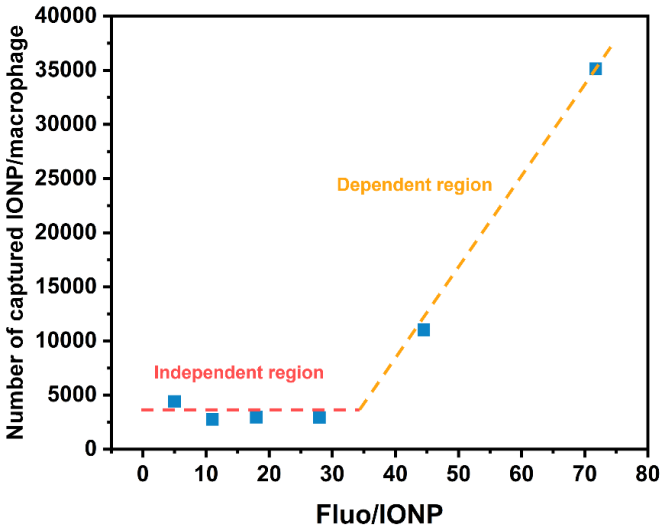

Figure.IV.38. Influence of the number of fluorophores on IONPs on their interaction with RAW cells. Measured by flow cytometry.

Therefore, to minimize the influence of fluorophore on the macrophage uptake performance, in the following experiments the average number of fluorophores per nanoparticle is controlled to be less than 30.

b. Interaction of SB-coated IONPs with macrophages

We determine the quantity of captured IONPs according to the fluorescence intensity measured by flow cytometer. However, it is challenging to distinguish between IONPs that are internalized by macrophages and those that are merely adsorbed on the cell surface. The internalization of IONPs is mainly through endocytosis, which is energy dependent. Therefore, at low temperature, the endocytosis of macrophages should be suppressed. We conducted an experiment by incubating IONPs with RAW cells at 4°C to block the endocytosis process. **Figure.IV.39** illustrates the results, showing that samples incubated with IONPs and RAW cells at 37°C exhibit significantly higher fluorescence intensity compared to samples incubated at 4°C. Moreover, for IONP concentrations ranging from 5 nM to 40 nM, the fluorescence intensities measured in samples at 4°C consistently account for approximately 25% of those measured at 37°C. These findings suggest that the increased fluorescence intensity observed at 37°C is primarily due to the endocytosis of IONPs by macrophages.

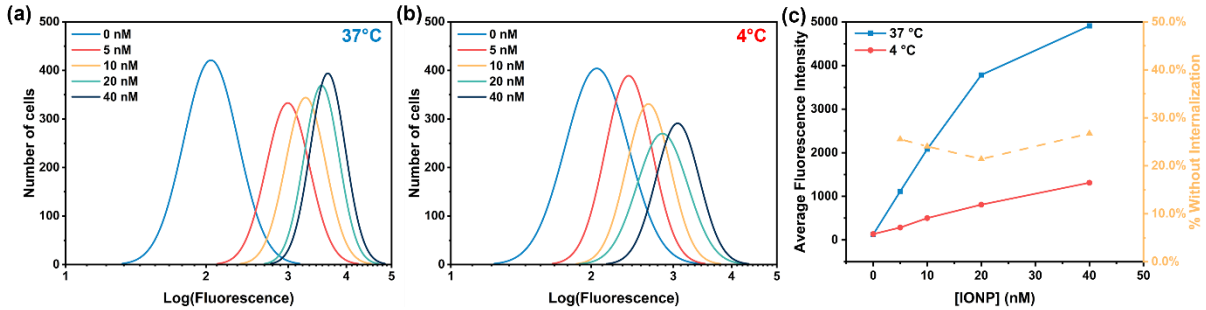

Figure.IV.39. Fluorescence distribution measured for RAW cells incubated with IONPs under (a). 37 °C; (b). 4 °C. (c). The average fluorescence intensity of RAW cells measured after incubation with IONPs at increasing concentrations ranging from 5 nM to 40 nM, at 4°C and 37 °C. Dash-dotted line: the percentage of fluorescence intensity attributed to non-internalized IONPs compared to the total fluorescence intensity.

In the next set of experiments, IONPs functionalized with pSPE ligands and pSPP ligands were incubated with RAW cells at increasing concentrations ranging from 5 nM to 50 nM. Consistent with previous findings, an increase in nanoparticle concentration during the incubation led to higher fluorescence intensity of cells as measured by flow cytometer, indicating an increased uptake of nanoparticles. **Figure.IV.40** clearly demonstrates that IONPs functionalized with pSPE ligands exhibited significantly lower uptake compared to those functionalized with pSPP ligands. This observation suggests that macrophages are less responsive to pSPE ligands, indicating that pSPE ligands possess better antifouling properties as polyzwitterion ligands.

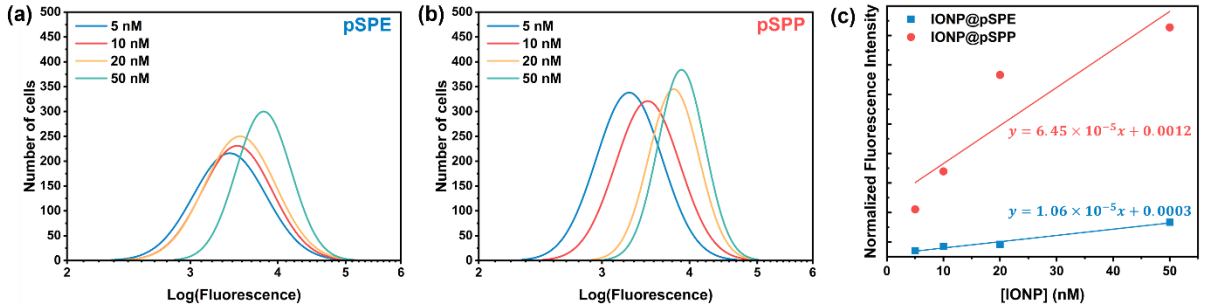

Figure.IV.40. Fluorescence distribution measured for RAW cells incubated with increasing concentration (from 5 nM to 50 nM) of IONPs functionliazed with (a). p(SPE-s-APMA-FP647-BS3-PA); (b). p(SPP-s-APMA-FP647-BS3-PA). (c). Normalized fluorescence intensity of RAW cells as a function of IONPs functionlaized with pSPE or pSPP ligands with concentrations ranging from 5 nM to 50 nM.

c. Interaction of pSPP functionalized IONPs with macrophages in the presence of free polyzwitterions

As discussed in IV.3.1, the presence of free polymer ligands can reduce the uptake of nanoparticles by macrophages, indicating that the uptake of nanoparticles by macrophages is partly due to the interaction of polymer ligands with receptors on macrophages. The polymer ligand contains three different functional groups: zwitterions, primary amines and phosphonate acids, among which the zwitterions are the main component in the polymer chain and thus have more possibility to interact with macrophages. Therefore, we prepared pSPP polymers with a molar mass of 10k Da which do not contain amine or phosphonic acid groups. Functionalized IONPs were incubated with RAW cells and with these free pSPP polymers whose concentration varies from 0.2 g/L to 1.0 g/L. As shown in **Figure.IV.41**, increasing the concentration of free pSPP ligands during the incubation leads to the decrease of

nanoparticle uptake by macrophage. When the concentration of free pSPP ligands increases to 1.0 g/L, the fluorescence intensity of IONPs captured by macrophages is about 70% of that in the samples without free pSPP ligands. In addition, we performed the same experiments with p(SPP-s-APMA-PA) and obtained similar results. (**Annex.V.5.2**. Polyzwitterion-coated IONPs incubated with free polymer ligands)

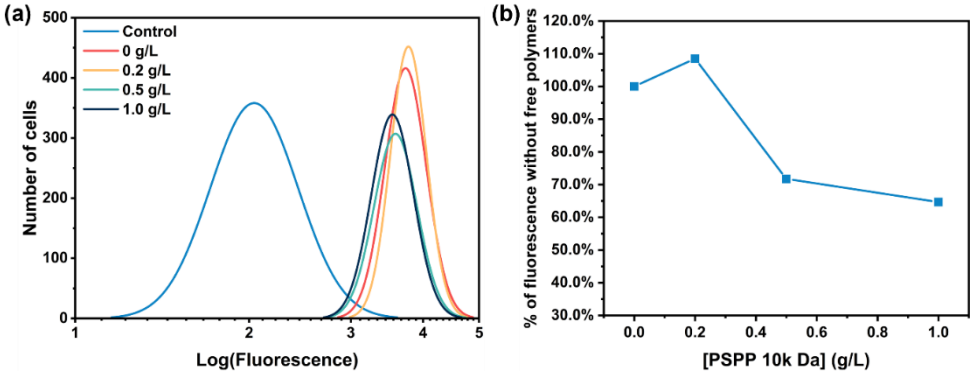

Figure.IV.41. (a). Fluorescence distribution measured for RAW cells incubated with increasing concentration (from 0.0 to 1.0 g/L) of free polymer ligands (pSPP) and IONPs. (b). Average fluorescence intensity detected in samples with free polymers compared to samples without free polymers, whose fluorescence intensity is set to 100%.

d. Interaction of pSPE functionalized IONPs with macrophages in the presence of free polyzwitterions

We also utilized another SB-base polyzwitterion pSPE to functionalize the IONPs. The ligand exchange process and the conjugation of FP647 fluorophores with pSPE ligands are similar to the preparation of pSPP functionalized IONPs.

IONPs eventually covered by p(SPE-s-APMA-FP647-BS3-PA) ligands were incubated with RAW cells at a concentration of 30 nM in the presence of free pSPE ligands (10k Da). After 1h of incubation, IONPs were collected and analyzed by flow cytometer, the results are shown in **Figure.IV.42**. In this experiment, the concentration of free pSPE polymer was increased from 0.5 g/L to 1.5 g/L, but there was no significant change in the uptake of nanoparticles. This result indicates that the interaction between pSPE ligands and macrophages may be less influential compared to the interaction with pSPP ligands. The addition of free pSPE ligands does not appear to interfere with the internalization of nanoparticles by macrophages. The reduced interaction of pSPE with macrophages could make pSPE a better polyzwitterion ligands for nanoparticle functionalization.

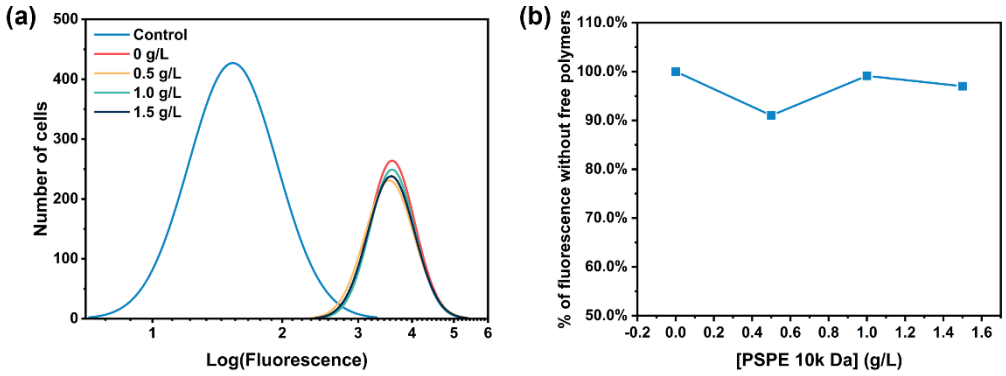

Figure.IV.42. (a). Fluorescence distribution measured for RAW cells incubated with increasing concentration (from 0 to 1.5 g/L) of free polymer ligands (pSPE)) and IONPs. (b). Average fluorescence intensity detected in samples with free polymers compared to samples without free polymers, whose fluorescence intensity is set to 100%.

To summarize, in this section, we investigated the interaction between polyzwitterion-coated IONPs and macrophages using flow cytometry. Our findings revealed that the uptake rate of IONPs by macrophages was higher at 37 °C compared to 4 °C, indicating that the energetic dependent internalization is the main pathway for macrophages to capture nanoparticles. Moreover, the presence of free pSPP polymers in the cell culture media competed with the uptake of pSPP-coated IONPs, suggesting that the interaction between macrophages and pSPP-covered IONPs is mediated by the polyzwitterion ligand. However, this competitive effect was not observed when pSPE polymers were incubated with pSPE-coated IONPs. Additionally, consistent with the QD results, we observed that the uptake rate of pSPE-coated IONPs was lower than that of pSPP-coated IONPs.

IV.3.3. Interaction between polyzwitterion coated AuNRmins and cells

Incubation of polyzwitterion-coated AuNRmin with RAW264.7 cells:

RAW267.4 cells were incubated in a 12-well plate until they covered approximately 60% of the surface of the well. The polyzwitterion-coated AuNRmins were introduced into the culture media to achieve a final concentration of 0.25 nM. And cells were exposed to AuNRmins for 24h. At the end of the experiment, wells were gently washed with calcium-free PBS three times. Then cells were removed from the wells by cell scraper and vigorous pipetting and pelleted in a 1.5 ml centrifuge tube. The number of cells was measured by an automated cell counter (LUNA II ™). The supernatant was separated by centrifugation, and the pellets with cells were frozen at −20 °C until analysis.

Gold nanoparticles lack inherent fluorescence and can quench the fluorescence of dye molecules attached to their surface. Therefore, to investigate the uptake of AuNRmin nanoparticles coated with different polyzwitterions by macrophages, collected cell samples were analyzed using ICP-MS to quantify the gold concentration in each sample (in ppb, µg/kg). This analysis was conducted in collaboration with Benoît Caron and Julie Noël from Institut des Science de la Terre de Paris. The measured gold concentration in each cell sample was then converted to the number of internalized AuNRmin nanoparticles per cell. The results, shown in **Figure.IV.43**, revealed that the macrophage uptake of AuNRmin nanoparticles coated with pSPE was the lowest, while those coated with PC

exhibited approximately 5 times higher uptake. Notably, the macrophage uptake of pSPP-coated AuNRmin nanoparticles was significantly higher compared to the other polyzwitterion coatings. It is worth mentioning that the observed partial aggregation of pSPP-coated AuNRmin nanoparticles, as indicated by DLS measurements, may have facilitated their recognition, capture by macrophages and pelleting under centrifugation. This could explain the high value observed with pSPP-coated gold particles.

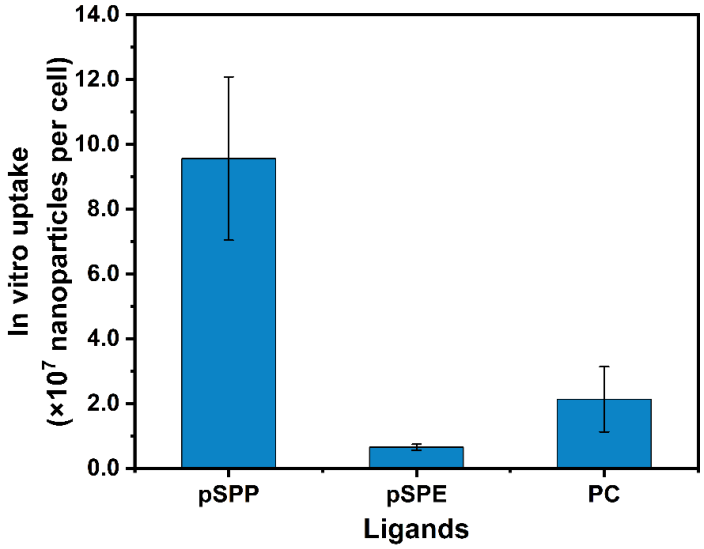

Figure.IV.43. *In vitro* macrophage uptake of AuNRmins covered by different polyzwitterions over 24 h.

IV.4. *In vivo* study of pharmacokinetics and biodistribution of polyzwitterion-coated AuNRs

Injection of polyzwitterion-coated AuNRmins and sample collection:

Polyzwitterion-coated AuNRmins were dispersed in saline solution ([NaCl] = 0.9% w/v) to have a concentration of 40 nM. 100 µL of AuNRmin solution was injected to nude mice intravenously via the tail vein (approximately 2.4 trillion of nanoparticles, 60.8 µg of Au for each injection). The blood samples of 1 min, 20 min, 40 min, 60 min, 120 min, 240 min were collected from the tail vein as well with a volume between 10 – 50 µL for each sample. 24h after injection, mice were euthanized and collected samples included: blood, liver, spleen, kidneys and brain.

Determination of gold concentration in collected samples by ICP-MS:

The collected samples were weighed and placed in 50 mL plastic tubes. Then, 2 mL of nitric acid (67 wt.%) was added to each tube, and the samples were digested at 70 °C for 2 hours in closed tubes. After digestion, the samples were dried overnight at 80 °C. The dried samples were then re-dispersed in a 2% nitric acid solution, and the volume of each sample was adjusted according to its initial weight to achieve a gold concentration within the range of the calibration curve. A standard curve for gold was prepared using concentrations ranging from 0.1 to 50 ppb (µg/kg), with a reference blank of 0.0 ppb. A series of samples collected from a mouse that did not receive nanoparticle injection was prepared as a "bio-blank" reference. All samples, including blood, liver, kidneys, spleen, and brain, were analyzed using an Agilent 8900 triple quadrupole ICP-MS (ICP-QQQ) specifically set to measure gold (Au 197). Each sample was measured five times, and the relative standard deviation (RSD, %) between each measurement was kept below 3%.

The *in vivo* experiments were performed in collaboration with Christophe Leboeuf and Guillaume Gapihan from Université de Paris 13. Five groups of nude mice were prepared, and each group contains four mice. For the first four groups, AuNRmins covered by pSPP, pSPE, pPC and PEG for reference were injected. For the last group, AuNRmins coated by pSPP were injected together with free pSPP ligands (1 g/L). These polyzwitterion-coated AuNRmins were injected to mice intravenously at the tail vein, followed by a successive collection of blood samples at 1, 20, 40, 60, 120 and 240 minutes after injection.

The collected samples were analyzed by ICP-MS at ISTeP (Sorbonne Université) with the help of Julie Noel and Benoit Caron to determine the gold concentration in the blood and organs. With the blood samples collected at different time, we can determine the blood pharmacokinetics of functionalized AuNRmins along with their blood circulation time. By analyzing the samples of different organs, we can have an idea of the biodistribution of AuNRmins.

IV.4.1. Blood pharmacokinetics of AuNRmins covered with different polyzwitterions

The injected quantity of AuNRmins varied among the mice, so it was necessary to normalize the gold concentration of different samples before comparing the blood pharmacokinetics within and between different mice and groups. To achieve this, the gold concentration in the blood sample collected 1 minute after injection was used as the reference for each mouse. For each group of mice, the average values of the gold concentration at each time point were calculated and plotted as a function of time

(**Figure.IV.44**). In general, in all the cases, most of the injected nanoparticles were eliminated from the bloodstream 4h after injection. Additionally, the results showed that AuNRmins coated with pSPP and PEG ligands were rapidly cleared from the bloodstream, with only 10% of the nanoparticles remaining after 20 minutes. In contrast, AuNRmins coated with pSPE exhibited a longer blood circulation time, with approximately 30% of the nanoparticles still present in the bloodstream after 60 minutes.

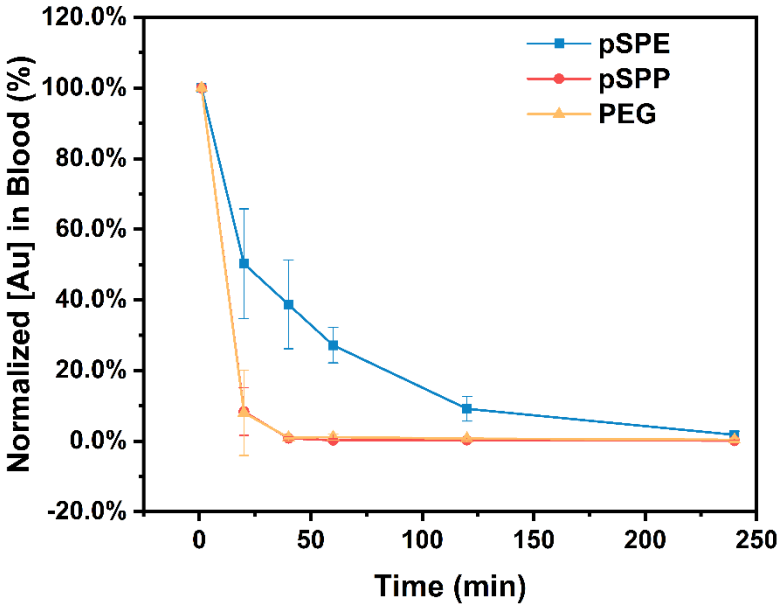

Figure.IV.44. Gold concentration in the blood normalized to the gold concentration at t=1 min as a function of circulation time after injection of AuNRmins functionalized with different polymer ligands.

In the group of mice injected with pPC-coated AuNRmins, the gold concentration in the blood samples collected at 1 minute after injection was found to be outside of the calibration range established for ICP-MS analysis. To address this issue, we used the gold concentration determined at 20 minutes as a reference point for the blood pharmacokinetics analysis. By comparing the blood pharmacokinetics of pPC-coated AuNRmins with that of pSPE-coated AuNRmins (**Figure.IV.45**), we observed that the gold concentration in the blood for both types of nanoparticles decreased in a similar manner over time. This indicates that despite the higher macrophage uptake observed for pPC-coated AuNRmins than for pSPE-coated AuNRmins *in vitro*, the difference in their *in vivo* blood circulation time was not significantly different.

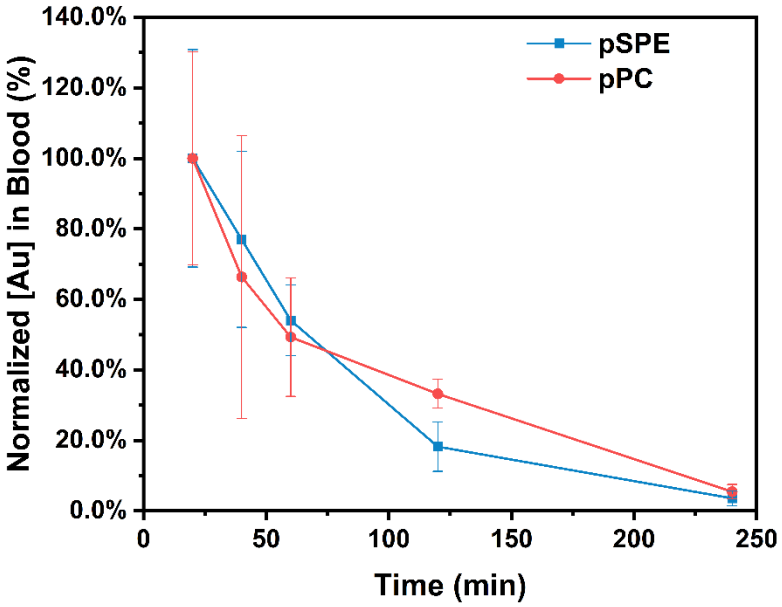

Figure.IV.45. Gold concentration in the blood normalized to the gold concentration at t=1 min as a function of circulation time after injection of AuNRmins functionalized with different polymer ligands.

In addition, as shown in **Figure.IV.46**, co-injection of free pSPP together with pSPP-coated AuNRmins can extend the blood circulation time of nanoparticles, with a slower clearance rate compared to AuNRmins injected without free pSPP ligands. This result is in accordance with what we observed in cell experiments *in vitro*.

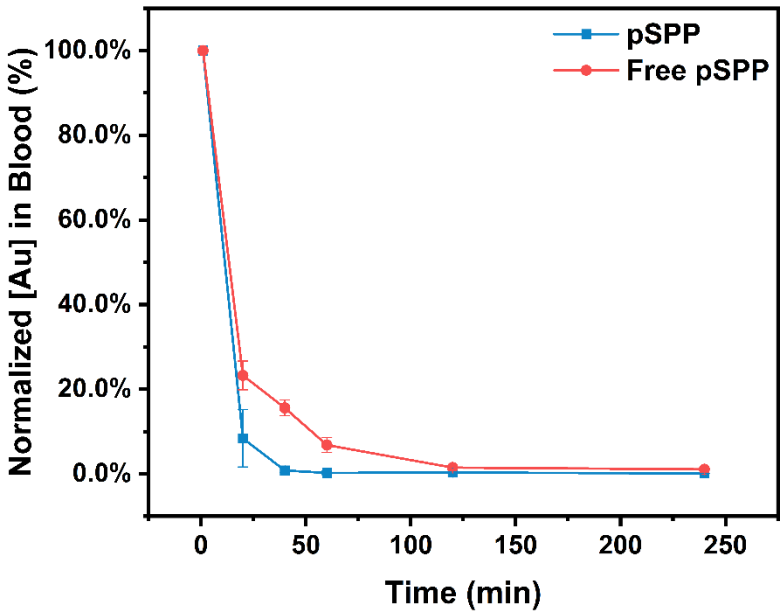

Figure.IV.46. Normalized gold concentration in the blood as a function of circulation time after injected with AuNRmins functionalized with pSPP with or without free pSPP ligands.

IV.4.2. Biodistribution of AuNRmins covered with different polyzwitterions

The biodistribution of AuNRmin after injection was evaluated by measuring the concentration of gold in the organs and blood after 24h of injection. The measured gold concentration in the samples were also normalized according to the gold concentration of blood sample at 1 min. As shown in the

Figure.IV.47, 24h after the injection of nanoparticles, the low gold concentration in the bloodstream is observed in all the five groups, indicating that nanoparticles have been removed from the blood circulation system. Most of the nanoparticles have been retained in the liver and the spleen, as evidenced by a high gold concentration detected in these organs, suggesting that nanoparticles functionalized with polyzwitterions can still be recognized and captured by macrophages during the blood circulation. Besides, AuNRmins were not only captured by the liver, an important amount of AuNRmins were also retained in the spleen, meaning that the macrophages in the spleen may also play an important role in capturing the nanoparticles. Additionally, a low gold concentration was found in the brain, indicating that these functionalized AuNRmins could not pass through the blood-brain barrier.

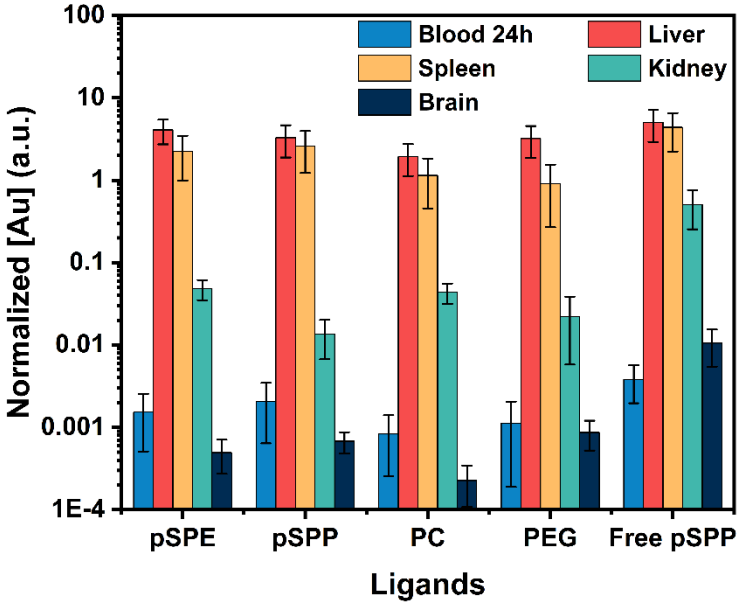

Figure.IV.47. Normalized gold concentration in the blood and organs of mice collected 24h after the injection of AuNRmins functionalized with different polymer ligands.

Overall, these *in vivo* experiments suggest that the *in vivo* macrophage capture and blood clearance of pSPE and pPC are similar, and slower than those of pSPP or PEG coated gold AuNRmins. Coinjection of free pSPP polymers slow down the blood clearance of pSPP coated AuNRmins. After 24h, most AuNRmins are located in the liver and spleen, consistently with an uptake by macrophages.

IV.5. Conclusions and perspectives

In this chapter, the objective was to study the interaction between polyzwitterion-coated nanoparticles and macrophages. We prepared various types of polyzwitterion ligands to functionalize inorganic nanoparticles including QDs, IONPs and AuNRs. Different anchoring groups, ligand exchange process and characterization methods were adapted according to the nature of the nanoparticles. These functionalized nanoparticles showed good stability in physiological solutions containing salts and proteins. Afterwards, we studied the interaction of functionalized nanoparticles with macrophages.

For polyzwitterion-coated QDs, we showed that RAW264.7 macrophages are more likely to capture nanoparticles than HeLa tumor cells. The recognition and capture of pSPP-coated QDs by

macrophages is likely mainly due to the interaction between the pSPP polyzwitterion ligands at the surface of QDs and the macrophages. Therefore, the addition of free pSPP polymer could competitively interact with macrophages and thus reduce the uptake of nanoparticles. Besides, in comparison to QDs covered with pSPP, QDs covered with pSPE are less captured by macrophages.

For polyzwitterion-coated IONPS, we first confirmed that the nanoparticles were mainly internalized by macrophages using energy-dependent internalization pathways instead of merely adsorbing at the surface of cells. Next, the decrease of uptake of pSPP-coated IONPs was also observed in the presence of free pSPP polymer during the incubation. Consistently with the observation of QDs, pSPE coated IONPs also exhibit a lower cell uptake rate than those coated with pSPP ligands.

For polyzwitterion-coated AuNRmins, we compared the macrophage uptake of AuNRmins coated with different polyzwitterions. We found that pSPE-coated AuNRmins exhibited the lowest uptake rate, while AuNRmins coated with pSPP and pPC showed higher uptake rates by macrophages. Furthermore, we conducted *in vivo* experiments by injecting these AuNRmins into mice and analyzing the gold concentration in the blood samples collected over time. The results indicated that AuNRmins coated with pSPE and pPC had longer blood circulation times compared to other coated nanoparticles. Interestingly, when free polymer ligands were injected along with the nanoparticles, the blood circulation time was further extended, which aligned with our *in vitro* findings. Despite the protection provided by the polyzwitterion ligands, a significant portion of the injected nanoparticles were eventually captured by the liver and spleen, indicating the crucial role of the immune system, particularly macrophages, in recognizing and capturing nanoparticles.

Further studies could be performed to confirm these trends of recognition of polyzwitterion-coated nanoparticles with zwitterions, wither other macrophage cell lines or primary cultures, or by testing different polymer length and/or surface density on nanoparticles. Moreover, it is important to investigate factors that contribute to the macrophage uptake of polyzwitterion-coated nanoparticles. This includes studying the influence of nanoparticle shape and size on uptake, polymer density at the nanoparticle surface, potential production of antibodies against the surface ligands, and the enzymatic degradation of polymer ligands in the blood.

Advancements in technology, such as organ-on-a-chip systems, offer promising opportunities for studying nanoparticle-immune system interactions in a more physiologically relevant setting. For example, by integrating engineered or natural miniature tissues within microfluidic chips, one can simulate realistic conditions and examine the effects of shearing forces on nanoparticles circulating in flowing blood. This approach enables better replication of human physiology and reduces the consumption of experimental animals, while allowing control over cell microenvironments and the maintenance of tissue-specific functions.

In future research, there are several avenues to explore for further improvement and understanding of polyzwitterion-coated nanoparticles. One approach is to enhance the functionality of the polyzwitterion ligands by incorporating additional functional groups that specifically target proteins, receptors, or the tumor microenvironment. This targeted approach can facilitate rapid accumulation of nanoparticles at the tumor site, improving nanoparticle delivery efficiency before clearance from the bloodstream.

General conclusions and perspectives

Conclusions

This thesis is dedicated to developing hybrid AuNR/semiconductor nanoparticles for applications in photodynamic therapy.

In Chapter II, we synthesized AuNR/TiO_2 dumbbell shaped nanoparticles. In this hybrid nanostructure, under illumination, excited hot electrons within AuNRs can be injected into the conduction band of TiO_2 via charge transfer pathway. We firstly demonstrated that the dumbbell morphology of these nanoparticles, which is important for their photoactivity, can be achieved by finely tuning the pH value of the system during the synthesis of nanoparticles. This type of hybrid nanoparticles is proved to be able to produce hydroxyl radicals under irradiation of NIR laser. We further found that the radical production rate is proportional to the laser intensity, suggesting the production of hydroxyl radicals is mediated by a one-photon excitation process. Then we chose a polyethylene glycol based copolymer to functionalize the surface of the nanoparticles. These polymer ligands improved the colloidal stability of nanoparticles but their density at the surface also influences the photoactivity of nanoparticles. Finally, under irradiation, we found that these AuNR/TiO_2 nanoparticles can efficiently kill cancer cells. We confirmed that the observed cell death is mainly induced by the photodynamic effect of nanoparticles, rather than their photothermal effect.

In Chapter III, we combined AuNRs with semiconductors whose band gap energy overlaps the longitudinal plasmon absorbance band of AuNRs. For this hybrid structure, the absorbed light energy of AuNRs was transferred to the semiconductor via a dipole-dipole interaction and eventually excites electrons at the valence band of the semiconductor to the conduction band. These excited electrons can be utilized to produce reactive oxygen species. Initially, we synthesized AuNR@Ag_2S core-shell nanoparticles, but these nanoparticles did not demonstrate efficient production of hydroxyl radicals when exposed to NIR light. To address this issue, we introduced a silica layer between the AuNRs and Ag_2S, resulting in the formation of AuNR@SiO_2@Ag_2S hybrid nanostructures. The silica layer acted as an insulator, preventing the back transfer of excited electrons from the conduction band of Ag_2S to the AuNRs. As a result, the AuNR@SiO_2@Ag_2S nanoparticles exhibited improved hydroxyl radical production under NIR light irradiation. In contrast, when Cu_2S was used as the semiconductor instead of Ag_2S, efficient production of hydroxyl radicals was not observed. However, the AuNR@SiO_2@Cu_2S nanoparticles demonstrated a higher light-to-heat conversion efficiency, which was attributed to the energy transfer process taking place within the hybrid structure.

In Chapter IV, we studied the interaction between polyzwitterion-coated nanoparticles and macrophages. In the laboratory, polyzwitterion ligands have been successfully applied to functionalize QDs and IONPs. Based on these results, we designed and prepared polyzwitterions to functionalize AuNRs. Then we incubated these polyzwitterion-coated nanoparticles (QDs, IONPs and AuNRs) with macrophages and cancer cells. Our findings demonstrate that macrophages exhibit a higher uptake efficiency of nanoparticles compared to cancer cells. This uptake is primarily mediated by the interaction between polyzwitterion ligands and macrophage cells and is influenced by temperature. Importantly, the presence of free polymer ligands in the cell culture media competes with nanoparticles for interaction with macrophages, resulting in a reduced uptake rate. This phenomenon was observed in polyzwitterion-coated QDs and IONPs *in vitro*, as well as in polyzwitterion-coated AuNRs *in vivo*. Furthermore, we compared the effects of different polyzwitterion ligands composed of sulfobetaine (SPP and SPE) and

PC, on the macrophage uptake rate of nanoparticles. Our results indicate that pPC-based ligands induce a higher macrophage uptake rate *in vitro*, while pPC-coated AuNRs exhibit a relatively long blood circulation time after intravenous injection into mice. Finally, our *in vivo* experiments reveal that a significant proportion of the injected AuNRs is ultimately captured by the liver and spleen, indicating the continued recognition and capture of these functionalized AuNRs by the immune system.

Perspectives

In this thesis, one of the objectives is to explore AuNR/semiconductor hybrid nanostructures that utilize absorbed plasmon energy to produce ROS, in particular, the hydroxyl radicals.

The AuNR/TiO_2 hybrid nanostructure exhibits the ability to produce hydroxyl radicals through a one-photon excitation pathway, making it compatible with the use of a continuous wave laser for irradiation. This feature offers advantages in terms of simplicity and convenience compared to pulsed laser systems, which is beneficial for further applications in PDT. Future studies can focus on evaluating the PDT effect of these nanoparticles *in vivo*. It is worth considering the size of the AuNRs used to synthesize AuNR/TiO_2 nanoparticles, as they are relatively large (85 * 25 nm^2). To enhance the delivery of nanoparticles to the target tumor zone, smaller AuNRs can be utilized. However, it is important to note that the use of smaller AuNRs may pose challenges in the synthesis of dumbbell-shaped AuNR/TiO_2 nanoparticles. Optimization of the synthesis conditions, particularly the choice of surfactant, is necessary to achieve the desired smaller AuNRs.

In the case of AuNR@SiO_2@Ag_2S(Cu_2S) hybrid nanoparticles, their quantum yield in producing hydroxyl radicals is relatively low (~10^{-7}). To enhance their photoactivity, the thickness of the insulator layer can be optimized to ensure the grafted semiconductors are positioned in the enhanced electromagnetic field while minimizing the back transfer of excited electrons. Next, the semiconductors that are selected to be grafted at the surface of silica shell can be further optimized to gain a better photocatalytic capacity. Additionally, efficient transfer of the excited electrons in the conduction band to the surface of the semiconductor is essential to facilitate contact with oxygen or water molecules for effective photochemical reactions. For a good contact between electrons and oxygen, the design of surface ligands also plays a crucial role. Moreover, as the excited electrons are consumed during photochemical reactions, the positively charged holes left in the valence band of the semiconductor must be compensated to maintain balanced charge within the materials. Introducing reductive molecules into the system to capture the positively charged holes could be a potential solution to further improve the photocatalytic efficiency.

On the other hand, we have successfully developed a surface functionalization strategy for inorganic nanoparticles using polyzwitterions, particularly sulfobetaine. These polyzwitterion ligands have shown great potential in stabilizing nanoparticles in physiological environments and reducing the formation of protein corona on their surfaces. To further enhance their functionality, we can explore the incorporation of specific functional groups that can target tumor zones or cells, allowing for more precise and efficient delivery of nanoparticles to the desired locations. In addition to surface functionalization, alternative administration methods can be considered to improve the delivery efficiency of nanoparticles. Intratumoral injection, for example, enables direct delivery of nanoparticles to the tumor zone, bypassing the need for systemic circulation. This approach can enhance the accumulation of nanoparticles at the tumor site, increasing their effectiveness in targeted therapy. To mitigate the recognition and capture of

nanoparticles by the immune system, we can saturate macrophages by introducing excess free polymer ligands. This saturation can help nanoparticles evade detection and capture by the immune system, potentially improving their circulation time and biodistribution. Careful optimization of the ligand dose and size can minimize the risk of toxicity and side effects associated with excessive ligand usage. Furthermore, the development of techniques and devices that can simulate physiological environments and maintain tissue-specific functions can provide a more comprehensive understanding of the interactions between nanoparticles, polymer ligands, and the immune system. These advancements can help us gain insights into the intricate dynamics of nanoparticle-cell interactions.

Annex

V.1. Synthesis of nanoparticles

V.1.1. Synthesis of AuNRs

a. Seed-growth approach

To prepare the seed growth solution for AuNR growth, $HAuCl_4$ solution (25 mM, 200 µL) was mixed with cetyltrimethylammonium bromide (CTAB) solution (0.1 M, 7.5 mL) under stirring in a 20 mL scintillation vial. Then 100 µL of fresh $NaBH_4$ solution (0.1 M) was diluted in 900 µL of Milli-Q® water, and 600 µL of this newly prepared $NaBH_4$ solution (0.01 M) was rapidly injected into the Au(III) – CTAB solution under vigorous stirring (1200 rpm). The stirring was stopped after 2 min, and the seed solution was aged for at least 30 min before use.

To prepare the growth solution, CTAB – Sodium Oleate (NaOL) binary surfactant solution was firstly prepared and heated to 60 °C (CTAB: 37 mM – 85 mM, NaOL 0.008 M). 19.6 mL of this surfactant solution was added to a 20 mL scintillation vial and cooled down to 30 °C. Freshly prepared $AgNO_3$ solution (0.1 M, 20 – 40 µL) was then added, followed by $HAuCl_4$ solution (25 mM, 400 µL). The mixture was kept undisturbed at 30 °C for 90 min and then 50 – 100 µL of HCl (37 wt. % in water, 12 M) was introduced. After 15 min of slow stirring, fresh ascorbic acid solution (0.064 mM, 50 µL) was added to the mixture, followed by 30 s vigorous stirring. Finally, 10 – 20 µL of seed solution was injected. The final mixture was stirred for 30 s and left undisturbed at 30 °C for 17h. The synthesized AuNRs were precipitated under centrifugation (3400 g, 20 min), washed twice with distilled water, and stored in 4 mM CTAB solution.

Table.V.1. Summary of conditions used for AuNR synthesis and the AuNR morphology information measured from TEM images.

No.	HCl mM	CTAB mM	Seed µL	$AgNO_3$ mM	Length nm	Diameter nm	Aspect Ratio
1	24	62	10	0.15	61.0±5.9	12.3±1.0	5.0±0.6
2	36	62	10	0.15	62.1±4.6	11.4±1.1	5.5±0.6
3	48	62	10	0.15	70.2±7.0	11.3±0.9	6.3±0.8
4	30	48	10	0.15	81.0±6.3	22.8±1.6	3.6±0.4
5	30	62	10	0.15	81.4±7.9	17.9±1.3	4.6±0.5
6	30	82	10	0.15	84.3±8.9	15.8±1.6	5.4±0.8
7	30	48	10	0.125	74.1±9.8	22.4±1.4	3.3±0.5
8	30	48	10	0.175	87.7±9.1	22.8±1.9	3.9±0.6
9	30	48	15	0.15	77.0±6.8	20.1±2.1	3.9±0.1
10	30	48	20	0.15	78.3±6.6	19.2±1.8	4.1±0.4

b. Seedless growth synthesis of miniaturized AuNRs

In a 20 mL scintillation vial, to 10 mL of preheated CTAB solution (0.1 M) was added successively 200 µL $HAuCl_4$ solution (25 mM), 20 µL $AgNO_3$ solution (0.1 M), 200 µL HCl (0.1 M).

The resultant solution was stirred for 5 min at 400 rpm. 500 µL of hydroquinone (0.1 M) was added into vial under stirring. 18 µL of freshly prepared $NaBH_4$ solution (0.01 M) was then added into the vial followed by 30 s vigorous stirring. The final mixture was stirred for 30 s and left undisturbed at 30 °C for 17h. The synthesized AuNRs were precipitated under centrifugation (5000 g, 30 min), washed twice with distilled water, and stored in 4 mM CTAB solution.

V.1.2. Synthesis of AuNR/TiO_2 nanoparticles

a. Synthesis of dumbbell-shaped AuNR/TiO_2 nanoparticles

The previously prepared AuNR solution (0.7 nM, 1 mL) was mixed with CTAB solution (0.2 M, 1 mL) and 2.6 mL of distilled water. Then, in another 20 mL of scintillation vial, $TiCl_3$ solution (12 – 14 wt. %, 400 µL) was added into 8 mL distilled water. A certain quantity of $NaHCO_3$ solution (0.1 M, 900 – 1000 µL) was introduced drop by drop under vigorous stirring. At this step, the color of solution turned from violet to dark blue. The prepared AuNR solution was quickly injected into the dark blue solution. The resultant mixture was kept under stirring (100 rpm) for 20 min under room temperature. The AuNR/TiO_2 nanoparticles were precipitated under centrifuge (3400 g, 10 min), washed with water once and then with ethanol twice, and finally stored in ethanol.

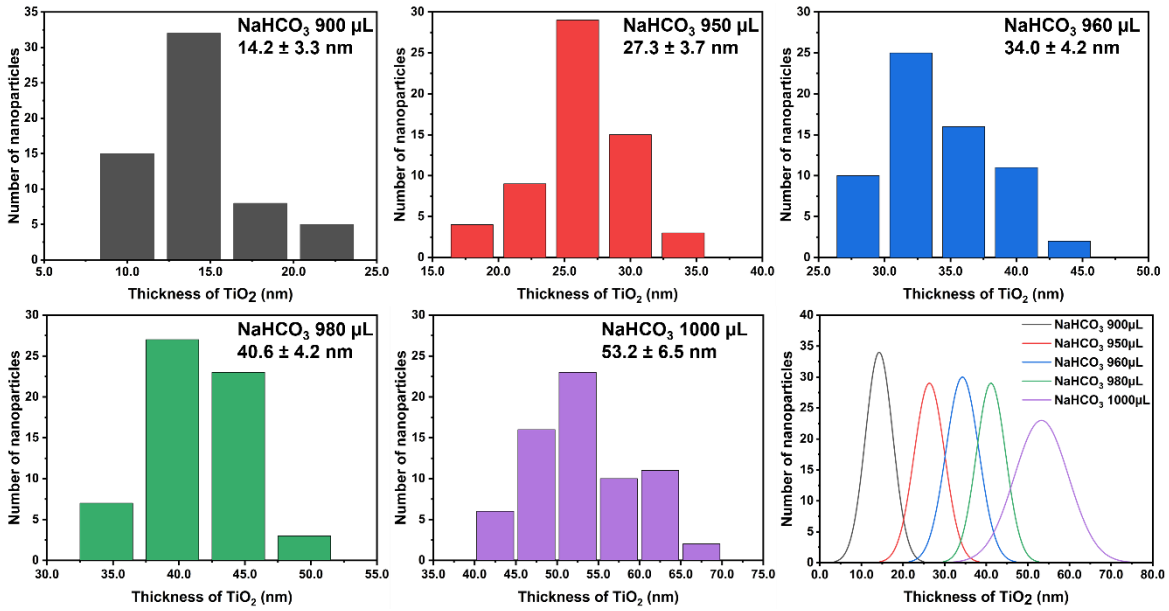

Figure.V.1. Distribution of the thickness of TiO_2 layer measured by TEM images.

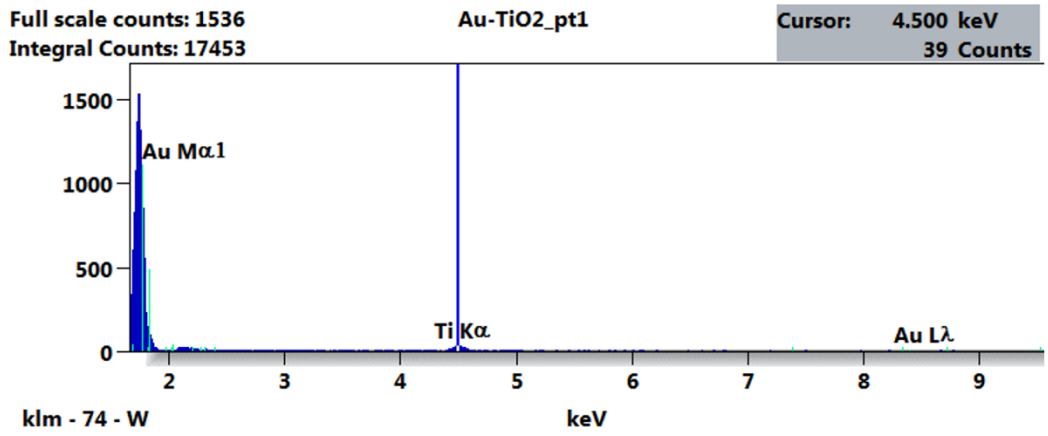

	O-K	Ti-K	Au-L
Net Counts	235	439	80
Intensity	7.83	14.62	2.66
Atom %	81.8±7.0	13.4±1.1	4.8±1.3

Figure.V.2. SEM-EDX analysis of AuNR/TiO_2 nanoparticles synthesized with 950 µL of $NaHCO_3$ (0.1 M).

b. Synthesis of Core-shell shaped AuNR/TiO_2 nanoparticles

AuNRs separated from the growth solution were dispersed into sodium dodecyl sulfate solution (0.1 M), the suspension was left for over 30 min and then precipitated (3400 g, 10 min) and washed once with distilled water. Then the SDS-stabilized AuNRs were used for the deposition of TiO_2 layers with the same protocol of dumbbell shaped AuNR/TiO_2 nanoparticles, except a longer reaction time for about 2 hours.

V.1.3. Synthesis of Cu_2S/Ag_2S nanoparticles

The synthesis of Ag_2S and Cu_2S nanoparticles follow the same protocol proposed by Zhang et al.[212].

Typically, to a 20 mL of scintillation vial was added subsequently 10 mL of distilled water, 1.4 mg of $CuCl_2$ (0.01 mM) or 1.769 mg of $AgNO_3$ (0.01 mM) and 2 mg of sodium citrate (0.007 mM). Next, under vigorous stirring, 200 µL of Na_2S solution (0.04 M) was added. The resulting solution was homogenized under stirring for 5 min and then heated at 90 °C for 30 min. The obtained nanoparticles were purified by centrifugation (12200 g, 5 min) using Vivaspin® 100k Centrifugal Concentrator.

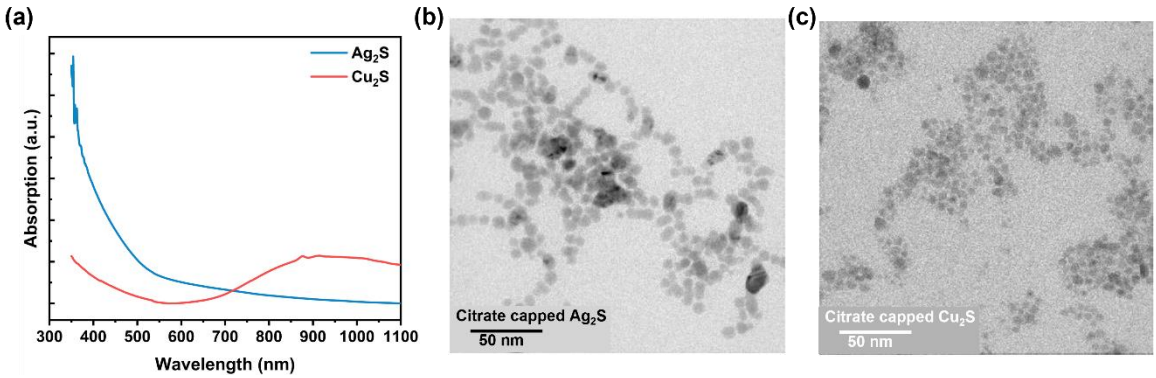

Figure.V.3. (a). UV-vis spectra of synthesized Ag_2S and Cu_2S nanoparticles stabilized in citrate solution. (b, c). TEM images of citrate capped Ag_2S nanoparticles and Cu_2S nanoparticles.

V.2. Ligand synthesis

V.2.1. Synthesis of Caffeic acid-PEG5k

In a 50 mL round-bottomed flask, caffeic acid (10.8 mg, 0.06 mmol), N,N′-Dicyclohexylcarbodiimide (DCC, 18.6 mg, 0.09 mmol), N-Hydroxysuccinimide (NHS, 10.4 mg, 0.09 mmol), amino-poly(ethylene glycol) (PEG5k-NH_2, 5000g/mol, 300 mg, 0.06 mmol) were introduced and dissolved in 30 mL of anhydrous dichloromethane (DCM). Then 20 µL anhydrous triethylamine (TEA) were added into the mixture. The resultant solution was left stirring at 400 rpm at 25 °C for 2 h. TLC of the final product can be performed after 2 h, using PEG5k-NH_2 as a co-spot to determine if the reaction is complete. The solvent of the collected fractions was evaporated by a rotary evaporator. The product is further dried by using a vacuum pump. ^{1}H NMR (400 MHz, $CDCl_3$): δ 1.1–1.2 (a, t, 3H), 3.50 (b, s, 500H), 6.35-6.40 (c, d, 1H), 6.8 (g, m, 1H), 7.0 (e, m, 1H), 7.08 (f, d, 1H), 7.0-7.4 (d, d, 1H). (**Figure.V.4**) The typical yield of this reaction is approximately 50%.

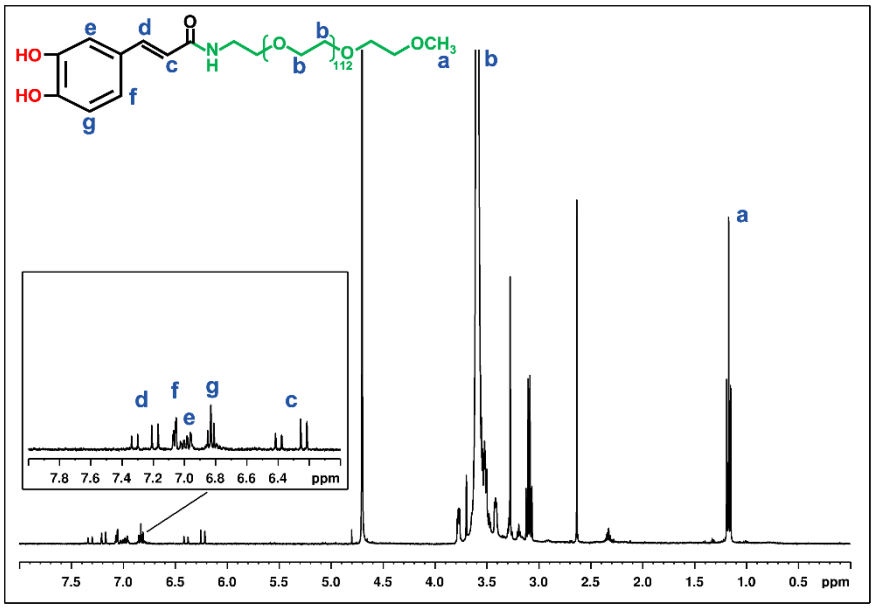

Figure.V.4. ^{1}H NMR spectrum of synthesized PEG-Caffeic acid ligand.

V.2.2. Synthesis of Silane-SPP

To 4.45 g of propane sultone in 37 mL of acetone under argon was added 7.5 g of (N,N dimethyl-3-aminopropyl)trimethoxysilane. The reaction was stirred vigorously for 6 h. The white precipitate was collected by vacuum filtration and washed twice with acetone. The white solid was dried and stored under Ar. The typical yield of this reaction is approximately 90%. ^{1}H NMR (400 MHz, D_2O): δ 0.5-0.6 (b, m, 2H), 1.7-1.9 (c, m, 2H), 2.0-2.2 (g, m, 2H), 2.8-2.9 (d, t, 2H), 3.0 (e, s, 6H), 3.3-3.4 (f, m, 2H), 3.5 (H, m, 2H), 3.3-3.4 (a, s, 9H).

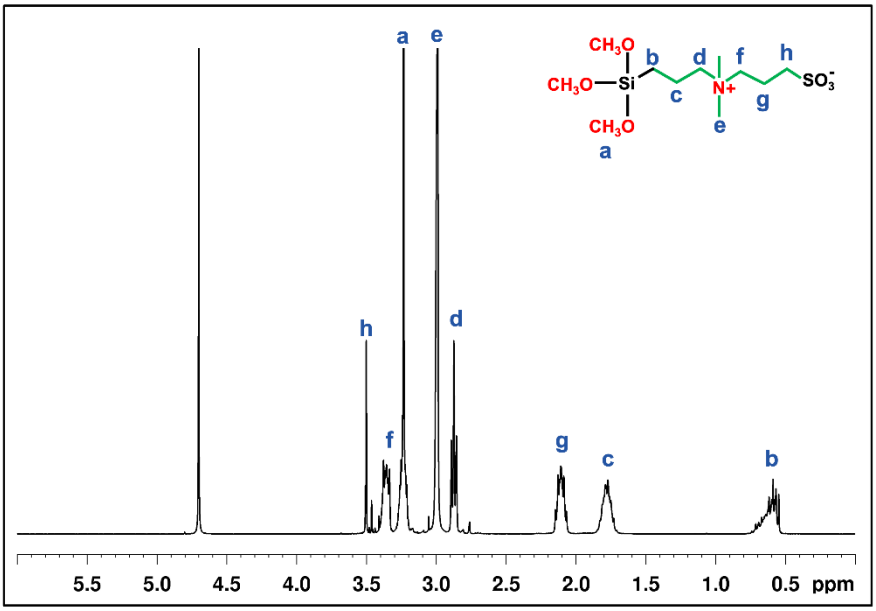

Figure.V.5. ^{1}H NMR spectrum of synthesized Silane-SPP ligand.

V.2.3. Synthesis of Phosphonic acid-PEG5k

The preparation of PEG-pPA polymer ligands contains two steps.

1. PEG5k-CADB: Typically, in a 50 mL round-bottomed flask, 4-Cyano-4-(phenylcarbonothioylthio) pentanoic acid (CADB, 52.8 mg, 0.19 mmol), DCC (46.8 mg, 0.23 mmol), NHS (26.1 mg, 0.23 mmol), PEG5k-NH_2 (5000g/mol, 945 mg, 0.19 mmol) were introduced and dissolved in 30 mL of anhydrous DCM. Then 20 µL anhydrous TEA were added into the mixture. The resultant solution was left stirring at 400 rpm at 25 °C for 4 h. TLC of the final product can be performed after 2-4 h, using PEG5k-NH_2 as a co-spot to determine if the reaction is complete. Using chloroform ($CHCl_3$):methanol(MeOH) = 10:1 (vol/vol) for elution, R_f(CADB) = 0.6, R_f(PEG5k-CADB) = 0.3, R_f(PEG5k-NH_2) = 0.1. The mixture was filtered through a filter paper and the crude product was chromatographed on a silica gel with 10:1 (vol/vol) $CHCl_3$:MeOH as the eluent. The solvent of the collected fractions was evaporated by a rotary evaporator. The pure product is further dried by using a vacuum pump. ^{1}H NMR (400 MHz, $CDCl_3$): δ 3.6–3.7 (m), 7.40 (t, 2H, J = 7.8 Hz), 7.60 (t, 1H, J = 7.3 Hz), 7.90 (d, 2H, J = 8.0 Hz). (**Figure.V.6**) The typical yield of this reaction is approximately 80%.

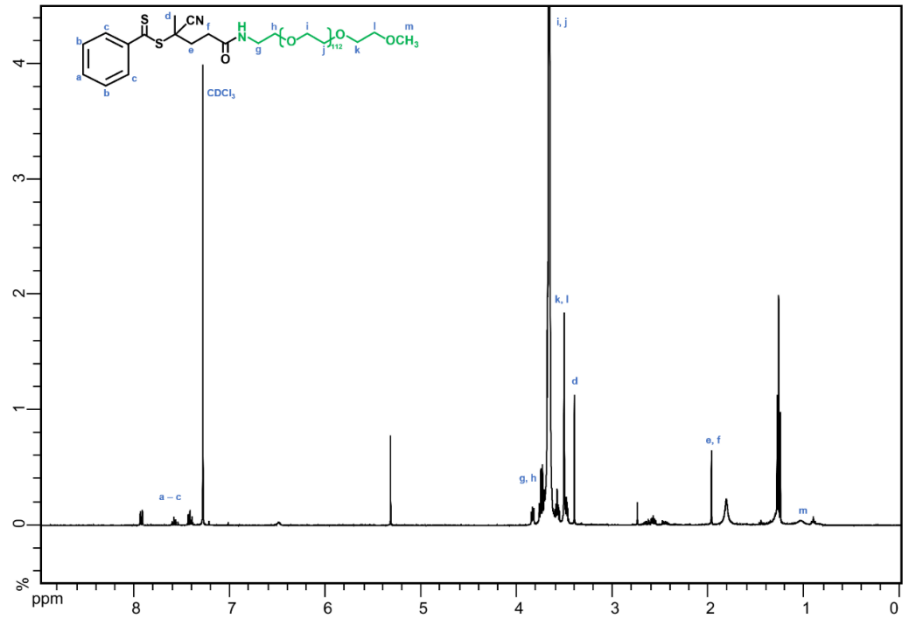

Figure.V.6. ^{1}H NMR spectrum of synthesized chain transfer agent PEG5k-CADB.

2. RAFT Polymerization of (methacryloyloxy)methyl phosphonic acid (PA) block. In a typical synthesis, in a 25 mL round-bottomed flask, PEG5k-CADB (100 mg, 0.02 mmol), (methacryloyloxy)methyl phosphonic acid (28 mg, 0.15 mmol; Specific Polymers), and 2,2′-Azobis(2-methylpropionamidine) dihydrochloride (V50, 5 mg, 0.02 mmol) were dissolved in 5 mL acetic acid. The flask was then sealed and degassed under argon flux. After 30 min, the reactive mixture was heated to 70 °C with an oil bath and kept under stirring (400 rpm) for 5 h. The obtained polymer was precipitated, washed twice with diethyl ether, and finally dried overnight under vacuum. The as-synthesized polymer is characterized by ^{1}H NMR (400 MHz, D_2O). (**Figure.V.7**)

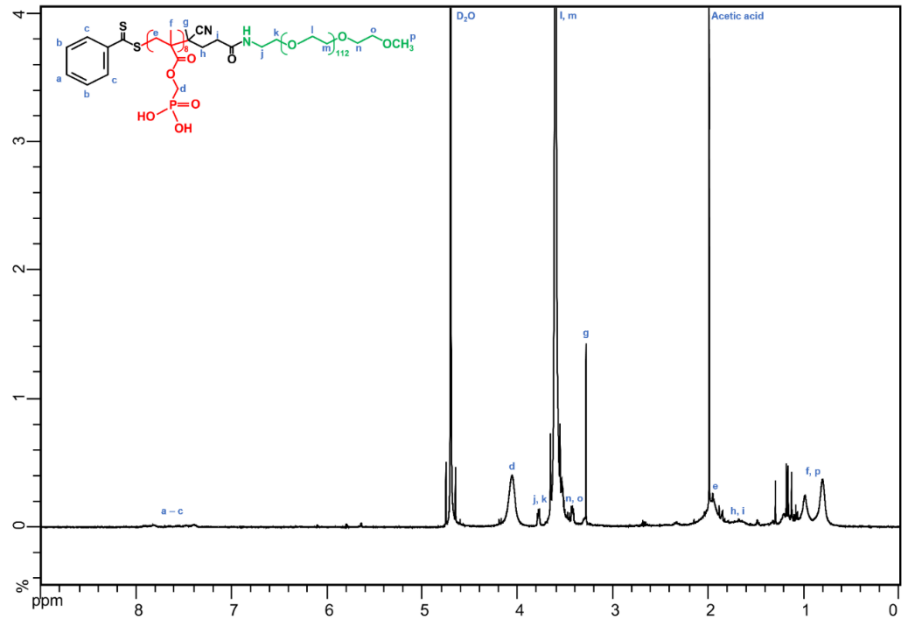

Figure.V.7. ^{1}H NMR spectrum of synthesized hydrophilic polymer PEG5k-pPA.

V.2.4. Synthesis of pSPP-Phosphonic acid

The preparation of pSPP-pPA ligand contains two subsequent RAFT polymerization.

1. Synthesis of Poly(sulfobetaine) (pSPP). To a round-bottomed flask of 250 mL, 3-[3-methacrylamidopropyl-(dimethyl)-ammonio]propane-1-sulfonate (SPP, 9.42 g, 32.4 mmol), V50 (29.1 mg, 0.1 mmol) were added and dissolved in 150 mL of acetate buffer (pH = 5.2, 0.2 M). Then, to a 20 mL scintillation vial, CADB (150 mg, 0.54 mmol) was added and dissolved in 4 mL NaOH (0.2 M), this resultant solution was rapidly added into the mixture of SPP and V50. The flask was then sealed and degassed under argon flux. After 30 min, the reactive mixture was heated to 70 °C with an oil bath and kept under stirring (400 rpm) for 4 h. The obtained polymer was precipitated in acetone, washed twice with diethyl ether, and finally dried overnight under vacuum. The as-synthesized polymer is characterized by ^{1}H NMR (400 MHz, D_2O).

2. Synthesis of Poly(sulfobetaine-b-(methacryloyloxy)methyl phosphonic acid) (pSPP-pPA). To a round-bottomed flask of 50 mL, the synthesized pSPP (1.0 g, 0.07 mmol), (methacryloyloxy)methyl phosphonic acid (70 mg, 0.38 mmol), V50 (20 mg, 0.07 mmol) were added and dissolved in 10 mL of distilled water. The flask was then sealed and degassed under argon flux. After 30 min, the reactive mixture was heated to 70 °C with an oil bath and kept under stirring (400 rpm) for 6 h. The obtained polymer was precipitated in acetone, washed twice with diethyl ether, and finally dried overnight under vacuum. The as-synthesized polymer is characterized by ^{1}H NMR (400 MHz, D_2O).

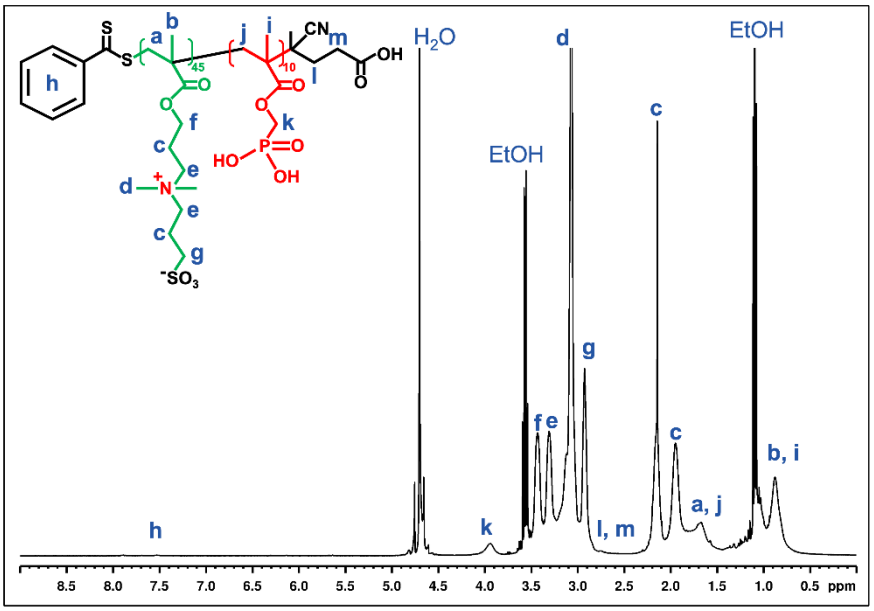

Figure.V.8. ^{1}H NMR spectrum of synthesized hydrophilic polymer pSPP-pPA.

V.2.5. Synthesis of p(SPP-b-VIM)

The synthesized pSPP polyzwitterion was used as a RAFT chain transfer agent in the addition of a terminal bloc of poly(vinylimidazole). Typically, 540 mg of pSPP (Mn = 9000 g/mol, DPn = 30, 0.06 mmol), 56.4 mg of 1-vinylimidiazole (VIM) and 10 mg AIBN (0.06 mmol) were dissolved in 5 mL

of acetic acid. After degassed for 40 min under argon, the mixture was heated up to 70 °C for 6 hours. The resulting copolymer was precipitated in acetone and washed twice with ethanol.

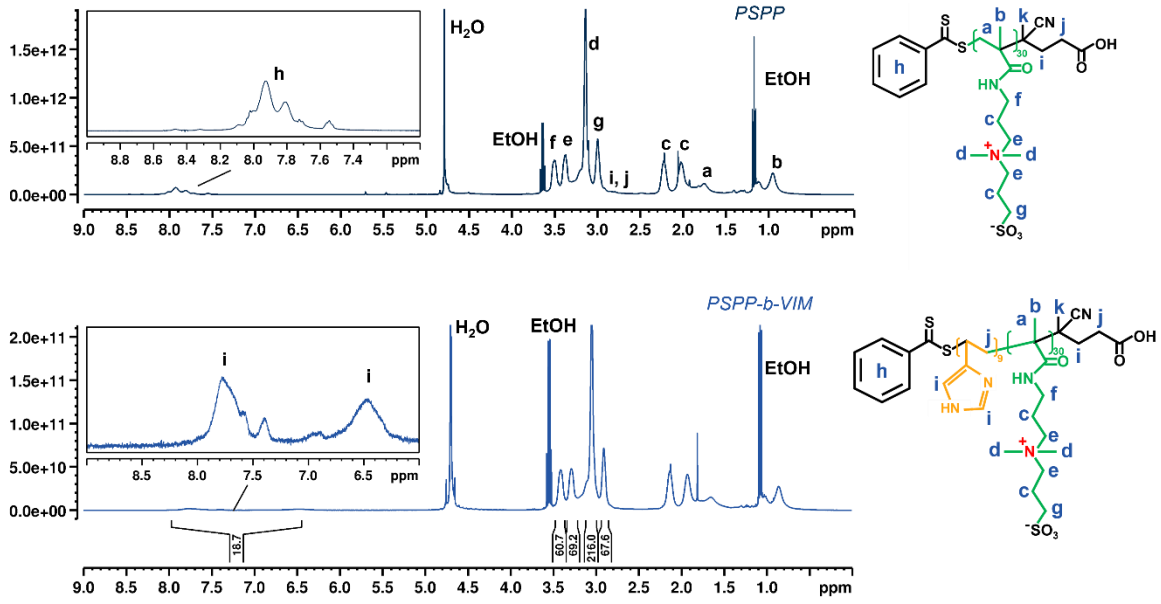

Figure.V.9. ^{1}H NMR spectra of pSPP and synthesized copolymer p(SPP-b-VIM).

V.2.6. Synthesis of TA-PEG1000-N_3

1. Synthesis of N_3-PEG1000-N_3. Add PEG (average M_W = 1000 g/mol) (1.0 g, 0.001 mol), THF (20 ml) and methanesulfonyl chloride (330 mg, 0.003 mol) in a 100 mL two-necked round-bottomed flask equipped with an addition funnel, septa and a magnetic stirring bar. Add triethylamine (0.5 mL, 0.003 mol) to the addition funnel. Purge the reaction vessel with nitrogen and cool the mixture to 0 °C in an ice bath. Add triethylamine dropwise to the reaction mixture through the addition funnel (addition takes 30 min). Warm up the reaction mixture gradually to room temperature and stir for overnight. TLC of the intermediate product (MsO–PEG–OMs, precursor to the bis-azide–PEG) can be performed after 2–4 h using PEG as a co-spot to determine if the reaction is complete. Using $CHCl_3$:MeOH = 10:1 (vol/vol) for elution, R_f(MsO–PEG1000–OMs) = 0.5, whereas R_f(HO–PEG1000–OH) = 0.36. Dilute the mixture with H_2O (20 ml) and add $NaHCO_3$ (84 mg, 0.001 mol). Add sodium azide (195 mg, 0.003 mol) and attach a distilling head with a round-bottomed flask as a solvent trap. Cool the solvent trap with an ice-bath. Heat the biphasic reaction mixture under Ar to distill off the THF, and then reflux overnight. Cool the reaction mixture and transfer to a separatory funnel. Extract the product five times with $CHCl_3$ (30 ml each). Dry the combined organic layers over Na_2SO_4 while stirring, filter through a filter paper and evaporate the solvent using a rotary evaporator; a pale brown oil is obtained.

2. Synthesis of N_3-PEG1000-NH_2. Add N_3-PEG1000-N_3 (1.0 g, 0.001 mol), EtOAc (20 mL) and 1 M HCl (10 mL, 0.06 mol) in a 100 mL two-necked round-bottomed flask equipped with an addition funnel, septa and a magnetic stirring bar. Add triphenylphosphine (0.4 g, 0.0015 mol) and 20 ml of EtOAc into the addition funnel. Purge the reaction vessel with Ar and cool the mixture to 0 °C in an ice-bath while stirring. Add a solution of triphenylphosphine dropwise through the addition funnel under Ar. Maintain the temperature below 5 °C during the addition. Once the addition is complete, let

the reaction mixture gradually warm up to room temperature and stir overnight under Ar. Transfer the reaction mixture to a separatory funnel and separate the biphasic solution. Collect the aqueous layer and wash it with EtOAc (20 mL, two times). Transfer the aqueous layer to a round-bottomed flask equipped with a magnetic stirring bar. Cool the solution in an ice bath. Add KOH (1.5 g, 0.027 mol) slowly to the aqueous solution and stir the mixture until the KOH is dissolved. Transfer the aqueous solution into a separatory funnel and extract the product repeatedly with EtOAc (5 times). Dry the combined organic layers over Na_2SO_4 with stirring and filter off Na_2SO_4 through filter paper. Evaporate the solvent using a rotary evaporator and dry the product under vacuum.

3. Synthesis of TA-PEG1000-N_3. Add N_3–PEG1000–NH_2 (1.0 g, 0.001 mol), 4-(N,N-dimethylamino)pyridine (DMAP, 24 mg, 0.2 mmol), DCC (0.3 g, 0.0015 mol) and CH_2Cl_2 (20 mL) in a 50 mL round-bottomed flask equipped with a magnetic stirring bar and an addition funnel. The mixture should be kept at 0 °C in an ice bath. Add thioctic acid (0.2 g, 0.001 mol) and 10 ml of CH_2Cl_2 into the addition funnel. Add thioctic acid solution dropwise over 30 min under Ar while stirring. Once the addition is complete, let the reaction mixture gradually warm up to room temperature and further leave it stirring overnight. Filter the mixture through celite and rinse the celite plug with CH_2Cl_2. Evaporate the solvent using a rotary evaporator. Add H_2O to the residue. Wash the aqueous mixture with ether (20 mL, two times). Saturate the aqueous layer with $NaHCO_3$. Extract the product with CH_2Cl_2 (20 mL, three times). Dry the combined organic layers over Na_2SO_4. Filter off Na_2SO_4 (using a paper filter) and evaporate the solvent using a rotary evaporator. Chromatograph the residue on silica gel with 10:1 (vol/vol) $CHCl_3$:MeOH as the eluent to collect the product. Evaporate the solvent and dry the product under vacuum.

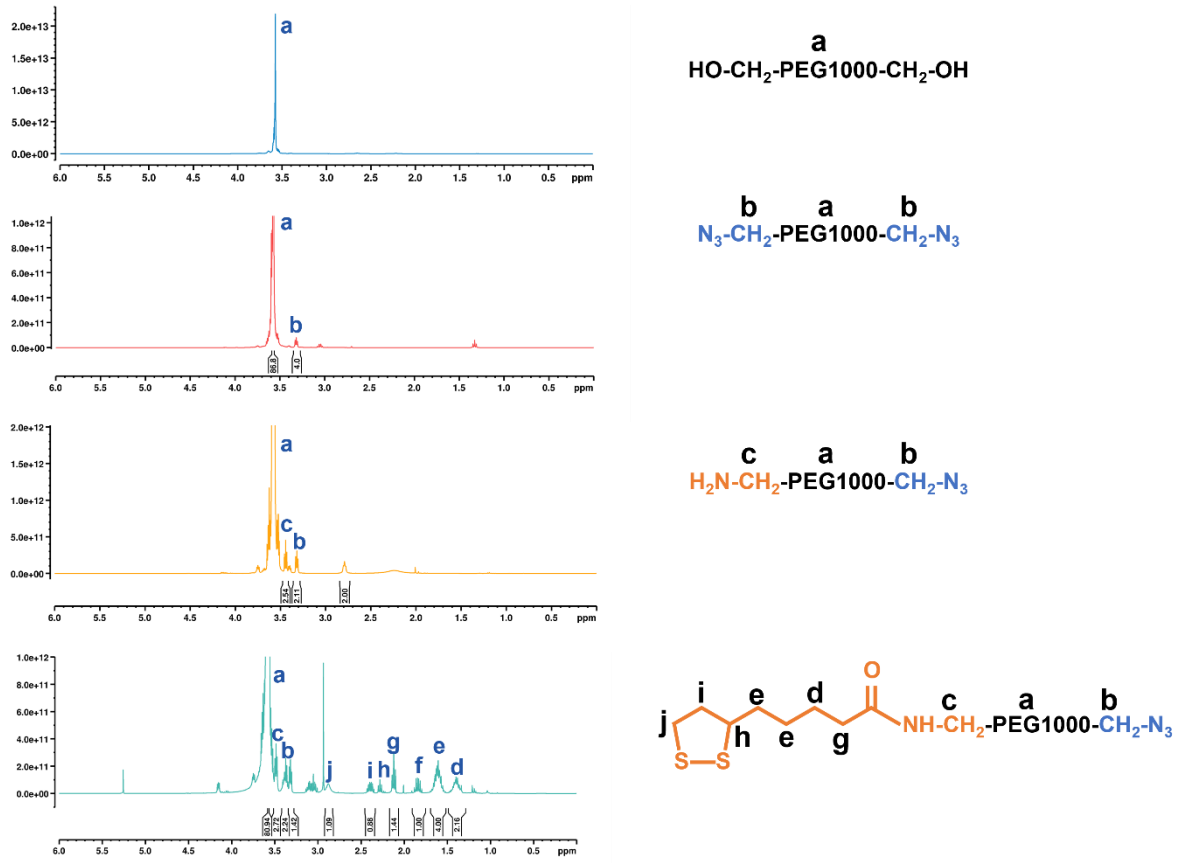

Figure.V.10. ^{1}H NMR spectra of PEG1000, N_3-PEG1000-N_3, N3-PEG1000-NH_2, and TA-PEG1000-N_3.

V.2.7. Synthesis of TA-PEG1k-p(SPE/SPP/PC)-OH

1. Synthesis of TA-PEG1000-CADB. To a round-bottom flask of 50 mL, TA-PEG1000-NH_2 (purchased from Biopharma PEG, 400 mg, 0.4 mmol), CADB (111.8 mg, 0.4 mmol), DCC (165 mg, 0.8 mmol), NHS (92 mg, 0.8 mmol) were added and dissolved in 20 mL of anhydrous DCM. Then 50 µL anhydrous TEA were added into the mixture. The resultant solution was left stirring at 400 rpm at 25 °C for 4 h. The mixture was filtered through a layer of cotton and the solvent was evaporated by a rotary evaporator. The resulting solid product was dissolved in 10 mL of water and washed 3 times with diethyl ether. The aqueous phase was then saturated by $NaHCO_3$ and was extracted 3 times with DCM. The resulting organic phase was concentrated and the crude product was chromatographed on a silica gel with 10:1 (vol/vol) $CHCl_3$:MeOH as the eluent. The solvent of the collected fractions was evaporated by a rotary evaporator and dried under vacuum. The yield of this synthesis is about 80%.

2. Synthesis of TA-PEG1000-p(SPE/SPP/PC)-CADB. Here gives a typical synthesis route for TA-PEG1000-PSPE-CADB, the synthesis protocols for the other two polyzwitterions are similar. To a 20 mL scintillation vial, the synthesized TA-PEG1000-CADB (255 mg, ~ 0.2 mmol), SPE monomer (1.8 g, 0.6 mmol), V50 (27 mg, 0.1 mmol) were added and dissolved in 10 mL of mixture of water/acetic acid (vol/vol = 1/3). The vial was then sealed and degassed under argon flux. After 30 min, the reactive mixture was heated to 70 °C with an oil bath and kept under stirring (400 rpm) for 6 h. The obtained polymer was precipitated in acetone, washed twice with diethyl ether, and finally dried overnight under vacuum.

3. Synthesis of TA-PEG1000-p(SPE/SPP/PC)-OH. 300 mg of the as-synthesized TA-PEG1000-P(SPE/SPP/PC)-CADB ligands were dissolved in 5 mL of distilled water. 10 µL of H_2O_2 solution (20 wt.%) was then added to the solution. The resulting solution was heated to 70 °C for 6h in the presence of oxygen. After the reaction, the polymer was precipitated in acetone and washed once with ethanol.

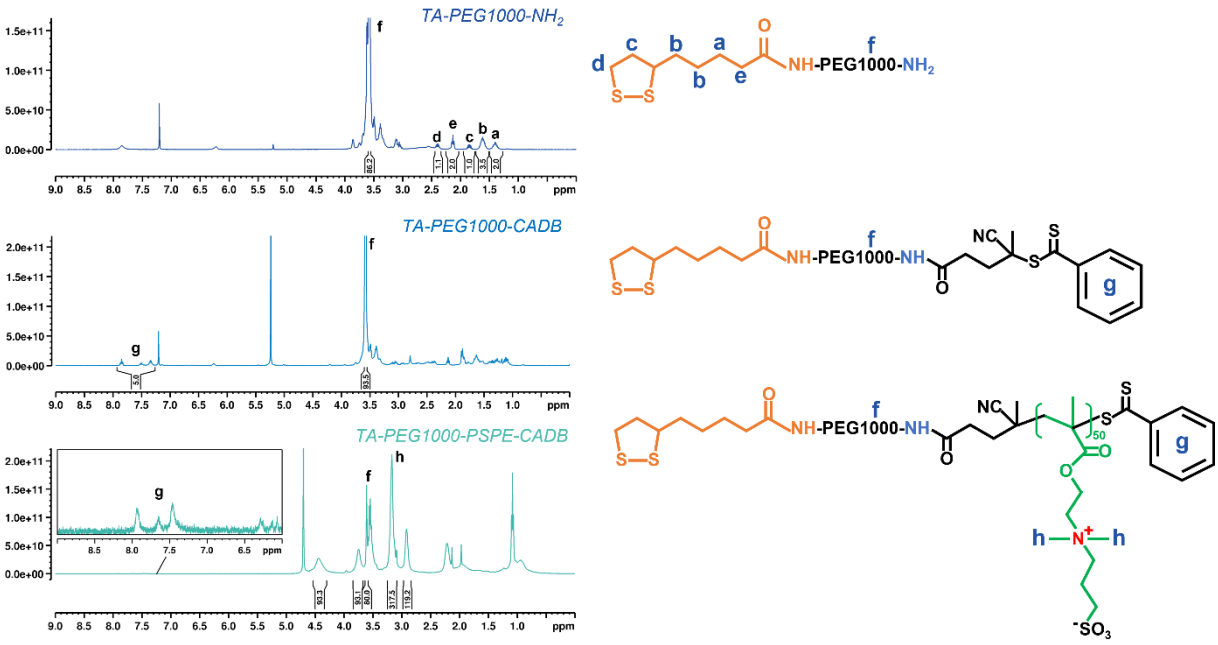

Figure.V.11. ^{1}H NMR spectra of TA-PEG1000-NH_2, TA-PEG1000-CADB and TA-PEG1000-pSPE-CADB.

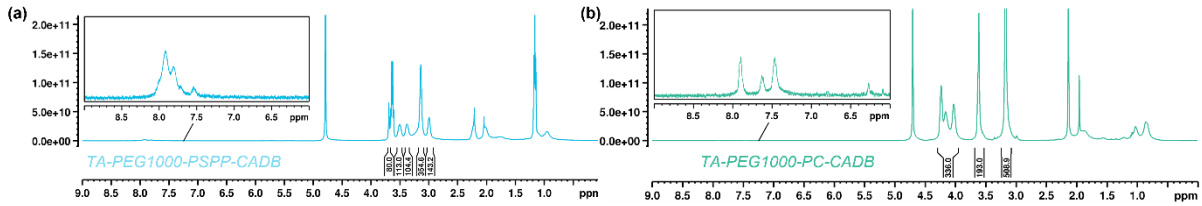

Figure.V.12. ^{1}H NMR spectra of (a). TA-PEG1000-pSPP-CADB; (b). TA-PEG1000-pPC-CADB.

V.3. Ligand exchange

V.3.1. AuNR ligand exchange

a. Preparation of citrate capped AuNRs

Typically, the stocked AuNR/AuNRmins ([AuNR/AuNRmin] = 1 nM) were precipitated by centrifuge (12,000 g, 25 min) and redispersed in Na-PSS solution (0.15 wt %, 70 kDa). After 2 hours, the residual CTAB was depleted by another round of centrifugation and redispersion in Na-PSS solution. The resultant PSS-stabilized AuNRmins were left overnight. Then AuNRs/AuNRmins were subjected to 2 rounds of centrifugation and redispersion in sodium citrate solution (5 mM) to exchange Na-PSS, eventually yielding stable citrate-capped AuNRs/AuNRmins.

b. Ligand exchange of citrate-capped AuNRmins with polyzwitteirons

To a 20 mL scintillation vial was added subsequently 4 mL of sodium citrate solution (5 mM), 40 mg polyzwitterion ligands (approximately 4 µmol), and 330 µL of $NaBH_4$ solution (0.1 M). This mixed solution was kept stirring at room temperature for at least 30 min. Then the citrate capped AuNRmin solution (1.1 mL, 15 nM) was added. The resulting solution was kept stirring overnight for a complete ligand exchange. Afterwards, the exchanged AuNRmins were collected by centrifuge (6000 g, 30 min) and washed with PBS three times.

V.3.2. AuNR/TiO_2 ligand exchange

In a 2 mL scintillation vial, 10 mg PEG-pPA polymer were dissolved in 1 mL distilled water under stirring. 2 mL AuNR/TiO_2 stock solution (0.1 nM) was centrifuged (3400 g, 10 min) and redispersed in 50 µL ethanol, then this nanoparticle solution was added into the polymer solution. After 10 min of stirring, the pH of the mixed solution was adjusted to 7.5 – 8 with 0.2 M NaOH solution. The final mixture was kept under gentle stirring overnight. Then the exchanged nanoparticles were collected by centrifugation (3400 g, 10 min), washed twice with sodium citrate solution (5 mM) and three times with HBS buffer solution (pH = 7.5).

V.4. Characterizations of photocatalytic activity

V.4.1. Irradiation experiments with AuNR/TiO_2 nanoparticles

The AuNR/TiO_2 nanoparticles were precipitated by centrifugation (3400 g, 10 min) and redispersed in sodium citrate solution (5 mM). Methylene blue (MB), which serves as the detector of OH•, was then introduced to the sodium citrate stabilized AuNR/TiO_2 solution. The final concentration of MB in the mixed solution was 10 µM and the optical density of AuNR/TiO_2 nanoparticles at 800 nm

was adjusted to 1.0 cm^{-1}, according to its UV-vis absorption spectrum. 500 µL of prepared solution was transferred into a UV quartz cuvette and was left under stirring for 30 min in the dark. Then the solution was irradiated with an 808 nm femto-second pulsed/continuous wave laser for a period of 1-2 h with vigorous stirring. The absorption spectra of the irradiated solution were taken every 10 min.

V.4.2. Irradiation experiments with Cu_2S/Ag_2S nanoparticles

The irradiation protocol of Cu_2S (or Ag_2S) nanoparticles is similar to that of AuNR/TiO_2 nanoparticles. However, citrate ligands cannot stabilize Cu_2S(Ag_2S) nanoparticles during the irradiation. we performed a ligand exchange process to replace citrate ligands at the surface of Cu_2S(Ag_2S) nanoparticles by L-Glutathione or 3-mercaptopropionic acid ligands. These ligands contain thiol group that ensures a better anchoring stability at the nanoparticle surface.

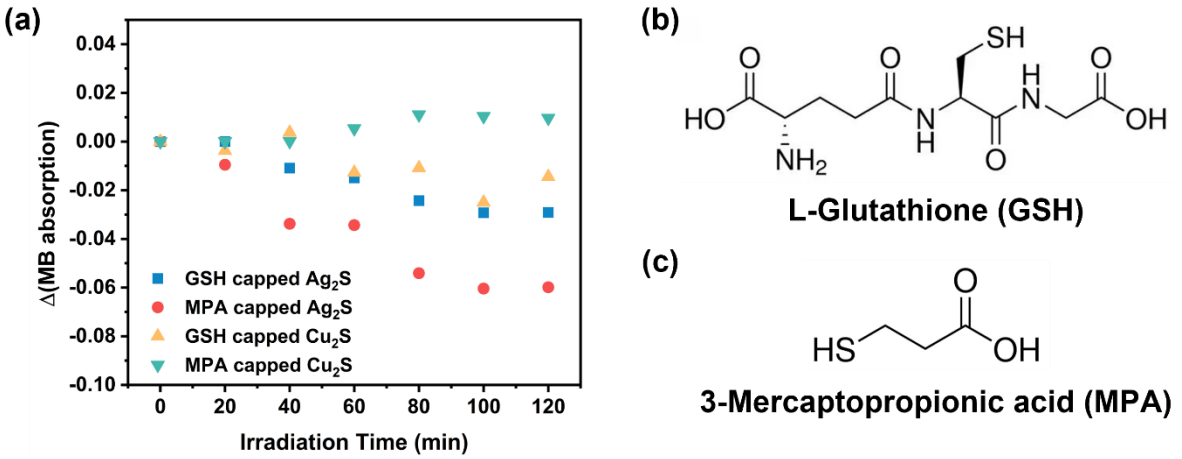

Figure.V.13. (a). MB degradation induced by Cu_2S(Ag_2S) nanoparticles capped by GSH or MPA ligands. (b, c). molecule structures of utilized GSH and MPA ligands.

V.4.3. Irradiation experiments with AuNR@SiO_2@Cu_2S nanoparticles: photothermal effect

To evaluate the contribution of Cu_2S on the solution temperature elevation, we analyzed the UV absorption spectra of AuNRs and Cu_2S. Firstly, as shown in **Figure.V.14. a**, we linearly superposed the absorption spectra of AuNR@SiO_2 and Cu_2S, the absorption spectrum of AuNR@SiO_2@Cu_2S constructed from this linear combination have a similar form to that taken from AuNR@SiO_2@Cu_2S nanoparticles, which allow us to further calculate the proportion of light absorption by the AuNR@SiO_2 and by the Cu_2S (**Figure.V.14. b**). We eventually find that at 800 nm, AuNR and Cu_2S account for 55% and 45% of light energy absorption, respectively. And the light-to-heat conversion efficiency calculated from the linear overlap of these two parts of material gives a value of $0.55 * 56.8\% + 0.45 * 89.4\% = 71.5\%$, which means that if there were no interaction between AuNR and Cu_2S, the light-to-heat conversion efficiency of this hybrid nanostructure should be around 70%, a value that is much lower than that measured from the experiment (87%). This result provides evidence supporting that by combining AuNRs with Cu_2S nanoparticles, we create new interactions between plasmonic nanoparticles and semiconductors which favoring the absorption and conversion of light energy, and finally, we can effectively improve the utilization of plasmonic energy by this method.

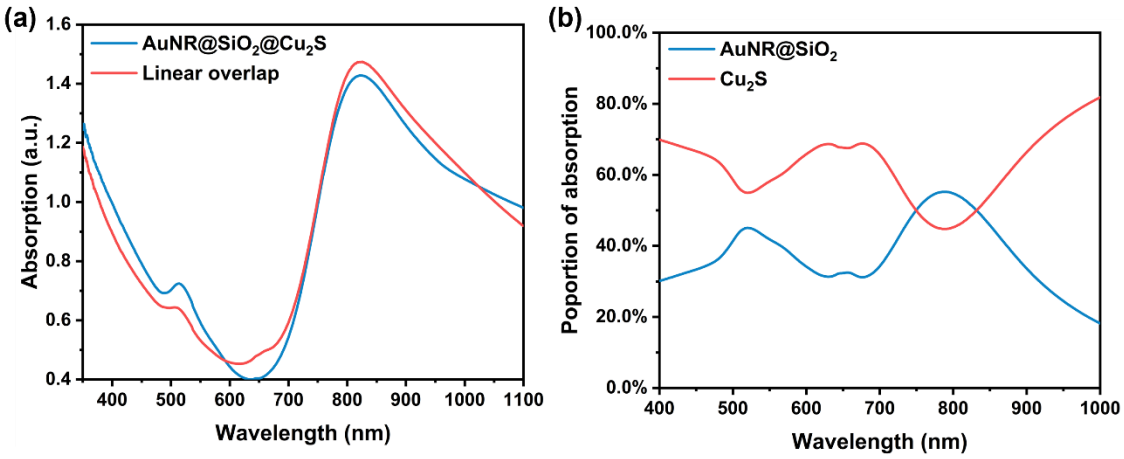

Figure.V.14. (a). Comparison of absorption spectra between AuNR@SiO_2@Cu_2S nanoparticles and that derived from linear overlap of AuNR@SiO_2 and Cu_2S. (b). Calculated proportion of light absorption induced by AuNR@SiO_2 and Cu_2S.

V.5. *In vitro* experiments

V.5.1. Cell culture methods

a. RAW264.7 cells

RAW 264.7 mouse macrophage cells come from Jacques Fattaccioli's laboratory at the Institut Pierre-Gilles de Gennes (IPGG). They were purchased from the European Collection of Authenticated Cell Cultures (Public Health England, United Kingdom), reference 91062702. They are cultured in T75 cell culture flasks with DMEM 4.5 g/L (Thermo Fischer, reference 21969035), supplemented with 10% fetal calf serum (Sigma-Aldrich), 1% penicillin/streptomycin and 2 mM L-Glutamine (Thermo Fischer). Culture is performed at 37°C and 5% CO_2. Cells are subcultured regularly, every 2 to 3 days, at 1:5 or 1:10 ratio, and are detached from the bottom of the flask with a cell scraper.

b. HeLa cells

HeLa cells were grown in the same culture medium as RAW 267.4, at 37°C and 5% CO_2. They are subcultured every 3 or 4 days at 1:8 or 1:10. They are detached from the flask with 3 – 5 mL of TryPLE (Thermo Fischer) after washing with PBS buffer.

V.5.2. Polyzwitterion-coated IONPs incubated with free polymer ligands

During the incubation of p(SPP-s-APMA-PA) covered IONPs, we introduced additional free polymer ligands to the cell culture media. The purpose of these free polymer ligands was to saturate the receptors on the macrophage membrane. By occupying the receptors with free polymer ligands, the macrophages would no longer be able to internalize IONPs that are covered by the same polymer ligands. Therefore, free polymer ligands (p(SPP-s-APMA-PA)) with concentrations ranging from 0.5 g/L to 2.0 g/L were added to the cell culture media. After 10 min of incubation, functionalized IONPs (5 Fluo/IONP or 11 Fluo/IONP) were added to the RAW cells with a final concentration of 30 nM. After 1h of incubation, RAW cells were collected and analyzed by flow cytometer. As shown in **Figure.V.15**, the inclusion of free polymer ligands in both cases resulted in a decreased uptake of nanoparticles compared to samples without free polymer ligands. This indicates that the free polymer ligands have the ability to replace the nanoparticles as the target for macrophage capture. Notably, in samples with a free polymer

concentration of up to 1 g/L, the measured fluorescence intensity was reduced to approximately 30% of the fluorescence intensity observed in samples without free polymer ligands. Further increasing the quantity of free polymer ligands did not lead to a further reduction in nanoparticle uptake.

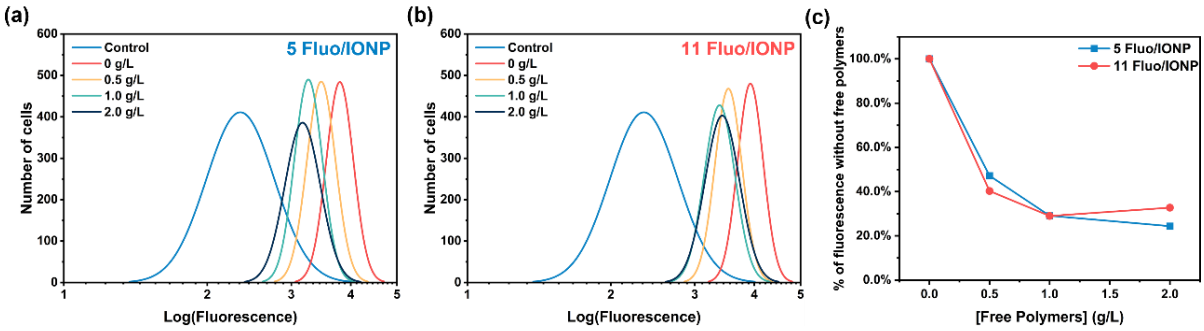

Figure.V.15. Fluorescence distribution measured for RAW cells incubated with increasing concentration (from 0 to 2 g/L) of free polymer ligands (p(SPP-s-APMA-PA)) and IONPs with (a). 5 Fluorophores/nanoparticle; (b). 11 Fluorophores/nanoparticle. (c). Average fluorescence intensity detected in samples with free polymers compared to samples without free polymers, whose fluorescence intensity is set to 100%.

V.6. Plasmon for bulk gold materials

V.6.1. Drude model for gold

The electron configuration of gold is $[Xe]4f^{14}5d^{10}6s^{1}$. The presence of electrons in the 6s subshell allows them to reside in the conduction band of gold, making them mobile and responsive to electromagnetic fields. Paul Drude proposed 1900 a classical model to describe these free electrons behavior in a solid, particularly, in a metal. In Drude's model, the valence electrons form an electron gas which wanders around the fixed ion centers. If an external electromagnetic field is applied to gold, the motion of an electron can be described as:

$$m\frac{\partial^2 \boldsymbol{r}}{\partial t^2} + \frac{m}{\tau}\frac{\partial \boldsymbol{r}}{\partial t} = -e\boldsymbol{E} \qquad (V.1)$$

where m is the effective mass of electron, e is the elementary charge of electron, τ is the relaxation time between two subsequent collisions of electron, and $\boldsymbol{r}$ is the displacement vector of electron. If we consider the external electric field as a harmonic time dependence wave $\boldsymbol{E} = E_0 e^{-i\omega t}$, electrons will also follow this harmonic field with: $\boldsymbol{r} = r_0 e^{-i\omega t}$. The equation (I.1) can be rewrite as:

$$\boldsymbol{r} = \frac{e\boldsymbol{E}}{m\left(\omega^2 + \frac{i\omega}{\tau}\right)} \qquad (V.2)$$

The displacement of electron results in the appearance of a dipole moment. The collective dipole moment in the atoms lead to the polarization of the gold. The total effect of the displacement of n electrons to the polarization is:

$$\boldsymbol{P} = -ne\boldsymbol{r} \qquad (V.3)$$

$$\boldsymbol{P} = \frac{-ne^2\boldsymbol{E}}{m\left(\omega^2 + \frac{i\omega}{\tau}\right)} \qquad (V.4)$$

where $\boldsymbol{P}$ describes the electric dipole moment per unit volume inside the gold, caused by the alignment of microscopic dipoles. According to Maxwell's equations, the dielectric displacement $\boldsymbol{D}$ is linked with the electric field $\boldsymbol{E}$ via the polarization $\boldsymbol{P}$ by:

$$\boldsymbol{D} = \varepsilon_0 \boldsymbol{E} + \boldsymbol{P} \tag{V.5}$$

therefore,

$$\boldsymbol{D} = \varepsilon_0 \left(1 - \frac{\frac{ne^2}{m\varepsilon_0}}{\omega^2 + \frac{i\omega}{\tau}} \right) \boldsymbol{E} \tag{V.6}$$

where ε_0 is the electric vacuum permittivity. And the term $\sqrt{\frac{ne^2}{m\varepsilon_0}}$ is defined as plasma frequency ω_p of bulk gold materials:

$$\omega_p = \sqrt{\frac{ne^2}{m\varepsilon_0}} \tag{V.7}$$

and therefore, the equation (I.6) becomes:

$$\boldsymbol{D} = \varepsilon_0 \left(1 - \frac{{\omega_p}^2}{\omega^2 + \frac{i\omega}{\tau}} \right) \boldsymbol{E} \tag{V.8}$$

If we limit ourselves to linear, isotropic and nonmagnetic materials, we can also define $\boldsymbol{D}$ as follows:

$$\boldsymbol{D} = \varepsilon_0 \varepsilon_r \boldsymbol{E} \tag{V.9}$$

Finally, by correlating the equations (I.8) and (I.9), we can deduce the complex relative permittivity of gold:

$$\varepsilon_r(\omega) = 1 - \frac{{\omega_p}^2}{\omega^2 + \frac{i\omega}{\tau}} \tag{V.10}$$

Indeed, the relative permittivity consists of a real part and an imaginary part. The real part is related to the energy refracted and scattered by gold materials, while the imaginary part represents the energy loss of electron gas during the displacement due to friction. At high frequencies, this relative permittivity can be approximated to an energy-lossless model:

$$\varepsilon_r(\omega) = 1 - \frac{{\omega_p}^2}{\omega^2} \tag{V.11}$$

This is a core equation of this section as it represents the relationship between the dielectric function of gold materials and the circular frequency of incident light. This relationship plays a crucial role in describing the optical properties and plasmonic characteristics of the material, which will be further discussed later. We can eventually plot the relative permittivity as a function of driving frequency of the field, as shown in **Figure.V.16**, if the frequency $\omega > \omega_p$, which lies in ultraviolet region, the ε_r becomes positive, gold materials in this case are transparent to electromagnetic field with no absorption; otherwise, if $\omega < \omega_p$, which falls in visible or near infrared region, the ε_r becomes negative, meaning

that no light can pass through the bulk gold material, and instead the gold demonstrates characteristic metallic properties with strong absorption and reflection. We will see, a negative ε_r is essential for interaction between light and gold materials, particularly in the visible to NIR light region, which is of interest in our study.

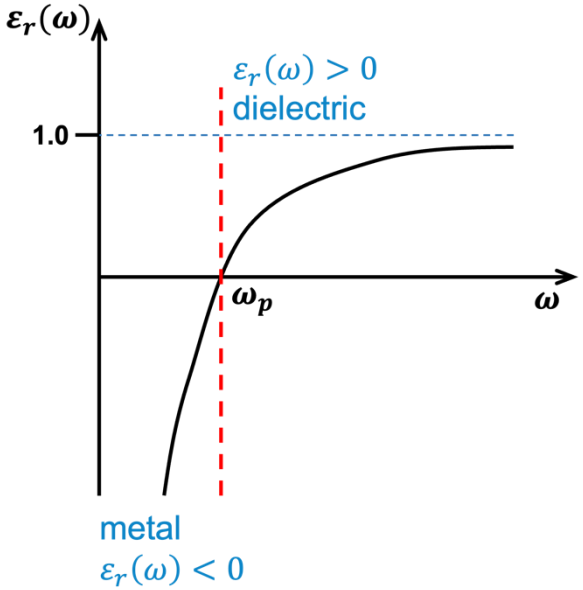

Figure.V.16. Illustration of the relationship between relative permittivity ε_r and the driving frequency of the electromagnetic field.

V.6.2. Surface plasmons

When light or other electromagnetic radiation interacts with the gold surface, it can excite the free conduction electrons, making them collectively oscillate at specific frequencies. This collective oscillation of electrons, referred to as plasmons, can be described as the elastic displacement of the electron gas with respect to the fixed ionic cores in the presence of external electromagnetic fields.

We first focus on the coupling between the electromagnetic field and the collective oscillation of conduction electrons at the surface of bulk gold materials. Generally, these electromagnetic excitations occur and propagate at the interface between a dielectric (ε_2, such as air or prism) and gold (ε_1), evanescently confined in the perpendicular direction, and are defined as surface plasmon polaritons (SPPs) (Figure.V.17).

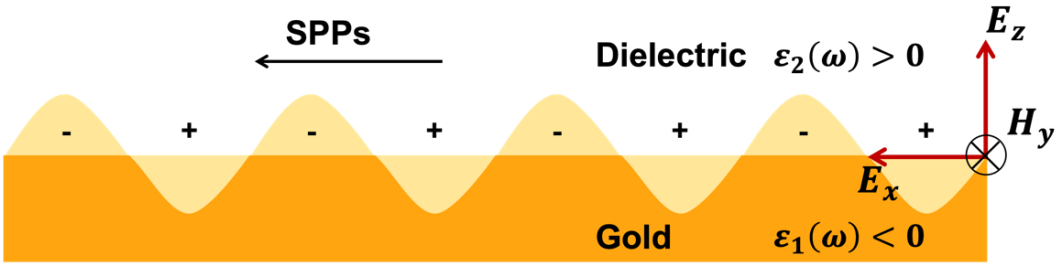

Figure.V.17. Illustration of SPPs at the interface of the bulk gold material and a dielectric.

By solving Maxwell's equations at the interface and considering the electromagnetic field continuity and boundary conditions, we can determine the conditions required for the propagation of SPPs. Firstly, only transverse magnetic (TM) modes allow the propagation of SPPs. Secondly, to enable the existence of SPP at the interface, the real parts of dielectric permittivity of two media must be of opposite sign, i.e. if $\varepsilon_2 > 0$, then the condition reads $\mathrm{Re}[\varepsilon_1] < 0$, and according to Drude's lossless model, $\omega < \omega_p$. Finally, we can obtain the dispersion relations of SPPs at the interface:

$$k_x = k_0 \sqrt{\frac{\varepsilon_1 \varepsilon_2}{\varepsilon_1 + \varepsilon_2}} \tag{V.12}$$

where k_x is the wave vector in the x direction, k_0 is the wave vectors of light propagating in vacuum ($k_0 = \frac{\omega}{c}$). The SPPs dispersion relation is then plotted in **Figure.V.18**, the yellow straight line represents light dispersion relation in vacuum. The green curve represents the radiative plasmon polaritons with $\omega > \omega_p$, as discussed before, in this situation, the gold materials are transparent to the light. Finally, the SPP excitation corresponds to the blue curve, with a saturation of frequency ω_{sp} which is called the surface plasmon frequency. According to the equation (V.12), when $\varepsilon_1 + \varepsilon_2 \to 0$, $k_x \to \infty$, and thus $\omega \to \omega_{sp}$. Particularly, if we apply the energy lossless Drude mode with equation (V.11), we can have:

$$\omega_{sp} = \frac{\omega_p}{\sqrt{\varepsilon_2 + 1}} \tag{V.13}$$

and if the dielectric refers to the air, $\varepsilon_2 = 1$, then:

$$\omega_{sp} = \frac{\omega_p}{\sqrt{2}} \tag{V.14}$$

The dispersion diagram also reveals that due to the propagation constant β is greater than the wave vector k in the dielectric, the SPP dispersion curve lies on the right side of light line of the dielectric, meaning that a momentum mismatch exists between incident light and SPPs, and thus propagating photons cannot generate SPPs at the gold-dielectric interface. This momentum mismatch can be circumvented by special excitation and coupling strategies including total internal reflection method[213,214] and gold surface grating[215,216].

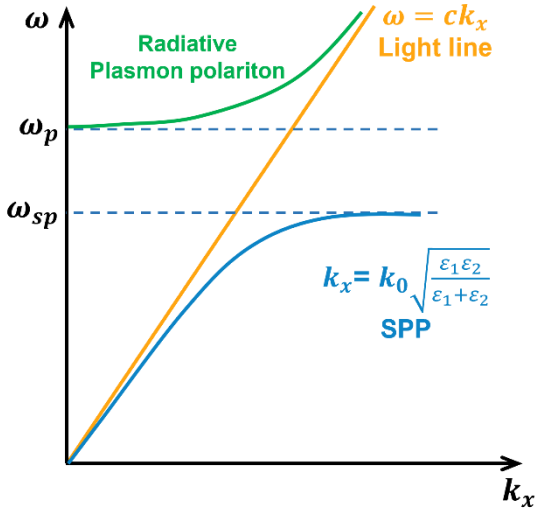

Figure.V.18. Dispersion relation of SPPs at the interface between energy lossless Drude metal and a dielectric.

V.7. RAFT polymerization

Since its first report in 1998[217], RAFT polymerization has been widely studied and applied as a versatile and powerful method to synthesize complicated polymer structures. RAFT process allows for the synthesis of polymeric architectures with predictable molecular weight, low dispersity (Đ), high end-group fidelity, and the possibility for continued chain growth. The mechanism of RAFT polymerization is illustrated in **Figure.V.19**. Indeed, the steps I, II and VI constitute a classical radical polymerization process: the initiators acting as the radical source are firstly activated to generate radicals (step I). These free radicals further react with monomers in the system and the transfer of the radicals from activated chains to inactivated monomers finally lead to the growth of polymer chain (step II). The polymer chain growth can be stopped when two active chains reacted between each other (step VI), which is also called the termination step. The inconvenience of the classical radical polymerization derives from the uncontrolled termination step, where a reactive polymer chain can be terminated by radicals, short polymer chains, or long polymer chains. This lack of control leads to a high dispersity of the synthesized polymer. In the RAFT process, the activated radical species (I· and P_n·) in the system are captured by the chain transfer agents (CTA), forming dormant species that are unreactive (step III). The formation of this dormant species is reversible and in equilibrium with active species in the system. In an efficient process, the rate of this addition/fragmentation equilibrium is higher than that of propagation, resulting in the addition of less than one monomer unit per activation cycle (step V). As a result, all polymer chains will grow at the same speed and have a similar degree of polymerization at a specific point in time. In addition, the CTA molecules are integrated in each polymer chain after the polymerization and remain "living", meaning that the as-synthesized polymer can act as a "larger" CTA agent for the following polymerization, which allows the further addition of monomers to the polymer chain.

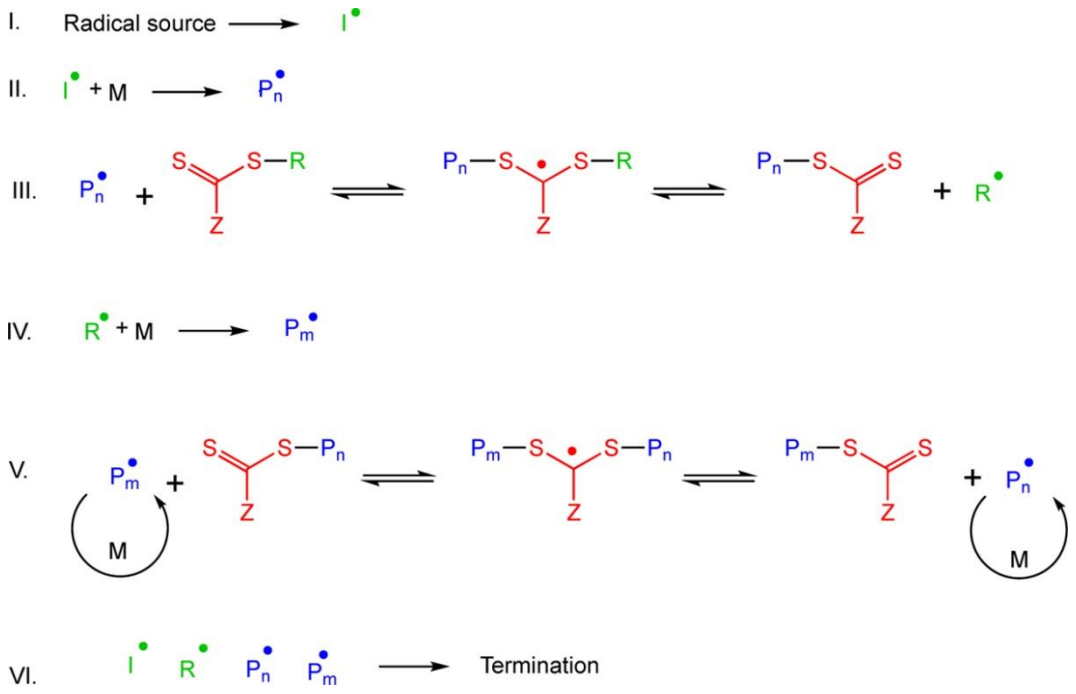

Figure.V.19. RAFT polymerization mechanism[218].

References

1. Pomerantseva, E., Bonaccorso, F., Feng, X., Cui, Y. & Gogotsi, Y. Energy storage: The future enabled by nanomaterials. *Science* **366**, eaan8285 (2019).
2. Kamyshny, A. & Magdassi, S. Conductive nanomaterials for 2D and 3D printed flexible electronics. *Chem. Soc. Rev.* **48**, 1712–1740 (2019).
3. Hofmann, T. *et al.* Technology readiness and overcoming barriers to sustainably implement nanotechnology-enabled plant agriculture. *Nat. Food* **1**, 416–425 (2020).
4. de Lázaro, I. & Mooney, D. J. Obstacles and opportunities in a forward vision for cancer nanomedicine. *Nat. Mater.* **20**, 1469–1479 (2021).
5. Germain, M. *et al.* Delivering the power of nanomedicine to patients today. *J. Controlled Release* **326**, 164–171 (2020).
6. Zhang, Y., Xu, C., Yang, X. & Pu, K. Photoactivatable Protherapeutic Nanomedicine for Cancer. *Adv. Mater.* **32**, 1–19 (2020).
7. Singh, P. *et al.* Insights from nanotechnology in COVID-19: Prevention, detection, therapy and immunomodulation. *Nanomed.* **16**, 1219–1235 (2021).
8. Huang, X. *et al.* Nanotechnology-based strategies against SARS-CoV-2 variants. *Nat. Nanotechnol.* **17**, 1027–1037 (2022).
9. Qiu, G. *et al.* Dual-Functional Plasmonic Photothermal Biosensors for Highly Accurate Severe Acute Respiratory Syndrome Coronavirus 2 Detection. *ACS Nano* **14**, 5268–5277 (2020).
10. Tang, Z. *et al.* Insights from nanotechnology in COVID-19 treatment. *Nano Today* **36**, 101019 (2021).
11. Weiss, C. *et al.* Toward Nanotechnology-Enabled Approaches against the COVID-19 Pandemic. *ACS Nano* **14**, 6383–6406 (2020).
12. Samak, D. H. *et al.* Developmental toxicity of carbon nanoparticles during embryogenesis in chicken. *Environ. Sci. Pollut. Res.* **27**, 19058–19072 (2020).
13. Talapin, D. V. *et al.* CdSe and CdSe/CdS nanorod solids. *J. Am. Chem. Soc.* **126**, 12984–12988 (2004).

14. Reiss, P., Protière, M. & Li, L. Core/shell semiconductor nanocrystals. *Small* **5**, 154–168 (2009).

15. García de Arquer, F. P. *et al.* Semiconductor quantum dots: Technological progress and future challenges. *Science* **373**, (2021).

16. Owen, J. & Brus, L. Chemical Synthesis and Luminescence Applications of Colloidal Semiconductor Quantum Dots. *J. Am. Chem. Soc.* **139**, 10939–10943 (2017).

17. Rabouw, F. T. & de Mello Donega, C. Excited-State Dynamics in Colloidal Semiconductor Nanocrystals. *Top. Curr. Chem.* **374**, 1–30 (2016).

18. Yakavets, I. *et al.* Nir imaging of the integrin-rich head and neck squamous cell carcinoma using ternary copper indium selenide/zinc sulfide-based quantum dots. *Cancers* **12**, 1–16 (2020).

19. Helle, M. *et al.* Visualisation of Sentinel Lymph Node with Indium-Based near Infrared Emitting Quantum Dots in a Murine Metastatic Breast Cancer Model. *PLoS ONE* **7**, (2012).

20. Gao, X., Cui, Y., Levenson, R. M., Chung, L. W. K. & Nie, S. In vivo cancer targeting and imaging with semiconductor quantum dots. *Nat. Biotechnol.* **22**, 969–976 (2004).

21. Smith, B. R. *et al.* Real-time intravital imaging of RGD-quantum dot binding to luminal endothelium in mouse tumor neovasculature. *Nano Lett.* **8**, 2599–2606 (2008).

22. Pons, T. *et al.* Cadmium-free CuInS2/ZnS quantum dots for sentinel lymph node imaging with reduced toxicity. *ACS Nano* **4**, 2531–2538 (2010).

23. Wang, S., Jarrett, B. R., Kauzlarich, S. M. & Louie, A. Y. Core/shell quantum dots with high relaxivity and photoluminescence for multimodality imaging. *J. Am. Chem. Soc.* **129**, 3848–3856 (2007).

24. Ducongé, F. *et al.* Fluorine-18-labeled phospholipid quantum dot micelles for in vivo multimodal imaging from whole body to cellular scales. *Bioconjug. Chem.* **19**, 1921–1926 (2008).

25. Sitbon, G. *et al.* Multimodal Mn-doped I-III-VI quantum dots for near infrared fluorescence and magnetic resonance imaging: From synthesis to in vivo application. *Nanoscale* **6**, 9264–9272 (2014).

26. Samia, A. C. S., Chen, X. & Burda, C. Semiconductor Quantum Dots for Photodynamic Therapy. *J. Am. Chem. Soc.* **125**, 15736–15737 (2003).

27. Li, X. *et al.* Current investigations into magnetic nanoparticles for biomedical applications. *Journal of Biomedical Materials Research - Part A* vol. 104 1285–1296 Preprint at https://doi.org/10.1002/jbm.a.35654 (2016).

28. Gloag, L., Mehdipour, M., Chen, D., Tilley, R. D. & Gooding, J. J. Advances in the Application of Magnetic Nanoparticles for Sensing. *Advanced Materials* vol. 31 1–26 Preprint at https://doi.org/10.1002/adma.201904385 (2019).

29. Chiang, C. S., Shen, Y. S., Liu, J. J., Shyu, W. C. & Chen, S. Y. Synergistic Combination of Multistage Magnetic Guidance and Optimized Ligand Density in Targeting a Nanoplatform for Enhanced Cancer Therapy. *Adv. Healthc. Mater.* **5**, 2131–2141 (2016).

30. Bobo, D., Robinson, K. J., Islam, J., Thurecht, K. J. & Corrie, S. R. Nanoparticle-Based Medicines: A Review of FDA-Approved Materials and Clinical Trials to Date. *Pharmaceutical Research* vol. 33 2373–2387 Preprint at https://doi.org/10.1007/s11095-016-1958-5 (2016).

31. Jeon, M., Halbert, M. V, Stephen, Z. R. & Zhang, M. Iron Oxide Nanoparticles as T1 Contrast Agents for Magnetic Resonance Imaging: Fundamentals, Challenges, Applications, and Prospectives. *Advanced Materials* vol. 33 1–18 Preprint at https://doi.org/10.1002/adma.201906539 (2021).

32. Chang, D. *et al.* Biologically targeted magnetic hyperthermia: Potential and limitations. *Frontiers in Pharmacology* vol. 9 Preprint at https://doi.org/10.3389/fphar.2018.00831 (2018).

33. Cotin, G. *et al.* Dendron based antifouling, MRI and magnetic hyperthermia properties of different shaped iron oxide nanoparticles. *Nanotechnology* **30**, (2019).

34. Fernández-Barahona, I., Muñoz-Hernando, M., Ruiz-Cabello, J., Herranz, F. & Pellico, J. Iron oxide nanoparticles: An alternative for positive contrast in magnetic resonance imaging. *Inorganics* **8**, 1–22 (2020).

35. Buonsanti, R., Llordes, A., Aloni, S., Helms, B. A. & Milliron, D. J. Tunable Infrared Absorption and Visible Transparency of Colloidal Aluminum-Doped Zinc Oxide Nanocrystals. *Nano Lett.* **11**, 4706–4710 (2011).

36. Gordon, T. R. *et al.* Shape-Dependent Plasmonic Response and Directed Self-Assembly in a New Semiconductor Building Block, Indium-Doped Cadmium Oxide (ICO). *Nano Lett.* **13**, 2857–2863 (2013).

37. Li, S., Huang, H., Shao, L. & Wang, J. How to Utilize Excited Plasmon Energy Efficiently. *ACS Nano* **15**, 10759–10768 (2021).

38. Jauffred, L., Samadi, A., Klingberg, H., Bendix, P. M. & Oddershede, L. B. Plasmonic Heating of Nanostructures. *Chem. Rev.* **119**, 8087–8130 (2019).

39. Zhang, J., Mou, L. & Jiang, X. Surface chemistry of gold nanoparticles for health-related applications. *Chem. Sci.* **11**, 923–936 (2020).

40. Thakor, A. S., Jokerst, J., Zavaleta, C., Massoud, T. F. & Gambhir, S. S. Gold Nanoparticles: A Revival in Precious Metal Administration to Patients. *Nano Lett.* **11**, 4029–4036 (2011).

41. Wang, J. *et al.* Gold nanoparticles in virus detection: Recent advances and potential considerations for SARS-CoV-2 testing development. *WIREs Nanomedicine Nanobiotechnology* **14**, (2022).

42. Chavan, S. G. *et al.* Enhanced Detection of Infectious Pancreatic Necrosis Virus via Lateral Flow Chip and Fluorometric Biosensors Based on Self-Assembled Protein Nanoprobes. *ACS Sens.* **4**, 2937–2944 (2019).

43. Englebienne, P., Verhas, M. & Van Hoonacker, A. High-throughput screening using the surface plasmon resonance effect of colloidal gold nanoparticles. *The Analyst* **126**, 1645–1651 (2001).

44. Ben Haddada, M. *et al.* Gold nanoparticle-based localized surface plasmon immunosensor for staphylococcal enterotoxin A (SEA) detection. *Anal. Bioanal. Chem.* **409**, 6227–6234 (2017).

45. Zhang, L., Salmain, M., Liedberg, B. & Boujday, S. Naked Eye Immunosensing of Food Biotoxins Using Gold Nanoparticle-Antibody Bioconjugates. *ACS Appl. Nano Mater.* **2**, 4150–4158 (2019).

46. Lee, J.-H., Kim, B.-C., Oh, B.-K. & Choi, J.-W. Highly sensitive localized surface plasmon resonance immunosensor for label-free detection of HIV-1. *Nanomedicine Nanotechnol. Biol. Med.* **9**, 1018–1026 (2013).

47. Kang, M. S., Lee, S. Y., Kim, K. S. & Han, D.-W. State of the Art Biocompatible Gold Nanoparticles for Cancer Theragnosis. *Pharmaceutics* **12**, 701 (2020).

48. Ou, L. *et al.* Application of silver nanoparticle-based SERS spectroscopy for DNA analysis in radiated nasopharyngeal carcinoma cells: SERS specroscopy of radiated nasopharyngeal carcinoma cells' DNA. *J. Raman Spectrosc.* **44**, 680–685 (2013).

49. Zhang, Q. *et al.* Gold Nanoparticle (AuNP)-Based Surface-Enhanced Raman Scattering (SERS) Probe of Leukemic Lymphocytes. *Plasmonics* **11**, 1361–1368 (2016).

50. Tam, N. C. M. *et al.* Porphyrin–Lipid Stabilized Gold Nanoparticles for Surface Enhanced Raman Scattering Based Imaging. *Bioconjug. Chem.* **23**, 1726–1730 (2012).

51. Chatterjee, H., Rahman, D. S., Sengupta, M. & Ghosh, S. K. Gold Nanostars in Plasmonic Photothermal Therapy: The Role of Tip Heads in the Thermoplasmonic Landscape. *J. Phys. Chem. C* **122**, 13082–13094 (2018).

52. Yang, J. *et al.* Spatially Confined Fabrication of Core–Shell Gold Nanocages@Mesoporous Silica for Near-Infrared Controlled Photothermal Drug Release. *Chem. Mater.* **25**, 3030–3037 (2013).

53. Smith, A. M., Mancini, M. C. & Nie, S. Second window for in vivo imaging. *Nat. Nanotechnol.* **4**, 710–711 (2009).

54. Ye, X., Zheng, C., Chen, J., Gao, Y. & Murray, C. B. Using Binary Surfactant Mixtures To Simultaneously Improve the Dimensional Tunability and Monodispersity in the Seeded Growth of Gold Nanorods. *Nano Lett.* **13**, 765–771 (2013).

55. Dreaden, E. C., Alkilany, A. M., Huang, X., Murphy, C. J. & El-Sayed, M. A. The golden age: gold nanoparticles for biomedicine. *Chem Soc Rev* **41**, 2740–2779 (2012).

56. Link, S., Mohamed, M. B. & El-Sayed, M. A. Simulation of the Optical Absorption Spectra of Gold Nanorods as a Function of Their Aspect Ratio and the Effect of the Medium Dielectric Constant. *J. Phys. Chem. B* **103**, 3073–3077 (1999).

57. Chang, S.-S., Shih, C.-W., Chen, C.-D., Lai, W.-C. & Wang, C. R. C. The Shape Transition of Gold Nanorods. *Langmuir* **15**, 701–709 (1999).

58. Van Der Zande, B. M. I., Böhmer, M. R., Fokkink, L. G. J. & Schönenberger, C. Colloidal Dispersions of Gold Rods: Synthesis and Optical Properties. *Langmuir* **16**, 451–458 (2000).

59. Lohse, S. E. & Murphy, C. J. The Quest for Shape Control: A History of Gold Nanorod Synthesis. *Chem. Mater.* **25**, 1250–1261 (2013).

60. Huang, X., Neretina, S. & El-Sayed, M. A. Gold Nanorods: From Synthesis and Properties to Biological and Biomedical Applications. *Adv. Mater.* **21**, 4880–4910 (2009).

61. Sau, T. K. & Murphy, C. J. Seeded High Yield Synthesis of Short Au Nanorods in Aqueous Solution. *Langmuir* **20**, 6414–6420 (2004).

62. Chen, H. M. *et al.* Controlling the Length and Shape of Gold Nanorods. *J. Phys. Chem. B* **109**, 19553–19555 (2005).

63. Kou, X. *et al.* Growth of Gold Nanorods and Bipyramids Using CTEAB Surfactant. *J. Phys. Chem. B* **110**, 16377–16383 (2006).

64. Ye, X. *et al.* Improved Size-Tunable Synthesis of Monodisperse Gold Nanorods through the Use of Aromatic Additives. *ACS Nano* **6**, 2804–2817 (2012).

65. Gole, A. & Murphy, C. J. Seed-Mediated Synthesis of Gold Nanorods: Role of the Size and Nature of the Seed. *Chem. Mater.* **16**, 3633–3640 (2004).

66. Johnson, C. J., Dujardin, E., Davis, S. A., Murphy, C. J. & Mann, S. Growth and form of gold nanorods prepared by seed-mediated, surfactant-directed synthesis. *J. Mater. Chem.* **12**, 1765–1770 (2002).

67. Scarabelli, L., Grzelczak, M. & Liz-Marzán, L. M. Tuning Gold Nanorod Synthesis through Prereduction with Salicylic Acid. *Chem. Mater.* **25**, 4232–4238 (2013).

68. Carbó-Argibay, E. *et al.* Chemical Sharpening of Gold Nanorods: The Rod-to-Octahedron Transition. *Angew. Chem. Int. Ed.* **46**, 8983–8987 (2007).

69. Scarabelli, L., Sánchez-Iglesias, A., Pérez-Juste, J. & Liz-Marzán, L. M. A "Tips and Tricks" Practical Guide to the Synthesis of Gold Nanorods. *J. Phys. Chem. Lett.* **6**, 4270–4279 (2015).

70. Jana, N. R. Gram-Scale Synthesis of Soluble, Near-Monodisperse Gold Nanorods and Other Anisotropic Nanoparticles. *Small* **1**, 875–882 (2005).

71. Ali, M. R. K., Snyder, B. & El-Sayed, M. A. Synthesis and Optical Properties of Small Au Nanorods Using a Seedless Growth Technique. *Langmuir* **28**, 9807–9815 (2012).

72. Orendorff, C. J. & Murphy, C. J. Quantitation of Metal Content in the Silver-Assisted Growth of Gold Nanorods. *J. Phys. Chem. B* **110**, 3990–3994 (2006).

73. Si, S., Leduc, C., Delville, M.-H. & Lounis, B. Short Gold Nanorod Growth Revisited: The Critical Role of the Bromide Counterion. *ChemPhysChem* **13**, 193–202 (2012).

74. Leonov, A. P. *et al.* Detoxification of Gold Nanorods by Treatment with Polystyrenesulfonate. *ACS Nano* **2**, 2481–2488 (2008).

75. Connor, E. E., Mwamuka, J., Gole, A., Murphy, C. J. & Wyatt, M. D. Gold Nanoparticles Are Taken Up by Human Cells but Do Not Cause Acute Cytotoxicity. *Small* **1**, 325–327 (2005).

76. Thierry, B., Ng, J., Krieg, T. & Griesser, H. J. A robust procedure for the functionalization of gold nanorods and noble metal nanoparticles. *Chem. Commun.* 1724 (2009) doi:10.1039/b820137d.

77. Pierrat, S., Zins, I., Breivogel, A. & Sönnichsen, C. Self-Assembly of Small Gold Colloids with Functionalized Gold Nanorods. *Nano Lett.* **7**, 259–263 (2007).

78. Niidome, T. *et al.* In Vivo Monitoring of Intravenously Injected Gold Nanorods Using Near-Infrared Light. *Small* **4**, 1001–1007 (2008).

79. Mehtala, J. G. *et al.* Citrate-Stabilized Gold Nanorods. *Langmuir* **30**, 13727–13730 (2014).

80. Wilson, C. G., Sisco, P. N., Gadala-Maria, F. A., Murphy, C. J. & Goldsmith, E. C. Polyelectrolyte-coated gold nanorods and their interactions with type I collagen. *Biomaterials* **30**, 5639–5648 (2009).

81. Pellas, V. *et al.* Gold Nanorods for LSPR Biosensing: Synthesis, Coating by Silica, and Bioanalytical Applications. *Biosensors* **10**, 146 (2020).

82. Carrasco, E., Stockert, J. C., Juarranz, Á. & Blázquez-Castro, A. Plasmonic Hot-Electron Reactive Oxygen Species Generation: Fundamentals for Redox Biology. *Front. Chem.* **8**, 591325 (2020).

83. Hartland, G. V., Besteiro, L. V., Johns, P. & Govorov, A. O. What's so Hot about Electrons in Metal Nanoparticles? *ACS Energy Lett.* **2**, 1641–1653 (2017).

84. Besteiro, L. V., Kong, X.-T., Wang, Z., Hartland, G. & Govorov, A. O. Understanding Hot-Electron Generation and Plasmon Relaxation in Metal Nanocrystals: Quantum and Classical Mechanisms. *ACS Photonics* **4**, 2759–2781 (2017).

85. Chang, L. *et al.* Electronic Structure of the Plasmons in Metal Nanocrystals: Fundamental Limitations for the Energy Efficiency of Hot Electron Generation. *ACS Energy Lett.* **4**, 2552–2568 (2019).

86. Brongersma, M. L., Halas, N. J. & Nordlander, P. Plasmon-induced hot carrier science and technology. *Nat. Nanotechnol.* **10**, 25–34 (2015).

87. Knavel, E. M. & Brace, C. L. Tumor Ablation: Common Modalities and General Practices. *Tech. Vasc. Interv. Radiol.* **16**, 192–200 (2013).

88. Bonfil, R. D., Bustuoabad, O. D., Ruggiero, R. A., Meiss, R. P. & Pasqualini, C. D. Tumor necrosis can facilitate the appearance of metastases. *Clin. Exp. Metastasis* **6**, 121–129 (1988).

89. Li, X., Lovell, J. F., Yoon, J. & Chen, X. Clinical development and potential of photothermal and photodynamic therapies for cancer. *Nat. Rev. Clin. Oncol.* **17**, 657–674 (2020).

90. Sultan, R. A. Tumour ablation by laser in general surgery. *Lasers Med. Sci.* **5**, 185–193 (1990).

91. Axiak-Bechtel, S. *et al.* Gum arabic-coated radioactive gold nanoparticles cause no short-term local or systemic toxicity in the clinically relevant canine model of prostate cancer. *Int. J. Nanomedicine* 5001 (2014) doi:10.2147/IJN.S67333.

92. Ali, M. R. K. *et al.* Efficacy, long-term toxicity, and mechanistic studies of gold nanorods photothermal therapy of cancer in xenograft mice. *Proc. Natl. Acad. Sci.* **114**, (2017).

93. Mackey, M. A., Ali, M. R. K., Austin, L. A., Near, R. D. & El-Sayed, M. A. The Most Effective Gold Nanorod Size for Plasmonic Photothermal Therapy: Theory and *In Vitro* Experiments. *J. Phys. Chem. B* **118**, 1319–1326 (2014).

94. Liao, H. & Hafner, J. H. Gold Nanorod Bioconjugates. *Chem. Mater.* **17**, 4636–4641 (2005).

95. Huang, X. *et al.* A Reexamination of Active and Passive Tumor Targeting by Using Rod-Shaped Gold Nanocrystals and Covalently Conjugated Peptide Ligands. *ACS Nano* **4**, 5887–5896 (2010).

96. Manivasagan, P. *et al.* Chitosan/fucoidan multilayer coating of gold nanorods as highly efficient near-infrared photothermal agents for cancer therapy. *Carbohydr. Polym.* **211**, 360–369 (2019).

97. Dickerson, E. B. *et al.* Gold nanorod assisted near-infrared plasmonic photothermal therapy (PPTT) of squamous cell carcinoma in mice. *Cancer Lett.* **269**, 57–66 (2008).

98. Von Maltzahn, G. *et al.* Computationally Guided Photothermal Tumor Therapy Using Long-Circulating Gold Nanorod Antennas. *Cancer Res.* **69**, 3892–3900 (2009).

99. Li, J. *et al.* Plasmon-induced resonance energy transfer for solar energy conversion. *Nat. Photonics* **9**, 601–607 (2015).

100. Zhang, Y. *et al.* Surface-Plasmon-Driven Hot Electron Photochemistry. *Chem. Rev.* **118**, 2927–2954 (2018).

101. Agostinis, P. *et al.* Photodynamic therapy of cancer: An update. *CA. Cancer J. Clin.* **61**, 250–281 (2011).

102. Hanahan, D. & Weinberg, R. A. Hallmarks of Cancer: The Next Generation. *Cell* **144**, 646–674 (2011).

103. Vankayala, R., Huang, Y.-K., Kalluru, P., Chiang, C.-S. & Hwang, K. C. First Demonstration of Gold Nanorods-Mediated Photodynamic Therapeutic Destruction of Tumors via Near Infra-Red Light Activation. *Small* **10**, 1612–1622 (2014).

104. Labouret, T., Audibert, J.-F., Pansu, R. B. & Palpant, B. Plasmon-Assisted Production of Reactive Oxygen Species by Single Gold Nanorods. *Small* **11**, 4475–4479 (2015).

105. Feng, Y. *et al.* Differential photothermal and photodynamic performance behaviors of gold nanorods, nanoshells and nanocages under identical energy conditions. *Biomater. Sci.* **7**, 1448–1462 (2019).

106. Wang, D. *et al.* Hybrid Plasmonic Nanodumbbells Engineering for Multi-Intensified Second Near-Infrared Light Induced Photodynamic Therapy. *ACS Nano* **15**, 8694–8705 (2021).

107. Thompson, T. L. & Yates, J. T. Surface Science Studies of the Photoactivation of TiO_2 New Photochemical Processes. *Chem. Rev.* **106**, 4428–4453 (2006).

108. Priebe, J. B. *et al.* Water Reduction with Visible Light: Synergy between Optical Transitions and Electron Transfer in Au-TiO_2 Catalysts Visualized by In situ EPR Spectroscopy. *Angew. Chem. Int. Ed.* **52**, 11420–11424 (2013).

109. Amidani, L. *et al.* Probing Long-Lived Plasmonic-Generated Charges in TiO_2 /Au by High-Resolution X-ray Absorption Spectroscopy. *Angew. Chem. Int. Ed.* **54**, 5413–5416 (2015).

110. Yuzawa, H., Yoshida, T. & Yoshida, H. Gold nanoparticles on titanium oxide effective for photocatalytic hydrogen formation under visible light. *Appl. Catal. B Environ.* **115–116**, 294–302 (2012).

111. Tang, L., Guo, X., Yang, Y., Zha, Z. & Wang, Z. Gold nanoparticles supported on titanium dioxide: an efficient catalyst for highly selective synthesis of benzoxazoles and benzimidazoles. *Chem. Commun.* **50**, 6145 (2014).

112. Wang, J.-H. *et al.* Ceria-Coated Gold Nanorods for Plasmon-Enhanced Near-Infrared Photocatalytic and Photoelectrochemical Performances. *J. Phys. Chem. C* **120**, 14805–14812 (2016).

113. Collins, S. S. E. *et al.* Plasmon Energy Transfer in Hybrid Nanoantennas. *ACS Nano* **15**, 9522–9530 (2021).

114. Cushing, S. K. *et al.* Photocatalytic Activity Enhanced by Plasmonic Resonant Energy Transfer from Metal to Semiconductor. *J. Am. Chem. Soc.* **134**, 15033–15041 (2012).

115. Chang, Y. *et al.* Resonance Energy Transfer-Promoted Photothermal and Photodynamic Performance of Gold–Copper Sulfide Yolk–Shell Nanoparticles for Chemophototherapy of Cancer. *Nano Lett.* **18**, 886–897 (2018).

116. Wu, B. *et al.* Anisotropic Growth of TiO_2 onto Gold Nanorods for Plasmon-Enhanced Hydrogen Production from Water Reduction. *J. Am. Chem. Soc.* **138**, 1114–1117 (2016).

117. Tu, Y.-J., Njus, D. & Schlegel, H. B. A theoretical study of ascorbic acid oxidation and **HOO**$^{\cdot}$/**O**$_2^{\cdot -}$ radical scavenging. *Org. Biomol. Chem.* **15**, 4417–4431 (2017).

118. Bullen, C., Zijlstra, P., Bakker, E., Gu, M. & Raston, C. Chemical Kinetics of Gold Nanorod Growth in Aqueous CTAB Solutions. *Cryst. Growth Des.* **11**, 3375–3380 (2011).

119. Langille, M. R., Personick, M. L., Zhang, J. & Mirkin, C. A. Defining Rules for the Shape Evolution of Gold Nanoparticles. *J. Am. Chem. Soc.* **134**, 14542–14554 (2012).

120. Grzelczak, M., Pérez-Juste, J., Mulvaney, P. & Liz-Marzán, L. M. Shape control in gold nanoparticle synthesis. *Chem. Soc. Rev.* **37**, 1783 (2008).

121. Vigderman, L., Khanal, B. P. & Zubarev, E. R. Functional Gold Nanorods: Synthesis, Self-Assembly, and Sensing Applications. *Adv. Mater.* **24**, 4811–4841 (2012).

122. Almora-Barrios, N., Novell-Leruth, G., Whiting, P., Liz-Marzán, L. M. & López, N. Theoretical Description of the Role of Halides, Silver, and Surfactants on the Structure of Gold Nanorods. *Nano Lett.* **14**, 871–875 (2014).

123. Xiong, Y. *et al.* Synthesis and Mechanistic Study of Palladium Nanobars and Nanorods. *J. Am. Chem. Soc.* **129**, 3665–3675 (2007).

124. He, L. *et al.* TiO_2 -Capped Gold Nanorods for Plasmon-Enhanced Production of Reactive Oxygen Species and Photothermal Delivery of Chemotherapeutic Agents. *ACS Appl. Mater. Interfaces* **10**, 27965–27971 (2018).

125. Cassaignon, S., Koelsch, M. & Jolivet, J.-P. From TiCl3 to TiO2 nanoparticles (anatase, brookite and rutile): Thermohydrolysis and oxidation in aqueous medium. *J. Phys. Chem. Solids* **68**, 695–700 (2007).

126. Pecsok, R. L. & Fletcher, A. N. Hydrolysis of Titanium(III). *Inorg. Chem.* **1**, 155–159 (1962).

127. Liu, R. & Sen, A. Controlled Synthesis of Heterogeneous Metal–Titania Nanostructures and Their Applications. *J. Am. Chem. Soc.* **134**, 17505–17512 (2012).

128. Cao, J., Sun, T. & Grattan, K. T. V. Gold nanorod-based localized surface plasmon resonance biosensors: A review. *Sens. Actuators B Chem.* **195**, 332–351 (2014).

129. Mudunkotuwa, I. A. & Grassian, V. H. Citric Acid Adsorption on TiO_2 Nanoparticles in Aqueous Suspensions at Acidic and Circumneutral pH: Surface Coverage, Surface Speciation, and Its Impact on Nanoparticle−Nanoparticle Interactions. *J. Am. Chem. Soc.* **132**, 14986–14994 (2010).

130. Nosaka, Y. & Nosaka, A. Y. Generation and Detection of Reactive Oxygen Species in Photocatalysis. *Chem. Rev.* **117**, 11302–11336 (2017).

131. Murakami, Y., Endo, K., Ohta, I., Nosaka, A. Y. & Nosaka, Y. Can OH Radicals Diffuse from the UV-Irradiated Photocatalytic TiO_2 Surfaces? Laser-Induced-Fluorescence Study. *J. Phys. Chem. C* **111**, 11339–11346 (2007).

132. Hawkins, C. L. & Davies, M. J. Detection and characterisation of radicals in biological materials using EPR methodology. *Biochim. Biophys. Acta BBA - Gen. Subj.* **1840**, 708–721 (2014).

133. Ma, H. *et al.* Impact of solar UV radiation on toxicity of ZnO nanoparticles through photocatalytic reactive oxygen species (ROS) generation and photo-induced dissolution. *Environ. Pollut.* **193**, 165–172 (2014).

134. Nakabayashi, Y. & Nosaka, Y. OH Radical Formation at Distinct Faces of Rutile TiO_2 Crystal in the Procedure of Photoelectrochemical Water Oxidation. *J. Phys. Chem. C* **117**, 23832–23839 (2013).

135. Satoh, A. Y., Trosko, J. E. & Masten, S. J. Methylene Blue Dye Test for Rapid Qualitative Detection of Hydroxyl Radicals Formed in a Fenton's Reaction Aqueous Solution. *Environ. Sci. Technol.* **41**, 2881–2887 (2007).

136. Nakabayashi, Y. & Nosaka, Y. The pH dependence of OH radical formation in photo-electrochemical water oxidation with rutile TiO_2 single crystals. *Phys. Chem. Chem. Phys.* **17**, 30570–30576 (2015).

137. Gao, L. *et al.* Plasmon-Mediated Generation of Reactive Oxygen Species from Near-Infrared Light Excited Gold Nanocages for Photodynamic Therapy *in Vitro*. *ACS Nano* **8**, 7260–7271 (2014).

138. Chen, Y.-S. *et al.* Enhanced thermal stability of silica-coated gold nanorods for photoacoustic imaging and image-guided therapy. *Opt. Express* **18**, 8867 (2010).

139. Chen, Y.-S., Zhao, Y., Yoon, S. J., Gambhir, S. S. & Emelianov, S. Miniature gold nanorods for photoacoustic molecular imaging in the second near-infrared optical window. *Nat. Nanotechnol.* **14**, 465–472 (2019).

140. O'Connor, A. E., Gallagher, W. M. & Byrne, A. T. Porphyrin and Nonporphyrin Photosensitizers in Oncology: Preclinical and Clinical Advances in Photodynamic Therapy. *Photochem. Photobiol.* **85**, 1053–1074 (2009).

141. Yuan, B., Chen, N. & Zhu, Q. Emission and absorption properties of indocyanine green in Intralipid solution. *J. Biomed. Opt.* **9**, 497 (2004).

142. Wiegand, H. L., Orths, C. T., Kerpen, K., Lutze, H. V. & Schmidt, T. C. Investigation of the Iron–Peroxo Complex in the Fenton Reaction: Kinetic Indication, Decay Kinetics, and Hydroxyl Radical Yields. *Environ. Sci. Technol.* **51**, 14321–14329 (2017).

143. Saiz-Poseu, J., Mancebo-Aracil, J., Nador, F., Busqué, F. & Ruiz-Molina, D. The Chemistry behind Catechol-Based Adhesion. *Angew. Chem. Int. Ed.* **58**, 696–714 (2019).

144. Cheng, F., Sajedin, S. M., Kelly, S. M., Lee, A. F. & Kornherr, A. UV-stable paper coated with APTES-modified P25 TiO2 nanoparticles. *Carbohydr. Polym.* **114**, 246–252 (2014).

145. Guerrero, G., Mutin, P. H. & Vioux, A. Anchoring of Phosphonate and Phosphinate Coupling Molecules on Titania Particles. *Chem. Mater.* **13**, 4367–4373 (2001).

146. Estephan, Z. G., Jaber, J. A. & Schlenoff, J. B. Zwitterion-Stabilized Silica Nanoparticles: Toward Nonstick Nano. *Langmuir* **26**, 16884–16889 (2010).

147. Bharti, R. *et al.* Diacerein-mediated inhibition of IL-6/IL-6R signaling induces apoptotic effects on breast cancer. *Oncogene* **35**, 3965–3975 (2016).

148. Riccardi, C. & Nicoletti, I. Analysis of apoptosis by propidium iodide staining and flow cytometry. *Nat. Protoc.* **1**, 1458–1461 (2006).

149. Xiang, Y. *et al.* Gold Nanorod-Seeded Growth of Silver Nanostructures: From Homogeneous Coating to Anisotropic Coating. *Langmuir* **24**, 3465–3470 (2008).

150. Jiang, R., Chen, H., Shao, L., Li, Q. & Wang, J. Unraveling the Evolution and Nature of the Plasmons in (Au Core)–(Ag Shell) Nanorods. *Adv. Mater.* **24**, (2012).

151. Chen, R., Nuhfer, N. T., Moussa, L., Morris, H. R. & Whitmore, P. M. Silver sulfide nanoparticle assembly obtained by reacting an assembled silver nanoparticle template with hydrogen sulfide gas. *Nanotechnology* **19**, 455604 (2008).

152. Brown, M. D. *et al.* Plasmonic Dye-Sensitized Solar Cells Using Core−Shell Metal−Insulator Nanoparticles. *Nano Lett.* **11**, 438–445 (2011).

153. Pellas, V. *et al.* Gold Nanorod Coating with Silica Shells Having Controlled Thickness and Oriented Porosity: Tailoring the Shells for Biosensing. *ACS Appl. Nano Mater.* **4**, 9842–9854 (2021).

154. Huang, L. *et al.* Plasmonic silver nanoshells for drug and metabolite detection. *Nat. Commun.* **8**, 220 (2017).

155. Zou, R. *et al.* Thermal stability of gold nanorods in an aqueous solution. *Colloids Surf. Physicochem. Eng. Asp.* **372**, 177–181 (2010).

156. Zhao, Y. *et al.* Plasmonic Cu $_{2-x}$ S Nanocrystals: Optical and Structural Properties of Copper-Deficient Copper(I) Sulfides. *J. Am. Chem. Soc.* **131**, 4253–4261 (2009).

157. Zhang, J., Li, J., Zhang, Q. & Guo, D. Constructing a novel CuS/Cu2S Z-scheme heterojunction for highly-efficiency NIR light-driven antibacterial activity. *Appl. Surf. Sci.* **624**, 156848 (2023).

158. Wang, S. *et al.* Plasmonic Copper Sulfide Nanocrystals Exhibiting Near-Infrared Photothermal and Photodynamic Therapeutic Effects. *ACS Nano* **9**, 1788–1800 (2015).

159. Jiang, K., Smith, D. A. & Pinchuk, A. Size-Dependent Photothermal Conversion Efficiencies of Plasmonically Heated Gold Nanoparticles. *J. Phys. Chem. C* **117**, 27073–27080 (2013).

160. Meyer, S. M., Pettine, J., Nesbitt, D. J. & Murphy, C. J. Size Effects in Gold Nanorod Light-to-Heat Conversion under Femtosecond Illumination. *J. Phys. Chem. C* **125**, 16268–16278 (2021).

161. Draine, B. T. & Flatau, P. J. Discrete-Dipole Approximation For Scattering Calculations. *J. Opt. Soc. Am. A* **11**, 1491 (1994).

162. Wilhelm, S. *et al.* Analysis of nanoparticle delivery to tumours. *Nat. Rev. Mater.* **1**, 16014 (2016).

163. Tasso, M. *et al.* Sulfobetaine–Vinylimidazole Block Copolymers: A Robust Quantum Dot Surface Chemistry Expanding Bioimaging's Horizons. *ACS Nano* **9**, 11479–11489 (2015).

164. Debayle, M. *et al.* Zwitterionic polymer ligands: an ideal surface coating to totally suppress protein-nanoparticle corona formation? *Biomaterials* **219**, 119357 (2019).

165. Delille, F. *et al.* Sulfobetaine-Phosphonate Block Copolymer Coated Iron Oxide Nanoparticles for Genomic Locus Targeting and Magnetic Micromanipulation in the Nucleus of Living Cells. *Nano Lett.* **23**, 5919–5926 (2023).

166. Hermansson, M. The DLVO theory in microbial adhesion. *Colloids Surf. B Biointerfaces* **14**, 105–119 (1999).

167. *Lipid and polymer lipid systems: conference, October 2000 in Chia Laguna, Sardinia*. (Springer, 2002).

168. Molina-Bolívar, J. A., Galisteo-González, F. & Hidalgo-Alvarez, R. The role played by hydration forces in the stability of protein-coated particles: non-classical DLVO behaviour. *Colloids Surf. B Biointerfaces* **14**, 3–17 (1999).

169. Ruckenstein, E. & Manciu, M. Specific ion effects via ion hydration: II. Double layer interaction. *Adv. Colloid Interface Sci.* **105**, 177–200 (2003).

170. Monopoli, M. P. *et al.* Physical−Chemical Aspects of Protein Corona: Relevance to *in Vitro* and *in Vivo* Biological Impacts of Nanoparticles. *J. Am. Chem. Soc.* **133**, 2525–2534 (2011).

171. Monopoli, M. P., Åberg, C., Salvati, A. & Dawson, K. A. Biomolecular coronas provide the biological identity of nanosized materials. *Nat. Nanotechnol.* **7**, 779–786 (2012).

172. Hirsh, S. L. *et al.* The Vroman effect: Competitive protein exchange with dynamic multilayer protein aggregates. *Colloids Surf. B Biointerfaces* **103**, 395–404 (2013).

173. Delille, F., Pu, Y., Lequeux, N. & Pons, T. Designing the Surface Chemistry of Inorganic Nanocrystals for Cancer Imaging and Therapy. *Cancers* **14**, 2456 (2022).

174. Tsoi, K. M. *et al.* Mechanism of hard-nanomaterial clearance by the liver. *Nat. Mater.* **15**, 1212–1221 (2016).

175. Arami, H., Khandhar, A., Liggitt, D. & Krishnan, K. M. In vivo delivery, pharmacokinetics, biodistribution and toxicity of iron oxide nanoparticles. *Chem. Soc. Rev.* **44**, 8576–8607 (2015).

176. Frank, M. M. & Fries, L. F. The role of complement in inflammation and phagocytosis. *Immunol. Today* **12**, 322–326 (1991).

177. Juliano, R. L. Factors affecting the clearance kinetics and tissue distribution of liposomes, microspheres and emulsions. *Adv. Drug Deliv. Rev.* **2**, 31–54 (1988).

178. Donahue, N. D., Acar, H. & Wilhelm, S. Concepts of nanoparticle cellular uptake, intracellular trafficking, and kinetics in nanomedicine. *Adv. Drug Deliv. Rev.* **143**, 68–96 (2019).

179. Tavares, A. J. *et al.* Effect of removing Kupffer cells on nanoparticle tumor delivery. *Proc. Natl. Acad. Sci.* **114**, (2017).

180. Gustafson, H. H., Holt-Casper, D., Grainger, D. W. & Ghandehari, H. Nanoparticle uptake: The phagocyte problem. *Nano Today* **10**, 487–510 (2015).

181. Ngo, W. *et al.* Why nanoparticles prefer liver macrophage cell uptake in vivo. *Adv. Drug Deliv. Rev.* **185**, 114238 (2022).

182. Dutta, D. *et al.* Adsorbed Proteins Influence the Biological Activity and Molecular Targeting of Nanomaterials. *Toxicol. Sci.* **100**, 303–315 (2007).

183. Schöttler, S. *et al.* Protein adsorption is required for stealth effect of poly(ethylene glycol)- and poly(phosphoester)-coated nanocarriers. *Nat. Nanotechnol.* **11**, 372–377 (2016).

184. Ouyang, B. *et al.* The dose threshold for nanoparticle tumour delivery. *Nat. Mater.* **19**, 1362–1371 (2020).

185. Nikitin, M. P. *et al.* Enhancement of the blood-circulation time and performance of nanomedicines via the forced clearance of erythrocytes. *Nat. Biomed. Eng.* **4**, 717–731 (2020).

186. Zelepukin, I. V. *et al.* Nanoparticle-based drug delivery *via* RBC-hitchhiking for the inhibition of lung metastases growth. *Nanoscale* **11**, 1636–1646 (2019).

187. Rodriguez, P. L. *et al.* Minimal 'Self' Peptides That Inhibit Phagocytic Clearance and Enhance Delivery of Nanoparticles. *Science* **339**, 971–975 (2013).

188. Susumu, K. *et al.* Enhancing the Stability and Biological Functionalities of Quantum Dots via Compact Multifunctional Ligands. *J. Am. Chem. Soc.* **129**, 13987–13996 (2007).

189. Uyeda, H. T., Medintz, I. L., Jaiswal, J. K., Simon, S. M. & Mattoussi, H. Synthesis of Compact Multidentate Ligands to Prepare Stable Hydrophilic Quantum Dot Fluorophores. *J. Am. Chem. Soc.* **127**, 3870–3878 (2005).

190. Yildiz, I. *et al.* Hydrophilic CdSe−ZnS Core−Shell Quantum Dots with Reactive Functional Groups on Their Surface. *Langmuir* **26**, 11503–11511 (2010).

191. Giovanelli, E. *et al.* Highly Enhanced Affinity of Multidentate versus Bidentate Zwitterionic Ligands for Long-Term Quantum Dot Bioimaging. *Langmuir* **28**, 15177–15184 (2012).

192. Li, Z. Multiple thiol-anchor capped DNA-gold nanoparticle conjugates. *Nucleic Acids Res.* **30**, 1558–1562 (2002).

193. Smolensky, E. D., Park, H.-Y. E., Berquó, T. S. & Pierre, V. C. Surface functionalization of magnetic iron oxide nanoparticles for MRI applications - effect of anchoring group and ligand exchange protocol. *Contrast Media Mol. Imaging* n/a-n/a (2010) doi:10.1002/cmmi.417.

194. Aldana, J., Wang, Y. A. & Peng, X. Photochemical Instability of CdSe Nanocrystals Coated by Hydrophilic Thiols. *J. Am. Chem. Soc.* **123**, 8844–8850 (2001).

195. Ensing, B. *et al.* On the origin of the extremely different solubilities of polyethers in water. *Nat. Commun.* **10**, 2893 (2019).

196. Suk, J. S., Xu, Q., Kim, N., Hanes, J. & Ensign, L. M. PEGylation as a strategy for improving nanoparticle-based drug and gene delivery. *Adv. Drug Deliv. Rev.* **99**, 28–51 (2016).

197. Abou-Saleh, R. H., Swain, M., Evans, S. D. & Thomson, N. H. Poly(ethylene glycol) Lipid-Shelled Microbubbles: Abundance, Stability, and Mechanical Properties. *Langmuir* **30**, 5557–5563 (2014).

198. Li, B. *et al.* Revealing the Immunogenic Risk of Polymers. *Angew. Chem. Int. Ed.* **57**, 13873–13876 (2018).

199. Jiang, S. & Cao, Z. Ultralow-Fouling, Functionalizable, and Hydrolyzable Zwitterionic Materials and Their Derivatives for Biological Applications. *Adv. Mater.* **22**, 920–932 (2010).

200. Bobo, D., Robinson, K. J., Islam, J., Thurecht, K. J. & Corrie, S. R. Nanoparticle-Based Medicines: A Review of FDA-Approved Materials and Clinical Trials to Date. *Pharm. Res.* **33**, 2373–2387 (2016).

201. Lammers, T. *et al.* Polymeric nanomedicines for image-guided drug delivery and tumor-targeted combination therapy. *Nano Today* **5**, 197–212 (2010).

202. Viegas, T. X. *et al.* Polyoxazoline: Chemistry, Properties, and Applications in Drug Delivery. *Bioconjug. Chem.* **22**, 976–986 (2011).

203. Erfani, A., Seaberg, J., Aichele, C. P. & Ramsey, J. D. Interactions between Biomolecules and Zwitterionic Moieties: A Review. *Biomacromolecules* **21**, 2557–2573 (2020).

204. Cheng, G. *et al.* Functionalizable and Ultrastable Zwitterionic Nanogels. *Langmuir* **26**, 6883–6886 (2010).

205. Sakamaki, T. *et al.* Ion-Specific Hydration States of Zwitterionic Poly(sulfobetaine methacrylate) Brushes in Aqueous Solutions. *Langmuir* **35**, 1583–1589 (2019).

206. Delgado, J. D. & Schlenoff, J. B. Static and Dynamic Solution Behavior of a Polyzwitterion Using a Hofmeister Salt Series. *Macromolecules* **50**, 4454–4464 (2017).

207. García, K. P. *et al.* Zwitterionic-Coated "Stealth" Nanoparticles for Biomedical Applications: Recent Advances in Countering Biomolecular Corona Formation and Uptake by the Mononuclear Phagocyte System. *Small* **10**, 2516–2529 (2014).

208. Susumu, K., Mei, B. C. & Mattoussi, H. Multifunctional ligands based on dihydrolipoic acid and polyethylene glycol to promote biocompatibility of quantum dots. *Nat. Protoc.* **4**, 424–436 (2009).

209. Jesson, C. P. *et al.* H_2O_2 Enables Convenient Removal of RAFT End-Groups from Block Copolymer Nano-Objects Prepared via Polymerization-Induced Self-Assembly in Water. *Macromolecules* **50**, 182–191 (2017).

210. Thompson, D., Pepys, M. B. & Wood, S. P. The physiological structure of human C-reactive protein and its complex with phosphocholine. *Structure* **7**, 169–177 (1999).

211. Yuan, Y.-Y. *et al.* Surface Charge Switchable Nanoparticles Based on Zwitterionic Polymer for Enhanced Drug Delivery to Tumor. *Adv. Mater.* **24**, 5476–5480 (2012).

212. Zhang, Z. *et al.* NIR-to-NIR Deep Penetrating Nanoplatforms Y_2O_3:Nd^{3+}/Yb^{3+}@SiO_2@Cu_2S toward Highly Efficient Photothermal Ablation. *ACS Appl. Mater. Interfaces* **10**, 14570–14576 (2018).

213. Špringer, T., Ermini, M. L., Špačková, B., Jabloňků, J. & Homola, J. Enhancing Sensitivity of Surface Plasmon Resonance Biosensors by Functionalized Gold Nanoparticles: Size Matters. *Anal. Chem.* **86**, 10350–10356 (2014).

214. Zhang, P., Ma, G., Wan, Z. & Wang, S. Quantification of Single-Molecule Protein Binding Kinetics in Complex Media with Prism-Coupled Plasmonic Scattering Imaging. *ACS Sens.* **6**, 1357–1366 (2021).

215. Hoa, X. D., Kirk, A. G. & Tabrizian, M. Enhanced SPR response from patterned immobilization of surface bioreceptors on nano-gratings. *Biosens. Bioelectron.* **24**, 3043–3048 (2009).

216. Rossi, S., Gazzola, E., Capaldo, P., Borile, G. & Romanato, F. Grating-Coupled Surface Plasmon Resonance (GC-SPR) Optimization for Phase-Interrogation Biosensing in a Microfluidic Chamber. *Sensors* **18**, 1621 (2018).

217. Chiefari, J. *et al.* Living Free-Radical Polymerization by Reversible Addition−Fragmentation Chain Transfer: The RAFT Process. *Macromolecules* **31**, 5559–5562 (1998).

218. Perrier, S. *50th Anniversary Perspective* : RAFT Polymerization—A User Guide. *Macromolecules* **50**, 7433–7447 (2017).

RÉSUMÉ

Les nanoparticules d'or possèdent une grande section efficace d'absorption de la lumière grâce à leur effet de résonance plasmonique de surface localisée. Cela en fait des photosensibilisateurs prometteurs pour diverses applications biomédicales. En particulier, les nano-bâtonnets d'or (AuNRs) peuvent absorber efficacement la lumière dans le proche infrarouge (NIR), la fenêtre optimale pour la pénétration de la lumière dans les tissus. Par conséquent, les AuNRs présentent un potentiel important comme photosensibilisateurs.

Lorsque les AuNRs absorbent la lumière, ils génèrent des électrons « chauds », à haute énergie au sein de leur structure. Ces électrons chauds peuvent convertir directement l'énergie absorbée en chaleur, ce qui entraîne une augmentation de la température dans l'environnement. Cet effet de chauffage localisé peut tuer efficacement les cellules cancéreuses. Alternativement, les électrons chauds peuvent réagir avec l'eau ou les molécules de dioxygène, ce qui produit des espèces réactives d'oxygène cytotoxiques. Ces espèces peuvent induire la mort cellulaire programmée. Cependant, les défis actuels des photothérapies réalisées par des AuNRs concernent la faible efficacité de la conversion et de l'utilisation de l'énergie plasmonique. Une solution possible pour relever ce défi consiste à combiner les AuNRs avec des semi-conducteurs. Cette combinaison permet le transfert de l'énergie lumineuse absorbée par les AuNR vers le semi-conducteur, soit par injection d'électrons chauds, soit par transfert d'énergie.

Nous avons synthétisé des nanoparticules hybrides en forme d'haltères composées d'AuNR et de dioxyde de titane (TiO_2) appelées AuNR/TiO_2. Dans cette hétérostructure, les électrons chauds générés au sein des AuNR sont injectés dans la bande de conduction du TiO_2. Ce transfert permet aux électrons chauds d'avoir une durée de vie prolongée, et de réagir efficacement avec les molécules de dioxygène dans l'environnement pour générer des radicaux hydroxyles. Pour assurer la stabilité de ces nanoparticules dans un environnement physiologique, nous avons fonctionnalisé les nanoparticules hybrides AuNR/TiO_2 avec des ligands polymères de polyéthylène glycol-phosphonate. La densité de ces ligands polymères à la surface des nanoparticules joue un rôle crucial dans l'obtention d'une photoactivité optimale. Nous avons démontré l'efficacité de ces nanoparticules hybrides pour la photothérapie *in vitro* sur des cellules cancéreuses en les irradiant dans le proche infrarouge.

De plus, nous avons synthétisé des nanoparticules hybrides AuNRs avec des matériaux semi-conducteurs tels que le sulfure d'argent et le sulfure de cuivre. Dans ces systèmes, l'énergie plasmonique présente dans les AuNRs peut être transférée aux matériaux semi-conducteurs. Ce processus conduit à la création d'excitons dans les semi-conducteurs, qui peuvent ensuite générer des espèces réactives d'oxygène. Pour améliorer l'efficacité de ce transfert d'énergie et empêcher une recombinaison indésirable entre les électrons et les trous excités, nous avons introduit une couche de silice isolante à l'interface entre l'or et le semi-conducteur. Nous avons également évalué la photoactivité de ces nanoparticules hybrides sous illumination infrarouge.

Enfin, l'efficacité thérapeutique des nanoparticules est souvent compromise par une mauvaise biodistribution, la majorité des nanoparticules injectées étant captées par les macrophages. Pour relever ce défi, nous avons testé différents polymères zwitterioniques pour fonctionnaliser différentes nanoparticules inorganiques et éviter leur capture par les macrophages. Leurs interactions avec les protéines et les macrophages ont été étudiées *in vitro*. De plus, nous avons mené des études pharmacocinétiques sur des AuNRs fonctionnalisées avec différents types de polyzwitterions, afin d'évaluer leur temps de circulation in vivo.

MOTS CLÉS

Nano-bâtonnet d'or, semiconducteur, photothérapie, chimie de surface zwitterionique

ABSTRACT

Gold nanoparticles possess high light absorption cross sections due to their localized surface plasmon resonance, making them promising photosensitizers for various biomedical applications. Among them, gold nanorods (AuNRs), can effectively absorb light in the near-infrared range, which is the optimal window for light penetration into the human body. As a result, AuNRs hold significant potential as photosensitizers for phototherapy.

When AuNRs absorb light, they generate high-energy “hot” electrons within their structure. These hot electrons can directly convert the absorbed energy into heat, leading to a temperature increase in the surrounding environment. This localized heating can effectively kill cancer cells. Alternatively, hot electrons can react with water or dioxygen in the environment, generating cytotoxic reactive oxygen species. These reactive oxygen species can induce programmed cell death. However, current challenges in phototherapies involving AuNRs revolve around the low efficiency of plasmonic energy conversion and utilization, limiting their further clinical trials. One possible solution to address this challenge is to combine AuNRs with specific semiconductors. This combination allows for the transfer of light energy absorbed by AuNRs to the semiconductor material, either through hot electron injection or energy transfer mechanisms.

We synthesized hybrid dumbbell-shaped nanoparticles consisting of gold nanorods (AuNRs) and titanium dioxide (TiO_2), AuNR/TiO_2. In this heterostructure, hot electrons generated within the AuNRs could be directly injected into the conduction band of TiO_2. This transfer extends the lifetime of energetic electrons, enabling them to effectively react with dioxygen in the environment and generate hydroxyl radicals. To ensure the stability of these nanoparticles in a physiological environment, we functionalized them with polyethylene glycol-phosphonate polymer ligands. The density of these polymer ligands on the nanoparticle surface plays a crucial role in achieving optimal photoactivity. We then evaluated the potential of these hybrid nanoparticles for photodynamic therapy *in vitro* on cancer cells after irradiation with near-infrared (NIR) light.

We also explored the combination of AuNRs with semiconductor materials such as silver sulfide and copper sulfide, resulting in the formation of core-shell hybrid nanostructures. In these hybrid systems, the plasmon energy present in the AuNRs is transferred to the semiconductor materials through dipole-dipole interactions. This energy transfer process leads to the creation of exciton pairs within the semiconductors, which can further generate reactive oxygen species. To enhance the efficiency of this energy transfer and prevent undesired recombination between excited electrons and holes, we introduced an insulating silica layer at the interface between the gold and semiconductor components. We also assessed the photoactivity of these hybrid nanoparticles under continuous-wave NIR illumination.

Lastly, the therapeutic efficacy of nanoparticles is often compromised by their poor biodistribution, as the majority of injected nanoparticles are recognized and captured by macrophages. To address this challenge, we tested the ability of different zwitterionic polymer ligands to avoid nanoparticle capture by macrophages. Semiconductor quantum dots, iron oxide and gold nanoparticles decorated with polyzwitterions were synthesized. Their interactions with proteins and macrophages were investigated *in vitro* to assess their potential for improved biocompatibility and reduced macrophage uptake. Furthermore, we conducted pharmacokinetic studies on AuNRs functionalized with different types of polyzwitterions. These studies aimed to evaluate the behavior of these functionalized nanoparticles within the body and gain insights into their distribution and clearance pathways.

KEYWORDS

Gold nanorod, semiconductor, phototherapy, zwitterionic surface chemistry